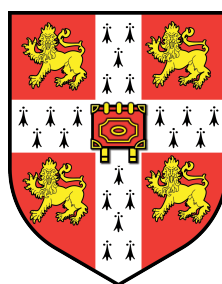# Phenomenology of new physics beyond the Standard Model: signals of Supersymmetry with displaced vertices and an extended Higgs sector at colliders

Giovanna Francesca Cottin Buracchio

Newnham College,
University of Cambridge

Phenomenology of new physics beyond the Standard Model: signals of Supersymmetry with displaced vertices and an extended Higgs sector at colliders

Giovanna Francesca Cottin Buracchio

Our current understanding of matter and its interactions is summarised in the Standard Model (SM) of particle physics. Many experiments have tested the predictions of the SM with great success, but others have brought our ignorance into focus by showing us there are new phenomena that we can not describe within the framework of the SM. These include the experimental observations of neutrino masses and dark matter, which confirms there must be new physics.

What this new physics may look like at colliders motivates the original work in this thesis, which comprises three studies: the prospects of future electron-positron colliders in testing a model with an extended Higgs sector with a scalar triplet, doublet and singlet; the discovery potential at the Large Hadron Collider (LHC) of a non-minimal Supersymmetric model via conventional sparticle searches and via searches for displaced vertices; and the experimental search for long-lived massive particles via a displaced vertex signature using data of proton-proton collisions collected at a collider center of mass energy of 8 TeV in 2012 by the ATLAS detector operating at the LHC.

Declaration

This dissertation is the result of my own work, except as declared in the Preface and specified in the text. It shares no substantial part with, nor it is substantively the same as, anything that has been previously submitted or is being concurrently submitted for any degree, diploma or qualification, be it at the University of Cambridge or elsewhere. As required by the Degree Committee for Physics and Chemistry, it contains fewer than 60,000 words.

Giovanna Francesca Cottin Buracchio

Acknowledgements

I thank Nick Barlow, who was my supervisor during the first two years of my PhD and my friend while we performed the ATLAS displaced vertex analysis. My sincere thanks to Andy Parker and Ben Gripaios for kindly taking me as supervise after I decided to switch paths from experiment to theory. Thank you Andy for accepting me into the PhD in the first place and for all your support towards the end of it.

Many thanks to Ben Allanach for giving me the opportunity to collaborate with him during my transition to theory. It has been really a pleasure to learn from you Ben. I am also grateful to all members of the High Energy Physics group at the Cavendish Laboratory and to the members of the Cambridge Supersymmetry Working Group for the many fruitful meetings and discussions, in particular, Marco Nardecchia and Chris Lester. I would also like to express my gratitude to Marco A. Díaz, who has been a mentor and collaborator ever since I started my career.

I also feel the need to thank my family. First my parents, Mauricio and Lorena, to which this thesis is dedicated to. Thank you Dad for inspiring me to pursue a career in fundamental physics and to you Mum for teaching me all the things one can not learn from books. Thanks to my sisters, Antonella and Sophia for their empathy during these years, and my twin Nicolás, for even while fighting cancer, always staying strong for me. Thank you my brother for your words four years ago at an airport gate - "you must go" -, when my heart was telling me to stay in Chile beside you. I would not be writing these words if the choice of yours would have been different.

Finally, I would like to thank my best friend, partner and husband, Gabriel Torrealba. Gabriel, we started this journey together and I am so lucky and grateful for having you by my side. I have truly had the time of my life in Cambridge next to you. Thank you for always believing in me. I could not have completed this PhD without your undying support and love.

Preface

This thesis describes most of the research work undertaking during my PhD, both in experiment and theory in the field of High Energy Particle Physics (HEP). Part I and II of this thesis should be read as a necessary introduction, motivation and literature review of material taken from the references cited within the text, and not as my original contributions to the field. Part III and IV highlights my work done in collaboration with other people, which is based on the contents of three published papers.

Chapter 7 [1] was a collaborative effort with members of the ATLAS displaced vertex (DV) team, and is based on years of optimisation of the DV analysis within ATLAS and also the smooth operation of CERN's LHC and the ATLAS experiment. This Chapter explains my contributions to the DV analysis, which focused in the implementation of the DV+p_T^{miss} and DV+jets searches. Parts of the analysis not related at all to my own work are not included. Only dominant systematic uncertainties in the DV+p_T^{miss} and DV+jets searches are stated in Section 7.3. Most of these were my own implementation, with the exception of the effect of initial and final-state radiation on jets, implemented by N. Pettersson and the uncertainty on trackless jets, done by N. Barlow. All systematic corrections described in [1] are included in the final results of this thesis, but the studies not mentioned are not my work, so are not described. The results from background estimation in Section 7.5 were performed by N. Barlow, H. Otono and N. Pettersson. These are incorporated into the final result of the thesis, but the studies themselves are not my own work so are not described. Some of the contents from this Chapter are copied almost verbatim from [1].

Chapter 8 [2] was done in collaboration with B.C. Allanach, N. Desai, M. Badziak, R. Ziegler and C. Hugonie. B.C. Allanach contributed to the idea of the project and supervised every aspect of it. M. Badziak and R. Ziegler contributed to the generation of the pNMSSM spectrum in Section 8.1 for our signal model. C. Hugonie performed the numerical scan leading to our benchmark point P0. N. Desai applied the standard "prompt" collider constrains to the model in Section 8.1 and performed the standard reconstruction

of jets and p_T^{miss} within the PYTHIA 8 event generator. My specific contribution was the implementation of displaced vertex searches on the model in Section 8.2. This included the creation of a model independent reconstruction algorithm for displaced vertices inside PYTHIA 8, in addition to the validation against ATLAS models of such algorithm and to develop a strategy - by combining standard prompt cuts with looser displaced vertex cuts - for discovering the model after realising current limitations from displaced searches at ATLAS. Significant content from this Chapter is copied almost verbatim from [2].

Chapter 9 [3] was done in collaboration with M.A. Díaz, S. Blunier and B. Koch. M.A. Díaz contributed to the idea of the project and supervised every aspect of it. B. Koch gave comments along the project. The extraction of the cross-sections with MADGRAPH5 in Sections 9.2 and 9.3 was done by S. Blunier. My specific contributions included the identification of the model benchmarks and constrains in Section 9.1 along with S. Blunier, the extraction of all relevant Feynman rules in Appendix A after the model was implemented in FEYNRULES by S. Blunier, the computation of all decays in Section 9.4 and identifying the promising channels for discovery in Section 9.5. Significant content from this Chapter is copied almost verbatim from [3].

Contents

"To Mum and Dad, for their inspiration and love"

"If I had to live my life again I should certainly not choose to be a writer and spend my days in a backward society where adventure is kept under the bed, like a dog. I should have a lion-like adventure: I would go in for theoretical physics in order to live at the very heart of true romance"
    — The Morning of the Magicians, Louis Pauwels and Jacques Bergier

Part I

Theoretical foundations

Chapter 1

The Standard Model of particle physics and beyond

Our current understanding of matter and its interactions is summarised in the Standard Model (SM) of particle physics [4–10], the theoretical framework that describes almost all known elementary particle interactions, except for gravity. It describes three of the four fundamental forces known in Nature - the electromagnetic, weak, and strong nuclear force - and classifies all the subatomic particles known to date. A pictorial summary of the SM is given in Figure 1.1. Table 1.1 shows relevant values and quantum numbers for all known elementary particles.

Many experiments have tested the predictions of the SM with great success[1], including in 2012 the last confirmation of the SM with the discovery of the Higgs boson[2]. Nevertheless, other observations have brought our ignorance into focus by showing us there are new phenomena that we can not describe within the framework of the SM. These include the preference of matter over antimatter in our Universe, neutrino masses and dark matter[3].

This Chapter aims to give a brief introduction to the SM and outline the reasons why it must be extended, exposing the need to search for new physics beyond the SM (BSM). Most of the content in this Chapter is based on Refs. [10, 16, 17] and emphasizes concepts and topics to be discussed in the rest of the thesis.

---

[1] The SM interactions have been tested very accurately (at the per mille level) mainly by LEP (Large Electron Positron collider) at CERN and the proton-antiproton collider Tevatron at Fermilab [13].

[2] Made by the ATLAS and CMS collaborations at CERN's Large Hadron Collider (LHC) [14, 15].

[3] These observations will be clarified in Section 1.3.
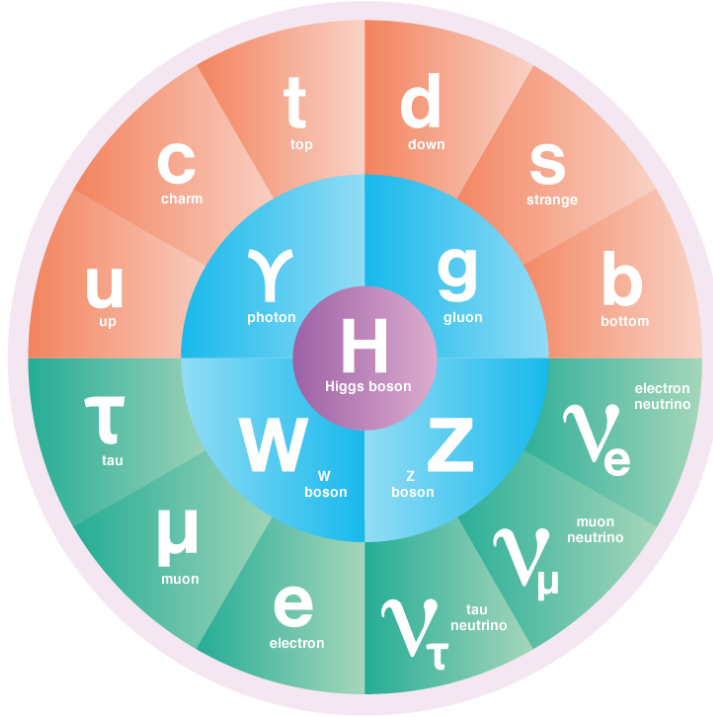
Figure 1.1: The Standard Model of particle physics, obtained from [11]. Quarks are in light red, leptons in green, gauge bosons in light blue and in purple is the Higgs boson. The photon is the carrier of the electromagnetic force. The gluon is the carrier of the strong force. The W and Z bosons are carriers of the weak force. The Higgs field gives mass to all fundamental particles.

Name	Discovered at	Mass	Charge	Colour	Spin	Lifetime
electron e	Cavendish Laboratory (1897)	0.511 MeV	-1	no	1/2	stable
muon μ	Caltech & Harvard (1937)	105.66 MeV	-1	no	1/2	2.2×10^{-6} sec
tau τ	SLAC (1976)	1776.82 MeV	-1	no	1/2	2.9×10^{-13} sec
electron neutrino ν_e	Savannah River Plant (1956)	< 2 eV	0	no	1/2	stable
muon neutrino ν_μ	Brookhaven (1962)	< 0.19 MeV	0	no	1/2	stable
tau neutrino ν_τ	Fermilab (2000)	< 18.2 MeV	0	no	1/2	stable
up quark u	SLAC (1968)	2.3 MeV	2/3	yes	1/2	stable
down quark d	SLAC (1968)	4.8 MeV	-1/3	yes	1/2	stable
charm quark c	Brookhaven & SLAC (1974)	1.275 GeV	2/3	yes	1/2	1.1×10^{-12} sec
strange quark s	Manchester University (1947)	95 MeV	-1/3	yes	1/2	1.24×10^{-8} sec
top quark t	Fermilab (1995)	173.21 GeV	2/3	yes	1/2	4.2×10^{-25} sec
bottom quark b	Fermilab (1977)	4.18 GeV	-1/3	yes	1/2	1.3×10^{-12} sec
photon γ	Washington University (1923)	0	0	no	1	stable
gluon g	DESY (1979)	0	0	yes	1	stable
W boson	CERN (1983)	80.385 GeV	± 1	no	1	3×10^{-25} sec
Z boson	CERN (1983)	91.1876 GeV	0	no	1	3×10^{-25} sec
Higgs boson H	CERN (2012)	125.7 GeV	0	no	0	1.56×10^{-22} sec

Table 1.1: Parameters of known elementary particles. Idea taken from [11]. Parameters extracted from [12].

1.1 An $SU(3) \times SU(2) \times U(1)$ theory

The SM is a gauge quantum field theory (QFT) with gauge symmetry $SU(3)_C \times SU(2)_L \times U(1)_Y$. $SU(3)_C$ is the gauge symmetry of quantum chromodynamics (QCD) [7,8], the theory of the strong interactions, and $SU(2)_L \times U(1)_Y$ is the symmetry of electroweak interactions [4–6]. The SM is essentially built by requiring invariance under local transformations of the gauge group (i.e gauge invariance), invariance under the Poincaré group (translations, rotations and Lorentz boosts) and renormalisability (which tells us that the quantitative predictions of the theory at low energies is not affected by the dynamics at much higher energies).

The matter content of the SM consists of 6 leptons and 6 quarks that pair up to transform under $SU(2)_L$. There are 3 generations[4] of left-handed $SU(2)$ doublet pairs of quarks and leptons (fermions), listed in Table 1.2. Right-handed fermions[5] are $SU(2)$ singlets and are indexed by the first-generation label (such that $U = u_R^\dagger$ and $D = d_R^\dagger$). Summarizing, SM fermions consists of 3 copies of 5 fields $\psi_i = Q, u_R^\dagger, d_R^\dagger, L, e_R^\dagger$.

Fermion name	Field	Spin 1/2	$SU(3)_C$, $SU(2)_L$, $U(1)_Y$
quarks	Q^i	$(u_L \; d_L),\ (c_L \; s_L),\ (t_L \; b_L)$	$(\,\mathbf{3},\,\mathbf{2}\,,\,\frac{1}{6})$
	U^i	$u_R^\dagger,\ c_R^\dagger,\ t_R^\dagger$	$(\,\overline{\mathbf{3}},\,\mathbf{1},\,-\frac{2}{3})$
	D^i	$d_R^\dagger,\ s_R^\dagger,\ b_R^\dagger$	$(\,\overline{\mathbf{3}},\,\mathbf{1}\,,\,\frac{1}{3})$
leptons	L^i	$(\nu_e \; e_L),\ (\nu_\mu \; \mu_L),\ (\nu_\tau \; \tau_L)$	$(\,\mathbf{1},\,\mathbf{2}\,,\,-\frac{1}{2})$
	E^i	$e_R^\dagger,\ \mu_R^\dagger,\ \tau_R^\dagger$	$(\,\mathbf{1},\,\mathbf{1}\,,\,1)$

Table 1.2: Fermion fields in the Standard Model. Quarks carry $SU(3)$ colour charge (red, green or blue), while leptons are colourless. The superscript $i = 1,2,3$ indexes the generation. The subscripts L and R indicate the implicit chirality of the field. Note that the two-component fields are written in a line for convenience. A Dirac fermion Ψ is formed with 2 Weyl spinors $\Psi = \begin{pmatrix} \psi_L \\ \psi_R \end{pmatrix}$. The table shows left-handed Weyl spinors ψ_L, as the Hermitian conjugate of any right-handed Weyl spinor is a left-handed Weyl spinor. The gauge representation in the last column indicates singlet, doublet or triplet representations and the last entry corresponds to Y, the weak hypercharge.

In addition to the fermions, the gauge sector of the SM contains spin-1 gauge boson fields of the symmetry group $SU(3)_C \times SU(2)_L \times U(1)_Y$. These are listed in Table 1.3.

---

[4] Also termed families, copies or flavours.
[5] Right-handed neutrinos have not been observed and are not present in the SM.

Boson name	Field	Spin 1		$SU(3)_C$, $SU(2)_L$, $U(1)_Y$
gluon	G_μ^a	g		(**8**, **1** , 0)
W bosons	W_μ^a	$W^\pm$	W^0	(**1**, **3** , 0)
B boson	B_μ	B^0		(**1**, **1** , 0)

Table 1.3: Gauge fields in the Standard Model. There are 8 gluon fields $a = 1, .., 8$ corresponding to the 8 generators of $SU(3)_C$. The 3 weak isospin generators of $SU(2)_L$ are W_μ^a with $a = 1, 2, 3$. The $U(1)_Y$ weak hypercharge symmetry has one singlet gauge field, B_μ. The gauge representation in the last column indicates singlet, triplet or octect representations and the last entry corresponds to Y, the weak hypercharge.

The SM also has a complex scalar Higgs doublet H, with (**1**, **2** , 1/2) representation under $SU(3)_C$, $SU(2)_L$, $U(1)_Y$, respectively. All fermions couple to the gauge bosons and the Higgs scalar field. The SM Lagrangian can be written generally as,

$$\mathcal{L}_{\text{SM}} = i\psi_i^\dagger \bar{\sigma}^\mu D_\mu \psi_i - \frac{1}{4} F^{a\mu\nu} F_{\mu\nu}^a - Y^{ij} \psi_i^\dagger \psi_j H + |D_\mu H|^2 + \mu^2 H^\dagger H - \lambda (H^\dagger H)^2 + \text{h.c}$$
(1.1)

with $\bar{\sigma}^\mu = (1, -\sigma^i)$ with σ^i the three Pauli matrices. The covariant derivative is $D_\mu = \partial_\mu - ig'Y B_\mu - \frac{i}{2} g \sigma^a W_\mu^a - \frac{i}{2} g_s \lambda_a G_\mu$. g', g and g_s are the $U(1)$, $SU(2)$ and $SU(3)$ couplings, respectively. The $\sigma^a W^a$ (with σ^a the three Pauli matrices, the generators of $SU(2)$) term will be absent when a particle is $SU(2)_L$ singlet and for a field with $SU(3)_C$ colour, the extra term $-\frac{i}{2} g_s \lambda_a G_\mu$ is included to the covariant derivative, where $\lambda_a, a = 1, .., 8$ are the Gell-Mann matrices, the generators of $SU(3)$. The field strength tensor is $F_{\mu\nu}^a = \partial_\mu F_\nu^a - \partial_\nu F_\mu^a + g f_{abc} F_\mu^b F_\nu^c$ for a gauge boson field $F = W, B, G$, with g the corresponding coupling. f_{abc} are known as structure constants. A Lie group is abelian if $f_{abc} = 0$ (in the case of $U(1)$) and non-abelian otherwise. We can note that for non-abelian gauge theories or Yang-Mills theories the presence of these structure constants leads to self-interactions of the gauge bosons. In the case of QCD, it is strongly believed that is the (coloured) gluon self-interaction that leads to confinement of quarks within a nucleus [18]. Free quarks have never been seen and only colour-neutral combinations (i.e. hadrons) are observed, such as mesons and baryons (states with two and three quarks). While at long distances QCD confines color, at short distances (or high energies) the theory is asymptotically free [19], meaning that the strong force becomes relatively weak, allowing quarks and gluons to behave as free particles inside hadrons.

The 3×3 complex matrices Y^{ij} in equation 1.1 are Yukawa matrices characterizing the flavour sector. The Higgs potential is

$$V(H) = -\mu^2 |H|^2 + \lambda |H|^4. \tag{1.2}$$

1.2 Electroweak symmetry breaking, the Higgs and particle masses

Electroweak unification is based on the symmetry breaking of $SU(2)_L \times U(1)_Y \to U(1)_Q$. The electroweak force is spontaneously broken down to the electromagnetic and weak forces at low energies. The massless photon arises as a linear combination of the hypercharge gauge boson and one of the generators of $SU(2)_L$. Gauge invariance forbids an explicit mass term for the gauge bosons in equation 1.1, and we know from experimental evidence the W and Z are indeed massive. The solution to this issue in the SM is provided by the Higgs mechanism of electroweak symmetry breaking (EWSB) [20–25].

In the SM, $SU(2)_L \times U(1)_Y$ is broken by the vacuum expectation value (vev) of the Higgs field H. The Higgs doublet complex field can be written in term of four real degrees of freedom,

$$H = \frac{1}{\sqrt{2}} \begin{pmatrix} \phi_1 + i\phi_2 \\ \phi_3 + i\phi_4 \end{pmatrix} \tag{1.3}$$

and we know that by gauge symmetry we can rotate this doublet $H \to U(x)H$ (with $U(x)$ being a general $SU(2)$ gauge transformation) such that three degrees of freedom are removed from H and are contained in $U(x)$, which has three parameters. We can then further fix the gauge by setting $\phi_1 = \phi_2 = \phi_4 = 0$, such that the only non-zero component of H is the neutral real scalar[6]$\phi_3 \equiv \phi$.

The Higgs potential in 1.2 must be bounded from below for it to be stable and to ensure it has a global minimum, forcing $\lambda > 0$. For $\mu^2 > 0$, it will have a minimum for field values satisfying $|H| = HH^\dagger = \mu/\sqrt{\lambda}$. Due to the gauge fixing we did before, only one component of the Higgs doublet will get a minimum or vev, so the gauge symmetry is spontaneously broken, meaning that the vacuum of the theory does not share the

---

[6] This particular choice of gauge or gauge fixing is called the unitary gauge.

symmetry of the Lagrangian in 1.1. The vev of the Higgs field is $\langle H \rangle = \begin{pmatrix} 0 \\ \frac{v}{\sqrt{2}} \end{pmatrix}$, with $v = \frac{\mu}{\sqrt{\lambda}}$.

Note that this vev breaks 3 of the 4 symmetries[7] and one combination of $U(1)_Y$ and $SU(2)_L$ remains unbroken: electromagnetism $U(1)_Q$. We can see this by checking that $(\frac{\sigma^3}{2} + Y)\langle H \rangle = 0$, which tells us the combination $Q = \frac{\sigma^3}{2} + Y$ is the unbroken generator, as it does not change the vev of the field (and corresponds to the unbroken symmetry). We identify Q with the electric charge[8]. The vacuum is invariant under a transformation $\langle H \rangle \to e^{i\alpha(x)Q}\langle H \rangle = \langle H \rangle$. All other electroweak generators are broken by vacuum. The gauge bosons corresponding to those generators will get masses.

By expanding H around its minimum we find the spectrum of the theory. We expand the field around the vev such that $\phi = v + h$, were the excitation h is a real scalar, corresponding to the physical Higgs boson particle. Using $H = \frac{1}{\sqrt{2}}\begin{pmatrix} 0 \\ v + h \end{pmatrix}$ in the kinetic term $|D_\mu H|^2$ in 1.1 the gauge bosons masses will arise from,

$$\mathcal{L} = g^2 \frac{v^2}{8}[(W_\mu^1)^2 + (W_\mu^2)^2 + (\frac{g}{g'}B_\mu - W_\mu^3)^2], \tag{1.4}$$

and the mass eigenstates are found by the following transformation of the fields,

$$W_\mu^\pm \equiv \frac{1}{\sqrt{2}}(W_\mu^1 \mp W_\mu^2)$$

$$Z_\mu \equiv \cos\theta_W W_\mu^3 - \sin\theta_W B_\mu$$

$$A_\mu \equiv \sin\theta_W W_\mu^3 + \cos\theta_W B_\mu \tag{1.5}$$

---

[7] Spontaneous symmetry breaking has different implications depending on the nature of the symmetry. If the symmetry is a continuous global symmetry, such as $\phi(x) \to e^{i\alpha}\phi(x)$, the breaking of the symmetry implies the existence of massless particles (Goldstone bosons). If the symmetry is gauged, such that $\phi(x) \to e^{i\alpha(x)}\phi(x)$ with an associated massles gauge field, then the gauge boson will acquire a mass (via the Higgs mechanism) [10]. In unitary gauge we say that the gauge boson "eats" the Goldstone boson through the Higgs mechanism. The original symmetry was $\phi_1^2 + \phi_2^2 + \phi_3^2 + \phi_4^2 = HH^\dagger/2 = $ constant, so three global symmetries are broken when choosing a particular direction and the three degrees of freedom (i.e the "would be" massless Goldstone bosons) will become the longitudinal part of the $W^\pm$ and the Z bosons.

[8] Note that $\frac{\sigma^3}{2} = T^3$ is the third component of weak isospin. Other convention used is $Q = T^3 + \frac{Y}{2}$ where $Y = -1$ for leptons for instance. Y in this sense is a free parameter of the theory and is adjusted appropriately so that the electric charges of the quarks and leptons come out correctly.

with $\tan\theta_W \equiv g'/g$, with θ_W the Weinberg angle. Inserting equations 1.5 in 1.4, we see that the mass terms for the gauge bosons are

$$
\begin{aligned}
m_A &= 0 \\
m_W &= \frac{gv}{2} \\
m_Z &= \frac{v}{2}\sqrt{g^2 + g'^2} = \frac{m_W}{\cos\theta_W}
\end{aligned}
\tag{1.6}
$$

where there is no mass term for the photon A_μ. The mass of the W and the Z are related. Often the ρ parameter [26] is defined as,

$$
\rho = \frac{m_W^2}{(m_Z\cos\theta_W)^2}
\tag{1.7}
$$

which is equal to 1 at the tree level in the SM and it is precisely measured[9].

Considering the terms for h in 1.1, we find that the mass of the Higgs is given by,

$$
m_h = \sqrt{2}\mu = \sqrt{2\lambda}v
\tag{1.8}
$$

The mass terms for fermions will arise from the Yukawa interaction terms in equation 1.1, given by

$$
\mathcal{L} = -Y_l^{ij}e_{Ri}^\dagger L_j H - Y_u^{ij}u_{Ri}^\dagger Q_j i\sigma_2 H^* - Y_d^{ij}d_{Ri}^\dagger Q_j H + \text{h.c}
\tag{1.9}
$$

After EWSB, the mass terms become

$$
\mathcal{L} = -\frac{v}{\sqrt{2}}Y_l^{ij}e_{Ri}^\dagger e_{Lj} - \frac{v}{\sqrt{2}}Y_d^{ij}d_{Ri}^\dagger d_{Lj} - \frac{v}{\sqrt{2}}Y_u^{ij}u_{Ri}^\dagger u_{Lj} + \text{h.c.}
\tag{1.10}
$$

from where we see that fermion masses are proportional to the Higgs vev. The Yukawa matrices are in general non-diagonal. Fermion masses are of the form

---

[9] Deviations from unity in this parameter could imply BSM physics.

$$m_f = \frac{v}{\sqrt{2}} Y_f \tag{1.11}$$

were $f = l, u, d$ stands for the leptons, up and down quarks, respectively and Y_f are the diagonal elements of the corresponding diagonalized Yukawa matrix. We can go to a diagonal mass basis by rotating the fields in the quark sector[10] via two unitary matrices U_d, U_u, so that the fields will transform as $u_L \to U_u u_L$ and $d_L \to U_d d_L$. The mass matrices mix the weak eigenstates of different generations and the resulting mixing matrix is defined as $V_{\text{CKM}} \equiv U_u^\dagger U_d$, and is known as the Cabibbo-Kobayashi-Maskawa (CKM) matrix. The CKM matrix can be parametrized by three angles and a phase. The presence of a non-zero phase implies $CP-$violation in the SM.[11]

1.3 The need for new physics and motivations of this thesis

Despite the success of the SM in explaining the observed data at low energies, there are many reasons we do not accept it as a final theory of Nature. The SM leaves many fundamental questions unanswered[12], starting by the fact that it must be extended to incorporate the effects of quantum gravity arising at the Planck scale $\Lambda \sim 10^{19}$ GeV. Other puzzles include the hierarchy of the parameters in the flavour sector (i.e fermion masses and CKM angles), the number of fermion families (why three?) and the lack of unification of the three gauge coupling constants at a certain (grand unification) scale. Another issue is the so-called hierarchy problem, which arises from the fact the SM does

---

[10] Rotating the fields in the quark sector only has an observable effect in the weak charged current interactions with the $W^\pm$, which transform flavour states. Neutral currents are not affected by the redefinition of the fields. Also, a field transformation in the lepton sector is not observable because we can also redefine the lepton and neutrino states and absorb the transformation matrix. However, we can see a similar mixing with the charged leptons and the neutrinos when neutrinos are massive, but we leave that discussion for Section 1.3, as this is a BSM effect.

[11] CP refers to charge conjugation and parity. As left-handed fields couple differently from right-handed ones, the SM violates parity. Charge conjugation interchanges particles with antiparticles. We know the CP combination is also violated in the SM weak interactions by rare processes involving hadrons. There is another possible form of $CP-$violation in the SM, known as strong $CP-$violation, which is expected but has never been observed. This issue is known as the "strong CP problem" [10] and it motivates BSM model building, such as models with axions [27, 28]. Axions are also good dark matter candidates [17].

[12] For a more extensive list of unsolved issues or problems in the SM, see Refs [17, 29].

not explain why the Higgs should be light. Looking at the SM as an effective field theory (EFT), we understand that it is valid until a certain scale (i.e cut-off scale) that we call Λ_{SM} (which could be the Planck scale, unless there is some new physics in between at the TeV scale). Why is $m_h \ll \Lambda_{\text{SM}}$? Or in other words, why is the electroweak scale so small in units of the cut-off? This is the hierarchy problem, and it has been a major motivation in the construction of BSM theories.

Even more, there is experimental data that can not be explained within the SM, including:

- neutrino masses and mixing angles [30–35]: neutrinos change their flavour while traveling free in space, implying they are massive and that their flavours mix. This is a clear indication of BSM physics.

- the presence of dark matter [36–41]: observations of galaxy rotation curves and the Cosmic Microwave Background (or CMB, the thermal radiation left over from the Big Bang) tells us there must be a different type of matter that is non-luminous (is "dark"). We can only infer is there via the gravitational effects it has on normal matter. About 27% of the mass of our Universe is made of this neutral, colourless, non-baryonic, cold dark matter, which is not accounted for in the SM.

- the observed abundance of matter over antimatter [42]: the Universe has more baryons than anti-baryons. Such an asymmetry in baryon number can be achieved if CP is violated, via a proposed mechanism known as baryogenesis [43]. However, the only known source of $CP-$violation in the SM is the phase in the CKM mixing matrix, and this amount of $CP-$violation is not enough to explain the baryon density.

This experimental evidence confirms that there must be BSM physics. In the rest of this Chapter we will detail the main motivations for the works in this thesis, which are:

- the study of a model with an extended Higgs sector, motivated by the need of a mechanism that explains why neutrinos are massive and the need for a dark matter particle candidate.

- the study of long-lived particles in Supersymmetry, a theoretical BSM scenario motivated by naturalness (the hierarchy problem), gauge unification and the need for a dark matter particle candidate.

- the (model independent) experimental search for long-lived particles via a displaced vertex signature, which is a motivation on its own in this thesis, as long-lived states can be present in many BSM theories.

1.3.1 Neutrino masses as a motivation for an extended Higgs sector

Neutrinos are massive and we need to extend the SM to account for this fact. There are two different mass terms that are allowed for neutral fermions like neutrinos: Dirac and Majorana. If we assume right-handed neutrinos exist[13], neutrino masses can be generated after EWSB via Yukawa interaction terms with the Higgs boson with a term of the form $Y_\nu^{ij} \nu_{Ri}^\dagger L_j H$, in an analogous way as in equation 1.9. The mass term that arises is of the same kind as other fermions, $m_\nu = \frac{v}{\sqrt{2}} Y_\nu$, and is called a Dirac mass term. This is the simplest possibility to give neutrinos mass.

However, a Dirac mass term for neutrinos does not naturally explains the smallness of neutrino masses. For a neutrino mass to be in the eV range, a value of $Y_\nu \sim \mathcal{O}(10^{-11})$ or less is needed, which is generally considered unnatural [44]. This is one of the reasons people turn to the so-called see-saw mechanism of neutrino mass generation [45], where a Majorana mass term of the form $M^{ij} \nu_{Ri}^c \nu_{Rj}$ can also be possible, where ν_R^c is the charge conjugate of ν_R. Another reason to consider a Majorana mass term is that nothing really forbids it. Once it is there, total lepton number is violated (as Majorana fermions are their own antiparticles), but lepton number conservation is an accidental symmetry of the SM, so a Majorana mass term is not forbidden by electroweak symmetry.

The most general mass term for neutrinos includes both Majorana and Dirac mass terms. A Dirac spinor for neutrinos would be $\Psi = \begin{pmatrix} \psi_L \\ \psi_R \end{pmatrix}$. We can construct Dirac spinors out of single Weyl spinors ν_L and ν_R by defining the (four-component) Dirac spinors $\Psi_L = \begin{pmatrix} \nu_L \\ i\sigma^2 \nu_L^* \end{pmatrix}$ and $\Psi_R = \begin{pmatrix} -i\sigma^2 \nu_R^* \\ \nu_R \end{pmatrix}$ (with $\nu_R = i\sigma^2 \nu_L^*$ and $\nu_R^c = \nu_R^T \sigma^2$) [10]. In this way, Dirac and Majorana mass terms can be written in a uniform notation as,

$$\mathcal{L} = -m \bar{\Psi}_L \Psi_R - \frac{M}{2} \bar{\Psi}_R \Psi_R \tag{1.12}$$

---

[13] Sometimes people also refer to right-handed neutrinos as sterile neutrinos.

considering one generation for simplicity. We can see that Ψ_L and Ψ_R mix, so the neutrino mass eigenstates will arise from diagonalizing the matrix,

$$\mathcal{M}_\nu = \begin{pmatrix} 0 & m \\ m & M \end{pmatrix}. \tag{1.13}$$

Majorana masses can be very large since they arise from effects beyond the SM, for example $M_{\text{GUT}} \sim 10^{16}$ GeV (the scale where the 3 gauge couplings meet when considering a larger group structure like $SU(5)$ [17]). Since Dirac masses are of the order of the electroweak scale, $m \approx 100$ GeV, we have $m \ll M$. The eigenvalues of 1.13 in this limit are,

$$m_N \simeq M \tag{1.14}$$

$$m_\nu \simeq \frac{m^2}{M} \tag{1.15}$$

This leads to an attractive mechanism for explaining the smallness of neutrinos masses compared to charged fermion masses. It is called the see-saw mechanism, as when m_N goes up, m_ν goes down [10].

The origin of neutrino mass can be attributed to a single, non-renormalizable, dimension 5, lepton number violating Weinberg operator [46] of the form,

$$\mathcal{L} = \frac{\lambda^{ij}}{\Lambda} L_i H (H L_j)^\dagger, \tag{1.16}$$

that we can add to the SM. After EWSB, the Higgs gets a vev v and neutrino masses are $m_\nu \sim \lambda \frac{v^2}{\Lambda}$. Note that this term accounts for the smallness of neutrino masses, irrespective of what is the UV theory that replaces this EFT at a given Λ (i.e without the specific need of right-handed neutrinos, which is the simplest possibility).

There are basically three ways to generate the dimension 5 operator in 1.16 at the tree level, or three see-saw models, known as see-saw Type-I, II and III (See Ref. [47, 48] and reference therein). These three mechanisms generate the operator by the exchange of new heavy states, that could be fermion singlets (like right-handed neutrinos), scalar triplets or fermion triplets, respectively. The main idea behind the Type I, II and III

see-saw is that, as the masses of the intermediate states are high, neutrinos naturally become light [47].

Irrespective of the model of neutrino mass generation, if neutrinos are massive Majorana particles, lepton number L is necessary broken. But the nature of the breakdown is not necessarily known. There are three possibilities [49]:

- L is explicitly broken in the Lagrangian (via a Majorana mass term for right-handed neutrinos or via a L violating coupling with the Higgs field).

- L is spontaneously broken locally (i.e gauged), with a resulting massive vector boson (i.e a la Higgs mechanism).

- L is spontaneously broken globally, in which case we have massless Goldstone boson appearing in the theory, the Majoron.

In this thesis, we focus on a particular Type-II see-saw model where lepton number is spontaneously broken globally. This model was first introduced in [50] and it extends the Higgs sector of the SM by adding a scalar singlet field σ and a scalar triplet Δ under $SU(2)$. Given the structure of one singlet, one doublet ϕ (the SM Higgs doublet) and a triplet, the authors in [50] termed it the "123" Higgs triplet model (HTM).

In the "123" HTM, the neutrino mass matrix takes the form [51]

$$\mathcal{M}_\nu = \begin{pmatrix} M_L & m \\ m^T & M_R \end{pmatrix}. \tag{1.17}$$

The entries M_L and M_R arise from the vevs of the triplet v_Δ and singlet v_σ, respectively. It is reasonable to assume the hierarchy $M_L \ll m \ll M_R$, as $m \sim v_\phi$, with v_ϕ is the vev of the Higgs doublet, and $M_L \sim v_\Delta$, this hierarchy is achieved when $v_\Delta \ll v_\phi \ll v_\sigma$[14]. See-saw neutrino masses arise from the diagonalization of the above mass matrix. The light neutrino masses have a contribution from the small triplet vev. The "123" HTM is studied further in the next Chapter.

Even though we do not know which type of mass neutrinos have nor where it comes from, we know that a mass term in the Lagrangian like the one in equation 1.13 can be diagonalized by rotating the charged leptons and neutrino fields, such that $e_L \to V_L e_L$

---

[14] It will be clear once we consider experimental constrains the fact v_Δ has to be small to account for the measured ρ parameter.

and $\nu_L \to U\nu_L$, in analogy with the quark sector. The diagonalizing unitary matrix in this case is $U_{\mathrm{PMNS}} \equiv V_L^\dagger U$ and is called the Pontecorvo-Maki-Nakagawa-Sakata (PMNS) matrix.

Most of what we know about neutrino masses comes from neutrino oscillation experiments. There are six parameters in the neutrino sector: two mass-squared differences (solar and atmospheric, which are around $10^{-3} - 10^{-5}$ eV^2), three mixing angles and one complex phase. Five of them have been measured (for detailed up-to-date numbers, see Ref. [52]), with the exception of the CP violating phase. So, there are still big open questions in neutrino physics, such as whether there is CP violation in the leptonic sector or whether or not neutrinos are Majorana particles.

Whether neutrinos have Dirac or Majorana masses, and independently of which specific mechanism their masses come from, testing these involve unobserved new physics, such as i) new particles (fermions or scalars) that could be observed at colliders or ii) lepton number violating processes, which can be tested at colliders or neutrinoless double β decay (i.e $K^+ \to \pi^- e^+ e^+$) type of experiments.

1.3.2 Naturalness, gauge unification and a dark matter particle candidate as motivations for Supersymmetry

We know that loop corrections to the mass of the Higgs boson are quadratically divergent. We can write the physical (or renormalized) Higgs mass as [53],

$$m_{\mathrm{physical}}^2 = m_{\mathrm{tree}}^2 + \mathcal{O}\left(\frac{\Lambda_{\mathrm{SM}}^2}{16\pi^2}\right) \tag{1.18}$$

with $\Delta m_H^2 = m_{\mathrm{physical}}^2 - m_{\mathrm{tree}}^2$, and the corrections come from both bosons and fermions running in loops, and are of order $\sim \frac{\Lambda_{\mathrm{SM}}^2}{16\pi^2}$. If the physical mass is much smaller than the cut-off, $m_{\mathrm{physical}}^2 \ll \Lambda_{\mathrm{SM}}^2$, miraculous cancellations are required between the bare mass and the quadratic correction. So we say there is no "natural" - without "too much" fine-tunning[15] - way to explain why the Higgs is light ($m_{\mathrm{physical}} \approx 125$ GeV). A natural scale for the Higgs mass would be the cut-off scale.

---

[15] Another issue is how to actually quantify fine-tunning. This is a subjective choice and there are still many ongoing debates within the theoretical community to decide how much is "too much" [54, 55].

A popular scenario that could - in principle - naturally explain the mass of the Higgs is Supersymmetry (SUSY), which is discussed further in Chapter 3. However, it is important to mention that there is a lot of tension among the theoretical community given the current experimental data, in particular in the Minimal Supersymmetric Standard Model (MSSM) [53], where the experimentally measured value of Higgs mass and naturalness do not fit perfectly together [56].

In the MSSM, the corrections to the Higgs mass become [53],

$$\Delta m_H^2 = \mathcal{O}\left(\frac{m_{\text{soft}}^2}{16\pi^2} \log \frac{\Lambda}{m_{\text{soft}}}\right). \tag{1.19}$$

We can see the terms $\sim \Lambda^2$ are gone, as SUSY solves the hierarchy problem due to cancellations between the contributions of bosons and fermions. These cancellations can take place since particles and their SUSY partners couple to the Higgs field with the same strength coupling and since loops of fermions acquire a minus sign as compared to scalars. So we are left with a standard logarithmic loop-level correction in 1.19.

Equation 1.19 tells us that the superpartner masses should not be too large, since mass splittings between the SM particles and their superpartners are determined by the parameter m_{soft} (that comes from the SUSY breaking needed so that SUSY partners are heavier than their SM partners). Otherwise, we would lose a successful cure for the hierarchy problem, since the corrections to the Higgs scalar squared mass parameter would be unnaturally large compared to $m_H^2 \approx (125\,\text{GeV})^2$. This is the argument of why SUSY partners of SM particles should not be much heavier than the TeV scale (as $m_H \approx 125$ GeV $\Rightarrow m_{\text{soft}} \leq 1$ TeV) [29], because otherwise its correction to the Higgs mass would be too large.

Since we still have not found SUSY particles close to the electroweak scale, there must be also an additional "little hierarchy problem" [57, 58] between the electroweak scale and the scale of new physics.

Even though the naturalness argument in Supersymmetric theories is in trouble, there are still models of non-minimal SUSY that can naturally accommodate the mass of the Higgs (like the DGS model [59] discussed later in Chapter 3), or other unnatural SUSY scenarios [60], such as split SUSY [61, 62] or mini-split SUSY [63]. It may be fair to say that a large fraction of the community feels that *"giving up naturalness maybe better than giving up the rest"* [56].
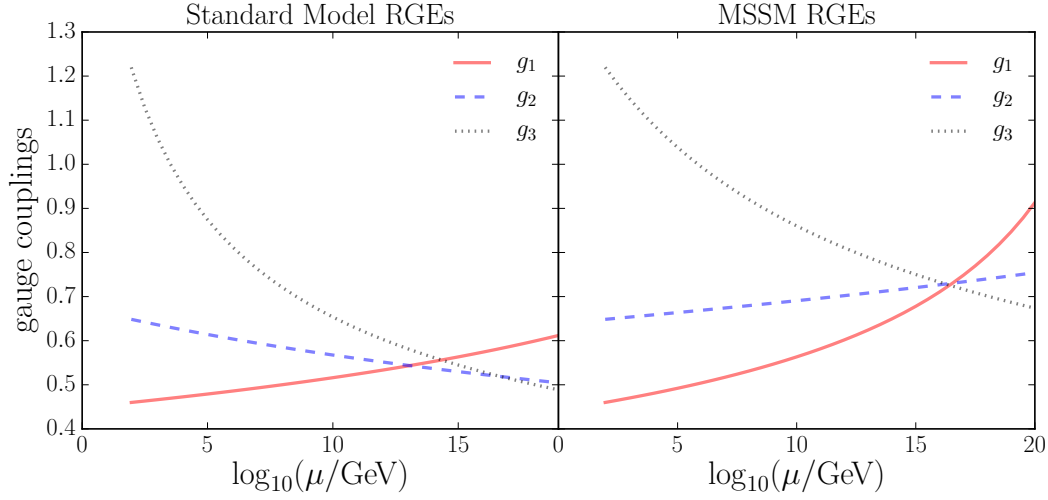
Figure 1.2: Running of the gauge couplings at two-loops using the renormalization group equations (RGEs) for the SM and the MSSM, with renormalization scale μ. Equations for the SM were taken from [64]. Equations for the MSSM were taken from [53]. The initial condition is given by the central values of the gauge couplings at the weak scale m_Z, taken from [12]. In terms of the conventional electroweak couplings defined in the covariant derivative one has $g_1 = \sqrt{5/3}g'$, $g_2 = g$ and $g_3 = g_s$. The intersection in the MSSM is achieved at grand unification scale $M_{\mathrm{GUT}} \sim 3 \times 10^{16}$ GeV.

Besides naturalness, another theoretically attractive reason to believe that Supersymmetry can be realised in Nature is the unification of the three gauge couplings at one single point at larger energies. The evolution of the gauge couplings can be seen in Figure 1.2, where unification in the MSSM of the three gauge coupling curves defines the grand unification scale $M_{\mathrm{GUT}} \sim 3 \times 10^{16}$ GeV.

Supersymmetry also provides the most studied examples for consistent dark matter candidates. We know that dark matter must be neutral, colourless, non-baryonic, massive and stable on cosmological time scales. No particle in the SM has these properties, except maybe neutrinos, but these are too light and therefore too warm to be dark matter. A popular BSM particle interpretation of dark matter suggests a weakly interactive massive particle (WIMP) with a mass of the order of $100 - 1000$ GeV. Although the WIMP dark matter "miracle" is in tension as no WIMPs have been discovered, still plausible candidates within SUSY exists such as the neutralino or the gravitino [65].

1.3.3 The search for long-lived massive particles as a general motivation given the need of beyond the Standard Model physics

Long-lived massive particles (LLPs) correspond to particles with large enough lifetimes to allow them to travel measurable distances before decaying inside a particle detector, or are stable enough so they can travel through the entire detector length before decaying.

The mean proper lifetime τ of a particle and the speed with which it travels relative to the detector determine if the particle will decay inside it or not. The lifetime of a particle at rest or proper lifetime is given by (in natural units) $\tau = 1/\Gamma$, where Γ is the total width or decay rate, which follows from Fermi's golden rule [12]. Due to relativistic effects, a particle in motion will transverse a distance of $\beta\gamma c\tau$, with β corresponding to the particle's speed in units of c, and $\gamma = 1/\sqrt{1 - \beta^2}$ is the Lorentz boost factor.

LLPs are present in many theories, including SUSY and the SM itself. If we think about the electron or the proton, their stability is protected by symmetry, due to conservation of electric charge and baryon number. The muon is long-lived due to a heavy propagator mediating its decay, the W boson. Also the neutron is long-lived due to a combination of small couplings and small phase space for its decay (as $\Gamma \propto \text{coupling}^2$). Thinking of these examples, we can state very generally that LLPs can occur in a theory if:

- there are small couplings in the decay chain.

- there are highly off-shell virtual propagators.

- there are very small mass differences in the decay chain, so there is not much phase space for the decay.

- there are conserved or approximately conserved quantum numbers.

The above mentioned properties are very general and thus present in many new BSM theories. These include gravity-mediated SUSY [66–70] with $R-$parity violation (RPV) [71], dynamical $R-$parity violation [72], gauge mediated SUSY breaking (GGM) [73], hidden-valley models (HV) [74], dark sector gauge bosons [75], stealth SUSY [76], split SUSY [61,62], next-to-minimal SUSY with gauge mediation (NMGMSB) [59, 77], anomaly mediated SUSY breaking (AMSB) [78,79], models with highly ionizing parti-

cles (HIPs), such as magnetic monopoles [80] and also alternative models for dark matter generation, such as models with feebly interactive massive particles (FIMPs) [81, 82].

Finally, a historical argument stated in [83] notes that in order to understand the stability of the atom, a new framework (quantum mechanics) was needed. This would mean that the discovery of a new state whose stability cannot be accounted for within the framework of QFT could drastically challenge our current understanding of particle physics. One can see this argument as an example of how probing the phenomenology of dark matter (if dark matter is a daughter of a long-lived particle for instance) could be very relevant from a purely theoretical point of view.

Chapter 2

A Higgs triplet model

Several extensions to the SM Higgs sector that give a mass term to neutrinos - without the need of extending the fermion sector - involve the spontaneous violation of lepton number via the vacuum expectation value of an $SU(2)$ scalar singlet, as discussed in the previous Chapter. A common feature of these models is the presence of a massless Goldstone boson, the Majoron J [49]. This is a rather simple possibility for the see-saw (to have ungauged lepton number) that can be studied without the need of extending the $SU(3) \times SU(2) \times U(1)$ gauge group.

The model under consideration in this thesis was first introduced in [50] where the authors termed it the "123" HTM. The scalar sector includes a singlet σ with lepton number $L_\sigma = 2$ and hypercharge $Y_\sigma = 0$, a doublet ϕ with lepton number $L_\phi = 0$ and hypercharge $Y_\phi = -1$, and a triplet Δ with lepton number $L_\Delta = -2$ and hypercharge $Y_\Delta = 2$. Models in which neutrino masses arise from the interaction with a triplet field have been discussed extensively in the literature [47, 84–91].

The scalar singlet, doublet and triplet of the model are,

$$
\begin{aligned}
\sigma &= \frac{1}{\sqrt{2}}(v_\sigma + \chi_\sigma + i\varphi_\sigma), \\
\phi &= \begin{pmatrix} \frac{1}{\sqrt{2}}(v_\phi + \chi_\phi + i\varphi_\phi) \\ \phi^- \end{pmatrix}, \\
\Delta &= \begin{pmatrix} \frac{1}{\sqrt{2}}(v_\Delta + \chi_\Delta + i\varphi_\Delta) & \Delta^+/\sqrt{2} \\ \Delta^+/\sqrt{2} & \Delta^{++} \end{pmatrix},
\end{aligned} \tag{2.1}
$$

where v_σ, v_ϕ, v_Δ are the vevs of the neutral components of each scalar field. The presence of the triplet allows to have a term that can give mass to neutrinos, as discussed earlier.

Following the notation of [51], the scalar potential can be written as

$$
\begin{aligned}
V(\sigma, \phi, \Delta) = {} & \mu_1^2 \sigma^\dagger \sigma + \mu_2^2 \phi^\dagger \phi + \mu_3^2 \text{Tr}(\Delta^\dagger \Delta) + \lambda_1 (\phi^\dagger \phi)^2 + \lambda_2 \big[\text{Tr}(\Delta^\dagger \Delta)\big]^2 \\
& + \lambda_3 (\phi^\dagger \phi) \text{Tr}(\Delta^\dagger \Delta) + \lambda_4 \text{Tr}(\Delta^\dagger \Delta \Delta^\dagger \Delta) + \lambda_5 (\phi^\dagger \Delta^\dagger \Delta \phi) \\
& + \beta_1 (\sigma^\dagger \sigma)^2 + \beta_2 (\phi^\dagger \phi)(\sigma^\dagger \sigma) + \beta_3 \text{Tr}(\Delta^\dagger \Delta)(\sigma^\dagger \sigma) - \kappa(\phi^T \Delta \phi \sigma + \text{h.c.}). \quad (2.2)
\end{aligned}
$$

Imposing the tadpole equations (the equations stating that the vev's are obtained at the minimum of the scalar potential) permits the elimination of the parameters μ_1^2, μ_2^2, and μ_3^2 in favor of the vev's [51].

When expanding around those vev's, the real neutral fields χ_σ, χ_ϕ, χ_Δ become massive. At the level of the Lagrangian this means that a term $\frac{1}{2}[\chi_\sigma\,\chi_\phi\,\chi_\Delta] M_\chi^2 [\chi_\sigma\,\chi_\phi\,\chi_\Delta]^T$ appears, where

$$
M_\chi^2 = \begin{bmatrix}
2\beta_1 v_\sigma^2 + \frac{1}{2}\kappa v_\phi^2 \frac{v_\Delta}{v_\sigma} & \beta_2 v_\phi v_\sigma - \kappa v_\phi v_\Delta & \beta_3 v_\Delta v_\sigma - \frac{1}{2}\kappa v_\phi^2 \\
\beta_2 v_\phi v_\sigma - \kappa v_\phi v_\Delta & 2\lambda_1 v_\phi^2 & (\lambda_3 + \lambda_5) v_\phi v_\Delta - \kappa v_\phi v_\sigma \\
\beta_3 v_\Delta v_\sigma - \frac{1}{2}\kappa v_\phi^2 & (\lambda_3 + \lambda_5) v_\phi v_\Delta - \kappa v_\phi v_\sigma & 2(\lambda_2 + \lambda_4) v_\Delta^2 + \frac{1}{2}\kappa v_\phi^2 \frac{v_\sigma}{v_\Delta}
\end{bmatrix} (2.3)
$$

By diagonalizing this matrix with $O_\chi M_\chi^2 O_\chi^T = \text{diag}(m_{h_1}^2, m_{h_2}^2, m_{h_3}^2)$, one obtains the masses of the neutral scalar fields h_1, h_2, and h_3. The fields are such that $O_\chi[\chi_\sigma, \chi_\phi, \chi_\Delta]^T = [h_1, h_2, h_3]^T$. We assume that the lightest of them is the Higgs boson discovered in 2012 [14, 15], with mass $m_{h_1} \approx 125$ GeV [92]. In this thesis we concentrate on the phenomenology of the second $CP-$even Higgs boson h_2, the massive $CP-$odd Higgs boson A, and the charged Higgs boson $H^\pm$, in consistency with the SM-like Higgs found at the LHC being h_1 in the "123" model.

The pseudoscalar fields φ_σ, φ_ϕ, and φ_Δ mix due to the mass matrix M_φ^2. The term in the Lagrangian has the form $\frac{1}{2}[\varphi_\sigma\,\varphi_\phi\,\varphi_\Delta] M_\varphi^2 [\varphi_\sigma\,\varphi_\phi\,\varphi_\Delta]^T$ with

$$
M_\varphi^2 = \begin{bmatrix}
\frac{1}{2}\kappa v_\phi^2 \frac{v_\Delta}{v_\sigma} & \kappa v_\phi v_\Delta & \frac{1}{2}\kappa v_\phi^2 \\
\kappa v_\phi v_\Delta & 2\kappa v_\Delta v_\sigma & \kappa v_\phi v_\sigma \\
\frac{1}{2}\kappa v_\phi^2 & \kappa v_\phi v_\sigma & \frac{1}{2}\kappa v_\phi^2 \frac{v_\sigma}{v_\Delta}
\end{bmatrix}. \quad (2.4)
$$

By inspection, we know that there are two null eigenvalues, since two rows are linearly dependent of the third. The mass matrix is diagonalized by another rotation given by $O_\varphi M_\varphi^2 O_\varphi^T = \mathrm{diag}(m_{G^0}^2, m_J^2, m_A^2)$, where G^0 is the massless nonphysical neutral Goldstone boson and J is the massless physical Majoron. A is the massive pseudoscalar, and $O_\varphi[\varphi_\sigma, \varphi_\phi, \varphi_\Delta]^T = [G^0, J, A]^T$ is satisfied. The pseudoscalar A has a mass,

$$m_A^2 = \frac{1}{2}\kappa\left(\frac{v_\sigma v_\phi^2}{v_\Delta} + \frac{v_\Delta v_\phi^2}{v_\sigma} + 4v_\sigma v_\Delta\right). \tag{2.5}$$

A value of κ different from zero is necessary to have a massive pseudoscalar A. For experimental reasons, we would like to take the massless Majoron as mainly singlet in order to comply with the well measured Z boson invisible width [12, 93]. Nevertheless, in the "123" model imposing this is unnecessary because the Majoron results mostly singlet as long as the triplet vev is small (see Appendix A.1). The Majoron can acquire a small mass via different possible mechanisms [94]. In cases where this particle has a small mass, it can be a candidate for dark matter [95, 96], which further motivates the model.

We mention also the electrically charged scalars. The singly charged bosons ϕ^{-*} and Δ^+ mix to form the term in the Lagrangian $[\phi^-, \Delta^{+*}]M_+^2[\phi^{-*}, \Delta^+]^T$, with

$$M_+^2 = \begin{bmatrix} -\frac{1}{2}\lambda_5 v_\Delta^2 + \kappa v_\Delta v_\sigma & \frac{1}{2\sqrt{2}}\lambda_5 v_\Delta v_\phi - \frac{1}{\sqrt{2}}\kappa v_\phi v_\sigma \\ \frac{1}{2\sqrt{2}}\lambda_5 v_\Delta v_\phi - \frac{1}{\sqrt{2}}\kappa v_\phi v_\sigma & -\frac{1}{4}\lambda_5 v_\phi^2 + \frac{1}{2}\kappa v_\phi^2 v_\sigma/v_\Delta \end{bmatrix}, \tag{2.6}$$

which is diagonalized by a rotation given by $O_+ M_+^2 O_+^T = \mathrm{diag}(m_{G^+}^2, m_{H^+}^2)$. As in the previous case, by inspection this mass matrix has a null eigenvalue corresponding to the charged Goldstone boson. The mass eigenstate fields satisfy $O_+[\phi^{-*}, \Delta^+]^T = [G^+, H^+]^T$. The charged Higgs mass is,

$$m_{H^\pm}^2 = \frac{1}{2}\left(\kappa\frac{v_\sigma}{v_\Delta} - \frac{1}{2}\lambda_5\right)\left(v_\phi^2 + 2v_\Delta^2\right). \tag{2.7}$$

Finally, the doubly charged boson Δ^{++} mass is given by

$$m_{\Delta^{++}}^2 = -\lambda_4 v_\Delta^2 - \frac{1}{2}\lambda_5 v_\phi^2 + \frac{1}{2}\kappa v_\phi^2\frac{v_\sigma}{v_\Delta}. \tag{2.8}$$

since it does not mix (it is purely triplet).

Chapter 3

Supersymmetry

Supersymmetry (SUSY) was originally proposed in the 1970s [97, 98] by extending the Poincaré algebra - with bosonic generators - to include new fermionic, anti-commuting operators which generate an extended spacetime symmetry. This symmetry states that each fermionic particle has a bosonic supersymmetric partner (and vice-versa) and that both partners are connected by a symmetry transformation. Nowadays, SUSY is understood as a class of theories with this underlying symmetry. Although there is no convincing evidence for its existence in Nature, SUSY is still considered as one of the most appealing candidates for physics beyond the SM. Its uniqueness and theoretical beauty makes it very interesting for physicists, as it gives elegant solutions to some of the undesirable issues in the SM, such as the hierarchy problem, and the fact it provides a suitable particle candidate for dark matter.

There is extensive literature on SUSY, describing the motivations, foundations and complete formulation of the theory. For a comprehensive review, see [99] and also [53] for a modern one. In this Chapter, the aim is to simply explain fundamental concepts of supersymmetric theories and to give a brief review of the SUSY models where long-lived particles can be present, which will be of interest in the interpretation of the experimental search presented in Chapter 7 and the collider phenomenology of the model studied in Chapter 8.

3.1 Supersymmetry basics, the MSSM and NMSSM

The particle states of a supersymmetric theory fall into irreducible representations of the supersymmetric algebra, called supermultiplets. Each supermultiplet contains both

Names	Superfield $\hat{S}$	Spin 0	Spin 1/2	$SU(3)_C,\ SU(2)_L,\ U(1)_Y$
squarks, quarks	$\hat{Q}$	$(\widetilde{u}_L\ \ \widetilde{d}_L)$	$(u_L\ \ d_L)$	$(\ \mathbf{3},\ \mathbf{2}\ ,\ \frac{1}{6})$
($\times 3$ families)	$\hat{U}$	$\widetilde{u}_R^*$	$u_R^\dagger$	$(\ \overline{\mathbf{3}},\ \mathbf{1},\ -\frac{2}{3})$
	$\hat{D}$	$\widetilde{d}_R^*$	$d_R^\dagger$	$(\ \overline{\mathbf{3}},\ \mathbf{1},\ \frac{1}{3})$
sleptons, leptons	$\hat{L}$	$(\widetilde{\nu}\ \ \widetilde{e}_L)$	$(\nu\ \ e_L)$	$(\ \mathbf{1},\ \mathbf{2}\ ,\ -\frac{1}{2})$
($\times 3$ families)	$\hat{E}$	$\widetilde{e}_R^*$	$e_R^\dagger$	$(\ \mathbf{1},\ \mathbf{1},\ 1)$
Higgs, higgsinos	$\hat{H}_u$	$(H_u^+\ \ H_u^0)$	$(\widetilde{H}_u^+\ \ \widetilde{H}_u^0)$	$(\ \mathbf{1},\ \mathbf{2}\ ,\ +\frac{1}{2})$
	$\hat{H}_d$	$(H_d^0\ \ H_d^-)$	$(\widetilde{H}_d^0\ \ \widetilde{H}_d^-)$	$(\ \mathbf{1},\ \mathbf{2}\ ,\ -\frac{1}{2})$

Table 3.1: Chiral supermultiplets in the Minimal Supersymmetric Standard Model. Updated from [53].

Names	Superfield $\hat{S}$	Spin 1/2	Spin 1	$SU(3)_C,\ SU(2)_L,\ U(1)_Y$
gluino, gluon	$\hat{G}^a$	$\widetilde{G}$	g	$(\ \mathbf{8},\ \mathbf{1}\ ,\ 0)$
winos, W bosons	$\hat{W}$	$\widetilde{W}^\pm\ \ \widetilde{W}^0$	$W^\pm\ \ W^0$	$(\ \mathbf{1},\ \mathbf{3}\ ,\ 0)$
bino, B boson	$\hat{B}$	$\widetilde{B}^0$	B^0	$(\ \mathbf{1},\ \mathbf{1}\ ,\ 0)$

Table 3.2: Gauge supermultiplets in the Minimal Supersymmetric Standard Model. Updated from [53].

fermionic and bosonic states (particle and superpartner). The Minimal Supersymmetric Standard Model (MSSM) [53] corresponds to the standard low energy supersymmetry, with minimal particle content in order to make the theory supersymmetric. All particles in the MSSM are represented in supermultiplets, including both particle and superpartner, with spin differing by 1/2 unit. Chiral supermultiplets are a combination of a two-component Weyl fermion and a complex scalar field. Gauge superfields are composed by a spin 1 gauge boson and a two-component Weyl fermion. They are resumed in Tables 3.1 and Table 3.2, where their component fields, quantum numbers and names are shown. It is understood that the scalar part of each superfield has a "tilde" ($\tilde{S}$) on top while the fermionic part does not (S).

The MSSM superpotential is given by [53][1],

$$\hat{W} = \varepsilon_{ab}\left\{ Y_u^{ij}\hat{Q}_i^a\hat{U}_j\hat{H}_u^b + Y_d^{ij}\hat{Q}_i^b\hat{D}_j\hat{H}_d^a + Y_e^{ij}\hat{L}_i^b\hat{E}_j\hat{H}_d^a - \mu\hat{H}_d^a\hat{H}_u^b \right\}, \tag{3.1}$$

---

[1] A slightly different convention than in Ref. [53] is used in the name of the superfields, with explicit gauge and family indices.

where $\hat{Q}$ is the superfield $SU(2)$ doublet for the quarks and squarks, $\hat{U}$ and $\hat{D}$ are the up and down $SU(2)$ singlet for the quarks and the squarks, respectively. $\hat{L}$ is the superfield corresponding to the $SU(2)$ doublet and $\hat{E}$ is the $SU(2)$ singlet for leptons and sleptons. $\hat{H}_u$ and $\hat{H}_d$ are $SU(2)$ doublets for the Higgs boson up and down, respectively. $Y_{u,d,e}$ are Yukawa couplings and μ is the Higgsino mass term. The indexes go $a, b = 1, 2$ for each doublet component and $i, j = 1, 2, 3$ for each generation. Finally, the antisymmetric tensor is $\varepsilon = i\sigma_2$.

From 3.1 the Yukawa terms, SM fermion and Higgsino masses arises via the Lagrangian,

$$\mathcal{L}_{\text{Chiral}} = -\frac{1}{2} \left[(\frac{\partial^2 \tilde{W}}{\partial \phi_i \partial \phi_j}) \psi_i \psi_j + \text{h.c} \right]. \tag{3.2}$$

The scalar fields are $\phi_i = \tilde{Q}, \widetilde{u}_R^*, \widetilde{d}_R^*, \tilde{L}, \widetilde{e}_R^*, H_u, H_d$ and fermions $\psi_i = Q, u_R^\dagger, d_R^\dagger, L, e_R^\dagger, \tilde{H}_u, \tilde{H}_e$. $\tilde{W}$ is the scalar part of the superpotential in 3.1. For example, if we consider the top-quark terms, from the above Lagrangian we can find the following interactions,
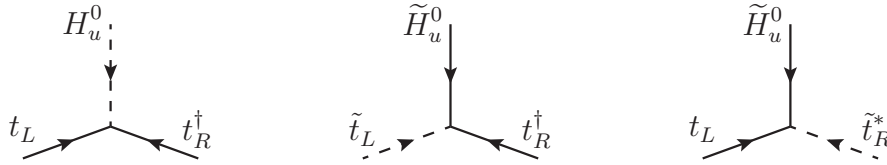
Figure 3.1: The Higgs top-quark Yukawa coupling and its "supersymmetrizations". Reproduced from [53].

In the exact supersymmetric limit, fermions and bosons have the same mass. If this was the case in Nature, we should have been able to detect a particle with the same mass of the electron for example, but with different spin. Thus, we know that if SUSY exists, then it must be a spontaneously broken symmetry. In this case, SUSY would be hidden at low energies in a manner analogous to the fate of the electroweak symmetry in the SM.

There are many models of broken supersymmetry. The mechanisms to break it always involve extending the MSSM to include new particles and interactions at very high mass scales, and there is no consensus on exactly how this should be done. It is useful then to simply parameterize our ignorance of these issues by just introducing extra terms that break supersymmetry explicitly (the so called "soft" terms) in the MSSM Lagrangian. It is usually stated that supersymmetry breaking occurs in a "hidden sector" of particles that

have no (or only very small) direct couplings to the "visible sector" chiral supermultiplets of the MSSM. However, the two sectors do share some interactions that are responsible for mediating supersymmetry breaking from the hidden sector to the visible sector, resulting in the MSSM soft terms. For example, there are gravity-mediated models in which the spontaneous supersymmetry breaking sector connects with the MSSM sector mostly through gravitational-strength interactions [66, 67, 69, 100, 101]. In gauge mediated SUSY breaking (GGM) models [73, 102, 103], the ordinary gauge interactions, rather than gravity, are responsible for the appearance of soft supersymmetry breaking in the MSSM.

The MSSM soft Lagrangian is given by [99]

$$\mathcal{L}_{\text{SUSY}}^{\text{soft}} = (M_Q^{ab})^2 \tilde{Q}_a^{i*} \tilde{Q}_b^i + (M_U^{ab})^2 \tilde{U}_a \tilde{U}_b^* + (M_D^{ab})^2 \tilde{D}_a \tilde{D}_b^* + (M_L^{ab})^2 \tilde{L}_a^{i*} \tilde{L}_b^i + (M_E^{ab})^2 \tilde{E}_a \tilde{E}_b^*$$

$$+ m_{H_d}^2 H_d^{i*} H_d^i + m_{H_u}^2 H_u^{i*} H_u^i + [\frac{1}{2} M_3 \tilde{G}^A \tilde{G}^A + \frac{1}{2} M_2 \tilde{W} \tilde{W} + \frac{1}{2} M_1 \tilde{B} \tilde{B} + \text{h.c}]$$

$$+ \varepsilon_{ij} [A_U^{ab} \tilde{Q}_a^i \tilde{U}_b H_u^j + A_D^{ab} \tilde{Q}_a^j \tilde{D}_b H_d^i + A_E^{ab} \tilde{L}_a^j \tilde{E}_b H_d^i - b_\mu H_d^i H_u^j] + \text{h.c.} \quad (3.3)$$

The M terms correspond to the masses of each sfermion, m_{H_u} and m_{H_d} are the Higgs up and down mass, respectively. M_3, M_2, M_1 are the gluino, wino, and bino (gauginos) mass terms, respectively. The $A_{U,D,E}$ terms are trilinear couplings for scalars. $i, j = 1, 2$ for each doublet component and $a, b = 1, 2, 3$ for each generation. $A = 1, 2...8$ for gluinos and $\varepsilon = i\sigma_2$.

The masses of the physical particles (or mass eigenstates) will arise after EWSB. The neutral components of each of the Higgs fields acquires a vev, $v_u \equiv \langle H_u^0 \rangle \sqrt{2}$ and $v_d \equiv \langle H_d^0 \rangle \sqrt{2}$, where the parameter $\tan\beta \equiv v_u/v_d$ is defined. Three of the Higgs scalars are eaten, leaving five physical Higgs bosons: two neutral $CP-$even scalars h_1 and h_2; two charged $H^\pm$; and one neutral $CP-$odd pseudoscalar A. The four accompanying higgsinos mix with the gauginos. The neutral higgsinos ($\tilde{H}_u^0$ and $\tilde{H}_d^0$) and the neutral gauginos ($\tilde{B}, \tilde{W}^0$) combine to form four mass eigenstates called neutralinos. The charged higgsinos ($\tilde{H}_u^+$ and $\tilde{H}_d^-$) and winos ($\tilde{W}^+$ and $\tilde{W}^-$) mix to form two mass eigenstates with charge ± 1 called charginos. The neutralinos are labeled $\tilde{N}_i$ ($i = 1, 2, 3, 4$) and charginos are $\tilde{C}^\pm$ ($i = 1, 2$). Some other notation is $\tilde{\chi}_i^0$ for neutralinos and $\tilde{\chi}_i^\pm$ for charginos (we use both in this thesis).

The MSSM is not safe from undesirable issues or problems. We already discussed naturalness in the MSSM in the previous Chapter. Another undesirable consequence of

the MSSM is related to the existence of heavy SUSY partners that upset the understanding of the suppression of flavour changing neutral currents (FCNC)[2]. The different mixing matrices in the quark and squark sectors leads to arbitrary amounts of flavour violation. Detailed calculations in the flavour sector constrain the mass splittings between squarks of different flavour to be $\Delta m_{\tilde{q}}^2/m_{\tilde{q}}^2 \leq 10^{-3}$ or so [16]. This issue is sometimes referred to as the SUSY flavour problem [105].

There is another issue, the so-called μ problem [106], which refers to the difficulty in understanding why the SUSY Higgs mass term μ in the superpotential in 3.1 is of the same order of the SUSY breaking scale if these two scales have different origins. μ has to be of the order of the SUSY breaking scale for phenomenological reasons (i.e to get correct EWSB).

In order to cure these problems (as well as to understand the origin of the soft SUSY breaking terms) we must go beyond the MSSM [16]. A solution to the μ problem is provided by the next-to-minimal Supersymmetric Standard Model or NMSSM [107], where an effective mass term μ is generated via a Yukawa coupling of $\hat{H}_u$, $\hat{H}_d$ and a new singlet chiral supermultiplet $\hat{S}$. The vev of the singlet $\langle S \rangle \equiv v_s$ is of the desired order since it is induced by the soft SUSY breaking terms [107]. The superpontential is extended by [107]

$$W_{\text{NMSSM}} = \lambda S H_u H_d + \frac{\kappa}{3} S^3 \qquad (3.4)$$

with λ and κ dimensionless Yukawa couplings. When the singlet gets a vev, an effective term $\mu_{\text{eff}} = \lambda v_s$ appears, solving the μ problem of the MSSM.

The scalar component of $\hat{S}$ mix with the neutral scalar components of $\hat{H}_u$ and $\hat{H}_d$, leading to three $CP-$even and two $CP-$odd Higges, resulting in seven physical Higgs bosons in total. The fermion component of $\hat{S}$ mixes with the neutral Higgsinos and gauginos, resulting in five neutralinos, so the Higgs and the neutralino sector can be very different from the MSSM.

---

[2] FCNC are suppressed in the SM via the Glashow-Iliopoulos-Maiani (GIM) mechanism [104].

3.2 Supersymmetric scenarios with long-lived massive particles

Here we focus on the theoretical description of four SUSY scenarios that contain LLPs. These models will be of interest in the following Chapters.

3.2.1 $R-$parity violating Supersymmetry

In the SM, lepton and baryon number are conserved. They are so called "accidental symmetries", since they are not imposed by hand. In the MSSM, since new particles are introduced, a variety of interactions do not respect lepton and baryon number conservation. Lepton and baryon number violating interactions are eliminated by imposing a new symmetry termed $R-$parity [71], defined by the quantum number

$$R = (-1)^{3B+2S+L}, \tag{3.5}$$

where B corresponds to the baryon number, L the lepton number and S the spin of the particle. One finds that $R = +1$ for the SM particles, and $R = -1$ for sparticles. The MSSM superpotential in equation 3.1 is invariant under this new symmetry. An important implication of $R-$parity conservation is that the lightest supersymmetric particle (LSP), often the lightest neutralino, is stable, since sparticles can only decay to an odd number of sparticles due to $R-$parity conservation [53]. This feature can lead to an acceptable dark matter candidate.

Nevertheless, nothing prevents us from including new gauge invariant terms to the superpotential which violate $R-$parity [71],

$$\hat{W}_{\mathrm{RpV}} = \varepsilon_{ab}[\epsilon_i \hat{L}_i^a \hat{H}_u^b + \lambda_{ijk} \hat{L}_i^a \hat{L}_j^b \hat{E}_k + \lambda'_{ijk} \hat{L}_i^a \hat{Q}_j^b \hat{D}_k] + \lambda''_{ijk} \hat{U}_i \hat{D}_j \hat{D}_k, \tag{3.6}$$

where λ, λ' and λ'' are the new $R-$parity violating (RPV) couplings with $a, b = 1, 2$ and $i, j, k = 1, 2, 3$ with $i < j < k$. The chiral supermultiplets are defined in Table 3.1. The first three terms in equation 3.6 violate lepton number by 1 unit. The λ'' term violates baryon number by 1 unit. Note that once we allow the RPV terms in the superpotential, the neutralino is no longer stable, so it can no longer play the role of dark

matter unless its lifetime is large enough. The gravitino could also take the neutralino's place as a viable dark matter candidate [108] when $R-$parity is broken.

It is also known that a combination of the λ' and λ'' lepton and baryon number violating couplings leads to proton decay. Lower limits on the proton lifetime imply $\lambda'\lambda'' \leq 10^{-24}$ for squarks of order 1 TeV [109]. So we see that $R-$parity violation could predict a very short lifetime for the proton, because baryon number would no longer be conserved. One can include just trilinear or just bilinear terms to the superpotential to avoid simultaneous breaking of B and L. Keeping the $R-$parity violating terms under control provides a major constraint in model building [16].

The last three terms in equation 3.6 are trilinear and involve the decay of: slepton (sneutrino) to lepton and a neutrino (leptons) through λ, the decay of sleptons or sneutrinos to quarks through λ', and the decay of an squark to two quarks through λ''. The first term with ϵ is bilinear and introducing it is one attractive mechanism to generate neutrino masses [110].

We are interested in the decay of the lightest neutralino via a non-zero λ' coupling, as this will be the coupling probed in the experimental search in Chapter 7. Neutralinos will decay into a fermion and a virtual sfermion, with the virtual sfermion subsequently decaying to standard fermions. Thus, the direct decay of the lightest neutralino is characterized by three fermions in the final state, with the fermion type depending on the dominant λ' coupling [71].

The Lagrangian density comes from inserting the scalar part of the RPV superpotential in equation 3.6 into the chiral Lagrangian in 3.2. Using our notation from 3.1, for the λ' couplings we have

$$
\begin{aligned}
\mathcal{L}_{\text{Chiral}} = -\frac{\lambda'_{ijk}}{2} [& \widetilde{d^*_{kR}}\nu_i d_{jL} + \tilde{\nu}_i d_{jL} d^*_{kR} + \tilde{d}_{jL}\nu_i d^*_{kR} \\
& - \widetilde{d^*_{kR}}e_{iL}u_{jL} - \tilde{e}_{iL}u_{jL}d^*_{kR} - \tilde{u}_{jL}e_{iL}d^*_{kR}] + \text{h.c}
\end{aligned} \tag{3.7}
$$

These terms give rise to a neutralino decay via a non-zero λ'_{ijk} coupling. The first three and the last three terms give rise to the same final state

$$
\begin{aligned}
\tilde{\chi}^0_1 &\to \nu_i d_{jL} d^*_{kR} \\
\tilde{\chi}^0_1 &\to e_{iL} u_{jL} d^*_{kR}
\end{aligned} \tag{3.8}
$$

respectively (plus their hermit conjugates). We can generally represent the RPV decay of a long-lived neutralino via a non-zero λ' coupling as in Figure 3.2.
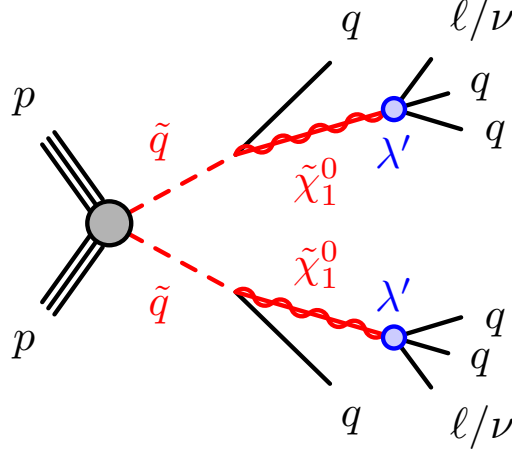
Figure 3.2: Diagram representing an $R-$parity violating decay. In RPV scenarios, the long-lived neutralino may decay via the λ'_{ijk} couplings. The quarks and leptons shown may have different flavors. Filled circles indicate effective interactions (the virtual sfermion is not shown) [1].

The neutralino lifetime is given by [71, 111]

$$ c\tau \simeq \frac{3}{\lambda'^2_{ijk}} \left(\frac{m_{\tilde{f}}}{100 \text{ GeV}} \right)^4 \left(\frac{1 \text{ GeV}}{m_{\tilde{\chi}^0_1}} \right)^5 \text{mm} \tag{3.9} $$

with $m_{\tilde{f}}$ the mass of the virtual sfermion. For values of the coupling between $10^{-6} \lesssim \lambda'_{ijk} \lesssim 10^{-4}$, $m_{\tilde{f}} \sim 1$ TeV and $m_{\tilde{\chi}^0_1} \sim 100$ GeV we get 10^2 mm $< c\tau < 10^6$ mm, implying that the neutralino can decay some distance away from its production point, leading to a displaced vertex signature (see Chapter 6).

3.2.2 Split Supersymmetry

Another popular extension to the SM is split Supersymmetry (split SUSY) [61, 62, 112]. In split SUSY, all scalars in the theory are very heavy, mass-degenerated, for simplicity, at a mass $\tilde{m} \gg m_Z$, except for one Higgs doublet, whose behavior is like the SM Higgs. Split SUSY maintains some of the nice aspects of the MSSM, like gauge unification, and it can be understood as an effective theory of the MSSM, since heavy scalars are integrated out, meaning, there are no sleptons and no squarks in this low energy theory.

The discovered Higgs mass can also be accommodated in this theory [63, 113, 114]. But, since $\tilde{m} \gg 1$ TeV, the Higgs mass has to be fine-tuned. Nevertheless, in the original articles it is argued that there is a much larger fine-tuning associated to the cosmological constant. In this sense, the hierarchy problem is not addressed in split SUSY (except maybe anthropically) and gauge unification and a dark matter solution are the guiding principles in its construction as a BSM theory.

A very striking effect of split SUSY is the long lifetime of the gluino [113, 115], as the decay is suppressed by the large mass difference between the gluino mass M_3 and $\tilde{m}$. Since all squarks are very heavy, with a mass of order of the split SUSY scale $\tilde{m}$, the gluino will decay via highly off-shell squarks[3], and with an increasing lifetime as $\tilde{m}$ increases. The gluino lifetime in split SUSY is given by [113, 115]

$$c\tau \simeq 2 \times 10^{-1} \left(\frac{2 \text{ TeV}}{M_3} \right)^5 \left(\frac{\tilde{m}}{10^6 \text{ GeV}} \right)^4 \text{ mm} \qquad (3.10)$$

For $\tilde{m} \sim 10^5$ GeV (which is consistent for a Higgs mass of ~ 125 GeV) and $M_3 \sim 100$ GeV, we have that $c\tau \sim 10^2$ mm, so the gluino could then decay leaving a displaced vertex signature (see Chapter 6).
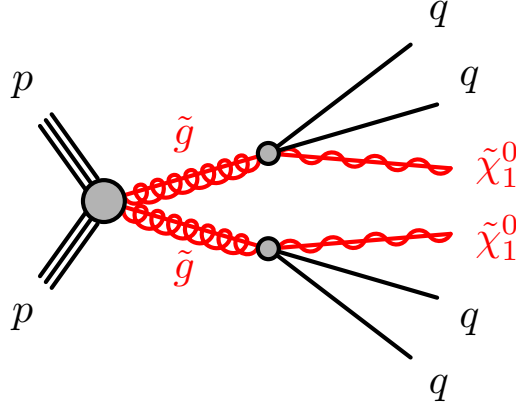
The gluino could hadronize before decaying, forming an $R-$hadron [116]. $R-$hadrons are hypothetical particles analogous to the ordinary hadrons but including a coloured SUSY particle (so we can have QCD bound states with gluinos, squarks, quarks and gluons). The $R-$hadron then would decay into a $\tilde{\chi}^0$ via $\tilde{g} \to q\bar{q}\tilde{\chi}^0$ or via the loop process $\tilde{g} \to g\tilde{\chi}^0$. A simplified diagram representing the decay of a long-lived gluino is shown in Figure 3.3.

3.2.3 Gauge mediated Supersymmetry breaking

This general gauge mediated (GGM) mechanism for SUSY breaking includes a hidden (or secluded) sector and a messenger sector, in addition to the observable sector that contains MSSM fields [102]. The idea is that the known gauge forces are the messengers of SUSY breaking. These messengers are chiral superfields $\Phi_i, \bar{\Phi}_i$[4] and can come in multiplets of $SU(5)$, that contains the SM gauge group (for instance, N copies of the

---

[3] Since gluinos carry colour charge they can only decay via squarks (or quarks in RPV).

[4] The bar in $\bar{\Phi}$ is used to indicate that the left-handed chiral superfields $\bar{\Phi}$ transform as the complex conjugate representations of the left-handed chiral superfields Φ [53].

Figure 3.3: Diagram representing a gluino decay. In split SUSY scenarios, the long-lived
gluino may hadronize before decaying, forming an $R-$hadron. One of the quarks
should be read as an anti-quark. Filled circles indicate effective interactions (the
heavy squark is not shown) [1].

$\mathbf{5} + \bar{\mathbf{5}}$ representations of $SU(5)$), so are charged under the SM gauge interactions. The
MSSM fields feel SUSY breaking only through SM gauge interactions.

The supersymmetry breaking mechanism is parameterized by a spurion chiral super-
field X, whose auxiliary component F is assumed to acquire a vev [102]. The messengers
acquire a mass M in the hidden sector through Yukawa couplings with X, whose non-zero
vev generates the SUSY breaking. The superpotential is [117]

$$W_{\mathrm{GM}} = \kappa_{ij} X \Phi_i \bar{\Phi}_j \qquad (3.11)$$

The parameters M and F (which is the measure of SUSY breaking in the messenger
sector [102]) are the fundamental mass scales in the theory. In the visible sector, particle
supermultiplets are degenerate at the tree level, since they do not directly couple to X,
but splittings arise at the loop level because of gauge interactions between observable
and messenger fields. Gauginos for example obtain their masses from messenger field
loops, and are given by [102, 117]

$$M_i = N g_i^2 \tilde{m} \qquad (3.12)$$

with N the number of generations in the messenger sector, g_i with $i = 1, 2, 3$ are the
gauge couplings and the effective SUSY breaking scale $\tilde{m}$ in the visible sector given by,

$$\tilde{m} = \frac{1}{16\pi^2}\frac{F}{M} \tag{3.13}$$

Gauge mediation leads naturally to a near mass degeneracy of the squarks and sleptons (which arise at two loop), since these depend only on their gauge quantum numbers. This mass degeneracy is needed for suppression of flavor-changing effects and therefore solves the SUSY flavour problem [117].

A diagrammatic representation of the hidden, messenger and visible sector can be seen below

| hidden SUSY break-ing sector ($\langle X \rangle$) | → | messenger sector ($\Phi\bar{\Phi}$) | → | observable sector (MSSM/NMSSM fields) |
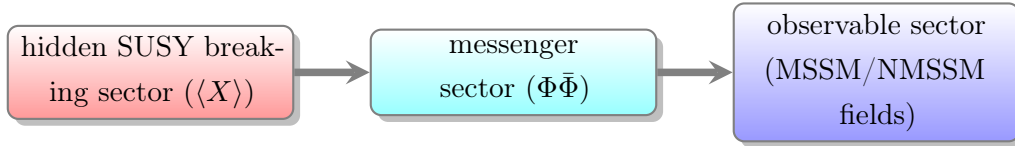
Another distinctive feature of gauge mediated models is that they have the gravitino as the LSP, because of the relatively low scale of SUSY breaking (the gravitino mass is $m_{3/2} \sim \tilde{m}$ [102]). The next-to-lightest supersymmetric particle (NLSP) can therefore decay into its SM partner and the gravitino $\tilde{G}$. In the case that the lightest neutralino $\tilde{\chi}_1^0$ is the NLSP, we can have decays $\tilde{\chi}_1^0 \to Z\tilde{G}$. The NLSP width is suppressed by the SUSY breaking scale. The neutralino lifetime is [73]

$$c\tau \simeq 130\left(\frac{100\text{ GeV}}{m_{\tilde{\chi}_1^0}}\right)^5\left(\frac{\sqrt{F}}{100\text{ TeV}}\right)^4 \times 10^{-3}\text{ mm} \tag{3.14}$$

so it may be that its decay leads to the formation of a displaced vertex (see Chapter 6) for $\sqrt{F}$ between roughly 100 and 1000 TeV.

A simplified diagram showing the neutralino decay in GGM can be seen in Figure 3.4.

3.2.4 Next-to-minimal gauge mediated Supersymmetry

While GGM scenarios provides a neat solution to the SUSY flavour problem (i.e. the absence of large sources of flavor violation in the soft terms), its minimal realisations are in trouble because they typically predict a SM-like Higgs mass that is too low compared to the observed value around 125 GeV.
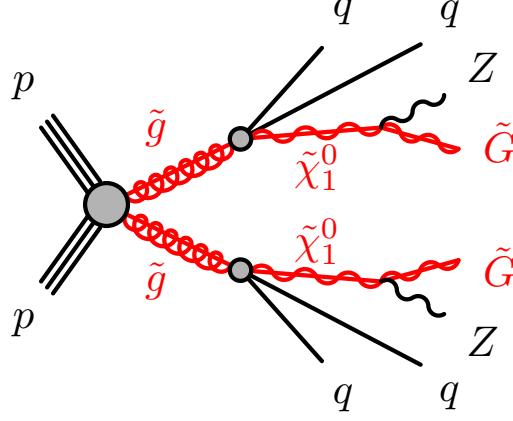
Figure 3.4: Diagram representing a neutralino decay. In GGM scenarios, the long-lived neutralino decays to a gravitino and a Z boson. One of the quarks should be read as an anti-quark. Filled circles indicate effective interactions (the heavy squark is not shown) [1].

In Ref. [77], a model by Delgado, Giudice and Slavich [59] (DGS) that combines gauge mediation (GGM) and the next-to-minimal Supersymmetric Standard Model (NMSSM) was proposed. The field content of the model is the one of the NMSSM, plus two copies of messengers in $\mathbf{5}+\mathbf{\bar{5}}$ representations of $SU(5)$, denoted by $\Phi_i, \bar{\Phi}_i$, respectively ($i = 1, 2$), with doublet and triplet components $\Phi_i^D, \bar{\Phi}_i^D$ and $\Phi_i^T, \bar{\Phi}_i^T$.

Aside from Yukawa interactions, the superpotential contains spurion-messenger couplings and singlet S-messenger couplings (first introduced in the context of gauge mediation in Ref. [118])

$$
\begin{aligned}
W \;=\; & \ldots + \lambda S H_u H_d + \frac{\kappa}{3} S^3 + X \sum_i (\kappa_i^D \bar{\Phi}_i^D \Phi_i^D + \kappa_i^T \bar{\Phi}_i^T \Phi_i^T) \\
& + S(\xi_D \bar{\Phi}_1^D \Phi_2^D + \xi_T \bar{\Phi}_1^T \Phi_2^T),
\end{aligned}
\tag{3.15}
$$

where the singlet-messenger couplings unify at the grand unified theory scale M_{GUT}: $\xi_D(M_{\mathrm{GUT}}) = \xi_T(M_{\mathrm{GUT}}) \equiv \xi$ with unified coupling ξ. The scale of the SUSY breaking terms is fixed by the parameter $\tilde{m} = 1/(16\pi^2)F/M$.

It was shown in Ref. [77] that in the DGS model one can obtain a 125 GeV Standard Model-like Higgs boson with stops as light as 1.1 TeV, thanks to the mixing of the Higgs with a singlet state at $\mathcal{O}(90 - 100)$ GeV which is compatible with LEP data [119]. With these Higgs constraints, essentially all parameters are fixed except for the GGM messenger scale M which mainly controls the phenomenology.

The central feature of the model, apart from the light Higgs that might explain the LEP excess [120] is the peculiar structure of the light sparticle spectrum. The LSP is the gravitino $\tilde{G}$ with mass and couplings effectively set by the GGM messenger scale, the NLSP is a singlino-like neutralino $\tilde{N}_1$ of mass around 100 GeV, and the next-to-NLSP (NNLSP) is a bino-like neutralino $\tilde{N}_2$ or stau $\tilde{\tau}$, depending on the GGM messenger scale. The presence of the singlino alters SUSY decay chains as compared to the MSSM, leading to additional b-jets or taus.

One distinctive feature of this scenario is that the singlino decays to a gravitino and a light singlet-like pseudoscalar a_1 of mass around 20 GeV, with the latter decaying predominantly to $b\bar{b}$ as well as to $\tau\tau$. Depending on the messenger scale, the two b-jets may be produced far outside the detector (when the $\tilde{N}_1$ is quasi-stable, at high GGM scales) or at low GGM scales, they may be produced within the detector from displaced vertices (DVs). This peculiar feature of a long-lived singlino decay was already noticed in Ref. [59].

The neutralino lifetime is given by [77]

$$c\tau \simeq 25 \left(\frac{100 \text{ GeV}}{m_{\tilde{N}_1}}\right)^5 \left(\frac{M}{10^6 \text{ GeV}}\right)^2 \left(\frac{\tilde{m}}{\text{TeV}}\right)^2 \text{ mm} \qquad (3.16)$$

which leads to a displaced vertex signature for values of the GGM scale $M \sim 10^6 - 10^7$, as $\tilde{m}$ is almost fixed in this model to be ~ 1 TeV when maximizing the tree level contribution to the mass of the Higgs [77]. An example diagram showing LHC sparticle production in the DGS model is shown in Figure 3.5.
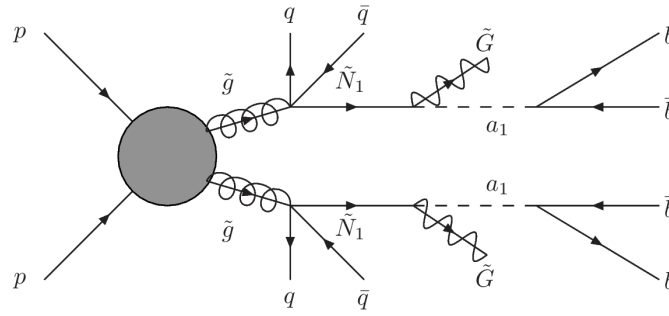
Figure 3.5: Diagram representing sparticle production and decay in the DGS model. In this example, we have four hard prompt jets from gluinos decaying into quarks q and anti-quarks $\bar{q}$; the lightest neutralino $\tilde{N}_1$ may have an intermediate lifetime, producing displaced vertices, each generating $b\bar{b}$. The gravitino $\tilde{G}$ leaves a missing transverse momentum signature. The lightest pseudo-scalar a_1 has a lower branching ratio for decays into $\tau\bar{\tau}$ than $b\bar{b}$. The $\tilde{g} \to \tilde{N}_1$ part of the decay may commonly be more complicated, involving a cascade decay and concomitant additional SM states [2].

Part II

Experimentation

Chapter 4

The ATLAS experiment at CERN's Large Hadron Collider

The interest in understanding the true fundamental laws of our Universe has led the international community of physicists to built giant accelerators and detectors, designed to seek for new phenomena and explore the unknown. The highest energy particle accelerator ever built, the Large Hadron Collider (LHC), was constructed with the purpose of finding the Higgs boson, and thus to elucidate the nature of EWSB. It was also built with the hope of answering the questions the SM can not (as discussed in Chapter 1), by performing different searches for new physics.

The LHC runs in a 27 kilometer circumference tunnel, about 100 metres beneath the border between France and Switzerland, at the CERN laboratory. The LHC is a ring of superconducting magnets. Proton beams (pp) circulate inside them at very high speeds, close to the speed of light. These proton beams are circulating in opposite directions, and the experiment is designed to collide them at certain points within specialized detectors.

The LHC was designed to deliver a luminosity[1] of $\mathcal{L} = 10^{34}$ cm^{-2}s^{-1}. Bunches of up to 10^{11} protons collide 40 million times per second, resulting in an average of 23 interactions per bunch crossing, at a center of mass energy $\sqrt{s} = 14$ TeV. The LHC can also collide heavy ions, in particular lead nuclei, at 5.5 TeV per nucleon pair, at a design luminosity of 10^{27} cm^{-2}s^{-1} .

---

[1] Luminosity is an important variable to quantify the performance of particle colliders. Instantaneous luminosity $\mathcal{L}$ is defined via $N = \sigma \times \int \mathcal{L}(t)dt$, where N is the number of events we can expect for a a given process with cross section σ. Note that luminosity is stated in units of cm^{-2}s^{-1}. Integrated luminosity is quoted as the inverse of the standard measures of cross section such as femtobarns (fb) or attobarns (ab) [12].

Four huge detectors were built around points where the pp collide inside the LHC ring: ALICE, LHCb, CMS and ATLAS[2]. ALICE's specific aim is to understand the primordial quark-gluon plasma through heavy ion collisions. LHCb is specializing in bottom and charm physics. ATLAS and CMS are the largest, general purpose experiments, and were designed to explore the highest energies at the TeV scale, study in depth the SM and what lies beyond it. These experiments are organized as international collaborations. ATLAS involves 38 countries around the globe.
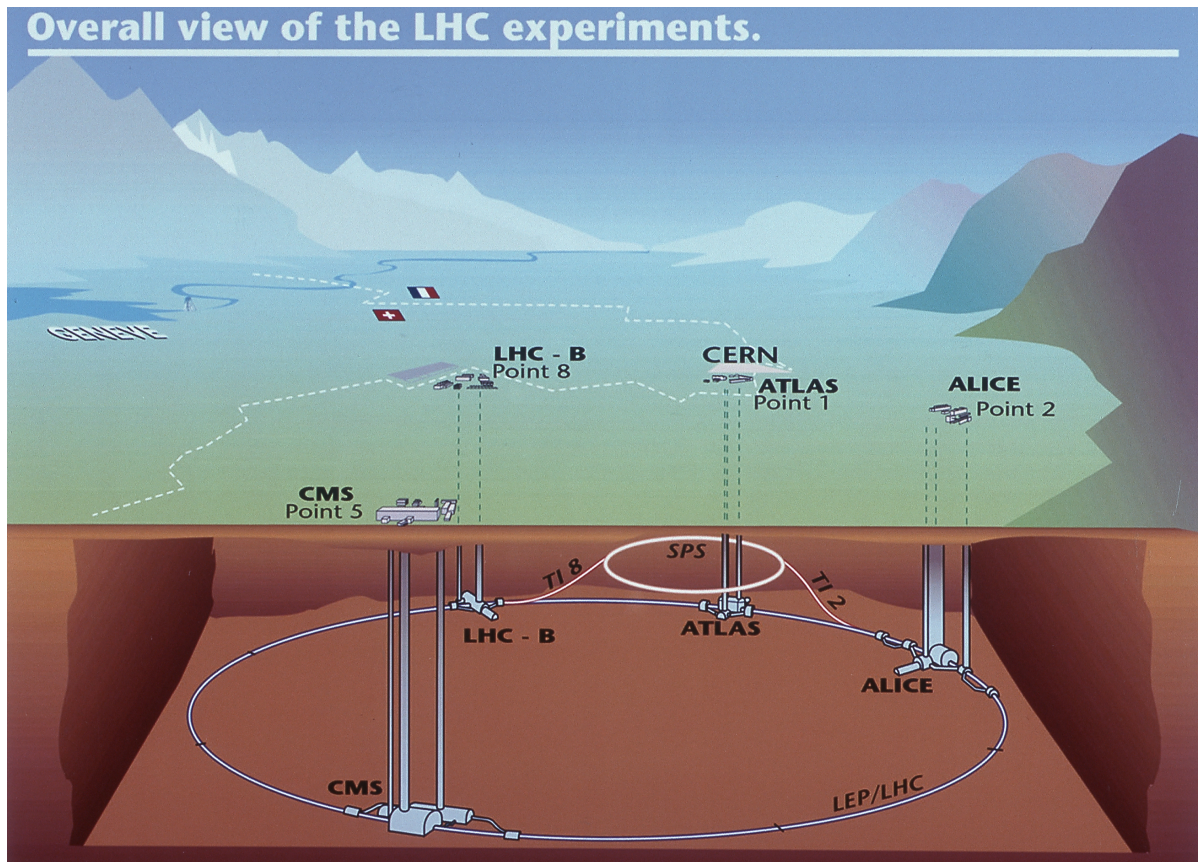
Figure 4.1: Locations of the four main experiments (ALICE, ATLAS, CMS and LHCb) that take place at the LHC. Image credit CERN 2016 [121].

One particular result of the ATLAS experiment will dominate Chapter 7 of this thesis, so a brief description of the detector is given below, including the details of the ATLAS Inner Detector, since it is the relevant part of the detector for the experimental analysis. Reconstruction of the relevant observables within the experiment used in the analysis

---

[2] ALICE stands for *A Large Ion Collider Experiment*, LHCb for *Large Hadron Collider beauty*, CMS for *Compact Muon Solenoid* and ATLAS is *A Toroidal* LHC *Apparatus*.

in Chapter 7 are also explained. A full description of ATLAS with all its technical specifications can be found in the official Technical Design Report [122].

4.1 Detector overview and observables

ATLAS has a cylindrical layout. It is about 44 metres long, more than 25 metres high, and weighs about 7,000 tons. An image can be seen in Figure 4.2. ATLAS uses a right-handed coordinate system. The beam direction defines the $z-$axis, and the $x - y$ plane is transverse to the beam direction, with the $x-$axis pointing towards the centre of the LHC tunnel. Cylindrical coordinates (r, ϕ, z) are used. The azimuthal angle $-\pi \leq \phi \leq \pi$ is measured around the beam axis and the polar angle $0 \leq \theta \leq 90°$ is the angle from the beam axis. Pseudorapidity is defined as,

$$\eta = - \ln \left[\tan \left(\frac{\theta}{2} \right) \right]. \tag{4.1}$$

so $0 \leq \eta \leq \infty$. In the case of massive objects (such as jets) the rapidity

$$y = \frac{1}{2} \ln \left(\frac{E + \vec{p}_Z}{E - p_Z} \right) \tag{4.2}$$

is used, where E denotes the energy and p_Z is the component of the momentum along the beam direction. Transverse momentum, $p_T = p \sin \theta$, the transverse energy $E_T = E \sin \theta$ and the missing transverse momentum $p_T^{\text{miss}3}$ are defined as the momentum and energy perpendicular to the LHC beam axis (in the $x - y$ plane)[4].

The distance ΔR in the pseudorapidity-azimuthal angle space is defined as

$$\Delta R = \sqrt{\Delta \eta^2 + \Delta \phi^2}. \tag{4.3}$$

The ATLAS detector is constructed in layers, with four major components: the Inner Detector (ID), which measures the momentum of each charged particle, the Calorimeters (Electromagnetic (EM) and Hadronic (HAD)), the latter composed by the Tile, Liquid

---

[3] I prefer to use the more accurate descriptor $p_T^{\text{miss}} = |\vec{p}_T^{\text{miss}}|$ rather than the "E_T^{miss}" officially quoted by ATLAS.

[4] For $p \gg m$, $E \approx p$ and pseudorapidity is a good approximation to rapidity.
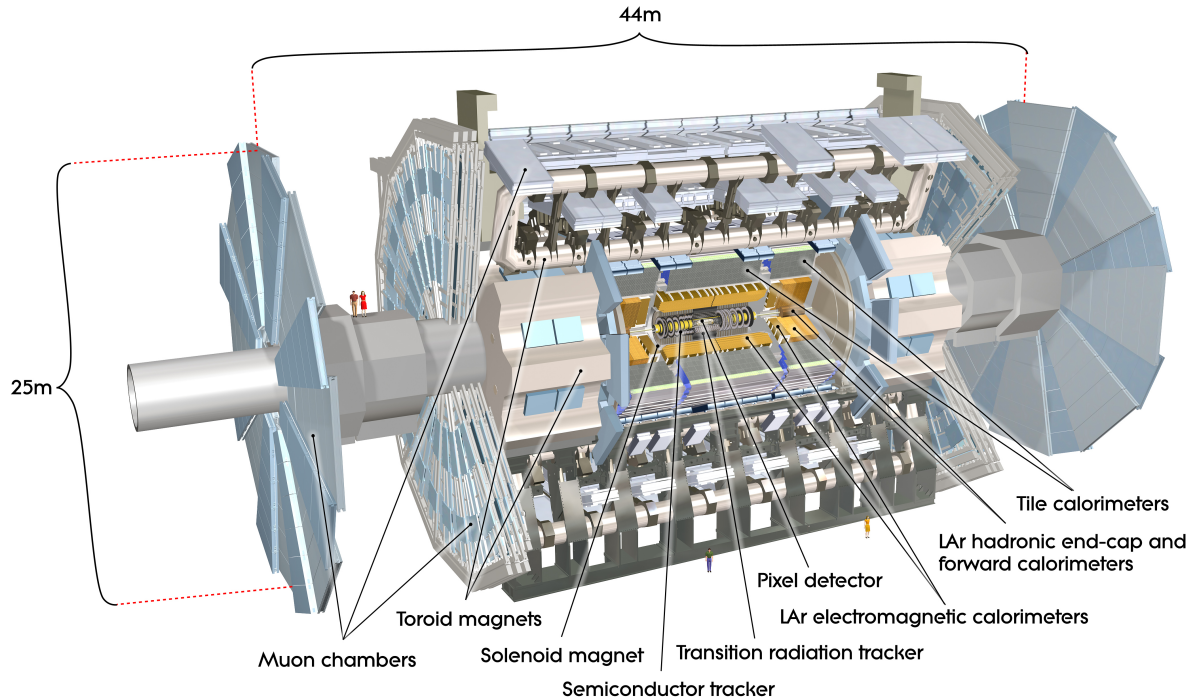
Figure 4.2: A computer-generated image of the ATLAS detector and its systems [123].

Argon Hadronic End-Cap (LArHEC) and Liquid Argon Forward (FCal) Calorimeters), that measure the energies carried by the particles, the Muon Spectrometer (MS), which identifies and measures the momenta of muons, and the Magnet Systems which forces charged particles to follow curved tracks for momentum measurements. Particles produced in a collision will radiate outward from the collision point passing through the different layers until they decay or are captured or they escape the detector. Figure 4.3 shows how a *pp* collision looks inside ATLAS.

Since the interactions in the ATLAS detector will create an enormous dataflow, a multi level computing Trigger system [124] has been developed in order to reduce the flow of data to manageable levels. The Trigger selects events with distinguishing characteristics that makes them interesting for physical analysis. The Trigger selection process is done in three levels, Level 1 (L1), Level 2 (L2) and Event Filter (EF), where each level refines the decision made by the previous level by applying additional selection criteria.

The L1 trigger is hardware-based and uses information from the calorimeters and muon detectors to identify Regions of Interest (RoI). This first selection reduces the rate to 75 kHz (100 kHz for Run 2). Both L2 and EF are software-based. The L2 trigger

is a large array of custom processors that analyze in greater detail the RoIs from L1, which it takes as inputs, and access information from other subsystems of the detector (calorimeters and muon chambers and also the inner tracker which is not used at L1) to reduce the trigger rate to approximately 3.5 kHz. The final selection is done by the EF, where detailed analysis is performed on the full event data to come up with a final rate of about 400 Hz (1 kHz for Run 2). These events are then stored, recorded, processed and distributed in the computing centres around the world (which together form the ATLAS grid), for future analysis.
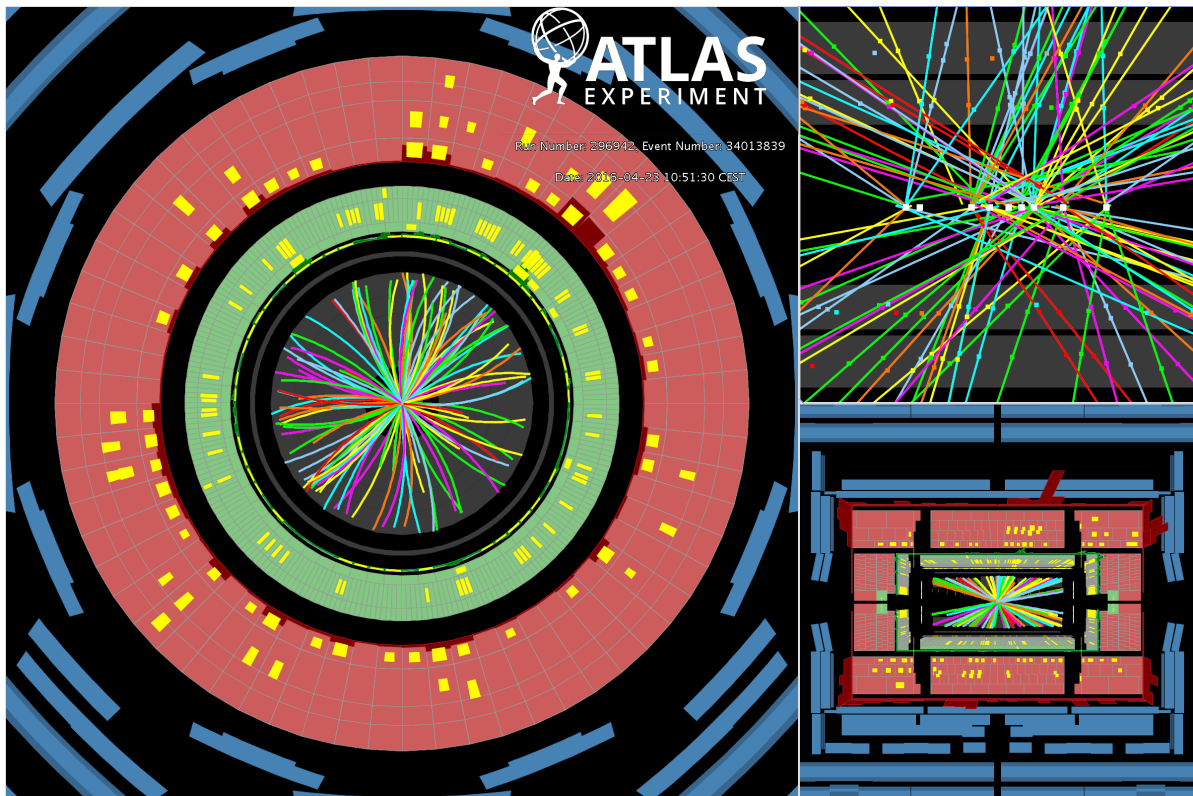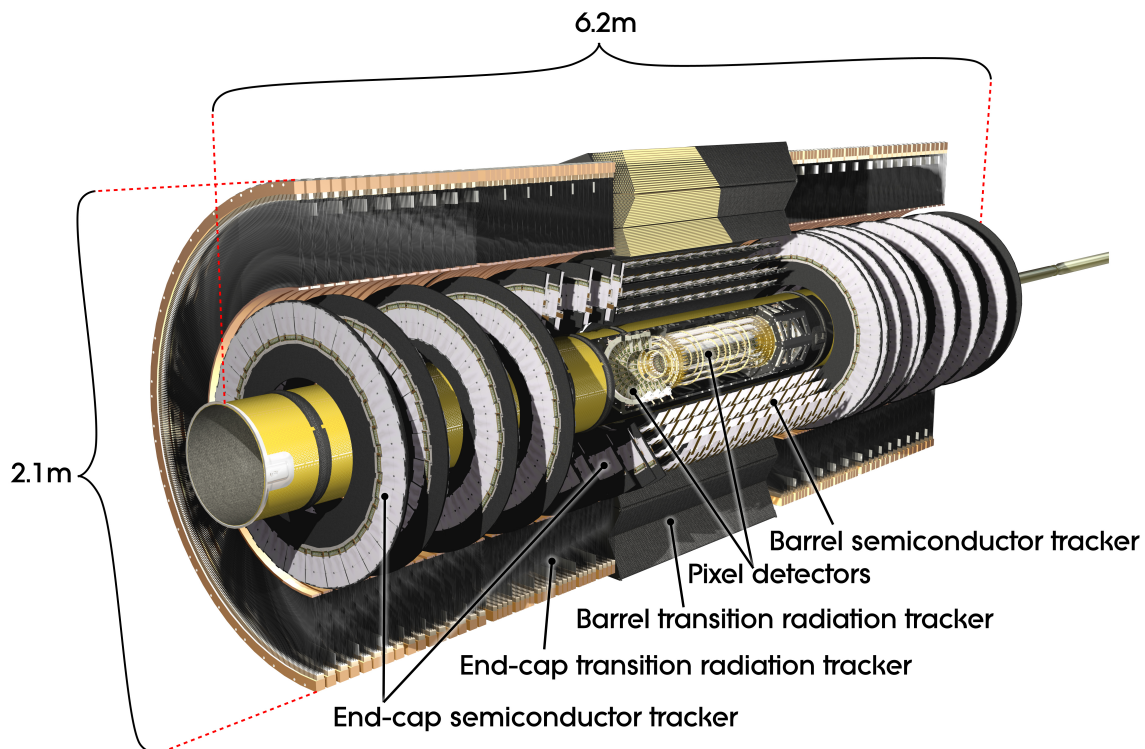

Figure 4.3: One of the collision events recorded by ATLAS on 23 April 2016. The picture shows the region where the two beams from the LHC collide inside the ATLAS detector. In this event the colliding protons give birth to nine primary interactions, as shown in the picture. The left and bottom right pictures show the standard projections of the detector transverse to the beam line and along the beam line ($r - z$ view) respectively. The top right picture is a $r - z$ zoom-in to within a few cm of of the luminous region, showing nine reconstructed pp collision vertices (white squares) and the hits associated with reconstructed tracks with transverse momentum above 1 GeV [125].
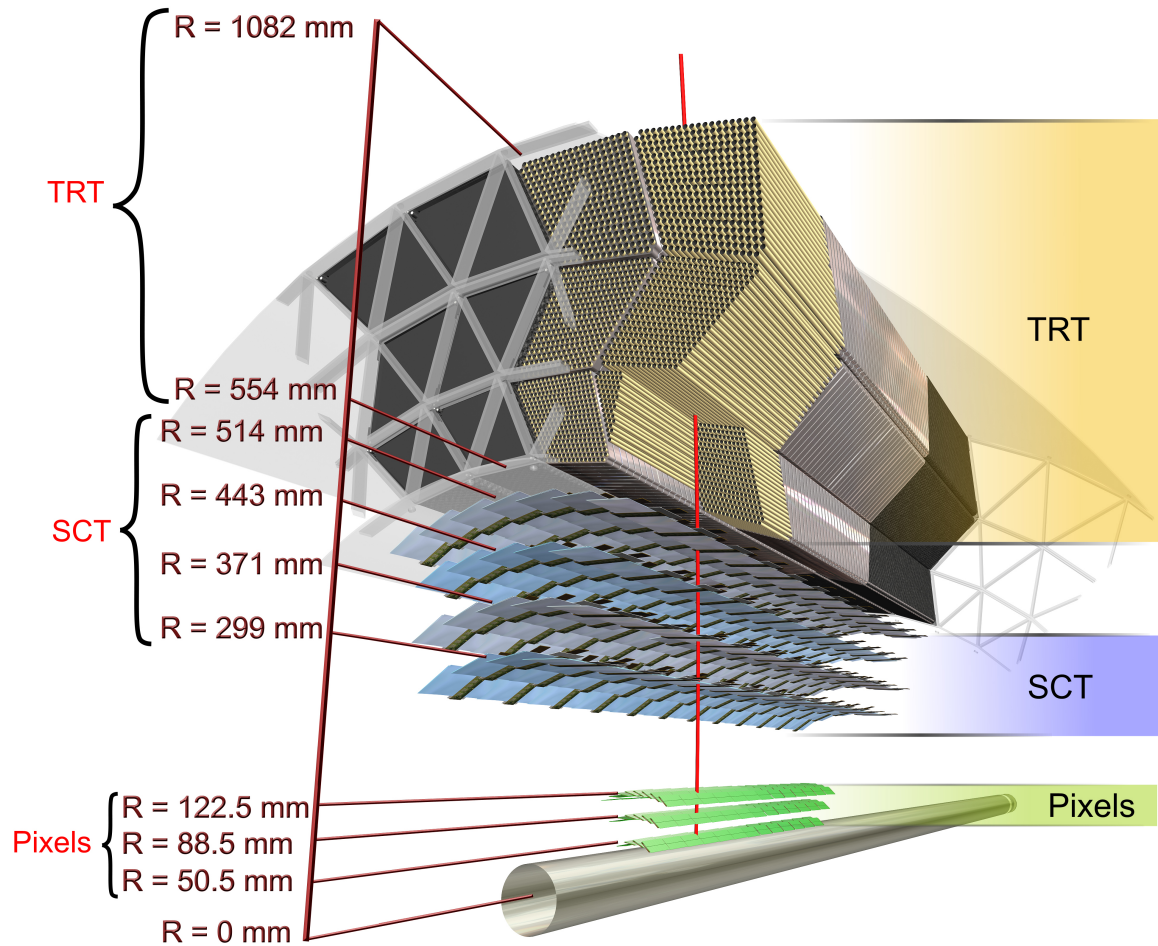
4.2 Details of the ATLAS Inner Detector

The ATLAS Inner Detector tracking system is the innermost system of the detector. Its job is to record the trajectories (tracks) of the $\mathcal{O}(1000)$ charged particles that will emerge from the collision point for every beam crossing. It is designed to detect the resulting ionization electrons from the energy loss of a charged particle in a particular medium.

The ID consists of Pixel detectors, Silicon microstrip detectors (SCT), and the Transition Radiation Tracker (TRT), and it provides measurements of charged particle tracks within $|\eta| < 2.5$. The Pixel Detector and the SCT are arranged in concentric cylinders around the beam axis (in the barrel region), and on disks perpendicular to the beam axis (in the endcaps). The TRT consists of layers of tubes placed parallel to the beam direction in the barrel and also layers placed radially in each of the two endcaps. The detector layout is shown in Figures 4.4 and 4.5. The ID is immersed in a 2 T axial magnetic field provided by a superconducting solenoid.

Figure 4.4: A computer-generated overview image of the ATLAS Inner Detector [126].

R = 1082 mm

TRT

R = 554 mm
R = 514 mm
R = 443 mm

SCT

R = 371 mm

R = 299 mm

TRT

SCT

Pixels

R = 122.5 mm
Pixels R = 88.5 mm
R = 50.5 mm

R = 0 mm

Figure 4.5: A computer-generated image of the barrel part of the ATLAS Inner Detector. Radial distances from the center of the beam pipe to the various module layers are shown [126].

Pixel detector and SemiConductor tracker

High precision and high efficiency detector elements are needed near the collision point in order to distinguish individual particle tracks from the hundreds produced in each collision and measurements must be made with fine detector granularity to achieve good momentum and vertex resolution.
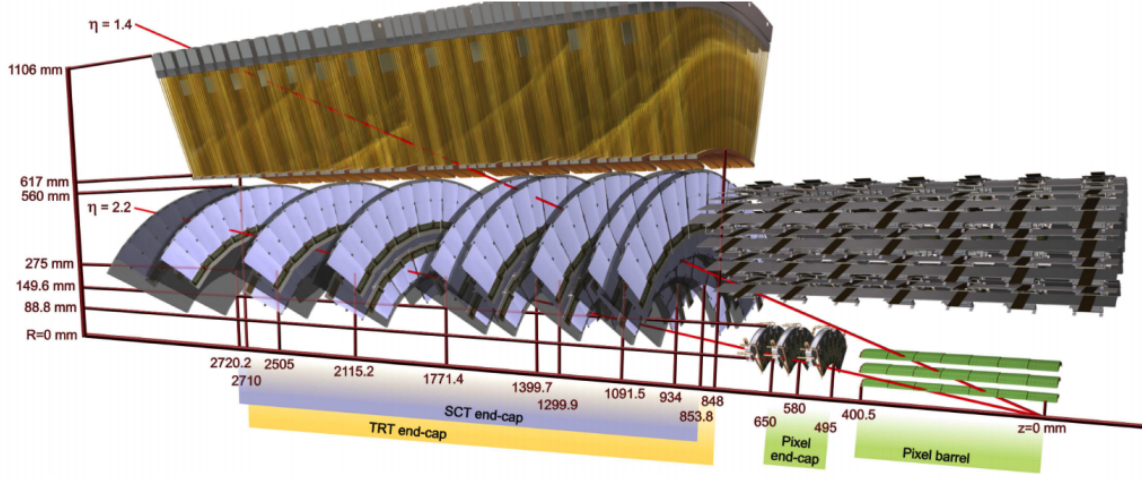
Figure 4.6: A computer-generated image of the ATLAS Inner Detector showing the endcap region. η coverage and radial distances are shown [122].

The highest granularity is achieved around the vertex region using silicon pixel detectors. These must be radiation hard to withstand the intense levels of radiation from the colliding beams. The Pixel Detector contains about 80.4 million rectangular pixels of a minimum pixel size of $50 \times 400 \mu m^2$, which are capable of resolving particle positions to about 10 microns in the barrel region.

Around the Pixel Detector is the SemiConductor Tracker (SCT) where the tracking of charged particles continues using layers of sensors with over 6 million silicon microstrips, with pitch of 80 μm and accuracy of 20 microns. These strips are placed on silicon wafers that are attached end-to-end and wirebonded (so the strips go across the boundary). These wafers compose a module (each module has two wafers per side) and the 2 sides of a module are glued back-to-back with a stereo angle (to measure the 3D position of hits).

Heat from the readout electronics is removed by an evaporative cooling system, keeping the silicon temperature at -7°C.

Transition Radiation Tracker

Further from the collision point is the Transition Radiation Tracker (TRT) which contains about 350,000 polyimide drift tubes ("straws") of 4 mm diameter. Each straw is coated on the inside with aluminium (a high voltage cathode), threaded with a gold-plated tungsten wire (the anode wire).

The TRT straws are filled with a gas mixture that includes argon and xenon. As charged particles cross the straws, they ionize the gas and the resulting charge is detected. However, for fast particles (usually electrons), X-ray transition radiation is also emitted[5]. This X-radiation also ionizes the xenon gas, leaving an even bigger signal. Since the rate of transition radiation depends on the particle's velocity, this phenomenon is used to distinguish highly ionizing particles, like electrons, from pions.

The TRT can be operated at room temperature.

New insertable B-layer

The ATLAS ID went through some changes during its upgrade phase in 2014. An Insertable B-layer (IBL) was added to the present Pixel detector between a new beam pipe and the current inner Pixel layer (B-layer). One of the main motivations for this change was to improve tracking precision. This new sub-detector was not present during the analysis in Chapter 7 of this thesis. For more details, see Reference [127].

4.3　Reconstruction of physics objects

The ATLAS detector (along with other modern particle detectors) is able to reconstruct and identify the passage of electrons, photons, muons and hadrons. Neutrinos are also stable, but they do not interact perceptibly, and hence escape undetected.

Reconstruction and identification of physics objects within ATLAS is based on detailed algorithms that combine different measurements throughout the detector in order to convert detector readout to physics objects such as "electrons" or "jets". For the analysis in this thesis, we are interested in the reconstruction of tracks, vertices, jets and p_T^{miss}, and the relevant reconstruction techniques of these objects are discussed in this section. For more details and the details of the reconstruction of other physics objects (such as electrons or muons, not used in this thesis), the reader is referred to Reference [122].

---

[5] Transition radiation occurs when a charged particle travels from one kind of material to another. The transition radiation measurement works on the principle that an ultra-relativistic particle emits X-rays when crossing the boundary between two materials.

4.3.1 Prompt and displaced reconstruction of tracks

As explained in Section 4.2, the ATLAS ID detects charged particles. Each charged particle leaves a series of hits in the detector which are eventually reconstructed as tracks.

Track reconstruction involves pattern finding of hits to construct track seeds and also track fitting, which makes trajectories of the track candidates. Global χ^2, Kalman-filter techniques [128], where the probability of a given hit to be compatible with the track is evaluated, and more specialized fitters are used, which are responsible for finding the track candidates.

Standard ATLAS track reconstruction algorithms [124] works in two main stages. First, an "inside-out" or silicon-seeded stage, where tracking starts by identifying three space points from silicon-only hits to form track seeds, which are then extended into the TRT and converted into a first set of tracks. After this, a second "outside-in" or TRT-seeded algorithm is performed that starts by combining TRT hits which have not been used in the inside-out stage, to form track segments which are then extrapolated to the innermost silicon detectors. TRT segments that have no matching silicon hits are stored as "TRT only tracks"[6].

At the end, a trajectory of the fitted track is determined by only five parameters, measured at a point Q on the helix trajectory of the track[7], with respect to a reference point R. See Figure 4.7. These track parameters are:

- The transverse impact parameter d_0, which is the distance of closest approach of the track to R in the $x - y$ plane, which defines the point Q of the track.

- The longitudinal impact parameter z_0, which is the longitudinal distance of the point of closest approach of the track to R.

- The azimuthal angle ϕ, such that $\tan \phi = p_y/p_x$, with p_x, p_y the x and y component of the track momentum.

- The polar angle θ, such that $\tan \theta = p_T/p_z$, with $p_T = \sqrt{p_x^2 + p_y^2} = p \sin \theta$, p_z the transverse and z component of the track momentum.

---

[6] TRT only tracks are not used in the Displaced Vertex analysis described in Chapter 7.

[7] The direction of the magnetic field inside the ID is parallel to the z axis, so the charged particle feels a magnetic force in the $x - y$ plane. This has the effect of changing the momentum direction in this plane, while the z component of the momentum of the track is not affected. Therefore, the charged particle follows an helix trajectory. If there is no magnetic field present or in the limit of high p_T, the track's trajectory can be approximated to a straight line.
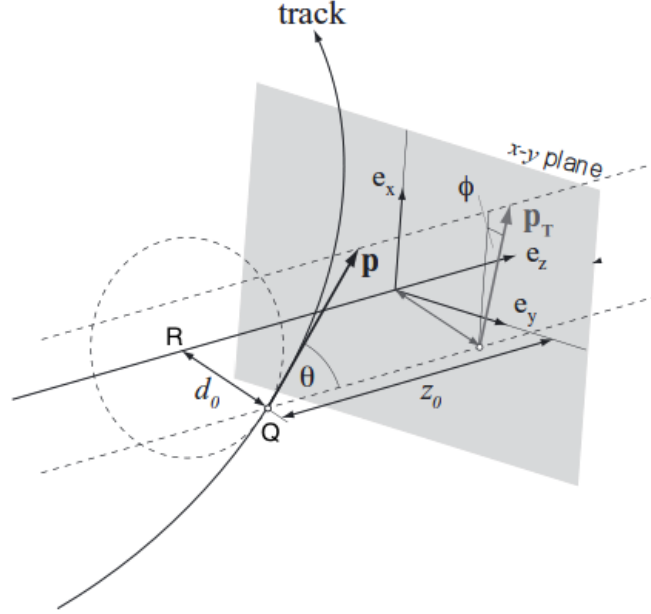
Figure 4.7: Schematic view of the five track parameters $(d_0, z_0, \phi, \theta, q/p)$ [129].

- The charge of the track (in units of e) divided by total momentum of the track q/p.

For better illustration, Figure 4.8 shows a schematic view in the transverse $x - y$ plane of a displaced decay.

Silicon-seeded and TRT-seeded algorithms always assume that tracks originate from close to the primary vertex (PV)[8], and therefore there is a low reconstruction efficiency for tracks coming from secondary vertices. Displaced tracks from a long-lived particle decay have a larger $|d_0|$ compared to prompt tracks. A procedure termed "re-tracking" [130], is performed when wanting to reconstruct displaced tracks, where the inside-out tracking algorithm is re-run on hits that are not used in the tracks found by standard ATLAS tracking, with looser cuts on impact parameters, extending the coverage from 10 to 300 mm in $|d_0|$ and from 320 to 1500 mm in $|z_0|$, in order to increase the efficiency for high-d_0 tracks (see Table 4.1).

---

[8] The PV is defined from the tracks coming from the primary pp interaction point (IP). These tracks are also termed prompt tracks.
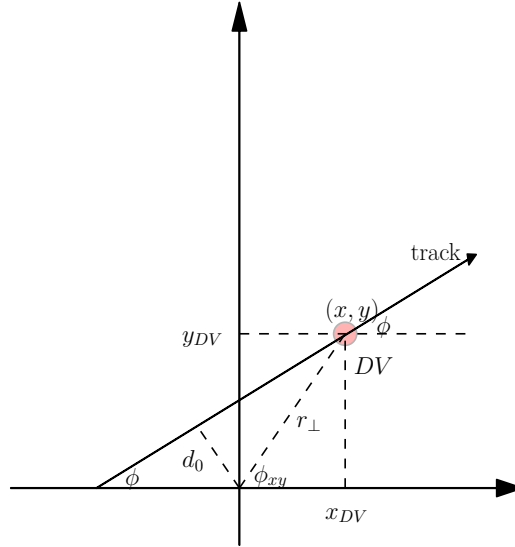
Figure 4.8: Schematic view in the transverse $x - y$ plane of a displaced decay. The transverse impact parameter d_0 is defined with respect to the origin $(0,0,0)$ as $d_0 = r_\perp \times \sin(\phi_{xy} - \phi)$, where $r_\perp = \sqrt{x^2 + y^2}$ corresponds to the transverse distance of the track's production vertex, ϕ is the azimuthal angle of the track and ϕ_{xy} corresponds to the angle in the transverse plane of the trajectory of the mother displaced particle. The daughter particle, which forms the track, was produced at (x, y, z) from the the decay of a long-lived particle. The displaced vertex (DV) position is represented by the pink disc. Note that at the truth level, the decay position of the displaced vertex matches that of the production vertex of the daughter particle, meaning the decay distance in the transverse plane of the vertex $r_{\mathrm{DV}} \equiv \sqrt{x_{\mathrm{DV}}^2 + y_{\mathrm{DV}}^2} = r_\perp$ [2].

4.3.2 Primary and displaced vertex reconstruction

Selected reconstructed tracks are input to the algorithms used to locate vertices. Very generally, reconstruction of vertices starts by identifying seed vertex candidates and then, dedicated algorithms attempt to fit the vertex's position. In this section, the main ideas behind the reconstruction of vertices will be stated. More details on the reconstruction of primary vertices (PV) can be found in Reference [131]. For full details on the reconstruction of displaced vertices (DV), see Reference [1] and references within.

The approach to identify a PV differs from the reconstruction of a DV mainly in the different track selection criteria used, as discussed already in Section 4.3.1, and the

Cut	Si-seeded	TRT-seeded	re-tracking
d_0	10 mm	100 mm	300 mm
z_0	320 mm	-	1500 mm
p_T	400 MeV	1 GeV	500 MeV
min pixel hits	0	-	0
min silicon hits	7	4	7
min TRT hits	-	15	-
min NOT shared	6	4	5
max shared	2	1	2

Table 4.1: Cuts applied in the different tracking algorithms [122, 130].

choice of the seed vertex candidates. However, the fitting procedure is based on the same hypothesis.

The goal of a 3D vertex fit is to obtain the vertex position $\vec{V}$ and the track momenta p at the vertex, as well as the associated covariance matrices C [132]. The input information for a vertex fit are the 5 track parameters and their covariance matrix of each track at a reference point. The charged tracks are characterized by parameters $q^i = (d_0^i, z_0^i, \phi^i, \theta^i, q/p^i)$, which are functions of the vertex position $\vec{V}$ and track momenta p^i at the vertex ($q^i = f(\vec{V}, p^i)$). The idea is to find the p and $\vec{V}$ that minimize,

$$\chi^2 = \sum_i^{\text{tracks}} (q^i - f(\vec{V}, p^i))C^{-1}(q^i - f(\vec{V}, p^i)) \tag{4.4}$$

in order to find the vertices.

For the identification of a PV, vertex candidates are reconstructed by seeds formed from prompt tracks. Tracks with similar longitudinal impact parameters are selected. The compatibility of the selected tracks with the assumption of a common origin in a vertex position is evaluated using the χ^2 described above. The PV originating from the pp collision must have at least 5 tracks and $|z_{\text{PV}}| < 200$ mm. In events with multiple interactions, the PV with the highest scalar sum of the p_T^2 of its tracks is used.

For the identification of a DV, the vertexing algorithm relies on a first seed selection where vertices are required to pass the following requirements:

- at least two tracks in the vertex to have $\vec{d} \cdot \vec{p} > -20$ mm, where $\vec{d}$ corresponds to the vector from the interaction point to the DV and $\vec{p}$ to be the momentum of the displaced track.

- $\chi^2/\mathrm{d.o.f} < 5$

- No silicon hits at smaller radius than the vertex position.

The first criterion ensures consistency of the vertex position and the direction of the tracks. The second criteria removes the major part of random combinations of tracks, while with the third one ensures that neither of the tracks has a hit in a silicon layer at a radius smaller than the vertex itself.

After this first seed selection, an incompatibility graph method [133] is applied to combine close-by 2-track seed vertices in order to form vertices with higher track multiplicities. The idea is to use the surviving seed vertices to create all possible N_{trk} vertices. Since it is possible that the same track is used in more than one vertex, an iterative "clean-up" algorithm is applied as follows:

1. For all tracks that are used in more than one vertex, the vertex+track combination with the largest χ^2 is found.

2. If this χ^2 is greater than 6, OR the two vertices are separated by more than 3σ (according to the uncertainties on their fitted positions), the track is removed from that vertex.

3. Otherwise, the two vertices are merged and refit.

4. Return to step 1.

5. Once the process has converged such that there are no tracks shared between vertices, a final merging step is performed where pairs of vertices separated by less than 1 mm are merged, and the combined vertex is refit.

The vertex reconstruction efficiency (described later in Section 7.4, but that relies on the procedure for reconstructing vertices just described) against the radial position of the DV, defined as $r_{\mathrm{DV}} \equiv \sqrt{x_{\mathrm{DV}}^2 + y_{\mathrm{DV}}^2}$, where x_{DV} and y_{DV} are the decay positions in the transverse plane, is shown in Figure 4.9, where the effect of re-tracking is also shown.
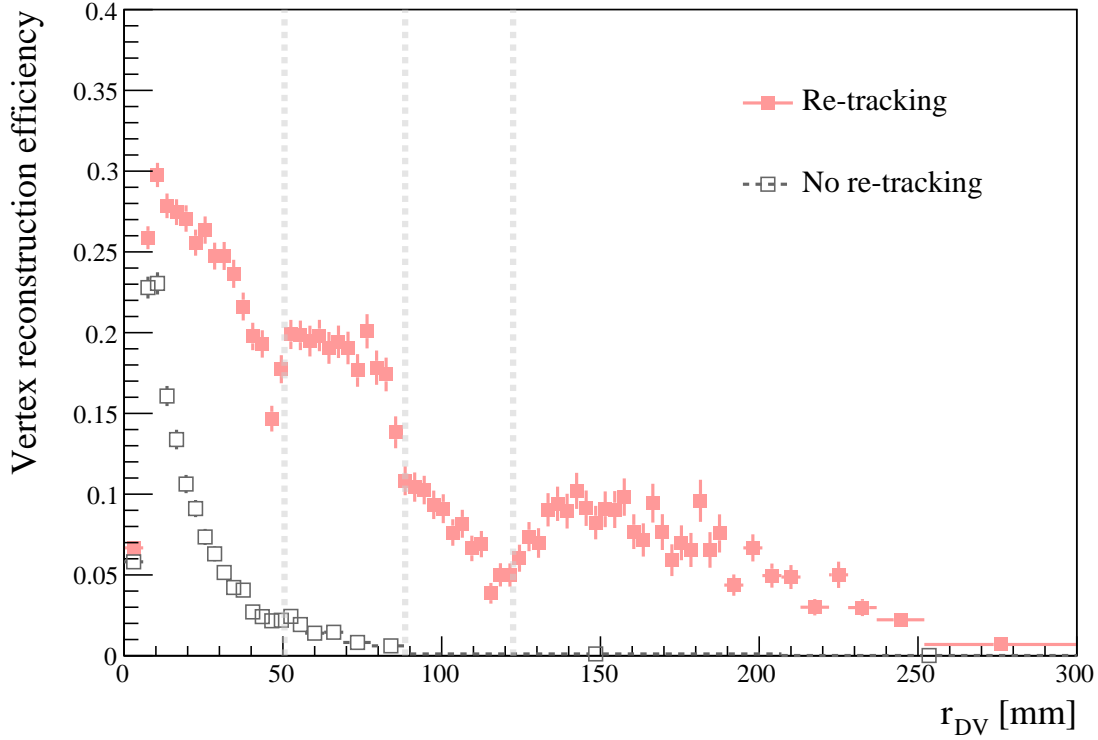
Figure 4.9: Efficiency of reconstructing a DV as a function of the vertex radial position r_{DV}. The vertical gray lines show the position of the first, second and third pixel layers. Drops in efficiency right before each layer correspond to losses in efficiency for decays immediately before a pixel layer, where many tracks from the vertex have shared pixel hits, so they fail the selection required by the tracking reconstruction algorithm (see Table 4.1).

4.3.3 Jet reconstruction

Jets are showers of hadrons that arise from the hadronization of quarks and gluons. A jet is reconstructed from energy deposits in both the EM and the HAD, associated with tracks in the ID.

Jet objects are made by jet clustering algorithms. In the analysis in this thesis, jet candidates are reconstructed using the anti-k_t jet clustering algorithm [134, 135] with a radius parameter $R = 0.6$. The inputs to this algorithm are the energies of clusters of calorimeter cells seeded by those with energy significantly above the measured noise [136, 137]. Jet momenta are constructed by performing a four-vector sum over these cell clusters, treating each cell as a four-momentum with zero mass.

Jets are initially calibrated to the electromagnetic energy scale, which correctly measures the energy deposited in the calorimeter by electromagnetic showers [136]. Further jet-energy scale corrections are derived from simulated events and data, and used to calibrate the energies of jets to the scale of their constituent particles [136]. Jets are required to satisfy $|\eta| < 4.5$ after all corrections are applied.

We can also have a special category of jets termed "trackless" jets, which may arise from decays of LLPs that take place far from the PV, where track-reconstruction efficiency is low. These are reconstructed as above, except that the anti-k_t radius parameter is $R = 0.4$, the jet pseudorapidity is in the range $|\eta| < 2.5$, and the scalar sum of the transverse momenta of the tracks in the jet is required to satisfy $\sum_{\text{tr}} p_T < 5$ GeV. Requiring the above ensures a trackless jet, as the jet needs to have no or close to no tracks in the ID.

4.3.4 Reconstruction of missing transverse momentum (p_T^{miss})

Particles that interact very weakly (such as the neutrino or the hypothetical neutralino) will be invisible to the detector. We can infer their presence indirectly by reconstructing the missing transverse momenta, defined as $p_T^{\text{miss}} = |\vec{p}_T^{\text{miss}}|$, where

$$\vec{p}_T^{\text{miss}} = -\sum_{\text{visible particles}} \vec{p}_T = \sum_{\text{invisible particles}} \vec{p}_T \tag{4.5}$$

The measurement of p_T^{miss} is based on the calibrated transverse momenta of all jet and lepton candidates, as well as all calorimeter energy clusters not associated with such objects [138, 139].

Chapter 5

Tools for discovery

Accurate simulation of event collisions is essential to contrast our physical models with real data from the experiments. Simulations are also relevant to make predictions and to develop techniques to propose to experiments. As the event topologies arising from the pp collisions are extremely complicated (mainly since they involve strong interactions), a wide group of Monte Carlo (MC) event generation algorithms are implemented to integrate over a many dimensional region. A brief overview on how the generation of pp collisions is done is presented in this Chapter. More details can be found in [140, 141].

In addition, statistical methods for establishing a discovery or setting upper limits in the absence of a statistically significant discovery claim are also fundamental in the search for new physics. In this Chapter, the standard statistical method used in the ATLAS collaboration for exclusion or discovery is explained briefly: the confidence-level or CL_S method [142, 143], which is used to set limits in Chapter 7. For a complete review on general statistics used in particle physics, see Reference [144].

5.1 Monte Carlo event generation of pp collisions

Event generation of collision events starts by deciding which hard process is wanted, as only a small fraction of events have a sufficient high-momentum transfer to make the process interesting. This is why is not really feasible to simulate all proton-proton collision, so event simulation needs to be structured with a focus on the particular hard scattering. This is done by calculating the probability distribution of a hard scatter in perturbation theory [141]. This relies on the Parton Distribution Functions (PDF), which correspond to the probability of extracting a parton (a quark or gluon) from the proton

at leading order in QCD. The partons involved in the hard scatter will then produce a parton shower, as scattered colour charged particles radiate gluons. The phase space fills up with (mostly soft) gluons. After the simulation of the parton shower, hadronization models take into account the confinement of a system of partons into hadrons. Hadrons are what we actually detect in the particle detectors. Some of these hadrons may decay, so a last step in the event generation of some generators is to model these decays.

Apart from the hard interaction, there is also a probability of other interaction between proton remnants. This is what is called the "underlying event", which produces soft hadrons that contaminate the hard process.

General purpose MC event generators widely used in HEP include PYTHIA [145, 146] and HERWIG ++ [147]. More specialized generators include MadGraph5 [148]. The event generation structure of a typical *pp* collision at the LHC can be seen in Figure 5.1.

After generation, events are passed through detector simulation in order to model the passage of the produced particles (and their decay products) through the detector and to also simulate the detector response. Physics objects such as tracks, electrons, jets and missing transverse momenta are then reconstructed from the simulated detector response and can be used for data analysis. Such programs include DELPHES [150] which is publicly available and is commonly used by theorists. The GEANT 4 package [151] is used inside the ATLAS collaboration. GEANT 4 is also public, but the ATLAS detector model (partly embedded in GEANT 4) is not.

The desired spectrum of a physics model is an input to the event generator program, as general purpose event generators do not have internal spectrum calculators for particular models. There are many publicly available software packages, that are model specific. In the case of SUSY models, the SOFTSUSY [152, 153] program is widely used and decays of SUSY particles can be computed with SDECAY [154]. For BSM models in general, the interface of the output of this programs with the event generator is done via Les Houches Accord (LHA) files [155, 156], that communicate the parameters of the model in an adequate format. Also, the FeynRules [157] program allows a complete derivation of Feynman rules and model parameters to be performed, that can be then interfaced with the event generators. A detailed chain of the full simulation procedure is shown below:
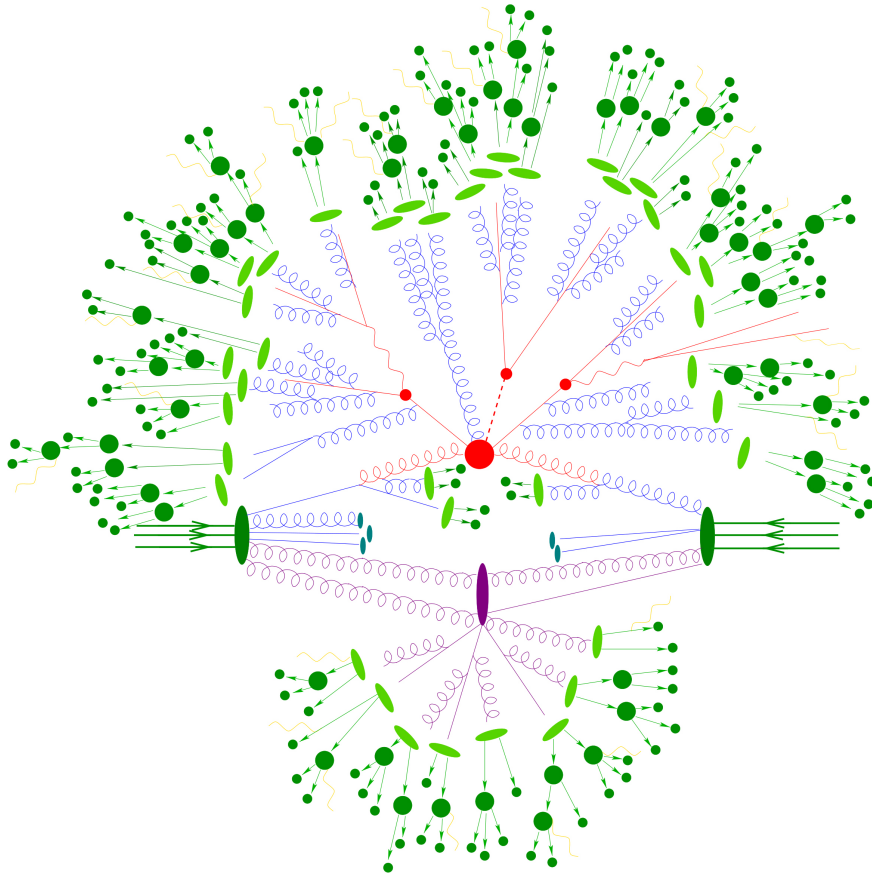
Figure 5.1: Structure of a typical *pp* collision. The hard scatter is shown as a red blob, whereas the purple blob represents the additional multi-parton interactions (i.e the underlying event). Initial and final-state radiation is depicted as curly and straight lines. The hadrons generated during the hadronization step are shown in light green, whereas the final stable hadrons are shown in dark green [149].
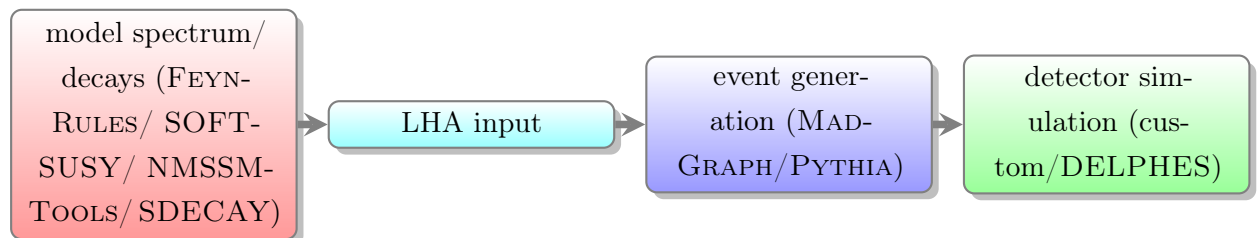
The above chain characterizes the simulations done in the phenomenological studies in Chapters 8 and 9.

5.2 Statistical analysis for new physics searches

For the statistical evaluation of a potential signal excess above the background (or the absence of one), a frequentist profile likelihood ratio technique [158] is widely used in the ATLAS collaboration: the CL_S method [142]. In this method, the idea is to test an hypothesis H_0 or b (often called the "null" or "background-only" hypothesis) where only background processes exists (i.e those due to SM processes) versus the alternative hypothesis H_1 or $s + b$ ("signal-plus-background"), where both signal and background exist (as, if there is a signal corresponding to a BSM process, then we will find both background and signal events).

Both hypotheses are put to the test by a so called "test statistic", which generally corresponds to a likelihood ratio for the two hypotheses of interest

$$\frac{L(H_1)}{L(H_0)} \quad \text{or} \quad \frac{L(s+b)}{L(b)} \tag{5.1}$$

where the likelihood ratio corresponds to the ratio of probability density functions (pdfs) for signal-plus-background and background models, which are usually simulated with sophisticated MC programs. The hypothesis testing procedure goes as follows. The goal is to determine whether a measurement is in agreement with our expectations or not. It is standard to define a parameter of interest μ to control the signal strength; $s\mu + b$, such that if $\mu = 0$ indicates an expected measurement of background-only, while $\mu = 1$ corresponds to the signal-plus-background model. We can construct the profile likelihood ratio, where the likelihood depends on the parameter of interest μ and nuisance parameters[1] $\theta = (\theta_1...\theta_N)$, defined as [158, 159],

$$\lambda(\mu) = \frac{L(\mu, \hat{\hat{\theta}}(\mu))}{L(\hat{\mu}, \hat{\theta})} \tag{5.2}$$

where $\hat{\hat{\theta}}(\mu)$, called the profiled values of the nuisance parameter θ, are the values that maximizes $L(\mu, \theta)$ for the specified value of μ, so the profile likelihood (the numerator in equation 5.2) depends only on μ. $\hat{\mu}$ and $\hat{\theta}$ are the values of the parameters that maximize the likelihood.

---

[1] These nuisance parameters can correspond to systematic uncertainties, for example.

The quantity $\lambda(\mu)$ is defined to vary between zero and one, with higher values indicating greater compatibility between the data and the hypothesized value of μ. The test statistic is defined as [158],

$$q_\mu = -2 \ln \lambda(\mu) \tag{5.3}$$

so higher values of q_μ thus correspond to increasing incompatibility between the data and the hypothesized μ.

Often a signal process is such that only positive values of μ are possible and a negative contribution is unphysical. In this case we would choose a critical region of our test of the background-only hypothesis ($\mu = 0$) to correspond to data outcomes characteristic of positive μ, when $\hat{\mu} > 0$. So, the statistic used to test the "discovery case" $\mu = 0$ is defined as follows:

$$q_0 = \begin{cases} -2 \ln \lambda(0) & \hat{\mu} \geq 0 \\ 0 & \hat{\mu} < 0 \end{cases} \tag{5.4}$$

If we are interested in an upper limit on μ, the statistic is set to zero when the best-fit signal strength parameter $\hat{\mu}$ is larger than one ($\mu = 1$ corresponds to the signal-plus-background hypothesis):

$$q_1 = \begin{cases} -2 \ln \lambda(1) & \hat{\mu} \leq 1 \\ 0 & \hat{\mu} > 1 \end{cases} \tag{5.5}$$

To quantify the level of disagreement between the data and the hypothesis of μ, using the observed value of q_0 or q_1 we compute the $p-$values for discovery ($\mu = 0$) and exclusion ($\mu = 1$) as,

$$p_\mu = \int_{q_{\mu,\text{obs}}}^{\infty} f(q_\mu | \mu, \theta) dq_\mu \tag{5.6}$$

where $f(q_\mu | \mu, \theta)$ denotes the pdf of the test statistic and $q_{\mu,\text{obs}}$ is the measured value of q_μ. In general, these pdfs are not easy to compute or integrate, so are performed with

so-called toy Monte Carlo pseudo-experiments where the nuisance parameters are fixed to their maximum likelihood estimates from data for a given signal strength parameter assumption.

Large $p-$values indicate good agreement of the data with the background-only hypothesis, while small values favors the signal-plus-background hypothesis. It is also customary to convert the $p-$value into the "sigma" of a unit Gaussian. The conversion is called the significance Z, and is defined as,

$$Z_\mu = \phi^{-1}(1 - p_\mu) \tag{5.7}$$

where ϕ is the Gaussian comulative distribution (with zero mean, unit variance) and ϕ^{-1} is its inverse function, also called the quantile of the standard Gaussian. Often in HEP, a significance of $Z_0 = 5$ is used as the threshold for claiming discovery of a new signal process. This corresponds to a very low $p-$value of $p_0 = 2.9 \times 10^{-7}$ for the background-only hypothesis, corresponding to a 5σ effect.

The criterion for exclusion of a signal model is given by,

$$\mathrm{CL_S} = \frac{p_\mu}{1 - p_0} \leq \alpha \tag{5.8}$$

and the typical test size is $\alpha = 0.05$, which means we have a confidence-level for excluding the signal-plus-background hypothesis of 95%. The $\mathrm{CL_S}$ upper limit on μ is denoted μ_{upper} and is obtained by solving $\frac{p_\mu}{1-p_0} = 5\%$, so a value of μ is excluded at the 95% confidence-level (CL) if $\mu < \mu_{\mathrm{upper}}$.

In the ATLAS collaboration (and in particular for the analysis in Chapter 7), exclusion limits are shown as numerical values comprising an upper limit on the BSM cross section, in order to get a limit on the visible cross section, defined as

$$\sigma_{\mathrm{visible}} = \sigma \times BR \times \epsilon. \tag{5.9}$$

where σ corresponds to the cross section, $BR = \Gamma_i/\Gamma$ decay branching fraction for the channel i (with $\Gamma = \sum_{i=1}^{n} \Gamma_i$ the total decay width of the n possible decay processes for the particle) and ϵ is the experimental efficiency, which includes the region of detector

acceptance. Note that in the analysis in Chapter 7 we are interested in reporting limits on a search targeting a specific signal production mechanism and a particular decay mode.

The signal strength μ with $\mathrm{CL_S} = 0.05$ is interpreted as the 95% CL upper limit N_{upper} on the number of expected BSM signal events consistent with observation. This upper limit is translated into an upper limit on the visible cross section dividing by the integrated luminosity, such that,

$$\sigma_{\mathrm{visible}}^{\max} = \frac{1}{\mathcal{L}} \times N_{\mathrm{upper}}. \tag{5.10}$$

Chapter 6

Overview of long-lived particle searches at ATLAS

Among the different searches for new physics, searches for long-lived, massive particles (LLPs) are an important part of the ATLAS program. These are theoretically very well motivated searches, as discussed in Chapter 1, where several extensions to the SM, including variants of Supersymmetry, predict the production of LLPs. Very generally, these are searches for heavy new particles with large enough lifetimes to allow them to travel measurable distances before decaying inside the detector, or are stable enough so they can travel through the entire detector length before decaying. A comprehensive review on theories with stable massive particles[1] and their detector signatures can be found in Reference [83]. LLPs with small enough lifetimes will decay inside the detector.

Different lifetimes, charge and velocities of LLPs will give rise to different detector signatures that require special triggers, reconstruction and simulation within ATLAS. These are summarized in Table 6.1, including references to the different analysis within ATLAS, and where possible theoretical models from which the LLP can arise are also stated (see Section 1.3.3 for References to these models). A diagram showing the different possible long-lived particle signatures we could see in the ATLAS detector is shown in Figure 6.1. If the lifetime of the LLP is of order of picoseconds to about a nanosecond ($\tau \sim 10^{-12} - 10^{-9}$ s), it will decay with a displaced vertex (DV) signature inside the tracker (within $\sim 1 - 300$ mm). This is the relevant long-lived particle signature discussed in this thesis, with its experimental search described in Chapter 7.

---

[1] Particles which do not decay during their passage through the detector are defined as stable massive particles (SMP).

Detector Signature	Decay Length [mm]	Model
Late decaying [160,161]	$\mathcal{O}(10000)$	split SUSY, HV
low β, large dE/dx [162]	$\mathcal{O}(1000)$	split SUSY, GGM, stealth SUSY, HIPs, AMSB
Stopped [163]	$\mathcal{O}(100 - 1000)$	split SUSY
Disappearing Tracks [164]	$\mathcal{O}(100 - 1000)$	AMSB
Non-pointing Photons [165]	$\mathcal{O}(100 - 1000)$	GGM
Displaced Vertex [1]	$\mathcal{O}(10 - 100)$	split SUSY, RPV, GGM, NMGMSB, HV

Table 6.1: Long-lived particle detector signatures according to their decay distance within the detector. References to the corresponding experimental analysis within ATLAS are given. Theoretical models in which these particles can be present are also stated.

Displaced vertex searches are especially challenging for LHC experiments due to the complication of assigning tracks originating far away from the primary interaction point to the correct pp interaction. Reconstruction of displaced decays becomes more difficult beyond the pixel layers, where vertex resolution is low. Nevertheless, these searches have an extremely low background as there are no irreducible contributions from the SM. Some recent theoretical reinterpretation of LHC displaced searches can be found in References [2,166–172], where some of the complications of reconstructing displaced decays are highlighted, especially when reconstruction is performed without all the private information from the experimental collaborations.

The ATLAS Run 1 multi-track DV search [1,173] is presented in this thesis, where displaced decays occur in the Inner Detector. ATLAS has also searched for long-lived particles leaving displaced vertices in the Muon Spectrometer [174]. Related searches have also been performed at other experiments. The CMS Collaboration has searched for decays of a long-lived particle into a final state containing two electrons, two muons [175,176], an electron and a muon [177], or a quark-antiquark pair [178]. The LHCb Collaboration has searched for long-lived particles that decay into jet pairs [179]. The Belle Collaboration has searched for long-lived heavy neutrinos [180], and the BABAR Collaboration has searched for displaced vertices formed of two charged particles [181]. The D0 Collaboration has searched for displaced lepton pairs [182] and $b\bar{b}$ pairs [183], and the CDF Collaboration has searched for long-lived particles decaying to Z bosons [184]. LLPs have also been searched for by the ALEPH Collaboration at LEP [185].
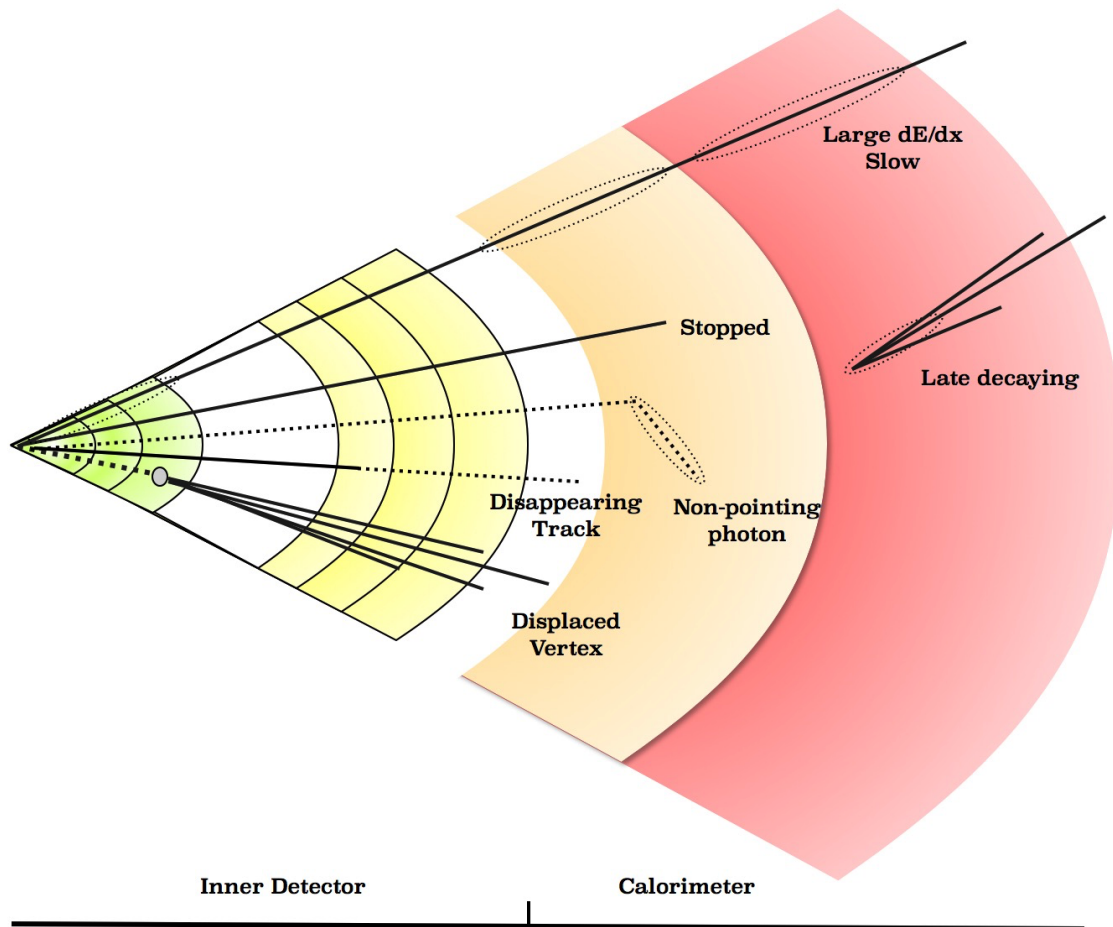
Figure 6.1: A cartoon image of the different long-lived particle signatures that are being looked for at ATLAS. The green section represents the Pixel detector, the white section the SCT and the yellow section the TRT. The light orange section represents the EM and the pink section the HAD. Solid lines represents charged particle tracks. Light dashed lines are invisible to the detector. The thick dashed line corresponding to the DV signature represents a particle that could either be charged or neutral. Dashed ovals represents energy deposits in the calorimeters.

Part III

Displaced Supersymmetry

Chapter 7

Searches for new physics with displaced vertices at ATLAS

This Chapter describes the ATLAS Run 1 DV multi-track search [1] of a characteristic massive long-lived particle signature, where the hypothetical long-lived particle can decay inside the ATLAS inner tracker, and the decay could give rise to a DV. This search has been interpreted in the context of the RPV, split SUSY and GGM simplified models described in Sections 3.2.1, 3.2.2 and 3.2.3 of Chapter 3.

The ATLAS DV analysis presented in this Chapter uses data from pp collisions taken at a center-of-mass energy of $\sqrt{s} = 8$ TeV, corresponding to an integrated luminosity of $\mathcal{L} = 20.3$ fb^{-1} collected in 2012 by the ATLAS detector. A preliminary result on this dataset, considering only the final state with a high-p_T muon, interpreted only in an RPV simplified model, was released as a conference note in 2013 [186]. Previous studies on this final state were also performed with the 2010 [187] and 2011 [188] data samples.

This search is the most up-to-date (at the time of writing) search for displaced Supersymmetry in ATLAS. The full analysis described in [1] is sensitive to final states containing displaced lepton pairs, and a displaced vertex with high track multiplicity and mass, either associated with: a high-p_T muon or electron, or in events with high jet multiplicity or large missing transverse momentum. The latter two are termed the DV+jets and DV+p_T^{miss} searches, and are the ones described in this thesis.

7.1 Monte Carlo simulation of the models[1]

This section describes the main features of the MC signal samples generated for the simulation of the three simplified models under study: RPV, split SUSY and GGM. In general, 50k, 10k and 60k events per sample are generated with the PYTHIA 6.426.2 [145] event generator[2] for the RPV, split SUSY and GGM models, respectively.

All samples are generated with the AUET2B ATLAS underlying event tune [189] and the CTEQ6L1 PDF set [190]. In each simulated event, two gluinos or two squarks are created in the pp collision. Both of these primary particles undergo decay chains. In the simulated GGM and RPV scenarios, the LLP is the lightest neutralino $\tilde{\chi}_1^0$. In the split SUSY scenario, the LLP is the gluino. Diagrams representing the simulated processes are shown in Figures 3.2, 3.3 and 3.4.

Each generated event is processed with the GEANT 4 [151] ATLAS detector simulation [191] and treated in the same way as the collision data. The samples include a realistic modeling of the effects of multiple pp collisions per bunch crossing observed in the data, obtained by overlaying additional simulated pp events generated using PYTHIA 8 [146], on top of the hard scattering events, and reweighting events such that the distribution of the number of interactions per bunch crossing matches that in the data.

In what follows, the notation $P \to A\,[L \to F]$ denotes an MC sample in which a primary particle P produced in the pp collision decays into a long-lived particle L and additional particles denoted A. The decay of the LLP into final state F is enclosed in square brackets. Samples where the primary particle is long-lived are denoted with $[L \to F]$. In both cases, masses may be indicated with parentheses, as in $[L(100\text{GeV}) \to F]$. The symbol q indicates a u or d quark unless otherwise specified, and ℓ indicates an electron or a muon. Charge conjugation of fermions is to be understood where appropriate.

Different RPV couplings can give rise to different decay channels of a neutralino LSP. RPV samples of $\tilde{q} \to q[\tilde{\chi}_1^0 \to \ell qq/\nu qq]$ are generated. The $\tilde{\chi}_1^0$ decays into two light quarks and an electron, muon, or neutrino, is governed by the nonzero RPV coupling λ'_{i11}. Samples containing heavy flavour quarks, $\tilde{q} \to q[\tilde{\chi}_1^0 \to \ell qb]$ (produced with $\lambda'_{i13} \neq 0$)

---

[1] The generation of the Monte Carlo samples used in this analysis were done within the ATLAS framework by members of the ATLAS MC Simulation group.

[2] We use PYTHIA 6 as it was easier to adapt the generation done in the previous analysis in [187]. PYTHIA also directly implements the RPV decays we need in our study.

and $\tilde{q} \to q[\tilde{\chi}_1^0 \to \ell c b]$ (corresponding to $\lambda'_{i23} \neq 0$) are also generated, in order to study the impact of long-lived charm and bottom hadrons on the efficiency of DV reconstruction. A $\tilde{g} \to qq[\tilde{\chi}_1^0 \to \ell qq]$ sample is used to verify that the production mechanism has minimal impact on our vertex selection efficiency, by comparing with the corresponding model with squark production. A summary of the RPV signal MC samples presented in this thesis is detailed in Table 7.1. The chosen values of squark and neutralino masses span a wide range in the quantities to which the signal efficiency is most sensitive, namely, the neutralino mass and boost (see Section 7.4). The values of the λ' coupling in the various samples are selected such that a significant fraction of neutralino decays occur in the detector volume considered in this analysis.

Within a split SUSY scenario we simulate production and hadronization of primary, long-lived gluinos. GEANT 4 simulates the propagation of the gluino $R-$hadron through the detector [192], and PYTHIA decays the $R-$hadron into a stable neutralino plus two quarks (u, d, s, c or b), a gluon, or two top quarks. The resulting samples are denoted $[\tilde{g} \to qq\tilde{\chi}_1^0]$, $[\tilde{g} \to g\tilde{\chi}_1^0]$, or $[\tilde{g} \to tt\tilde{\chi}_1^0]$, respectively. Different combinations of gluino and neutralino mass are considered, as shown in Table in 7.2. As with the RPV samples, the chosen values of gluino and neutralino masses try to span a range in relevant quantities such as mass and boost. The lifetime values ensure that a significant fraction of gluinos will decay inside our fiducial volume.

GGM samples are produced as $\tilde{g} \to qq[\tilde{\chi}_1^0 \to \tilde{G}Z]$, in which the NLSP $\tilde{\chi}_1^0$ is a higgsino-like neutralino. Both the leptonic and hadronic decays of the Z boson are considered. Details of these samples are listed in Table 7.3. As before, the chosen values of gluino and neutralino masses span a range in relevant quantities such as mass and boost. The lifetime values ensure that a significant fraction of neutralinos will decay inside our fiducial volume.

Event displays for the $R-$hadrons samples are shown for the purpose of illustration. Event displays in the $x - y$ and in the $r - z$ plane can be seen in Figure 7.1 and 7.2, respectively.

Production	Produced particle mass [GeV]	LLP decay channel	LLP mass [GeV]	$c\tau_{\mathrm{MC}}$ [mm]	RPV coupling	σ [fb]
$\tilde{q}$	700	$\tilde{\chi}_1^0 \to \mu+\text{jets}$	494	175	$\lambda'_{211} = 2 \times 10^{-6}$	124.3
$\tilde{q}$	700	$\tilde{\chi}_1^0 \to e+\text{jets}$	494	175	$\lambda'_{111} = 2 \times 10^{-6}$	124.3
$\tilde{q}$	700	$\tilde{\chi}_1^0 \to \mu+\text{jets}$	494	175	$\lambda'_{223} = 3.55 \times 10^{-6}$	124.3
$\tilde{q}$	700	$\tilde{\chi}_1^0 \to e+\text{jets}$	494	175	$\lambda'_{113} = 3.55 \times 10^{-6}$	124.3
$\tilde{q}$	700	$\tilde{\chi}_1^0 \to \nu+\text{jets}$	494	175	$\lambda'_{211} = 2 \times 10^{-6}$	124.3
$\tilde{q}$	700	$\tilde{\chi}_1^0 \to \nu+\text{jets}$	108	101	$\lambda'_{211} = 1.5 \times 10^{-4}$	124.3
$\tilde{q}$	1000	$\tilde{\chi}_1^0 \to \nu+\text{jets}$	108	220	$\lambda'_{211} = 2 \times 10^{-4}$	11.9
$\tilde{g}$	700	$\tilde{\chi}_1^0 \to \nu+\text{jets}$	494	175	$\lambda'_{211} = 1.03 \times 10^{-5}$	434.0

Table 7.1: The parameter values for the RPV signal MC samples used in this thesis. Production cross sections were calculated following the prescriptions in [193].

Production	Produced particle mass [GeV]	LLP decay channel	LSP mass [GeV]	$c\tau_{\mathrm{MC}}$ [mm]	σ [fb]
$\tilde{g}$	400	$\tilde{g} \to qq/g + \tilde{\chi}_1^0$	100	300	18.9
$\tilde{g}$	800	$\tilde{g} \to qq/g + \tilde{\chi}_1^0$	100	300	0.157
$\tilde{g}$	1000	$\tilde{g} \to qq/g + \tilde{\chi}_1^0$	100	300	0.0243
$\tilde{g}$	1400	$\tilde{g} \to qq/g + \tilde{\chi}_1^0$	100	300	7.14×10^{-4}
$\tilde{g}$	500	$\tilde{g} \to t\bar{t} + \tilde{\chi}_1^0$	20	300	4.45
$\tilde{g}$	800	$\tilde{g} \to t\bar{t} + \tilde{\chi}_1^0$	320	300	0.157
$\tilde{g}$	1100	$\tilde{g} \to t\bar{t} + \tilde{\chi}_1^0$	620	300	9.06×10^{-3}
$\tilde{g}$	1400	$\tilde{g} \to t\bar{t} + \tilde{\chi}_1^0$	920	300	7.14×10^{-4}

Table 7.2: The parameter values for the decaying $R-$hadron signal MC samples used in this thesis. Production cross sections were calculated following the prescriptions in [193].

Production	Produced particle mass [GeV]	LLP decay channel	LLP mass [GeV]	$c\tau_{\mathrm{MC}}$ [mm]	σ [fb]
$\tilde{g}$	1100	$\tilde{\chi}_1^0 \to Z\tilde{G}$	400	230.2	7.57
$\tilde{g}$	1100	$\tilde{\chi}_1^0 \to Z\tilde{G}$	1000	183.4	7.57

Table 7.3: The parameter values for the GGM signal MC samples used in this thesis. Production cross sections were calculated following the prescriptions in [193].
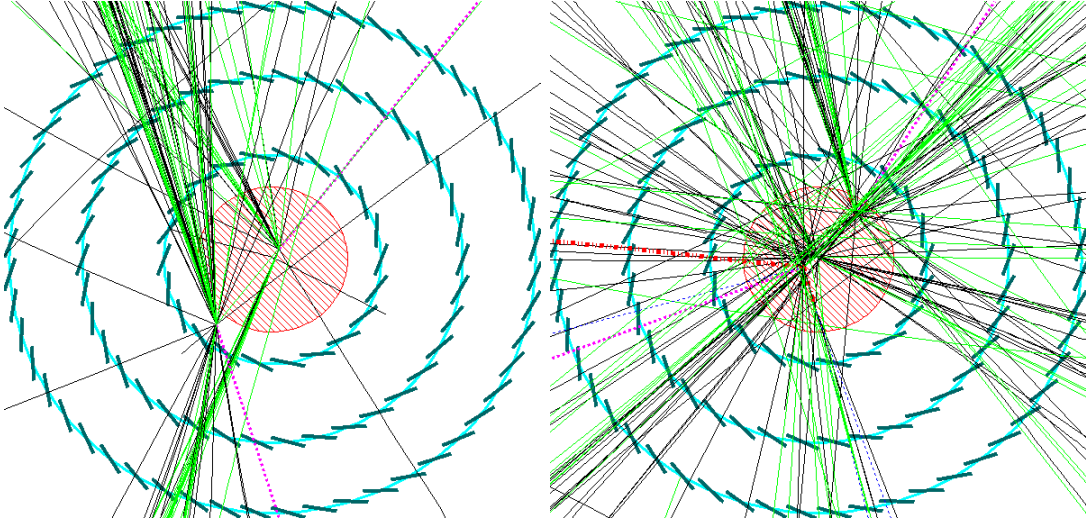
Figure 7.1: Event displays in the $x-y$ plane for two representative $R-$hadron signal samples. The three pixel layers and their modules are shown in blue. The beampipe corresponds to the circle in red. Green lines represent electrons and photons, black lines are pions and purple dashed lines are neutralinos. The orange lines corresponds to $b-$hadrons from top decays.

7.2 Event selection

The event selection is designed based on MC and experience from previous analyses [186, 187] to strongly suppress background while efficiently accepting signal events over a broad range of LLP masses, lifetimes, and velocities.

The first selection of events is performed with a combination of triggers that require the presence of jets or p_T^{miss}. The trigger requirement for the DV+p_T^{miss} search is:

- $p_T^{\mathrm{miss}} > 80$ GeV.

The DV+jets search requires:

- four jets with $p_T > 80$ GeV, five jets with $p_T > 55$ GeV, or six jets with $p_T > 45$ GeV.

Events passing the trigger are required to contain at least one "good" PV; with at least five tracks, and z position $|z_{\mathrm{PV}}| < 200$ mm. In addition, all events are required to satisfy standard ATLAS data quality requirements, as described in detail in [194, 195]. The main goal of these selections is to ensure a good quality of events to be selected for physics analysis. We veto events that for example have fake p_T^{miss} due to non operational cells in the calorimeters.
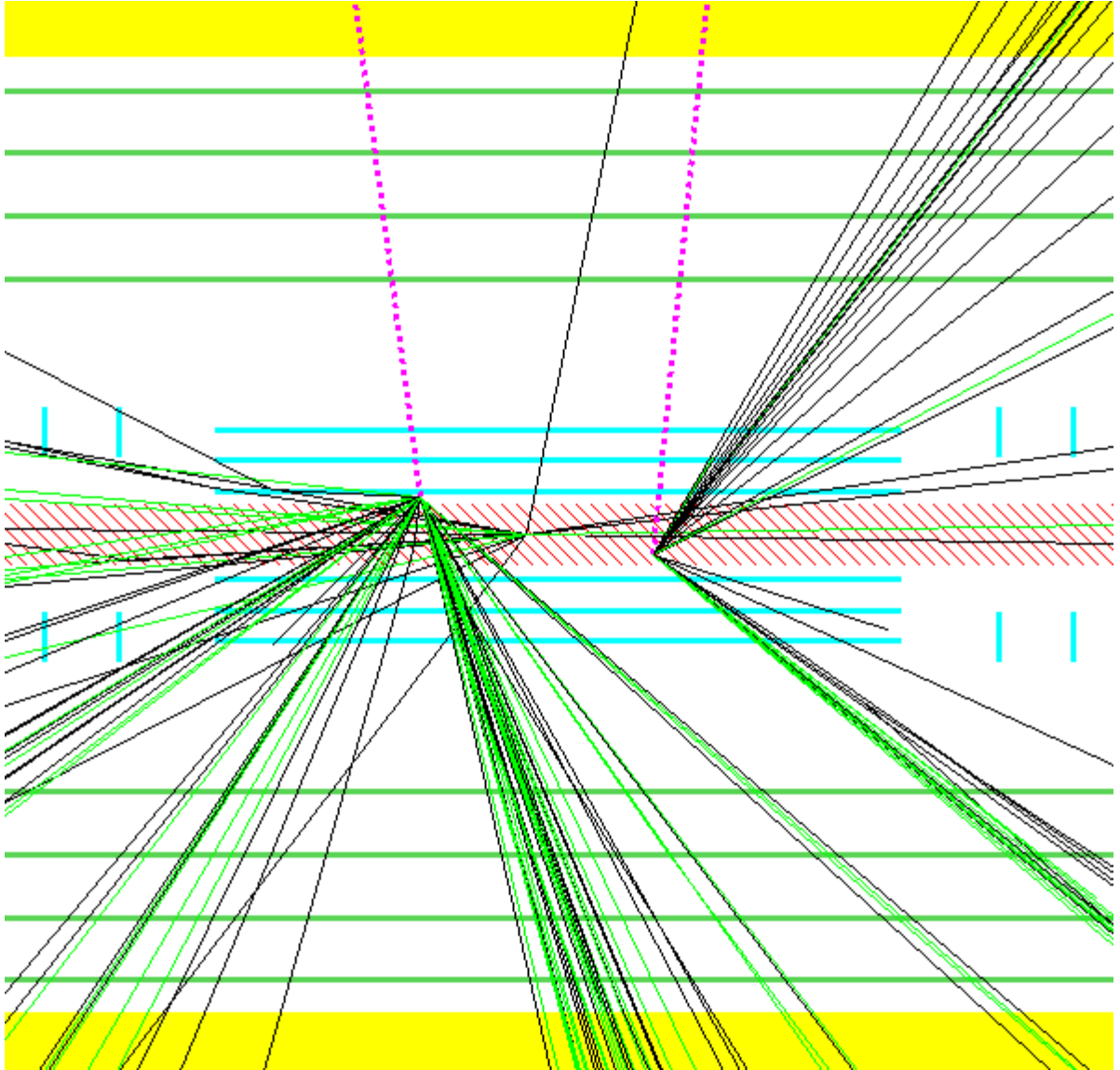
Figure 7.2: Event display in the $r-z$ plane for one representative $R-$hadron signal sample. The three pixel layers and their modules are shown in blue. The SCT layers are shown in green and the TRT is represented in yellow. The beampipe corresponds to the red strip. Green lines are electrons and photons, black lines are pions and purple dashed lines are neutralinos.

In addition, standard jet and p_T^{miss} "cleaning" is applied both to data and MC, as detailed in [196], where we veto events with "bad" jets. Following the same logic as before, these "bad " jets are not real energy deposits in the calorimeters and can arise for example from hardware problems, such as high voltage trips in the Tile calorimeter. We therefore need to veto events with jets pointing to these regions of the calorimeters.

An additional cleaning procedure [197] is applied both to data and MC to deal with masked modules[3]. In particular, events involving high p_T jets can be poorly reconstructed, as the jets are more collimated and thus can be more completely contained within masked modules. This is also relevant for p_T^{miss} since these masked regions can create large amounts of fake p_T^{miss}.

We apply further object requirements before considering the reconstructed vertices within these events. For the following selection criteria, the trigger efficiency is approximately independent of the p_T^{miss} and the jet transverse momenta. For DV+p_T^{miss}, we require:

- At least two trackless jets with $p_T > 50$ GeV.

- $p_T^{\mathrm{miss}} > 180$ GeV.

For the DV+jets search, we require:

- At least one trackless jet with $p_T > 50$ GeV.

- At least 4 jets with $p_T > 90$GeV and $|\eta| < 2.8$, OR

- At least 5 jets with $p_T > 65$GeV and $|\eta| < 2.8$, OR

- At least 6 jets with $p_T > 55$GeV and $|\eta| < 2.8$.

Where we have defined trackless jets in Section 4.3.3. After all the criteria described above are applied for either of the DV+p_T^{miss} and DV+jets searches, events are required to contain *at least one* reconstructed DV.

DVs are reconstructed from tracks reconstructed with standard tracking techniques and re-tracking, as explained in Section 4.3.1. After re-tracking, the following requirements on tracks are imposed:

- Transverse impact parameter $|d_0| > 2$ mm.

- Transverse momentum $p_T > 1$ GeV.

- At least 2 SCT hits.

---

[3] A masked module refers to a certain region of the calorimeter that has not been considered or has been vetoed for physics analysis. For a variety of reasons (such as hardware problems or digital errors), there are regions which are either temporarily or permanently masked throughout all data taking periods, so is important to evaluate and account for the effect this has in the reconstruction of jets and p_T^{miss}.

- Tracks are rejected if they have zero TRT hits and the number of Pixel hits is less than 2.

The first cut is applied in order to reject prompt tracks. The following cuts are placed to ensure that high quality tracks are used in the reconstruction of DVs. In particular, the last cut is effective at removing fake tracks made up of hits in the SCT endcaps.

Further selection of the DV requires that:

- The vertex position should be in the fiducial volume $r_{\mathrm{DV}}, |z_{\mathrm{DV}}| < 300$ mm.

- The vertex should not be in a region of dense material.

- The vertex should be separated by at least 4 mm in the (x, y) plane from all reconstructed primary vertices in the event ($\Delta_{xy} \equiv \sqrt{(x_{\mathrm{DV}} - x_{\mathrm{PV}})^2 + (y_{\mathrm{DV}} - y_{\mathrm{PV}})^2} > 4$ mm).

- The signal region[4] for vertex candidates is then defined as $N_{\mathrm{trk}} \geq 5$, and $m_{\mathrm{DV}} > 10$ GeV (where m_{DV} is the invariant mass of the vertex calculated using the charged pion mass hypothesis for the tracks).

A 3D material map of the detector is needed to veto vertices that are reconstructed in high density material regions[5]. These vertices are likely to have arisen from hadronic interactions of primary particles with the detector material (see Section 7.5). A plot showing the reconstructed vertices vetoed by the material map is shown in Figure 7.3, where the extension covers $r_{\mathrm{DV}} < 300$ mm and $|z_{\mathrm{DV}}| < 300$ mm, which corresponds to the fiducial volume used in this analysis. The following Δ_{xy} cut is placed to minimize background due to tracks originating from the PVs. The last two cuts define the signal region, as no contribution from the SM will give rise to high mass, high track multiplicity displaced vertices (see Section 7.5).

A summary of the cuts applied in both DV+jets and DV+p_T^{miss} multi-track searches can be seen in Table 8.1.

---

[4] Defined as the region where signal is expected to be found.
[5] This material map was developed by other members of the ATLAS DV group and has evolved since the first DV analysis in 2011. See [1, 173] and [198] for all the details.
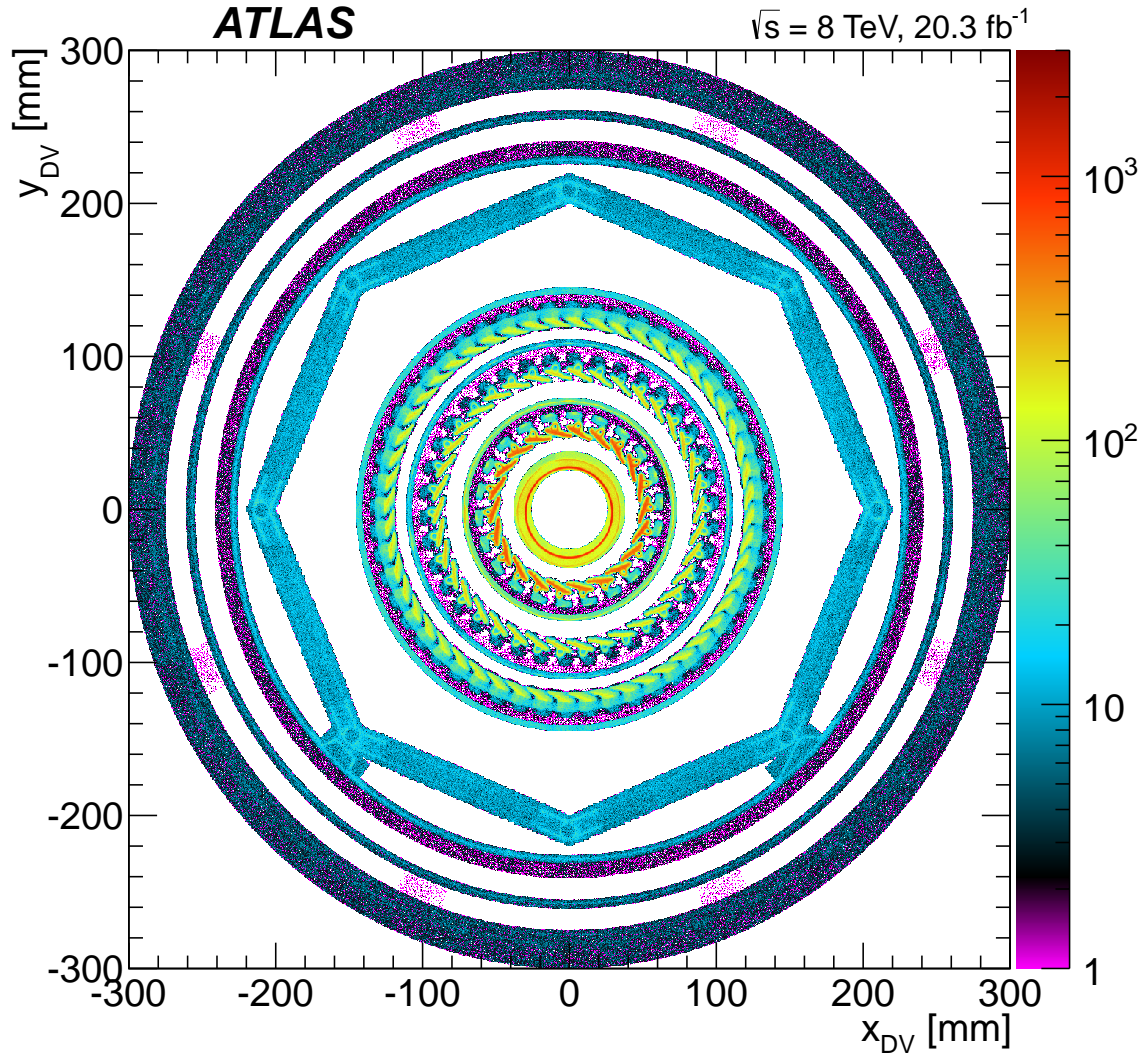
Figure 7.3: Transverse-plane density of vertices with fewer than five tracks in material regions that are excluded by the material veto in the region $|z| < 300$ mm. The innermost circle corresponds to the beampipe. This is surrounded by the three pixel layers. The octagonal shape and outermost circles are due to support structures separating the pixel and SCT detectors [1].

Selection	DV+jets	DV+p_T^{miss}
PV selection	PV with ≥ 5 tracks, $|z_{\text{PV}}| < 200$ mm	
jets/p_T^{miss} selection	4,5,6 jets, $p_T > 90, 65, 55$ GeV and $|\eta| < 2.8$	$p_T^{\text{miss}} > 180$ GeV
	One 50 GeV trackless jet	Two 50 GeV trackless jets
DV reconstruction	Made from tracks with $p_T > 1$ GeV, $|\eta| < 2.5$ and $|d_0| > 2$ mm wrt PV	
	$\Delta_{xy} > 4$ mm (DV position wrt. PV)	
DV fiducial	$r_{\text{DV}} < 300$ mm , $|z_{\text{DV}}| < 300$ mm (DV position wrt. origin)	
DV material	Material veto	
N$_{\text{trk}}$	$N_{\text{trk}} \geq 5$	
m_{DV}	$m_{\text{DV}} > 10$ GeV	

Table 7.4: Summary of selection criteria for the multi-track DV searches presented in this thesis.

7.3 Dominant systematic uncertainties: p_T^{miss} and jet reconstruction efficiency[6]

In this Section, we comment on the dominant systematic uncertainties on our signal samples. The dominant systematic uncertainties are those associated with the efficiency for reconstructing jets and p_T^{miss}. Since the background level is low, uncertainties on the background estimation have a minor effect on the results of the analysis. For full details on the signal uncertainties and corrections applied in the DV analysis, the reader is referred to Refs. [1, 173].

Systematic uncertainties in the p_T^{miss} measurement are evaluated with the usual methods within ATLAS described in Refs. [138, 139] and propagated to the efficiency uncertainty. The impact on the signal efficiency of uncertainties in the jet-energy scale calibration and jet-energy resolution is evaluated following the standard method used in ATLAS described in Refs. [199] and Ref. [200], respectively.

An additional uncertainty on the jet p_T is evaluated for jets that originate from the decay of a LLP (i.e displaced jets), as these jets may not have exactly the same properties as prompt jets, which are the ones that are reconstructed in ATLAS. The deviation (or shift) of displaced jets relative to normal jets increases with the decay

---

[6] The uncertainty associated to the effect of initial and final-state radiation was implemented by Nora Pettersson. The one associated to trackless jets was implemented by Nick Barlow.

length of the LLP. The uncertainty in the reconstructed jet p_T is then estimated by linearly parameterizing the p_T mismeasurement in MC simulation as a function of r_{DV} and z_{DV}. The only significant dependence observed is a p_T mismeasurement of

$$p_T^{\mathrm{shift}} = (4 \pm 1) \times 10^{-5}(r_{\mathrm{DV}}/\mathrm{mm}), \tag{7.1}$$

that is used to scale the jet p_T as $p_T^{\mathrm{shift}} \times p_T$. This is propagated to the jet selection efficiency as a systematic uncertainty [173]. Note the effect is so small that allows us to use standard (prompt) jet calibration tools in ATLAS.

To account for possible mismodeling of trackless jets, an uncertainty is obtained by varying the requirement on $\sum_{\mathrm{tr}} p_T$ for these jets [173].

The impact of uncertainties in the simulation of initial state radiation (ISR) is estimated by varying the p_T distribution of the primary particles according to the distribution observed in MADGRAPH 5 [201] samples [173]. This is because MADGRAPH simulates a more accurate description of radiative effects than PYTHIA.

After the corrections, the change in the signal efficiency varies between 2% and 10%. Figure 7.4 shows all systematics as a function of $c\tau$ for representative signal samples. In all cases, the dominant uncertainty at small lifetimes is statistical, as a result of our reweighting procedure (only events with DVs decaying at small $c\tau$ have significant contributions). This is particularly true for the split SUSY samples, where we only have 10k events per sample, while we have 50k or 60k events for the RPV and GGM samples.

Since many of the systematic uncertainties are evaluated by looking at the difference between the "nominal" efficiency-vs-$c\tau$ and the efficiency-vs-$c\tau$ curve after some change (e.g. jet-energy scale variation), there is a statistical component to these systematic uncertainties, again, particularly at very small or very large lifetimes where individual events can have large weights.

In addition to the statistical uncertainty which dominates at small lifetimes, the ISR-related uncertainty is also large, as a larger boost arising from the recoil against an ISR jet can increase the fraction of events passing the jet or p_T^{miss}cuts. At very large lifetimes, there can also be a dominant contribution from a systematic uncertainty associated with the lifetime reweighting procedure we apply, and is due to our finite-sized MC samples. Further details on this can be found in Reference [173].
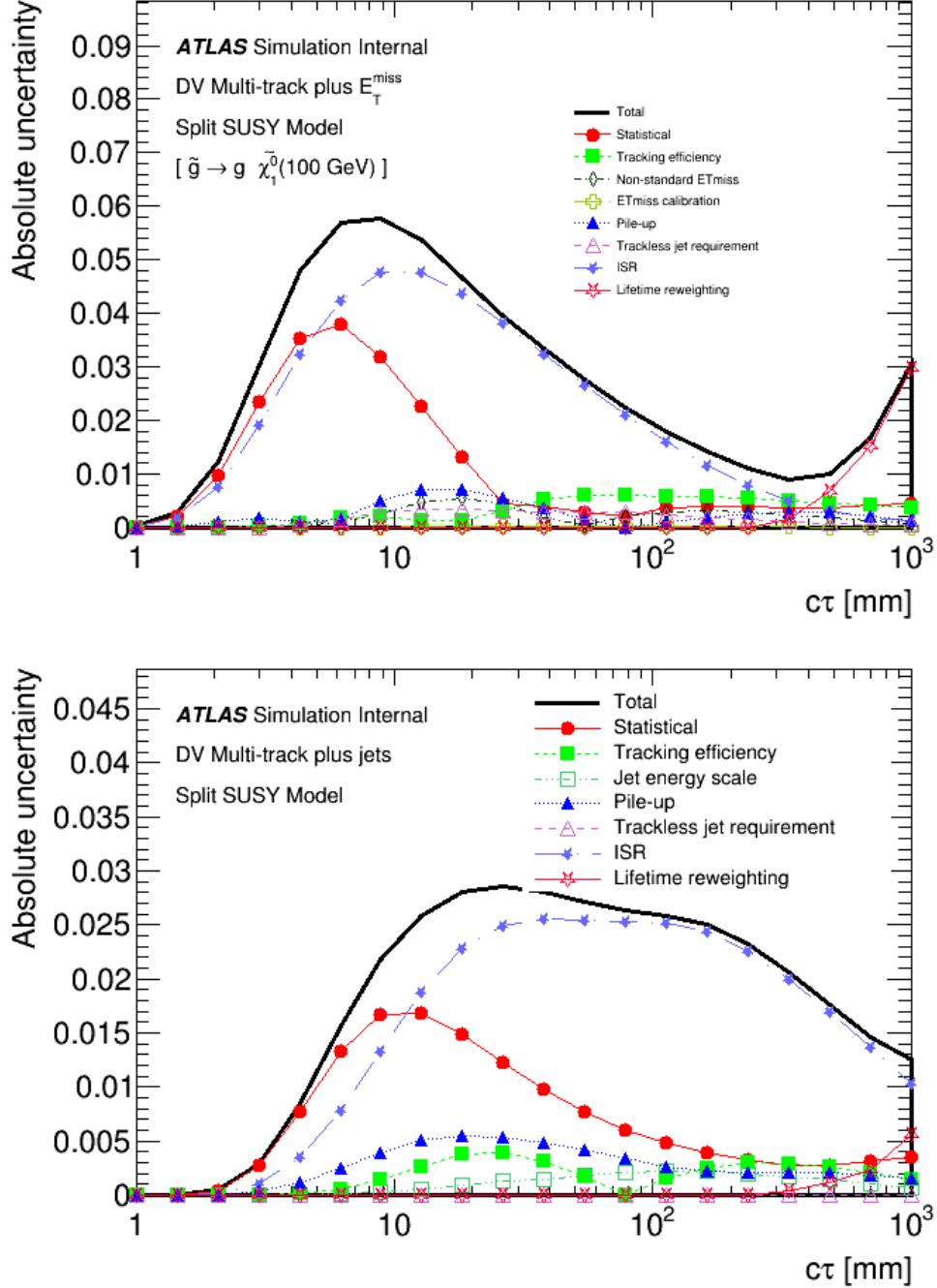
Figure 7.4: Contributions to the uncertainty for DV+p_T^{miss}(top) and DV+jets (bottom) as a function of $c\tau$. There is an uncertainty associated with the reconstruction efficiency for tracks that originate far from the interaction point (ie. tracking efficiency). For the DV+p_T^{miss}channel, there is a non-standard contribution related to the fact in this analysis we cut on a variable for p_T^{miss}which uses an older calibration. The standard uncertainty on $p_T^{\mathrm{miss}}$is shown separately. The "pile-up" correction takes into account the weighting of MC events such that the distribution of the average number of pp interactions per bunch crossing matches the one in data. The jet-energy scale uncertainty includes the non-standard shift of displaced jets relative to normal jets described in the text. The uncertainty associated with trackless jets is shown separately [1, 173].

7.4 Signal efficiency

We can now evaluate the event-level efficiency (ϵ_{evt}) for reconstructing vertices after applying all selections and uncertainties described in the previous Sections. ϵ_{evt} is defined as the probability for an event containing two DVs to be identified with at least one DV satisfying all the selection criteria. The efficiency for reconstructing a multi-track DV with the described selection criteria depends strongly on the efficiencies for track reconstruction and track selection, which are affected by several factors:

- The impact parameter d_0 of the track: the efficiency for reconstructing tracks decreases with increasing values of d_0, since the track algorithms are not optimized for prompt tracks and also the density of fine instrumentation decreases.

- The mass of the LLP: the number of tracks originating from the vertex increases with increasing mass, so the reconstruction efficiency is higher for a heavier LLP.

- The energy of the long-lived particle: the higher the boost, the more tracks will have a small angle with respect to the flight direction of the LLP and may therefore fail the minimal d_0 cut.

- The decay position of the vertex: when a LLP decays at a radius somewhat smaller than that of a pixel layer, many tracks share hits on that pixel layer, failing to meet the track selection criteria.

We can therefore see that the vertex reconstruction efficiency will be a non-trivial combination of different aspects of the track reconstruction efficiency.

7.4.1 Efficiency vs vertex displacement

The resulting impact on efficiency against vertex displacement is studied in this Section. Generally, the vertex reconstruction efficiency is worst at large radii, which is due to the tracking efficiency decreasing.

The efficiency for reconstructing a multi-track DV is reduced when the LLP decays to charm or bottom hadrons, resulting in two or more nearby DVs. Each of these DVs has a high probability of failing to meet the N_{trk} and m_{DV} criteria, resulting in low efficiency if these DVs are not merged. This happens less at large values of r_{DV}, where DVs are more readily merged due to the worse position resolution.

As discussed in Section 4.3.2, the final step of our vertexing algorithm is to merge pairs of vertices separated by less than 1 mm. Depending on the boost of the LLP, this may or may not be enough to recover the lost efficiency. This effect is studied by looking at RPV samples with different couplings, such that one or more b or c quarks come from the neutralino decay, and $R-$hadron samples with $\tilde{g} \to t\bar{t}\tilde{\chi}_1^0$ decays. Figure 7.5 shows a comparison of the event-level efficiency against vertex position for the RPV and split SUSY models. In the RPV model, the comparison is between a signal sample with only light jets, and with one heavy-flavour jet. It is noticable that at small radii ($r < 100$ mm) there is a significant drop in efficiency, while outside the third pixel layer the effect is less dramatic. This is likely to be due to the larger uncertainties on track parameters meaning that it is easier to fit all the tracks into a single vertex with reasonable χ^2.

We can also see the effects of heavy flavour jets for the $R-$hadron samples in Figure 7.5, where we compare one mass point for both $\tilde{g} \to t\bar{t}\tilde{\chi}_1^0$ and $\tilde{g} \to q\bar{q}/g\tilde{\chi}_1^0$ decays. For the $\tilde{g} \to t\bar{t}\tilde{\chi}_1^0$ decay, more of the energy goes into the ttbar system, than for $\tilde{g} \to q\bar{q}/g\tilde{\chi}_1^0$, so the truth-level mass will always be higher. However, at small radii, where position resolution is good, we lose some tracks that are in $b-$jets for $\tilde{g} \to t\bar{t}\tilde{\chi}_1^0$, so we have lower efficiency. At large radii ($r > 120$ mm), where position resolution is bad, everything gets merged into one vertex, so we recover that efficiency.

We also comment that the efficiency for reconstructing a displaced vertex does not depend appreciably on whether the primary particle is a squark or a gluino. However, the nature of the primary particle determines the number of jets, and hence impacts the event-level efficiency in the DV+jets and DV+p_T^{miss} channels.

7.4.2 Efficiency vs lifetime

Although all our signal MC samples each have only one value for the average lifetime $c\tau_{\mathrm{MC}}$ of the LLP particle (see Tables 7.1, 7.2 and 7.3), we would like to evaluate the efficiency for a range of lifetimes. In order to do this, we adopt a re-weighting strategy, where each LLP is given a weight

$$W_{\mathrm{DV}}(t, \tau) = \frac{\tau_{\mathrm{MC}}}{\tau} \exp\left(\frac{t}{\tau_{\mathrm{MC}}} - \frac{t}{\tau}\right), \tag{7.2}$$
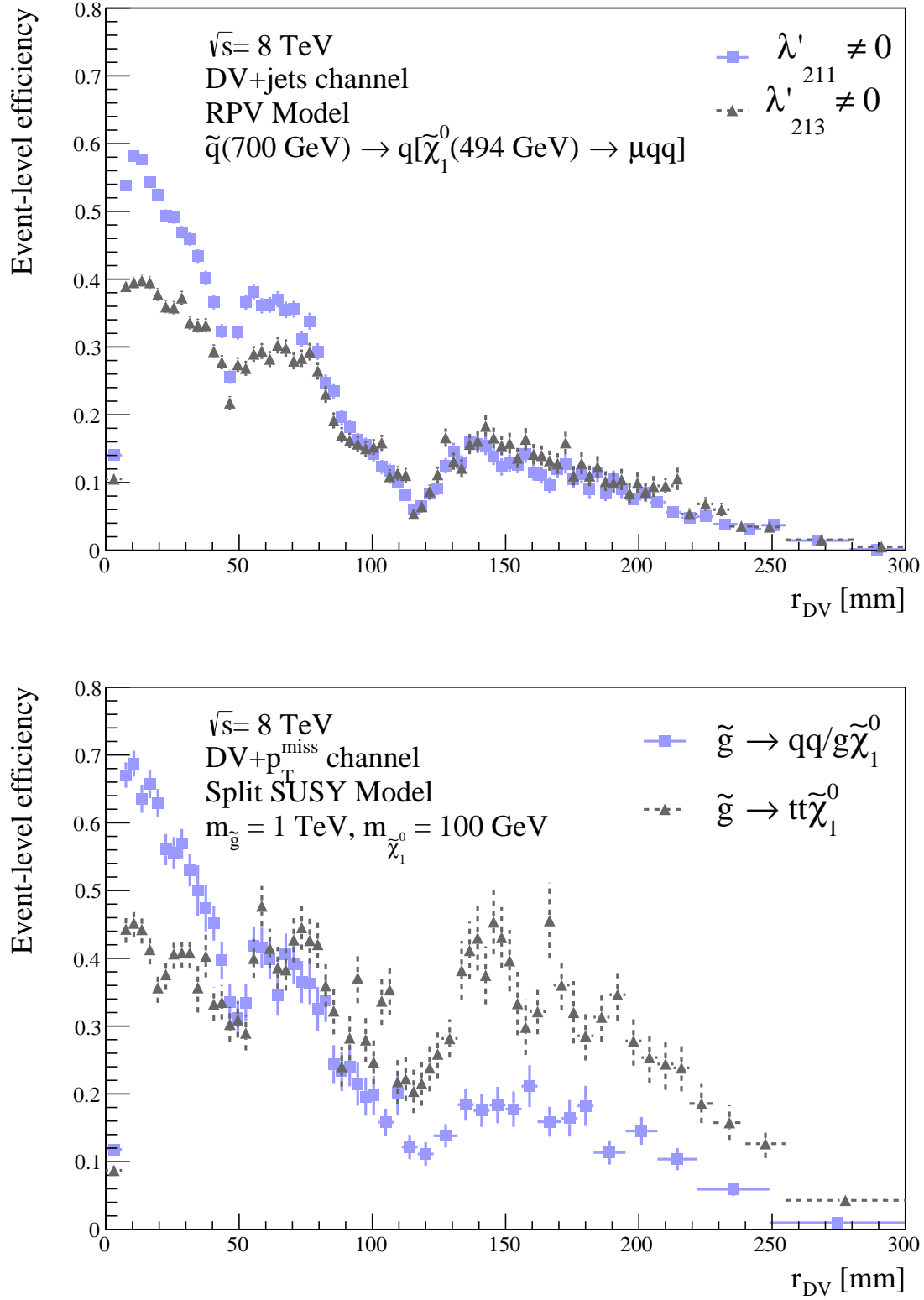
Figure 7.5: Comparison of efficiency as a function of the vertex radial position r_{DV}. The top frame shows two samples in the RPV simplified model, where a squark decays to $\tilde{\chi}_1^0 \to \mu qq$ through non zero λ'_{211} and to $\tilde{\chi}_1^0 \to \mu qb$ through non zero λ'_{213}. The bottom frame shows a split SUSY model, where a gluino decays to either $q\bar{q}/g\tilde{\chi}_1^0$ or $t\bar{t}\tilde{\chi}_1^0$.

where t is the true proper decay time of the generated LLP. The event-level efficiency for each lifetime is calculated by weighting the event by,

$$W_{\mathrm{evt}}(t_1, t_2, \tau) = W_{\mathrm{DV}}(t_1, \tau) W_{\mathrm{DV}}(t_2, \tau), \tag{7.3}$$

where t_1 and t_2 are the true proper decay times of the two LLPs in the event. The event level efficiency is then the sum of weights for LLPs that satisfy all the criteria in the sample.

The resulting dependence of ϵ_{evt} on the average proper decay distance $c\tau$ are shown in Figure 7.6 for the RPV models. Figures 7.7 and 7.8 shows the effect in ϵ_{evt} for the split SUSY models and for GGM see Figure 7.9. For most models considered in this analysis, the peak efficiency is typically greater than 5%, and it occurs in the range 10 mm $\leq c\tau \leq$ 100 mm.

7.5 Backgrounds[7]

A very strong feature of displaced vertex analysis in general is that this signature is scarce in the SM, so it is nearly a zero-background search. B mesons are examples of LLPs in the SM, but the large majority of these particles are removed by the track cut on $|d_0| < 2$mm, described in Section 4.3.1 (1% of the tracks from a $b-$vertex pass the minimal d_0 cut, as can be seen from Figure 7.10). The few remaining tracks will not pass the signal region requirements.

Nevertheless, any imaginable source of background vertices must be considered. Background vertices to the DV multi-track search can come from three sources:

- accidental spatial crossing of tracks

- heavy-flavor quark decays

- particle interactions with material

The material veto applied highly suppresses backgrounds from particle interactions with detector material. Moreover, all the above backgrounds have low values of m_{DV}

---

[7] Results in this section, with the exeption of Figure 7.10, were generated by the members of the ATLAS DV team Nick Barlow, Hidetoshi Otono and Nora Pettersson.
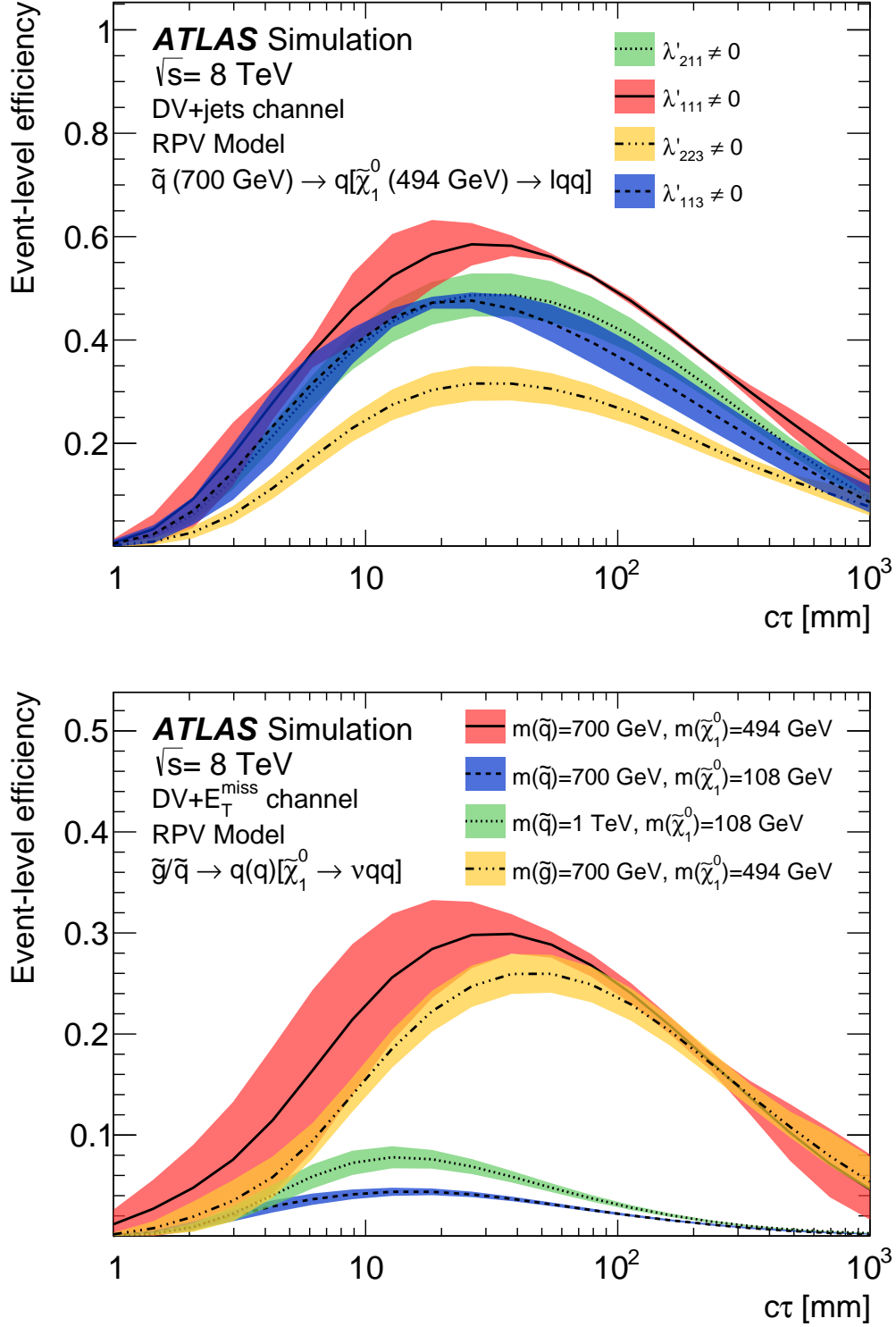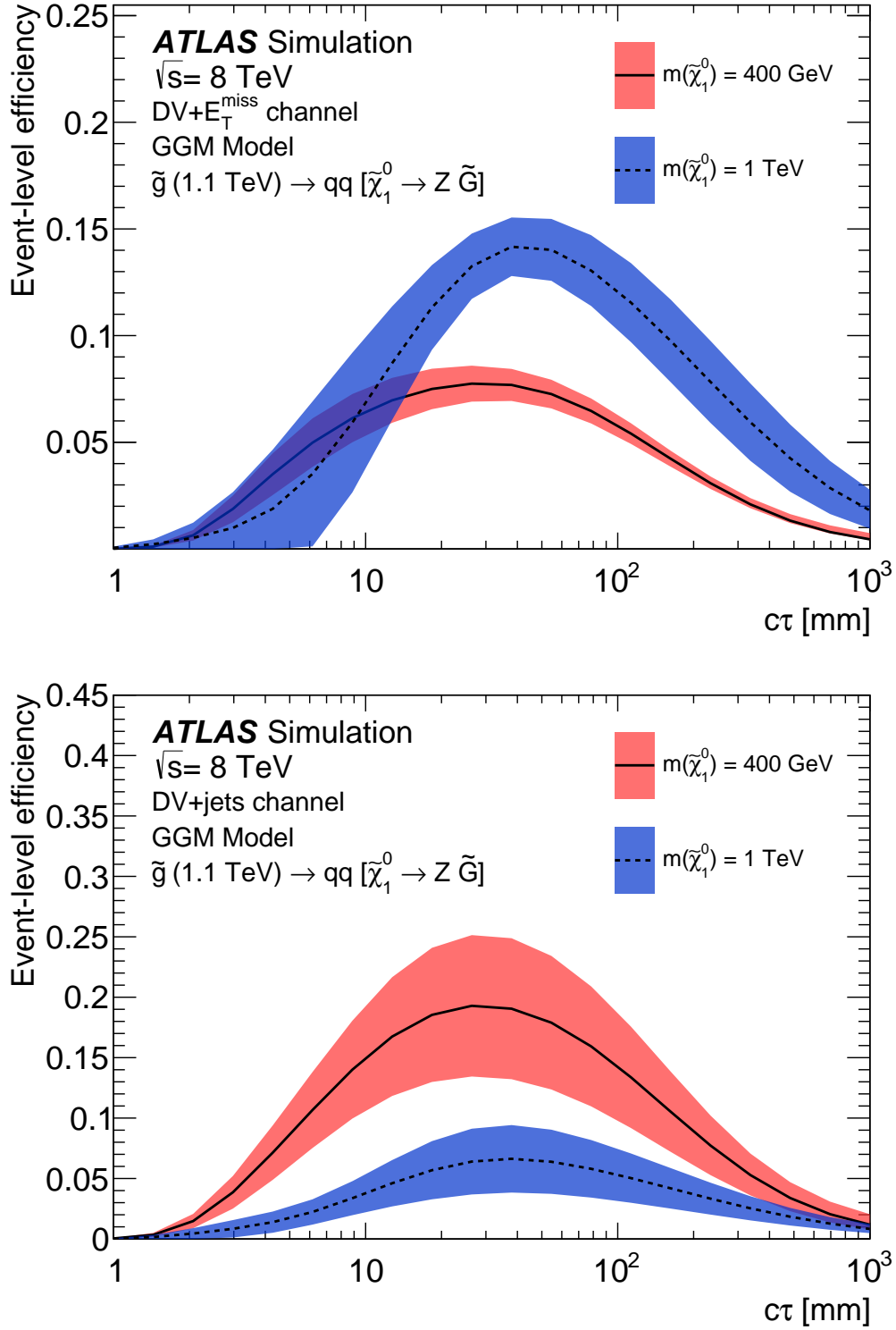
Figure 7.6: Event-level efficiency obtained from the DV+jets search (top), for a pair of squarks in the RPV scenario, with the neutralino decaying to a lepton and two quarks, according to the non-zero λ' couplings indicated in each case. The squark and neutralino masses are 700 GeV and 494 GeV. The bottom frame shows the event-level efficiency for RPV samples in the DV+p_T^{miss} channel for different squark or gluino and neutralino mass values, and heavy flavour samples. The total uncertainties on the efficiencies are shown as bands [202].
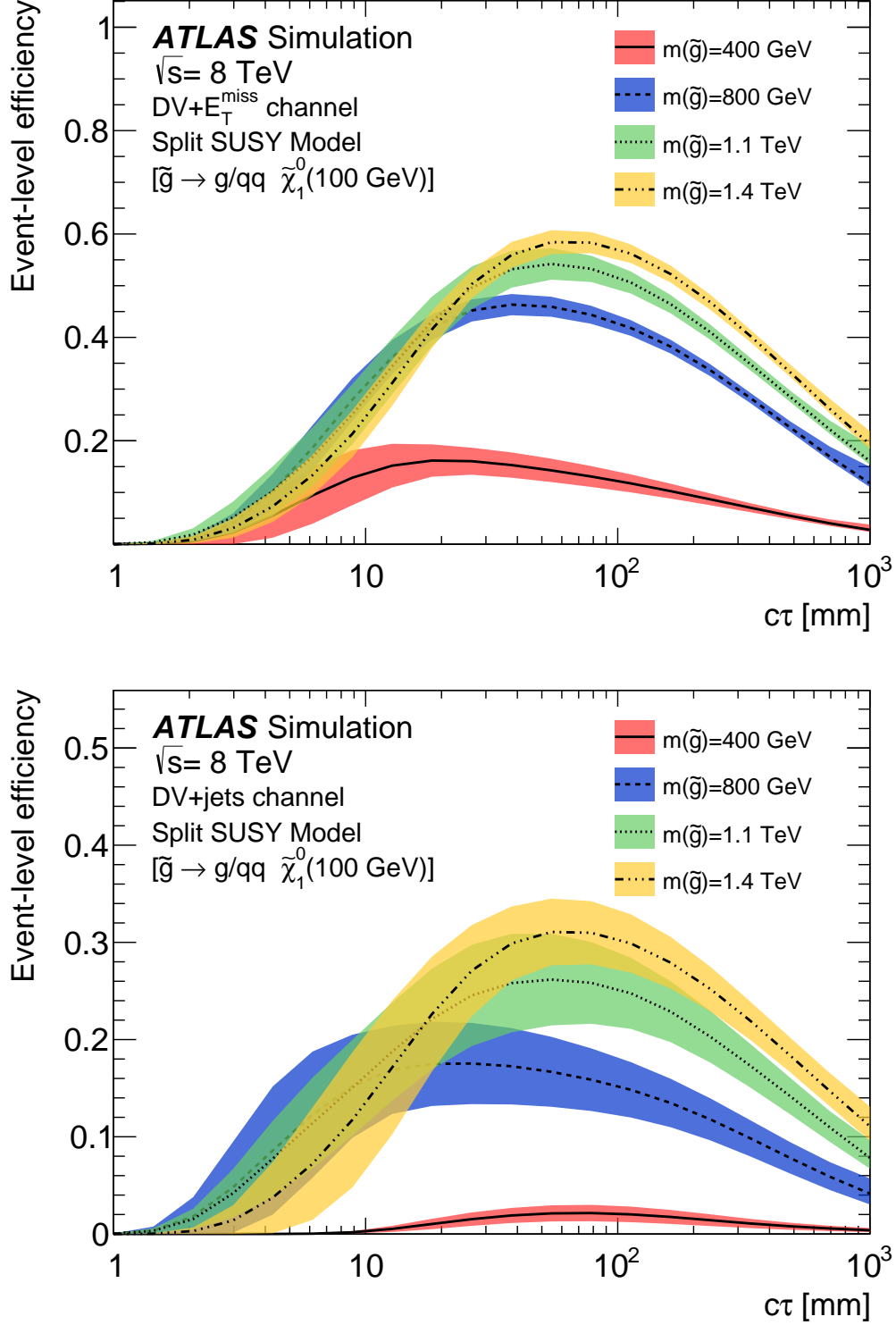
Figure 7.7: Event-level efficiency, obtained from the DV+p_T^{miss} (top) and DV+jets searches (bottom), on the cross section for gluino pair production in the split SUSY model, with the gluino decaying to a neutralino plus either a gluon or a light-quark pair or a pair of top quarks, for selected values of gluino mass. The mass of the neutralino is 100 GeV. The total uncertainties on the efficiencies are shown as bands [202].
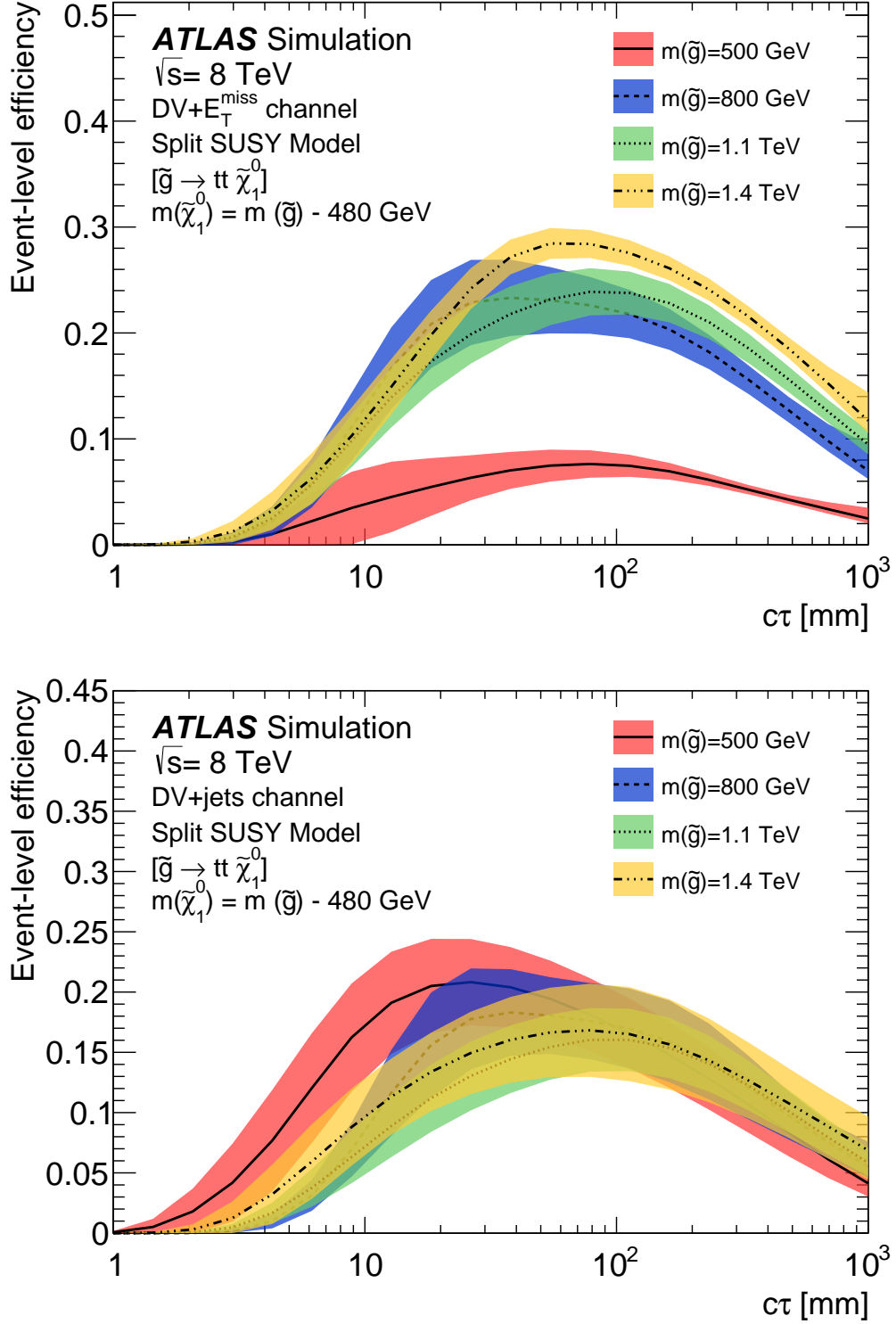
Figure 7.8: Event-level efficiency, obtained from the DV+p_T^{miss} (top) and DV+jets (bottom) searches, on the cross section for gluino pair production in the split SUSY model, with the gluino decaying to a neutralino plus a pair of top quarks, for selected values of gluino mass. The mass of the neutralino 480 GeV smaller than the gluino mass. The total uncertainties on the efficiencies are shown as bands [202].

Figure 7.9: Event-level efficiency, obtained from the DV+p_T^{miss} (top) and DV+jets searches (bottom), on the production cross section for a pair of gluinos of mass 1.1 TeV that decay into two quarks and a long-lived neutralino in the GGM scenario, for selected neutralino mass values. The total uncertainties on the efficiencies are shown as bands [202].
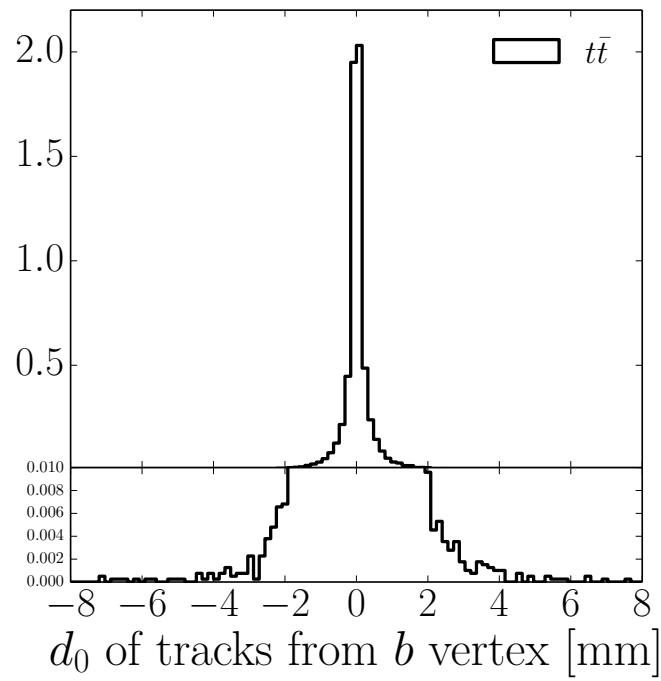
Figure 7.10: Transverse impact parameter d_0 of all tracks coming from reconstructed b-vertices from simulation with PYTHIA 8 [203] of Standard Model $t\bar{t}$ production. Events are generated with $\sqrt{s} = 13$ TeV. The bottom frame shows a zoom of the lower region of the top frame.

Channel	Number of background vertices
DV+jets	$0.41 \pm 0.007 \pm 0.06$
DV+p_T^{miss}	$0.0109 \pm 0.0002 \pm 0.0015$

Table 7.5: Estimated numbers of background vertices satisfying all of the multi-track signal selection criteria. In each entry, the first uncertainty is statistical, and the second is systematic [1].

and/or N_{trk} and thus will fail the selection requirements. Such vertices may contribute to high-m_{DV}, high-N_{trk} background vertices via two mechanisms:

- The dominant source of backgrounds are low-m_{DV} vertices that are accidentally crossed by an unrelated, high-p_T track at large angle ($\mathcal{O}(1 \text{radian})$) to the other tracks in the vertex. This is referred to as the accidental-crossing background.

- A much smaller background contribution is due to merged vertices. In this case, two low-m_{DV} vertices are less than 1 mm apart, and thus may be combined by the vertex-reconstruction algorithm into a single vertex that satisfies the N_{trk} and m_{DV} criteria.

The expected number of background vertices is estimated in both cases from the collision data. Since the number of events satisfying the final selection criteria is very small, the general approach is to first obtain a high statistical precision assessment of the probability for background vertex formation using a large data control sample. That probability is then scaled by the size of the signal-candidate sample relative to that of the control sample.

For the full details of the background estimation procedure in the multi-track DV analysis, see References [1, 198]. In all cases, the expected background is much less than one event. The final estimates are given in Table 7.5.

7.6 Results and Supersymmetric interpretation[8]

The results for the DV+jets and DV+p_T^{miss} searches are presented in this Section. All the vertices passing the full set of selection requirements described in Section 7.2, except for the signal region criteria, are plotted in Figure 7.11. Tables 7.6 and 7.7 show the

---

[8] Limits from Table 7.8 and the final results plots in Figure 7.11 were made by Nick Barlow.

	N	Relative Efficiency (%)	Overall Efficiency (%)
All events	26563830	100.	100.
Trigger	5654866	22.8	21.2
PV selection	458244	99.8	1.72
Jet selection	143177	36.2	0.53
DV selection	74758	97.3	0.28
DV material	44302	59.2	0.16
N_{trk}	73	0.16	0.00
m_{DV}	0	0.0	0.0

Table 7.6: Number of events N passing the different selection criteria, relative efficiencies (i.e. defined with respect to the previous cut) and overall efficiencies for the DV+jets channel on the ATLAS 2012 data.

	N	Relative Efficiency (%)	Overall Efficiency (%)
All events	26563830	100.	100.
Trigger	8640339	34.9	32.5
PV selection	19089	99.3	0.07
p_T^{miss} selection	6485	33.9	0.02
DV selection	1106	97.0	0.00
DV material	720	65.0	0.00
N_{trk}	0	0.0	0.0
m_{DV}	0	0.0	0.0

Table 7.7: Number of events N passing the different selection criteria, relative efficiencies (i.e. defined with respect to the previous cut) and overall efficiencies for the DV+p_T^{miss} channel on the ATLAS 2012 data.

number of events in data remaining after each of the selection cuts for DV+jets and DV+p_T^{miss} channels, respectively. No events are seen in the signal region in either of the channels.

Given the lack of a signal observation, we can place limits, making use of the statistical techniques described in Chapter 5. In general, an upper limit on the visible production cross section $\sigma_{\mathrm{visible}}$ (defined in Equation 5.9) given N observed events can be extracted from,
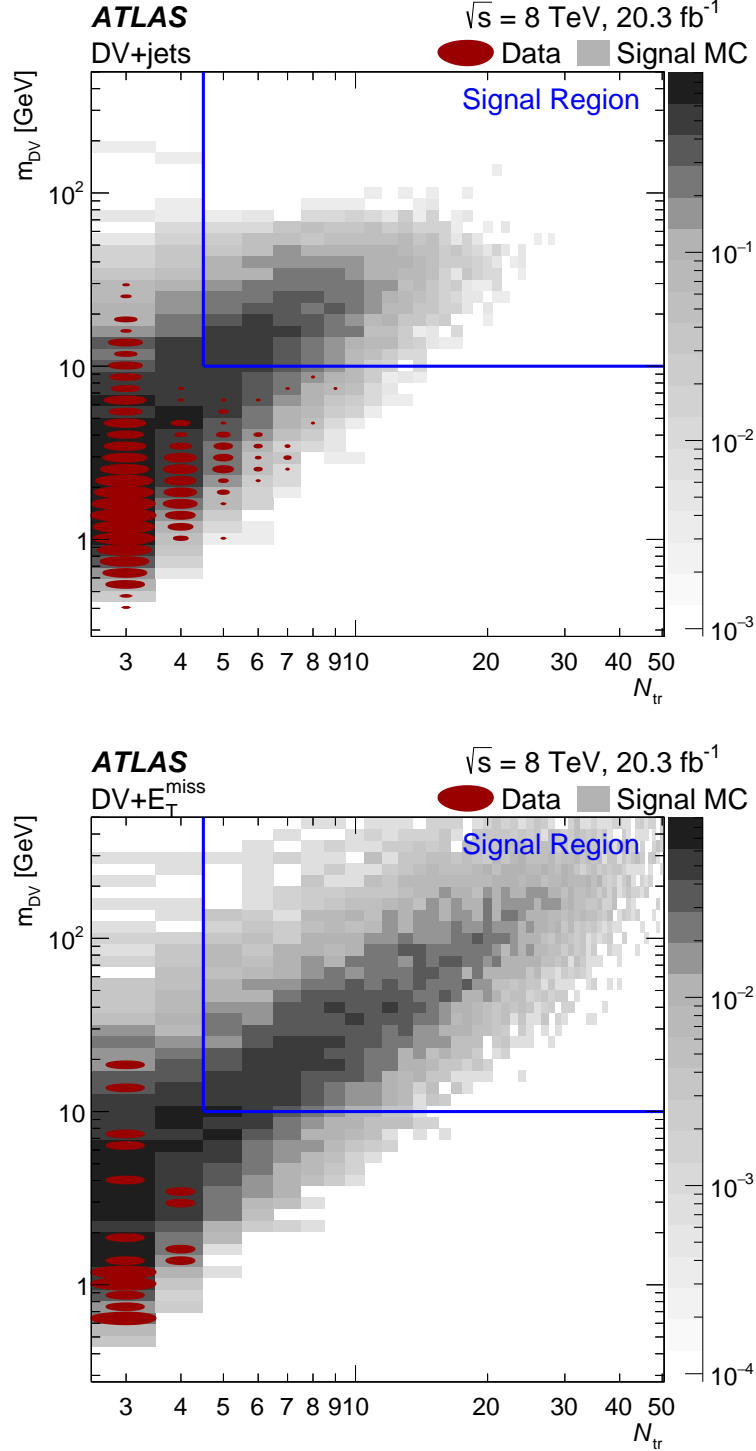
Figure 7.11: The distribution of DV+jets (top) and DV+p_T^{miss} (bottom) candidates in terms of the vertex mass versus the number of tracks in the vertex. The data distribution is shown with red ovals, the area of each oval being proportional to the logarithm of the number of vertex candidates in that bin. The gray squares show the [$\tilde{g}$ (1.1 TeV) $\rightarrow qq[\tilde{\chi}_1^0$ (400 GeV) $\rightarrow \tilde{G}Z]$ GGM signal MC sample in the left plot and the MC [$\tilde{g}$ (1.4 TeV) $\rightarrow \tilde{\chi}_1^0$ (100 GeV) qq/g] split SUSY sample in the right plot. The signal region $N_{\text{trk}} \geq 5$, $m_{\text{DV}} > 10$ GeV is indicated [1].

Channel	Upper limit on visible cross section [fb]
DV+jets	0.14
DV+p_T^{miss}	0.15

Table 7.8: Model-independent 95% CL upper limits on the visible cross section for new physics for the two searches presented in this thesis [1].

$$N_{\text{signal}} = \sigma_{\text{visible}} \times \mathcal{L}, \qquad (7.4)$$

where $N_{\text{signal}} = N - N_{\text{background}}$, $\mathcal{L}$ is the integrated luminosity.

Both the DV analysis searches presented are sensitive to any massive LLP decaying with sufficient amount of tracks in the ID, so this makes them fairly model independent searches. Owning to this fact, we extract 95% CL upper limits on the total visible cross section for new physics. Inserting in equation 7.4 the known values, assuming 100% efficiency, $N = N_{\text{upper}} = 3$ (which is a 95% interval of the observation of zero events) the luminosity $\mathcal{L} = 20.3$ fb^{-1} and the estimated number of background vertices of for example 0.41 for DV+jets (see Table 7.5), we get a rough estimate of $\sigma_{\text{vis}} = \frac{3-0.41}{20.3} \sim 0.13$ fb. Considering all uncertainties in the background ($\pm$ 0.06) and luminosity ($\pm 2.8\%$ in 2012 data [204]), upper limits on the visible cross section at a 95% CL for the DV+jets and DV+p_T^{miss} searches are presented in Table 7.8.

Furthermore, for each of the physics models considered, 95% CL upper limits on the production cross sections are calculated for different values of the proper decay distance $c\tau$ of the LLP. The limits are calculated using standard ATLAS software, using the CL$_{\text{S}}$ prescription [142] with the profile likelihood used as the test statistic, using the HISTFITTER [205] framework. Uncertainties on the signal efficiency and background expectation are included as nuisance parameters, and the CL$_{\text{S}}$ values are calculated by generating ensembles of pseudo experiments corresponding to the background-only and signal-plus-background hypotheses (see Section 5.2). Since less than one background event is expected in all cases and no events are observed, the observed limits are very close to the expected limits.

Figure 7.14 shows the upper limits on the production cross section of two squarks in the RPV simplified scenario, with different squark and neutralino masses, as well as

different λ' parameters governing the neutralino decay. These results exclude a $m_{\tilde{q}} = 1$ TeV squark for $m_{\tilde{\chi}_1^0} = 108$ GeV and 2.5 mm $< c\tau < 200$ mm with either light or heavy quark neutralino decays.

Figures 7.12 and 7.13 shows the upper limits on gluino-pair production cross section in the split SUSY model. The sensitivity is greater for the cases with $m_{\tilde{\chi}_1^0} = 100$ GeV than for those with $m_{\tilde{\chi}_1^0} = m_{\tilde{g}} - 480$ GeV, and the DV+p_T^{miss}search performs better than DV+jets in these scenarios, excluding $m_{\tilde{\chi}_1^0} < 1400$ GeV in the range of proper decay lengths 15 mm $< c\tau < 300$ mm.

Figure 7.15 shows the cross section upper limits for gluino-pair production within the GGM simplified scenario. The scenario is excluded, for instance, for $m_{\tilde{g}} = 1.1$ TeV and $m_{\tilde{\chi}_1^0} = 400$ GeV in the proper decay distance range 3 mm $< c\tau < 500$ mm.

7.7 Comparison with past ATLAS analysis

Improvements to the previous ATLAS search for displaced vertices [186] have been made to the physics analysis described in this thesis. One of them was the inclusion of a new track quality cut, where tracks are rejected if they have zero TRT hits and the number of Pixel hits is less than 2, described in Section 7.2. This cut is effective at removing fake tracks made up of hits in the SCT endcaps, and it is justified further in the ATLAS internal note in Ref. [173]. The advantage of applying this cut before making vertices is that we do not lose the entire vertex if a track inside it is badly reconstructed. The effect of this new cut on the vertex reconstruction efficiency is shown in Figure 7.16, where we can see a considerable gain, especially at large radii of the reconstructed displaced vertex.

The search channels and physics models interpretations have also been widely extended. The last version of the displaced vertex analysis with 8 TeV data reported a search only in a channel with a DV+μ (which requires a muon trigger, and a reconstructed muon associated with the DV), and was interpreted only in the context of RPV. Upper limits on the production cross section for a 1000 GeV squark were set at 5.4 fb in [186]. The new DV+jets search produces a stricter exclusion limit of 0.14 fb, indicating the power of the new DV+jets channel.
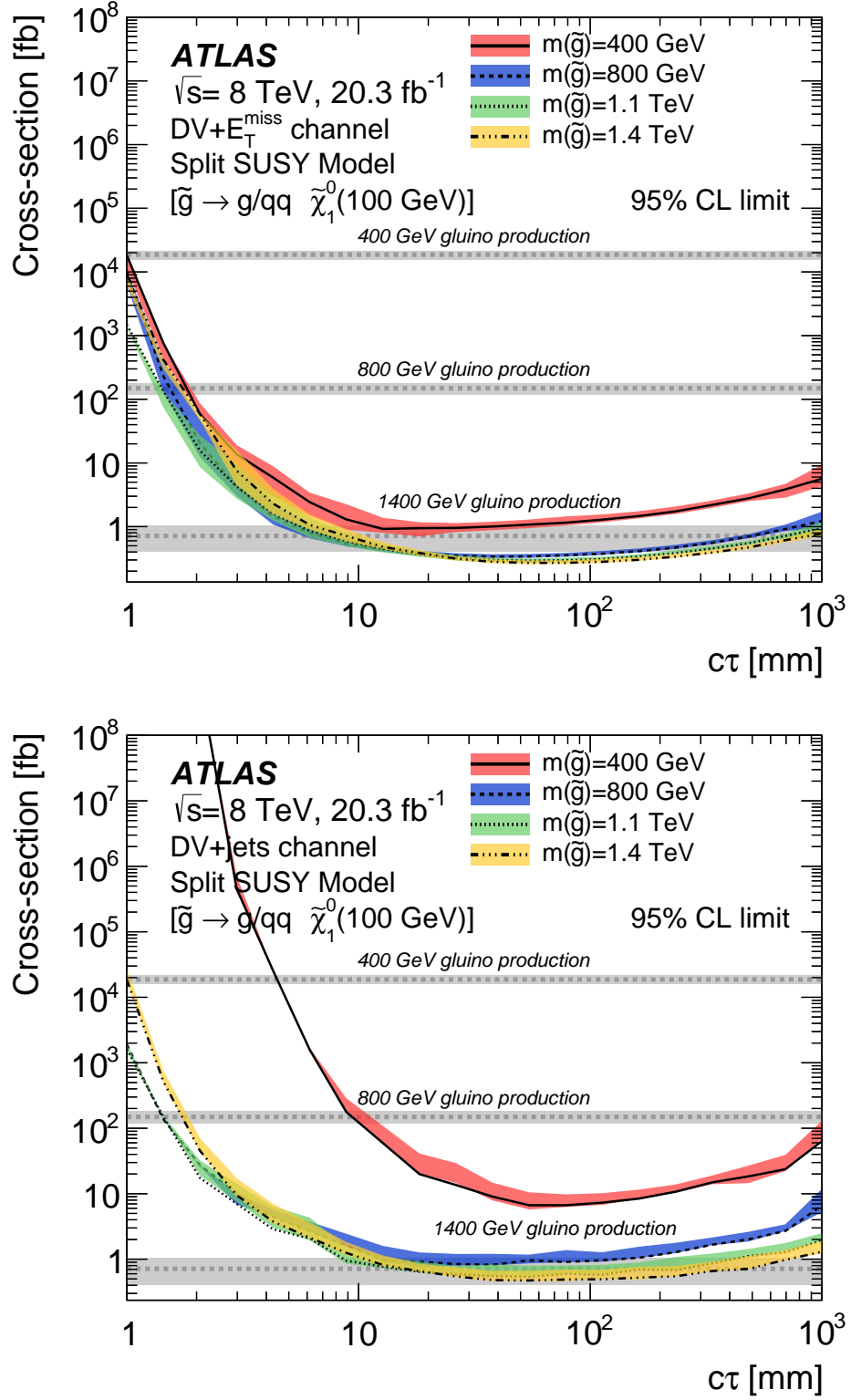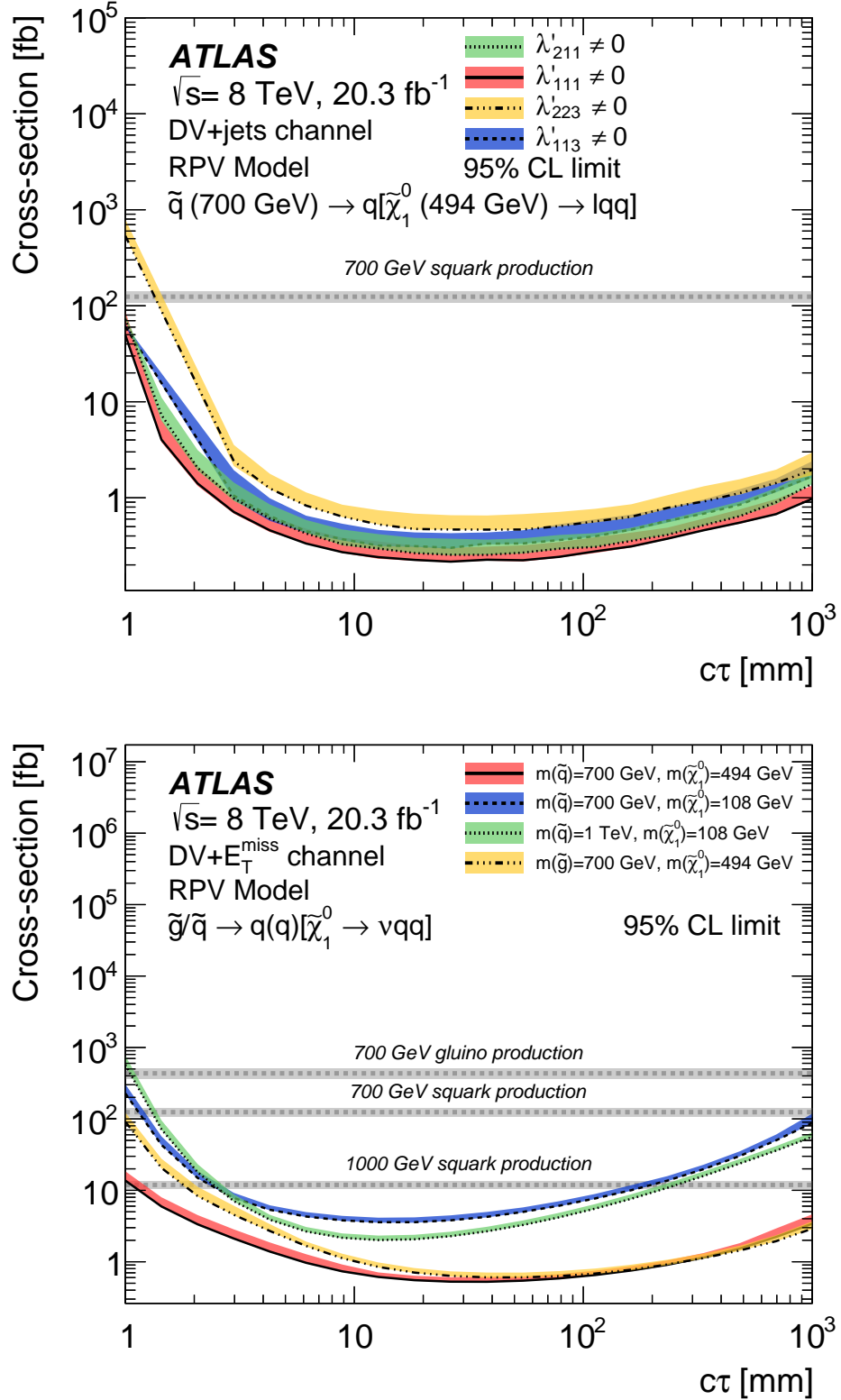
Figure 7.12: 95 % CL upper limits, obtained from the DV+p_T^{miss} (top) and DV+jets (bottom) searches, on the cross section for gluino pair production in the split SUSY model, with the gluino decaying to a neutralino plus a gluon or a light-quark pair. The mass of the neutralino is 100 GeV [1].
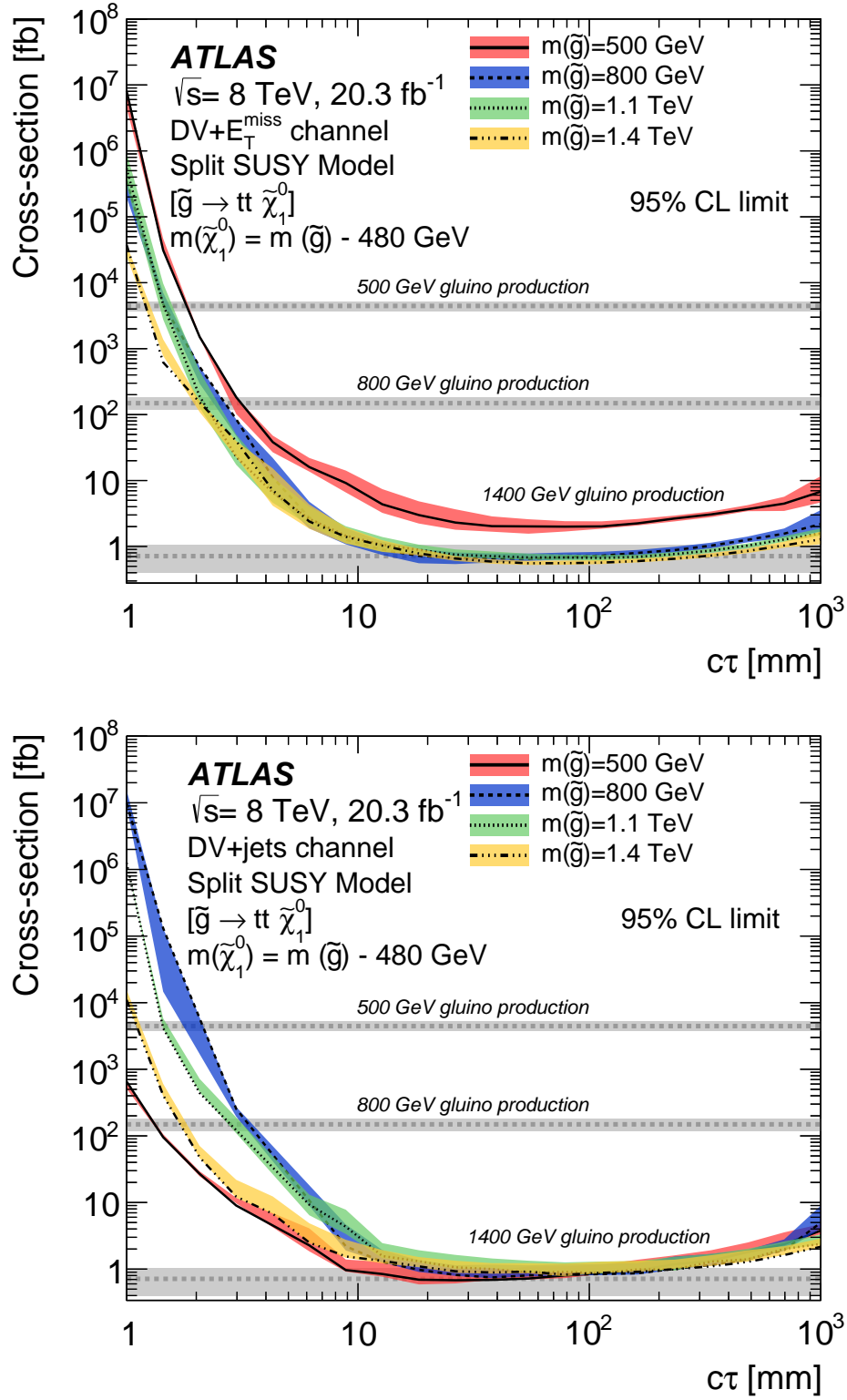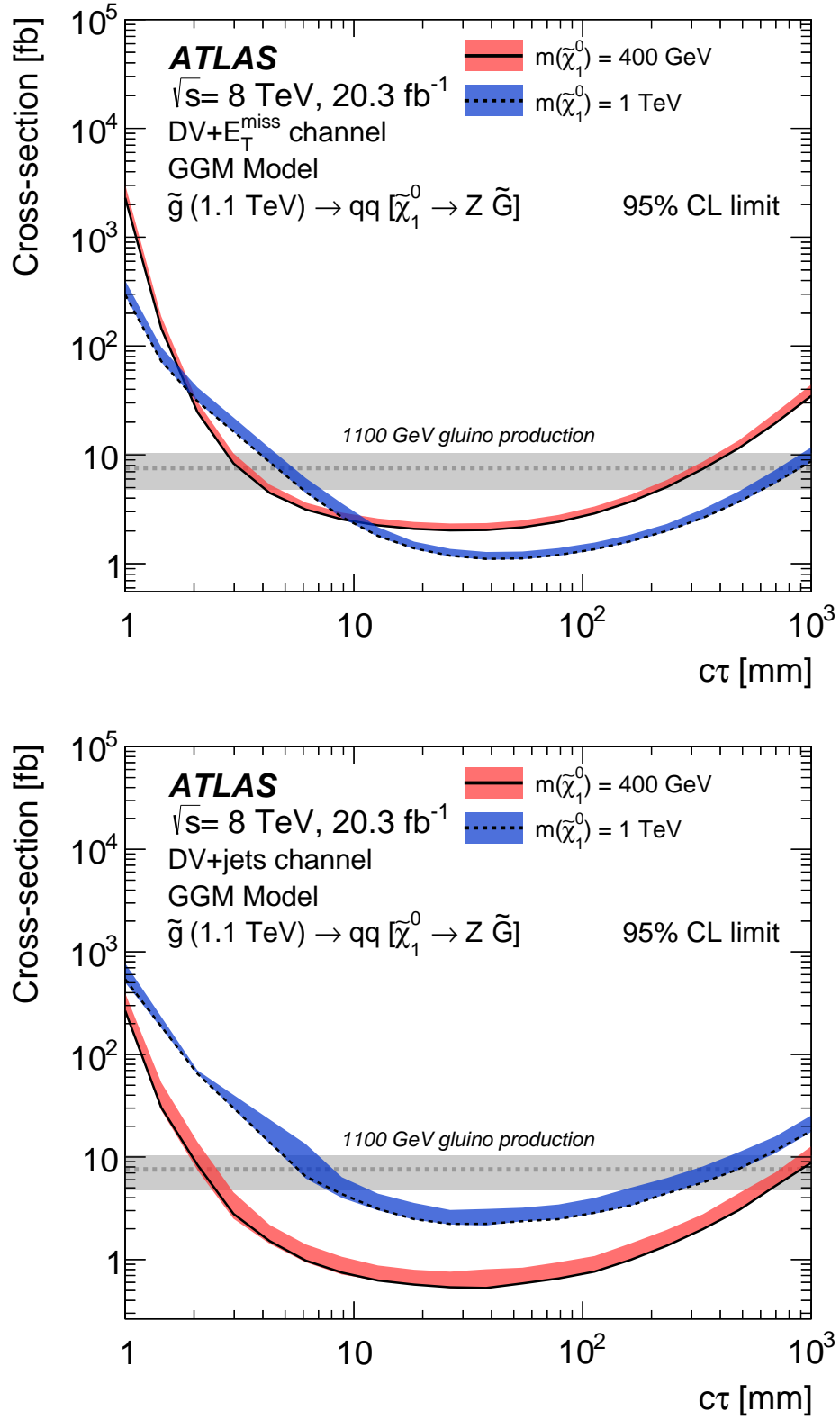
Figure 7.13: 95 % CL upper limits, obtained from the DV+p_T^{miss} (top) and DV+jets (bottom) searches, on the cross section for gluino pair production in the split SUSY model, with the gluino decaying to a neutralino and a pair of top quarks. The mass of the neutralino is 480 GeV smaller than the gluino mass [1].

Figure 7.14: 95 % CL upper limits, obtained from the DV+jets search (top), on the production cross section for a pair of squarks in the RPV scenario, with the neutralino decaying to a lepton and two quarks, according to the nonzero λ' couplings indicated in each case. The squark and neutralino masses are 700 GeV and 494 GeV. The bottom plots shows the 95 % CL upper limits, obtained from the DV+p_T^{miss} for different squark or gluino and neutralino mass values [1].

Figure 7.15: 95 % CL upper limits, obtained from the DV+p_T^{miss} (top) and DV+jets (bottom) searches, on the production cross section for a pair of gluinos of mass 1.1 TeV that decay into two quarks and a long-lived neutralino in the GGM scenario [1].
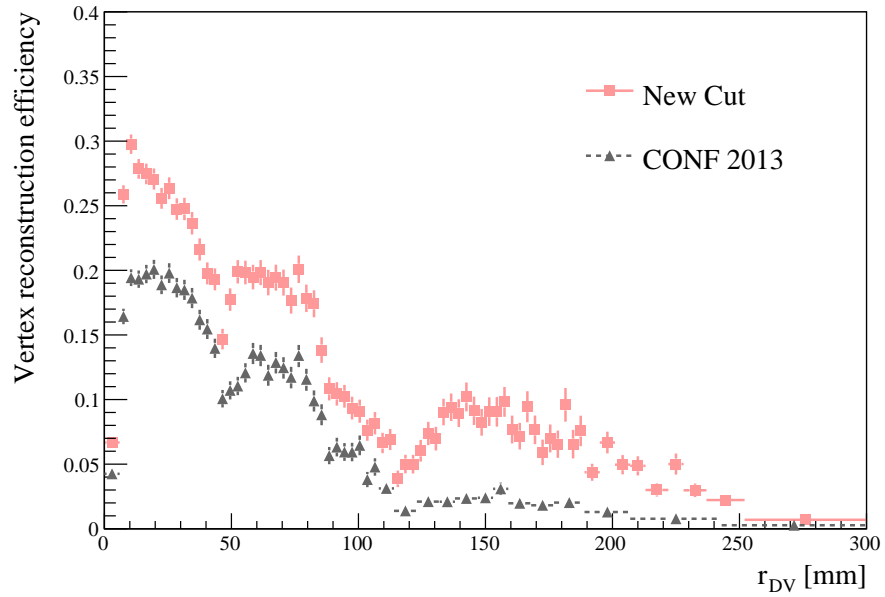
Figure 7.16: Vertex reconstruction efficiency against radial distance of the displaced vertex r_{DV} for the DV analysis in [186] (CONF 2013) and including the new hit based cut implemented in this thesis.
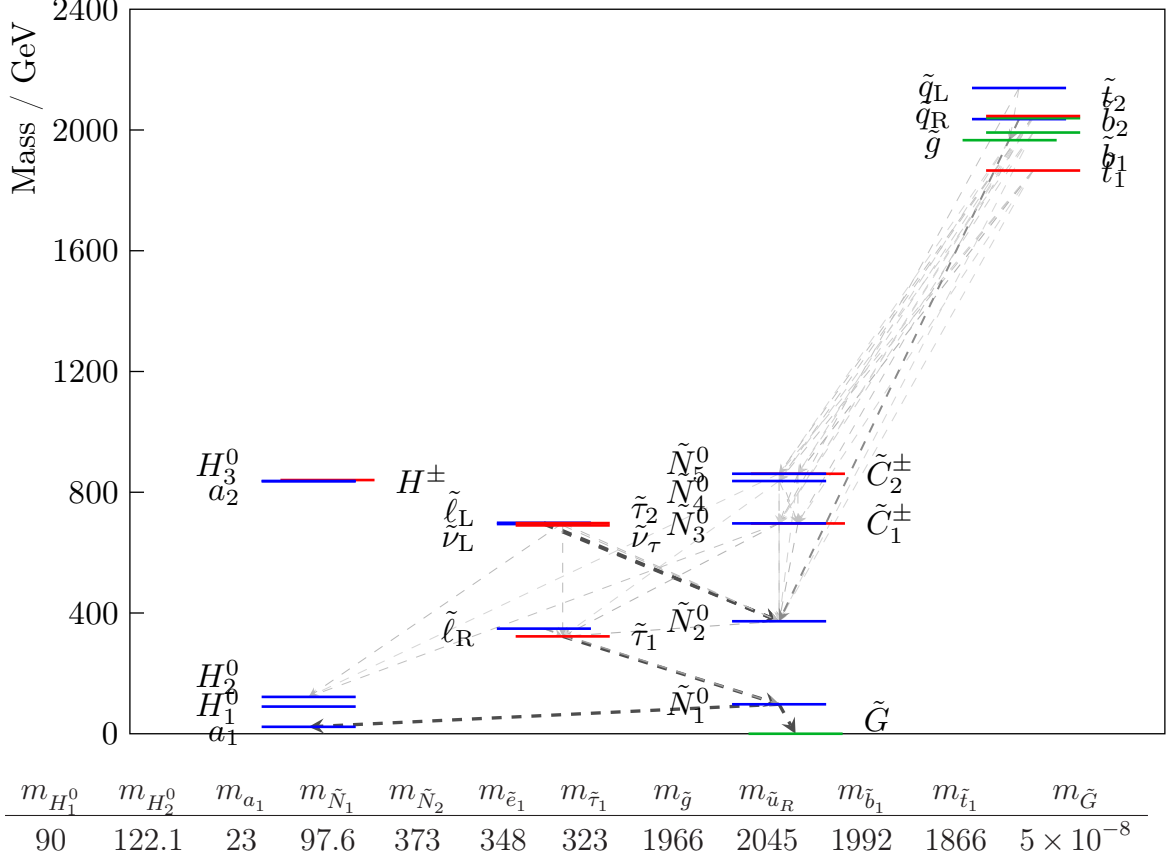
Chapter 8

Prompt signals and displaced vertices in searches for next-to-minimal gauge mediated Supersymmetry

In this Chapter, we evaluate the collider phenomenology of the DGS model described in Section 3.2.4. We discuss the limits from the LHC, both in prompt and displaced searches.

In order to be concrete, we choose to study a benchmark point P0, whose spectrum (as generated by NMSSMTooLs 4.9.2 [206, 207]) is shown in Figure 8.1. P0 has a SM-like Higgs in the vicinity of the measured mass at 125 GeV (allowing for a 3 GeV theoretical uncertainty in its prediction) and a lighter $CP-$even Higgs at 90 GeV that couples with a reduced strength (compared to a SM Higgs) to Z-bosons, commensurate with a 2σ LEP excess. In addition, the lightest singlet-like pseudoscalar a_1 has a mass of 23 GeV and the singlino-like NLSP $\tilde{N}_1$ has a mass of 98 GeV.

We generate event samples with PYTHIA 8.2 [203], using FASTJET 3.1.3 [209] for jet reconstruction. The ATLAS models we wish to validate, described in Section 8.2.1, are generated with SOFTSUSY 3.6.1 [152, 153] to calculate the spectra and SDECAY 1.5 [154] to generate the decays, communicating the spectrum and decay information via SUSY Les Houches Accord (SLHA) files [155, 156].

To take into account the size of the detector, we consider a cylinder with radius $r = 11$ m and length $|z| = 28$ m, corresponding to the ATLAS Inner Detector [124]. It is possible for a neutral particle that decays outside the Inner Detector to form trackless jets. However, it is difficult to model the detector response to these and so we consider

$m_{H_1^0}$	$m_{H_2^0}$	m_{a_1}	$m_{\tilde{N}_1}$	$m_{\tilde{N}_2}$	$m_{\tilde{e}_1}$	$m_{\tilde{\tau}_1}$	$m_{\tilde{g}}$	$m_{\tilde{u}_R}$	$m_{\tilde{b}_1}$	$m_{\tilde{t}_1}$	$m_{\tilde{G}}$
90	122.1	23	97.6	373	348	323	1966	2045	1992	1866	5×10^{-8}

Figure 8.1: Spectrum and the more likely sparticle decays of benchmark point P0: $\xi = 0.01$, $\lambda = 0.009$, $M = 1.4 \times 10^6$ GeV, $\tilde{m} = 863$ GeV and $\tan\beta = 28.8$. Decays into sparticles which have a branching ratio greater than 10% are displayed by the arrows. The figure was produced with the help of `PySLHA3.0.4` [208]. The table shows some more precise details of the spectrum of the benchmark point P0. All masses are listed in GeV units and the lightest neutralino has a decay length $c\tau_{\tilde{N}_1} = 99$ mm.

them to be beyond the scope of this study. Any particle that decays outside the Inner Detector is therefore considered to be stable for all intents and purposes. The detector response for measurement of jet p_T is modelled as follows[1]. The jet momentum is smeared by a gaussian with resolution of 20% of energy for $E_{\text{jet}} < 50$ GeV, falling linearly to 10% up to 100 GeV and then a flat 10%. A further scale correction of 1% is applied for jets with $|\eta| < 2$ and 3% for those with higher $|\eta|$.

With this parameterisation, we are able reproduce the cut flows for the ATLAS 0-lepton + jets + missing transverse energy (p_T^{miss}) analyses and the efficiencies are

---

[1] We find inconsistent results from standard detector simulation programs leading us to believe that the presence of DVs interferes with the standard reconstruction.

validated against published results for benchmarks provided in the ATLAS analysis documentation. Further fiducial and material cuts required for tracks in the DV studies are explained in Section 8.2.1.

8.1 Prompt searches[2]

In order to determine constraints on the gluino mass in our model, we focus on the 0-lepton + 2-6 jets + p_T^{miss} search [210,211] which is the most sensitive search for benchmark P0. However, to investigate the response of our model to dedicated SUSY searches, we deform it by moving on a line into the phenomenological next-to-minimal model space (pNMSSM): for instance, we vary the gluino mass soft parameter M_3 while keeping all other weak-scale parameters fixed. The spectrum, decays and lifetimes are recomputed at each point: to first order, only the gluino mass changes, but there are small loop-level effects on other masses. Since this deformation breaks the gauge mediated relation between the gaugino masses, we are deviating from the gauge mediated limit by doing this. This is a simple choice where we can change only one parameter; we could have equally made a different choice where we vary several weak-scale parameters - trying to preserve some of the gauge mediated relations. Keeping within the DGS model itself was not an option however, since a highly non-trivial multi-dimensional manipulation of parameters was required, which ended in some other phenomenological bound being violated. Our approach is mainly phenomenologically motivated, essentially to study the gluino mass bounds in the context of the very peculiar structure of singlino-like NLSP and gravitino LSP (with squarks decoupled). Nevertheless one might imagine a possible extension of the DGS scenario with additional sources for the Higgs mass that allow to lower the overall scale of sparticle masses to the investigated range.

We have also sometimes, for the purposes of illustration only, changed the singlino decay length $c\tau_{\tilde{N}_1}$ (while keeping all weak-scale parameters fixed). This deformation does not really constitute a consistent model, but is used instead to understand some features that are present in consistent models. When using this type of deformation we will refer to 'tweaked' parameters. We shall investigate the effect of varying the lifetime by scanning over a lifetime range of $c\tau = [10^{-3},\ 10^4]$ mm for $m_{\tilde{g}} \sim 1$ TeV.

---

[2]Plots from this Section were generated by Nishita Desai.

$\sqrt{s}$	8 TeV		13 TeV	
Signal Region	4jt-8	6jt-8	4jt-13	6jt-13
$p_T^{\text{miss}}/\text{GeV} >$	160	160	200	200
$p_T(j_1)/\text{GeV} >$	130	130	200	200
$p_T(j_2)/\text{GeV} >$	60	60	100	100
$p_T(j_3)/\text{GeV} >$	60	60	100	100
$p_T(j_4)/\text{GeV} >$	60	60	100	100
$p_T(j_5)/\text{GeV} >$	-	60	-	50
$p_T(j_6)/\text{GeV} >$	-	60	-	50
$\Delta\phi(\text{jet}_{1,2,3}, \vec{p}_T^{\text{miss}})_{min} >$	0.4			
$\Delta\phi(\text{jet}_{j>3}, \vec{p}_T^{\text{miss}})_{min} >$	0.2			
$p_T^{\text{miss}}/m_{\text{eff}}(N_j) >$	0.25		0.2	
$m_{\text{eff}}(\text{incl.})/\text{GeV} >$	2200	1500	2200	2000
σ_{95}^{obs} (fb)	0.15	0.32	2.7	1.6

Table 8.1: The cuts for more sensitive signal regions from the 0-lepton + jets + p_T^{miss} searches at 8 TeV [210] and 13 TeV [211] runs and 95% observed upper limits on a non-Standard Model contribution σ_{95}^{obs}. The limit σ_{95}^{obs} has not been unfolded, and so should be applied to the production cross-section times branching ratio times acceptance. The jets j are ordered in decreasing p_T. The effective mass, $m_{\text{eff}}(\text{incl.})$ is defined to be the scalar sum of p_T's of all jets with $p_T > 40(50)\,\text{GeV}$ for $\sqrt{s} = 8$ (13) TeV plus the missing transverse momentum p_T^{miss}, $m_{\text{eff}}(N_j)$ is the scalar sum of p_T's of N_j hardest jets ($N_j = 4$ for 4jt-X and $N_j = 6$ for 6jt-X) plus p_T^{miss} and ϕ is the azimuthal angle around the beam [2].

## 8.1.1 Current bounds from Run I and early Run II searches

In the DGS model under study, the squarks (including the third generation squarks) are usually heavier than the gluino, resulting in three-body decays through off-shell squarks of the form $\tilde{g} \to q\bar{q}\tilde{N}_1$, where $\tilde{N}_1$ is mostly singlino-like, followed by the potentially displaced decay $\tilde{N}_1 \to \tilde{G}a_1 \to \tilde{G}b\bar{b}$. Although the last step in the decay chain always ensures the presence of b's in the final state, they are usually too soft to satisfy the requirements of current $b-\text{jet} + p_T^{\text{miss}}$ searches. We find that $b-\text{jet}$ searches only become sensitive when the mass of the gluino is high enough that decays into third generation squarks dominate and their decays into top/bottom quarks (see an example event topology in Figure 3.5) result in high-p_T b-jets. Therefore these searches are never relevant for our benchmark P0 and the corresponding pNMSSM line that has

even lower gluino masses. Note however, that even when the gluino mass is high, the gluino branching fraction into b's is still only about 20% and is often accompanied by vector bosons in the final state. These sometimes produce leptons, which take events out of the 0-lepton + multi-jets + p_T^{miss} selection. As a result of the above considerations, the sensitivity is much lower than that from simplified models producing hard b-jets and missing transverse momentum. We find that the sensitivity in the simplest 0-lepton + jets + p_T^{miss} searches is greater than that of searches involving bs even at high gluino masses. The signal regions (i.e. the labelled sets of cuts) defined by ATLAS that have the highest sensitivity are the `4jt-8` and `6jt-8` signal regions (relevant for 8 TeV collisions) and the `4jt-13` and `6jt-13` signal regions (relevant for 13 TeV collisions). We reproduce the cuts in these signal regions in Table 8.1 along with the observed upper limits on production cross section at the 95% confidence level (CL).

Since in the DGS model the gluino sets the overall mass scale of the sparticle spectrum, we therefore present our results in the form of bounds on the gluino mass. We define the signal strength ratio r_{95} as the ratio of the predicted sparticle signal passing the selection cuts in a particular signal region to the 95% CL upper limit on the cross section in that region. Thus $r_{95} = 1$ is *just* ruled out to 95% CL, $r_{95} > 1$ is ruled out whereas $r_{95} < 1$ is allowed at the 95% CL. The signal region is always chosen to be the one giving the best *expected* exclusion. Figure 8.2 shows the signal strength ratio for varying gluino mass based on the pNMSSM line described in Section 8.1. The most sensitive signal region at $\sqrt{s} = 8$ TeV for gluinos from $0.9 - 1.2$ TeV is the `6jt-8` region (6 hard jets, tight cuts). For higher gluino masses up to 2 TeV, the sensitivities of the `6jt-8` and `4jt-8` signal regions are similar. The presence of a long-lived singlino which may decay within the detector leads to another possible signature — that of DVs, which we shall explore in the next Section. We see from the figure that the bound from Run I at 95% is $m_{\tilde{g}} > 1080$ GeV, where the `6jt-8` line intersects $r_{95} = 1$.

In 2015, ATLAS analysed 3.2 fb^{-1} of integrated luminosity collected at the higher centre-of-mass energy of 13 TeV, not observing any significant signal for sparticle production. We see that at 13 TeV, the `4jt-13` cuts are more sensitive to our pNMSSM model than the `6jt-13` cuts for any value of the gluino mass, mainly because the p_T requirements are not satisfied by the jets from singlino decay products (which give $N_{\mathrm{jets}} > 4$). We see that the early Run II data from 2015 constrained $m_{\tilde{g}} > 1000$ GeV, not as sensitive as the Run I limit. Later, we shall examine the expected sensitivity from Run II with 100 fb^{-1} of integrated luminosity.
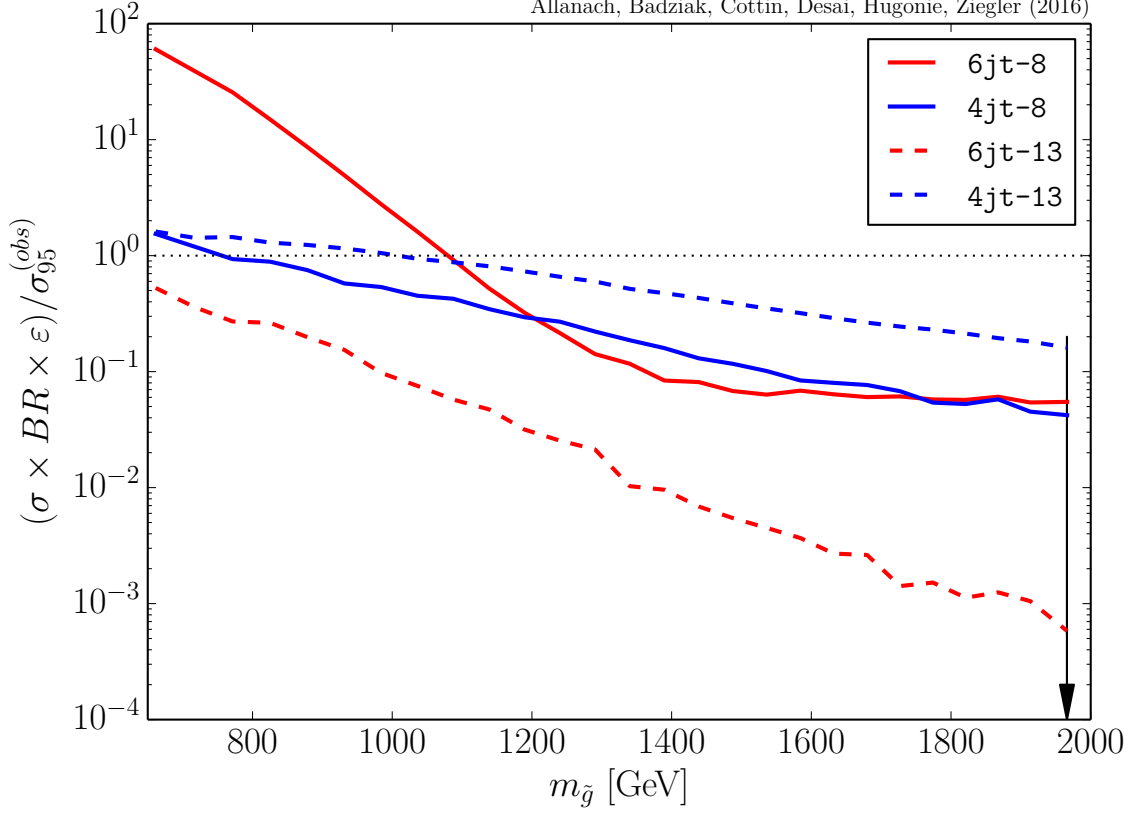
Figure 8.2: 95% lower limits on the gluino mass from Run I and Run II jets + p_T^{miss} searches. We show the ratio of the predicted gluino cross-section times branching ratio times acceptance ($\sigma \times BR \times \varepsilon$) to the 95% upper bound on signal cross-sections determined by ATLAS, for a scan-line based on benchmark P0 ($\tilde{N}_1$ lifetime of $c\tau_{\tilde{N}_1} = 99\,\text{mm}$). The horizontal dotted line shows the exclusion limit at $r = (\sigma \times BR \times \varepsilon)/\sigma_{95}^{\text{obs}} = 1$. The arrow shows the position of our benchmark P0 in DGS, whereas elsewhere we are strictly in pNMSSM parameter space [2].

In Figure 8.3, we show how changing the lifetime of the $\tilde{N}_1$ affects the cut acceptances (shown here for the signal region 6jt-8). The lines should be read in one-to-one correspondence from top to bottom with the cuts listed in Table 8.1 (except the second line which is the combined efficiency for $p_T(j_1)$ and $p_T(j_2)$). Thus, the first line corresponds to the cut $p_T^{\text{miss}} > 160$ GeV and the last to $m_{\text{eff}} > 1500$ GeV. As expected, when the singlino is stable, we find large missing energy as all the momentum it carries is invisible. As the lifetime decreases, more and more singlinos decay within the detector volume resulting in a flat efficiency below lifetimes of 10 mm. This gain in efficiency for long-lived $\tilde{N}_1$ is somewhat diluted once we demand jets with high p_T. In particular, once we demand $N_{\text{jets}} > 4$, the efficiency is lower for stable singlinos, since the extra hard jets mainly come
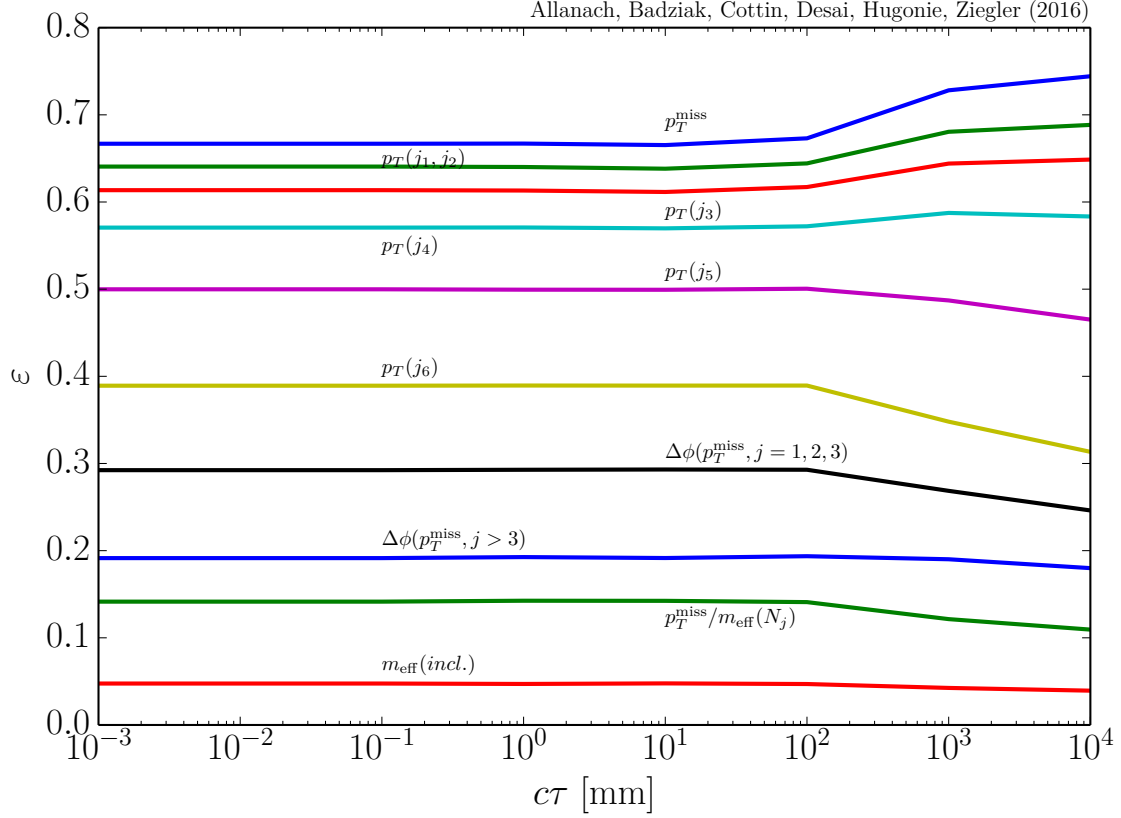
Figure 8.3: The dependence of overall efficiency on lifetime in the signal region `6jt-8`. We find that the strong dependence on p_T^{miss} is strongly anti-correlated with the cuts on jet p_T, resulting in a fairly small dependence of the efficiency on $c\tau$ after all cuts. The curves correspond from top to bottom to the cuts in Table 8.1 and the corresponding variables are shown in the plot [2].

from decay products of the $\tilde{N}_1$. However, this downturn is balanced by the requirements on $\Delta\phi$ between the jets and the missing momentum p_T^{miss}, since the presence of more jets in the final state makes it harder to satisfy this cut. Finally, after all cuts, we find that the efficiency is rather flat across all lifetimes. Therefore the gluino mass limits presented above may be considered fairly robust for the model studied here.

8.1.2 Future search reach of prompt searches

We now estimate what the future might bring for discovery or exclusion of the pNMSSM model from the LHC. In Figure 8.4, we re-display the current limits on the gluino in pNMSSM from the 13 TeV run, as the gluino mass is changed for the `6jt-13` and `4jt-13`
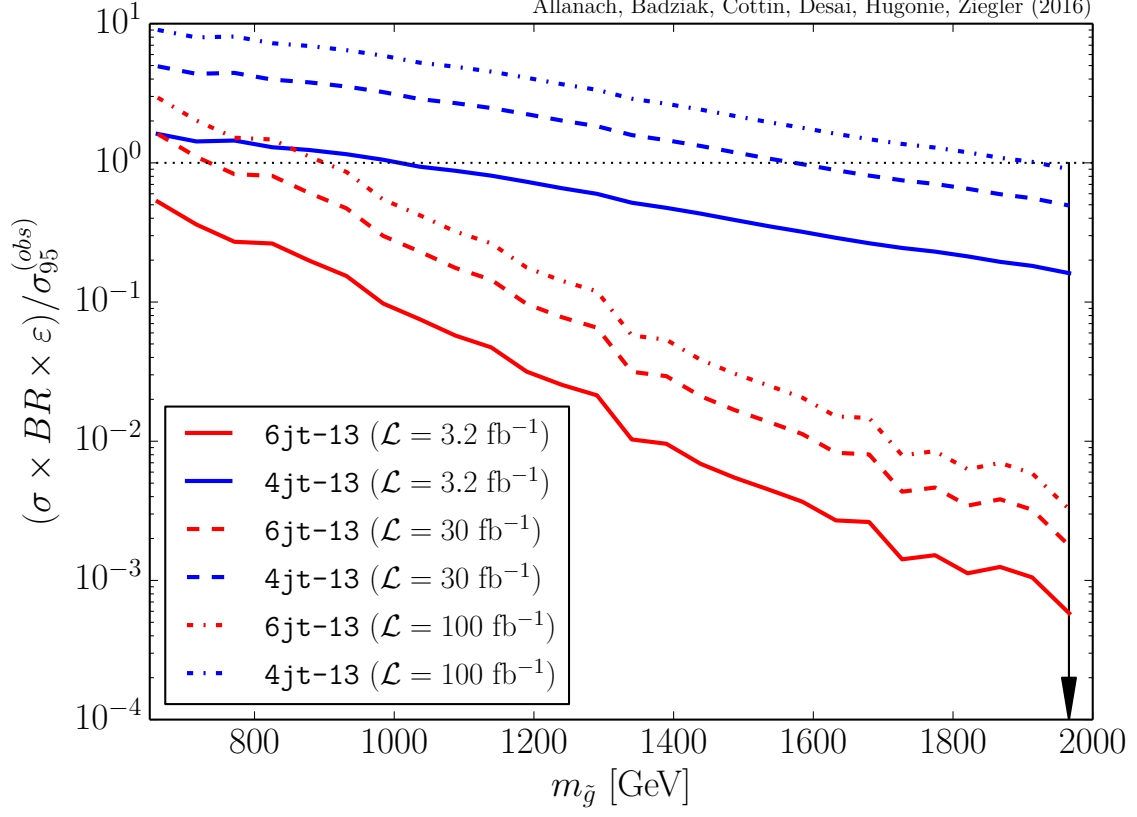
Figure 8.4: 95% CL limits the gluino mass from the $\sqrt{s} = 13$ TeV jets $+ p_T^{\mathrm{miss}}$ searches and projected sensitivity with higher luminosity in the pNMSSM model. The signal regions `4jt-13` and `6j-13` are defined in Table 8.1. The arrow shows the position of our benchmark P0 in DGS, whereas elsewhere we are strictly in pNMSSM parameter space [2].

signal regions. The solid lines show the current lower limit from the 2015 run of 1000 GeV. For our model, the `4jt-13` region performs better than the `6jt-13` region. Model sensitivity (ignoring systematic errors) is equal to the number of signals events S divided by the square root of the number of background events B. Since $S \propto$ the total integrated luminosity $\mathcal{L}$, and $B \propto \mathcal{L}$, the sensitivity scales $\propto \sqrt{\mathcal{L}}$. Thus, we expect $\sigma_{95}^{\mathrm{obs}} \propto 1/\sqrt{\mathcal{L}}$. Using this dependence, we scale the $\mathcal{L} = 3.2$ fb^{-1} lines to 30 fb^{-1} and 100 fb^{-1} to show the projected sensitivities in the figure. We see that with 100 fb^{-1} and 13 TeV centre of mass collision energy, the LHC can reach up to 1900 GeV gluinos.

8.2 Searches with displaced vertices

DV searches are especially challenging, as detailed in Chapters 6 and 7. As mentioned in Chapter 6, recent reinterpretation of LHC displaced searches can be found in Refs. [166–172]. Displaced signatures have received far less attention in the literature as compared to prompt signatures. Modelling the detector's response to DVs is a difficult task, as we shall illustrate. Validation is therefore essential in order to tell how good or bad a job of modelling the response we achieve. Refs. [166, 168] used truth information to identify displaced decays. Our work goes further by fully detailing the steps of reconstruction for DVs, in a similar way to Ref. [167], but here we determine an explicit functional form for the tracking efficiency, which is needed to be able to model the efficiencies from the experiments to a reasonable (if somewhat rough) level.

8.2.1 Validation of Run I displaced vertex searches

In the absence of publicly available multi-dimensional, model-independent efficiency maps for the reconstruction efficiency of a DV, we make use of the efficiencies published for specific models and construct a function that approximately simultaneously reproduces them. The ATLAS DV+jets search [1] has been interpreted in the context of two General Gauge Mediation (GGM) and several $R-$parity violating supersymmetry (RPV) simplified models, as explained in Chapter 7. Of these, the ones most relevant to signatures predicted by the DGS model (where we expect only jets from the DV) are the two GGM model benchmarks and one RPV benchmark where a displaced neutralino decays through a non-zero λ'_{211} to light quarks and a muon.

The ATLAS DV+jets cuts are summarised in Table 8.2. The ATLAS analysis re-runs the experiment's standard tracking algorithms on events passing the trigger in order to determine the efficiency for the displaced tracks. Given the fact that we do not have access to such algorithms outside ATLAS, we assign each track a reconstruction probability depending on its p_T and the *true* co-ordinates of its displaced origin. The functional form found to reproduce the efficiencies for the three benchmark models is given by

DV jets	4 or 5 or 6 jets with $|\eta| < 2.8$ and $p_T > 90, 65, 55$ GeV.
DV reconstruction	DV made from tracks with $p_T > 1$ GeV, $|\eta| < 2.5$ and $|d_0| > 2$ mm, satisfying a tracking efficiency given by equation 8.1. Vertices within 1 mm are merged.
DV fiducial	DV within 4 mm $< r_{DV} < 300$ mm and $|z_{DV}| < 300$ mm.
DV material	No DV in regions near beampipe or within pixel layers: Discard tracks with $r_{DV}/$mm $\in \{[25, 38], [45, 60], [85, 95], [120, 130]\}$.
N_{trk}	DV track multiplicity ≥ 5.
m_{DV}	DV mass > 10 GeV.

Table 8.2: Our implementation of cuts applied in the ATLAS multi-track DV+jets search, from Ref. [1] [2].

$$
\begin{aligned}
\varepsilon_{\mathrm{trk}} = & \ 0.5 \times (1 - \exp(-p_T/[4.0 \text{ GeV}])) \times \exp(-|z|/[270 \text{ mm}]) \\
& \times \max(-0.0022 \times r_\perp/[1 \text{ mm}] + 0.8, 0),
\end{aligned} \tag{8.1}
$$

where $r_\perp$ and z are the transverse and longitudinal distance of the track's production vertex (see Figure 4.8).

We pick this particular parameterisation of the tracking efficiency after trying several functional forms and varying the constants, picking the one that had the best goodness of fit statistic (χ^2) for the three models combined that we validate against (at various different values of lifetimes of the decaying sparticle) (see Figure 8.6 for our validation of the efficiency curves). Eq. (8.1) is not expected to be perfect by any stretch: it is a simple, universal and factorised form for the track efficiency that is a rough approximation. The overall χ^2 statistic did not indicate a particularly good fit, however inspection by eye showed that the shapes of the efficiency curves were reasonable. We display contours of the function in Figure 8.5.

The efficiency for reconstructing a multi-track DV is highly dependent on track reconstruction and track selection, as detailed in Section 7.4. We stress again that the vertex reconstruction efficiency will be a non-trivial combination of different aspects of the track reconstruction efficiency. For instance the vertex reconstruction efficiency is worst at large radii, which is due to tracking efficiency decreasing. Here, we focus only on assigning each track a reconstruction probability dependent on some relevant variables,
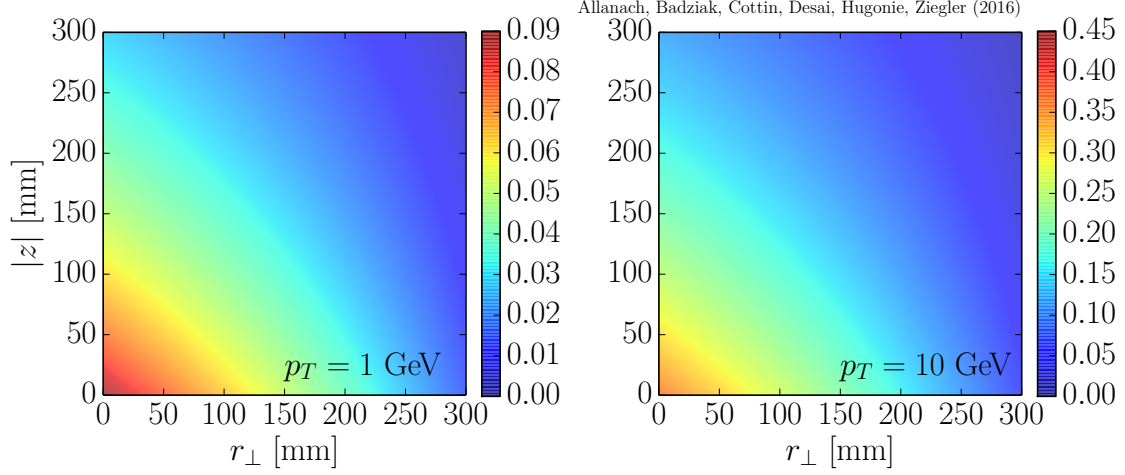
Figure 8.5: Contours of track efficiency as a function of $r_\perp$ and $|z|$, for a p_T value fixed at 1 GeV (left) and 10 GeV (right). Note the difference scales of track efficiency (labelled by the legend at the right hand side) of each panel [2].

such as the transverse and longitudinal distance of the production vertex of the track and its transverse momentum. The particular choice of the variables in equation 8.1 (for instance the fact we use $r_\perp$ instead of d_0) was made because we found these fitted the best across the three different signal models out of a few different simple factorised functional forms that we tried.

We find that validating against only one of the benchmark models at a time leads to different best-fit parameters for each. Using three benchmarks for validation therefore gives us more confidence in applying the efficiency to our own model. We believe this is a key improvement in our work. Choosing a functional form for the tracking efficiency in order to recast displaced results has already been attempted in the literature [167]. Here we show the explicit functional form used, since knowing it is necessary to be able to reproduce our results. Figure 8.6 shows the validation of our simulation (dashed lines) for three different ATLAS benchmarks, against the ATLAS determination (solid lines). We see that the efficiency, while far from being perfectly modeled by our function, is adequately modelled (within a few sigma) for most of the range of lifetimes considered.

We could improve the above fits by including an additional selection efficiency at the vertex level, as discussed above. We could also take into account the topology of the different signatures. Ideally, a parameterisation of the tracking efficiency should be

(a) GGM1

(b) GGM2

(c) RPV
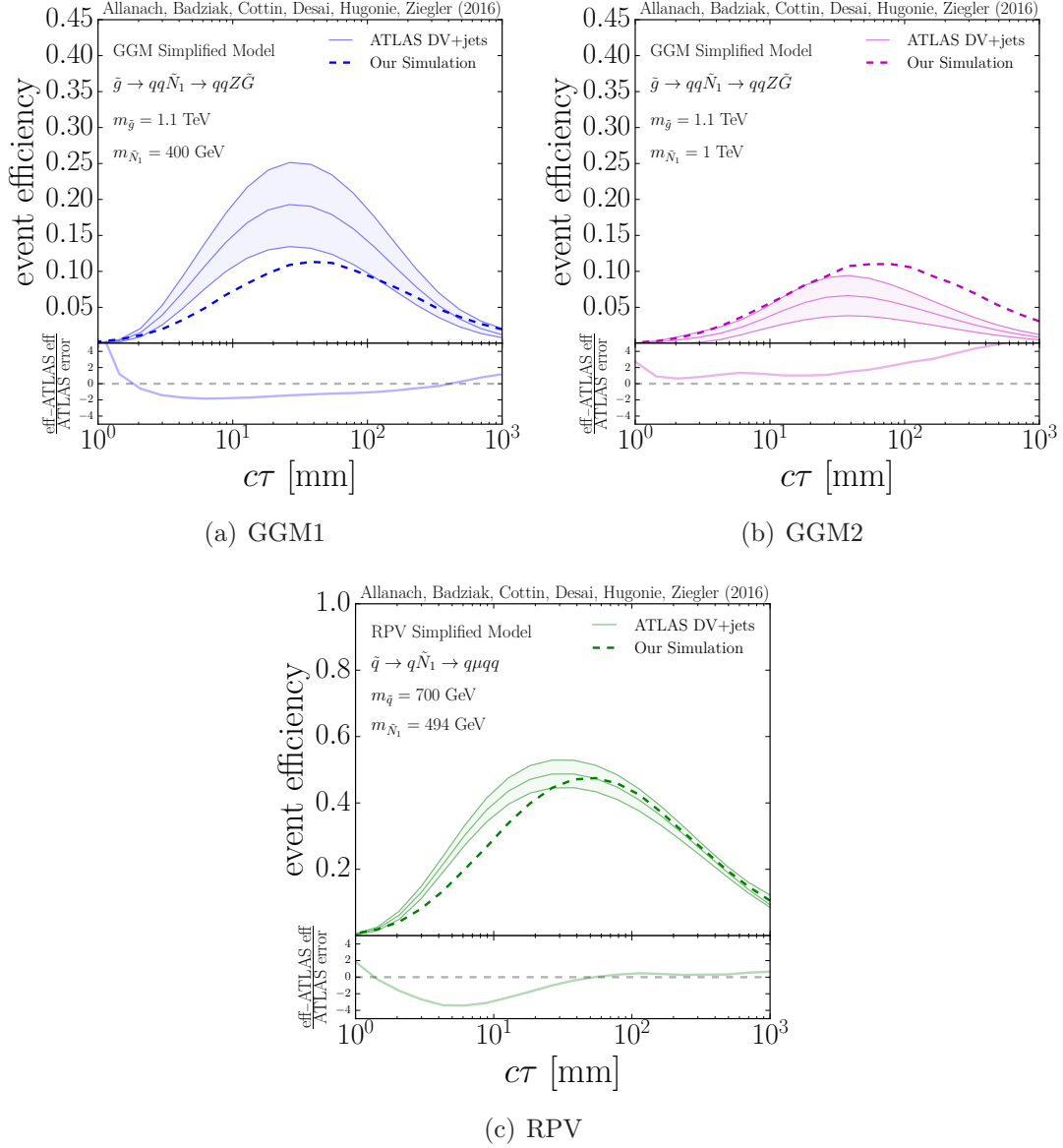
Figure 8.6: Validation of our DV+jets estimate of efficiency for three models against ATLAS's determination: (a) a simplified GGM model where a 1.1 TeV gluino decays to a 400 GeV neutralino, which in turn decays to a Z and a gravitino, (b) a simplified GGM model where a 1.1 TeV gluino decays to a 1 TeV neutralino, which in turn decays to a Z and a gravitino, (c) a simplified RPV model with a 700 GeV squarks decaying to a 500 GeV neutralino, which subsequently decays through a non-zero λ'_{211} coupling into a muon and two quarks. Events are generated with $\sqrt{s} = 8$ TeV. The bottom rectangle in each case shows the discrepancy between our estimate and ATLAS's, measured in units of the ATLAS error [2].

validated against all the ~ 20 signal benchmarks used in the ATLAS search, which is beyond the scope of this work.

Undiscarded displaced tracks are input into our vertex reconstruction algorithm, which compares and clusters the tracks' origins[3]. If the origins of two displaced tracks are less than 1 mm apart, then they are clustered together into one DV. Picking the first track, we compute the d value (i.e. the physical distance in the laboratory frame $\sqrt{\Delta x^2 + \Delta y^2 + \Delta z^2}$) to each of the other tracks, clustering tracks that have a small enough d value to the first track. Then we repeat for the next unclustered track and so on, until each track is assigned to a single vertex. The ATLAS analysis (and ours) combines vertices into a DV if they are less than $d = 1$ mm apart. The DV position is defined as the average position of all the track origins in the cluster.

To ensure consistency of the vertex position and the direction of the tracks, we require at least two tracks in the vertex to have $\vec{d} \cdot \vec{p} > -20$ mm, where we define $\vec{d}$ to be the vector from the interaction point to the DV and $\vec{p}$ to be the momentum of the displaced track. In the ATLAS analysis, DVs are vetoed if they are reconstructed in high density material regions, since this is the main source of background vertices. We simulate this by requiring 4 mm $< r < 300$ mm and $|z| < 300$ mm. We also require decay positions of the DVs to not be inside any of the three ATLAS pixel layers (our approximation to this DV material cut is shown in Table 8.2)[4]. As the table shows, events are further selected if they have at least one reconstructed DV with 5 tracks or more and a DV invariant mass (computed assuming all tracks have the pion mass) of at least 10 GeV.

8.2.2 Run I sensitivity of displaced vertex searches

We now apply the simulation described in the previous Section to the DGS model benchmark P0. We find that the sensitivity of the ATLAS study to our benchmark is extremely limited. From the 8 TeV columns of Table 8.3, it is clear that the primary cause for this is failure to satisfy the requirements $N_{\mathrm{trk}} \geq 5$ and the vertex mass cut $m_{\mathrm{DV}} > 10$ GeV.

---

[3] ATLAS performs a complicated vertex χ^2 fit in order to reconstruct DVs, as detailed in Section 4.3.2. Here, we simply use the truth information to define the track's origin to be the point at which the $\tilde{N}_1$ decays, and start comparing the distance between tracks' origins to cluster them into vertices.

[4] Note that the material veto performed in the ATLAS analysis is far more complex than this (see Figure 7.3), since ATLAS makes use of a 3D material map of the detector that we do not have access to.

	$\sqrt{s} = 8$ TeV		$\sqrt{s} = 13$ TeV	
	N	ϵ [%]	N	ϵ [%]
All events	100000	100.	100000	100.
DV jets	96963	97.	98306	98.3
DV reconstruction	16542	17.1	16542	16.8
DV fiducial	16459	99.5	16460	99.5
DV material	16146	98.1	16210	98.5
N_{trk}	584	3.6	544	3.4
m_{DV}	4	0.7	3	0.6

Table 8.3: Numbers of simulated events N and relative efficiencies ϵ (i.e. defined with respect
to the previous cut) for our DGS model (P0 benchmark) with $c\tau_{\tilde{N}_1} = 99$ mm at
$\sqrt{s} = 8$ TeV and $\sqrt{s} = 13$ TeV for the ATLAS selection of cuts in Table 8.2 [2].

This is due to the fact that the displaced jets are mainly $b-$jets. The $b-$hadrons are
themselves long-lived, and the neutral B^0 leaves no tracks before its decay. The topology
of this final state then has two further DVs, each with less than 5 tracks. The ATLAS
analysis does merge vertices (defined as having at least two tracks) that are within 1 mm
of each other to possibly obtain a better vertex. However, the $b-$hadrons are sufficiently
long-lived so that the resultant vertices are almost always more than 1 mm apart[5]. For
the benchmark P0 for instance, the average displaced track efficiency is 0.06, and the
average number of tracks coming from a displaced b is 18.1 (after hadronisation, but
before cuts). Thus, on average, there are only $18.1 \times 0.06 = 1.2$ visible tracks per displaced
b.

A further consideration is the small mass of the a_1 which decays to $b\bar{b}$ (23 GeV for
the benchmark P0) since softer $b-$quarks means less radiation, implying fewer tracks.
The distribution of track multiplicity versus invariant mass is shown in Figure 8.7. One
can see clearly from the right panel that increasing the a_1 mass to 70 GeV (done *ad hoc*
for the purposes of illustration) improves the sensitivity of the cuts by two orders of
magnitude. A higher mass could also mean the resultant products are more collimated
and hence the b-hadron vertices are likely to be closer to each other. The improvement
in efficiency with increasing a_1 mass can be seen in Figure 8.8.

---

[5] The ATLAS analysis [1] also reports that the sensitivity is severely reduced if they use the RPV
benchmark with $b-$quarks in the final state. An earlier work on displaced Higgs decays [169], also
shows how displaced b-quarks can be problematic, particularly given the $d < 1$ mm requirement for
merging vertices.
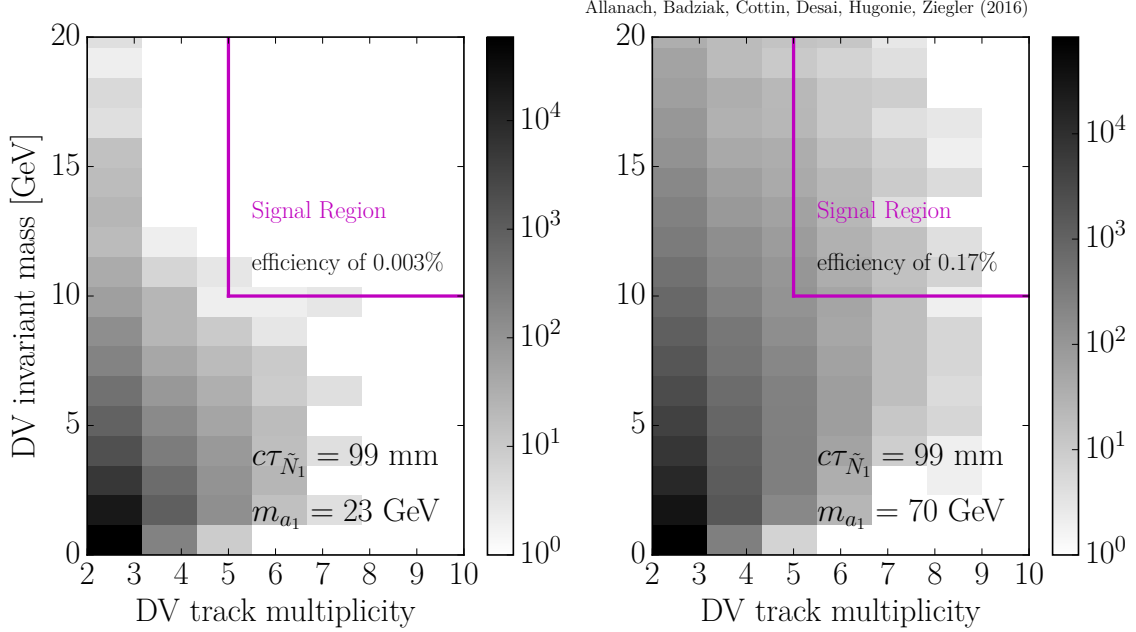
Figure 8.7: DV invariant mass against number of tracks for the DGS benchmark P0 with $m_{\tilde{g}} = 1.96$ TeV, $m_{\tilde{N}_1} = 98$ GeV and $c\tau_{\tilde{N}_1} = 99$ mm. Gluinos and squarks only are generated with $\sqrt{s} = 8$ TeV. Events in the plot pass all of the DV cuts except for the last two, which define the boxed ATLAS signal region. The left-hand frame shows a scenario where $m_{a_1} = 23$ GeV (in the DGS good-fit region, as in P0) and the right-hand frame has a tweaked $m_{a_1} = 70$ GeV in the SLHA file (i.e. inconsistent with the soft parameters, which are left constant - for the purposes of illustration only) [2].

8.2.3 Improving the sensitivity of displaced vertex searches

Given the very low sensitivity of the DV searches, we shall now attempt to improve it by loosening the most restrictive cuts. Firstly, to catch DVs coming from two $b-$quarks from the same a_1, we relax the requirement of maximum merging distance from 1 mm to 5 mm. Further, we can also relax the last two cuts: track multiplicity and invariant mass of the DV.

The background to the DV multi-track search comes from three sources — heavy flavour quark decays, interactions with material in the detector and the accidental crossing of tracks, all of which have a low multiplicity of tracks and a small invariant mass of the DV. Thus, if we loosen these cuts to achieve better signal efficiency, we also raise the background rate thus reducing the signal to background ratio. However, given that our model has good sensitivity in the prompt p_T^{miss}-based channels, background
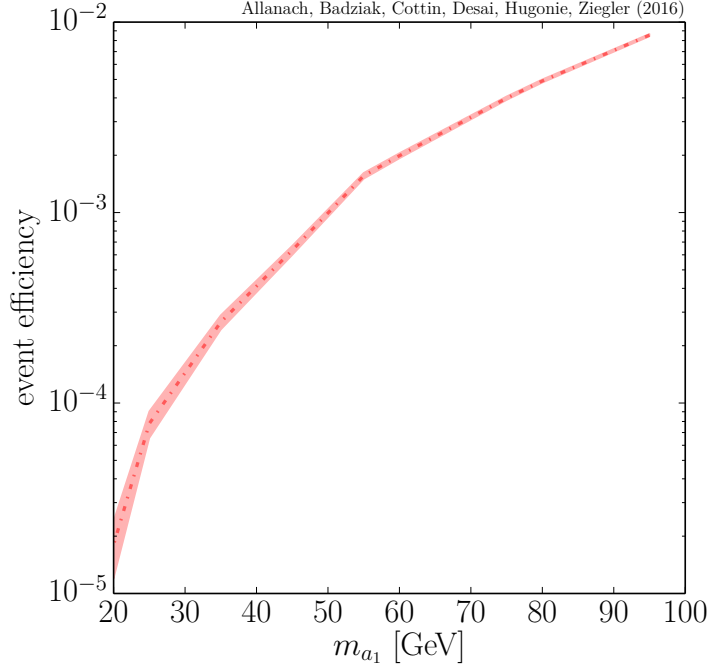
Figure 8.8: Event efficiency against pseudoscalar mass for a DGS benchmark with $c\tau_{\tilde{N}_1} = 99$ mm (our P0 benchmark). Events are generated with $\sqrt{s} = 8$ TeV considering strong production. We have tweaked m_{a_1} "by hand" in the SLHA files without changing soft parameters for the purposes of illustration [2].

rates can be controlled by taking advantage of the hard prompt signals that come in association with the DVs. Requiring a large m_{eff} in the event would reduce backgrounds significantly. It may also be possible to increase the sensitivity by loosening the DV cuts but requiring displaced jets to have a muon inside them [183, 212] (which often come from a b). However, we do not consider this route here.

We now investigate the effect of applying prompt cuts used in standard jets + p_T^{miss} sparticle searches on top of relaxed DV cuts. This, of course, will have a lower signal efficiency than purely applying the standard jets + p_T^{miss} cuts, which are already designed to remove the SM background very effectively. Ideally, one would optimise the jets + p_T^{miss} cuts along with the DV cuts to reach an overall best sensitivity. However, we have clear estimates of the background to the prompt channels from the analysis which serves as an upper bound to any DV contributions we may have from heavy flavour. Of course, the contributions from systematic sources cannot be bounded in this way, however, we can reasonably assume that the number of DVs from systematic sources is not biased by the hard cuts we place.

At 8 TeV, we choose the ATLAS `6jt-8` signal region cuts described in Table 8.1, because they were found to have the highest sensitivity to our signal, as shown above. Figure 8.9 shows efficiency curves against lifetime for the DGS model with the default ATLAS DV analysis cuts and some choices of relaxed cuts. This includes (i) allowing N_{trk} to be ≥ 2 rather than ≥ 5, (ii) increasing the vertex merging distance from 1 mm to 5 mm, and (iii) lowering the vertex mass cut from 10 GeV to 5 GeV. For comparison, we also show the response for the original tight ATLAS DV (`DVT`) cuts as well as our loose cuts (`DVL`) for the `6jt-8` signal region. With this combination, we already achieve an improvement in signal efficiency by a factor of ten. Without the `6jt-8` cuts, the improvement is a factor of several hundred. An optimised analysis will be between these two limiting cases and may therefore be reasonably expected to offer an improvement of two orders of magnitude or so.
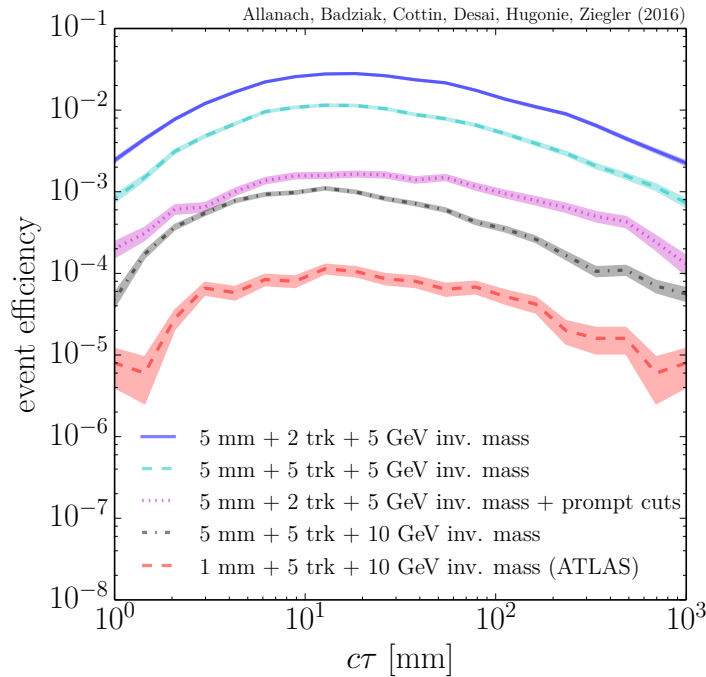
Figure 8.9: Signal efficiencies of different sets of DV+jets analyses on a DGS benchmark with $m_{\tilde{g}} = 1.96$ TeV, $m_{\tilde{N}_1} = 98$ GeV, $m_{a_1} = 23$ GeV (our P0 benchamark) against the lifetime of the long-lived singlino $c\tau_{\tilde{N}_1}$ (changed "by hand" in the SLHA files without changing the soft terms for the purposes of illustration). Events are generated with $\sqrt{s} = 8$ TeV, considering gluino/squark production only. The bottom curve corresponds to the efficiency after the default ATLAS DV cuts. The top curve corresponds to the loosest of our selections in DV merging distance, track multiplicity and invariant mass. We also show different sets of cuts in between, including the inclusion of standard prompt cuts, as defined in the text [2].

	$\sqrt{s} = 8$ TeV		$\sqrt{s} = 13$ TeV	
	N	ϵ [%]	N	ϵ [%]
All events	100000	100.	100000	100.
Prompt $p_T^{\text{miss}*}$	91709	91.7	87737	87.7
Prompt jets*	72075	78.6	84178	95.9
Prompt $\Delta\phi(\text{jet}_{1,2,3}, \vec{p}_T^{\text{miss}})_{min}{}^*$	49095	68.1	57261	68.
Prompt $\Delta\phi(\text{jet}_{j>3}, \vec{p}_T^{\text{miss}})_{min}{}^*$	27315	55.6	33832	59.1
Prompt $p_T^{\text{miss}}/m_{\text{eff}}(N_j)^*$	6670	24.4	18409	54.4
Prompt $m_{\text{eff}}(\text{incl.})^*$	6636	99.5	16848	91.5
DV jets	6636	100.	16848	100.
DV reconstruction†	1524	23.	3850	22.9
DV fiducial	1516	99.5	3825	99.4
DV material	1494	98.5	3750	98.
$N_{\text{trk}} \geq 2$	1494	100.	3750	100.
$m_{\text{DV}} > 5$ GeV	88	5.9	265	7.1

Table 8.4: Numbers of simulated events N and relative efficiencies ϵ (i.e. defined with respect to the previous cut) for our DGS model with $c\tau_{\tilde{N}_1} = 99$ mm (our P0 benchmark) at $\sqrt{s} = 8$ TeV and $\sqrt{s} = 13$ TeV for our tuned cuts, as explained in the text. Events are generated considering strong production. An asterisk denotes that the prompt cuts are taken from signal regions `6jt-8` at $\sqrt{s} = 8$ TeV and `4jt-13` at $\sqrt{s} = 13$ TeV as listed in Table 8.1. The dagger is a reminder of the increased vertex merging distance of 5 mm [2].

8.2.4 Recommendations for displaced vertex searches at 13 TeV

We used `6jt-8` for the prompt cuts at 8 TeV, however keeping in mind that the best sensitivity at 13 TeV is for the `4jt-13` signal region, we also perform efficiency calculations with the combination `DVL + 4jt-13`. The efficiencies are shown in Table 8.4. The signal efficiency at 13 TeV is $\sim 0.2\%$. It would be desirable to relax the prompt cuts further in order to increase this number, but a proper estimate would require a full estimation of the DV background, which is beyond the scope of this work.

However, an estimate of the contribution from heavy flavours may be obtained. Given the hard multi-jet, p_T^{miss} and m_{eff} cuts, the dominant SM background is from $t\bar{t}$ + jets production which is also a source of b-hadrons and therefore a potential background for DVs. In order to examine this possibility, we simulate 10^6 $t\bar{t}$ events, and inspect the
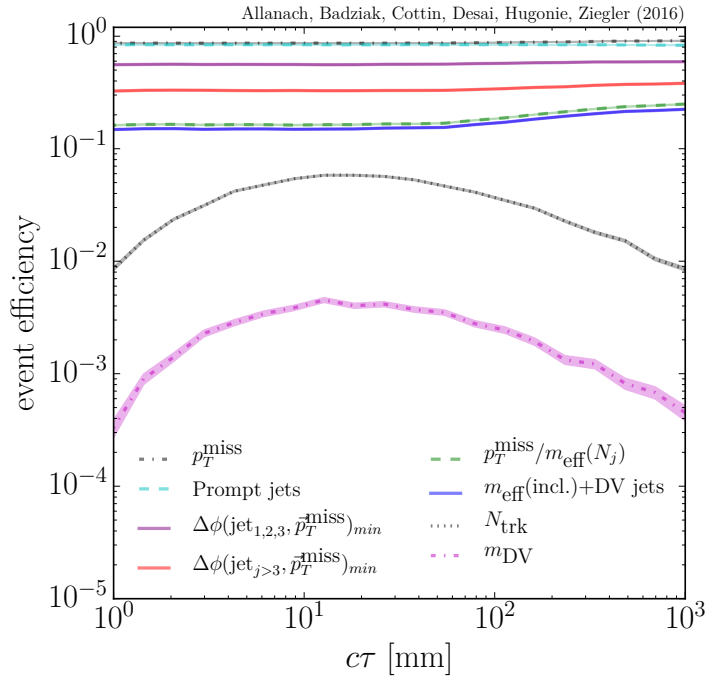
transverse impact parameter d_0 of the tracks coming from the displaced b vertices. We see that only a tiny fraction of tracks pass $|d_0| > 2$ mm from $t\bar{t}$ events ($\sim 1\%$). Furthermore, imposing the DV cuts (without any restrictions on hard jets), gives us an efficiency of 0.1% for $N_{\text{trk}} \geq 2$ and imposing $m_{\text{DV}} > 5$ GeV gives us no events at all. We therefore do not expect any DV contributions from heavy flavour once the hard jet cuts are made. This implies zero background events at 3.2 fb^{-1} and we are already potentially sensitive to signal cross sections of approximately 0.3 fb.

The total strong sparticle production cross-section at 13 TeV before cuts is 5.8 fb, and so with our illustrative cuts (`DVL + 4jt-13`), one would achieve a signal cross-section after cuts of 0.01 fb. With no expected background, the observation of a single event already corresponds to discovery, which for a gluino mass of ~ 2 TeV (as in P0) is not achievable in prompt search channels with 100 fb^{-1} at 13 TeV. We may reasonably set the observation of at least three signal events as a requirement for discovery, which results in a best-case scenario of discovering a DGS model with $m_{\tilde{g}} \sim 2$ TeV with 300 fb^{-1} data at 13 TeV.

We can also make an estimate of the worst-case scenario where there is a large DV background from systematic sources. Such a background occurs when a spurious track crosses an existing DV resulting in a reconstructed vertex satisfying the N_{trk} and m_{DV} requirements. The ATLAS DV analysis [1] estimates only ~ 0.4 background vertices in the DV + jet channel for the full 20 fb^{-1} data of Run I (see Table 1 of Ref. [1]). Given a $t\bar{t}$ production cross section $\sim O(100$ pb$)$ at 8 TeV, this implies an efficiency $\sim 10^{-5}$. To be conservative about the effect of our relaxed cuts, we can assume that this happens in about 1% of events that pass the `4jt-13` cuts. Starting with a total prompt background of ~ 1 fb (see Table 4 of Ref. [211]) in the `4jt-13` channel as reported in the ATLAS analysis, we arrive at 0.01 fb for `DVL + 4jt-13`. A 3-sigma discovery may then be viable with ~ 1 ab^{-1} data at 13 TeV.

This situation may be improved considerably by relaxing the prompt cuts. An indication of where we may further relax the selection cuts comes from examining the relative efficiencies at 8 and 13 TeV for the cut on the ratio of p_T^{miss} and $m_{\text{eff}}(N_j)$. We see that a change from > 0.25 at 8 TeV to > 0.2 at 13 TeV (see Table 8.1) already results in a gain of a factor 2. Although, this is obviously also due to the increased energy of the overall event, given that we have high p_T^{miss} and m_{eff} cuts, an additional factor of 3 may be gained by dropping the $p_T^{\text{miss}}/m_{\text{eff}}(N_j)$ cut altogether.

We now study how the cut efficiencies behave with singlino lifetime for benchmark P0. The result is shown in Figure 8.10, where we plot the effect of the cuts DVL + 4jt-13 as a function of the decay length $c\tau_{\tilde{N}_1}$. Note that we have merged the $m_{\text{eff}}(\text{incl.})$ and the DV jets cuts together into one curve, as applying the DV jets cut after the $m_{\text{eff}}(\text{incl.})$ one does not change the number of events, for any lifetime (this can also be appreciated for P0 in Table 8.4).

Allanach, Badziak, Cottin, Desai, Hugonie, Ziegler (2016)

Legend:
- p_T^{miss}
- Prompt jets
- $\Delta\phi(\text{jet}_{1,2,3}, \vec{p}_T^{\text{miss}})_{min}$
- $\Delta\phi(\text{jet}_{j>3}, \vec{p}_T^{\text{miss}})_{min}$
- $p_T^{\text{miss}}/m_{\text{eff}}(N_j)$
- $m_{\text{eff}}(\text{incl.})+\text{DV jets}$
- N_{trk}
- m_{DV}

x-axis: $c\tau$ [mm]; y-axis: event efficiency

Figure 8.10: Signal event efficiency of our simulation on a DGS benchmark with $m_{\tilde{g}} = 1.96$ TeV, $m_{\tilde{N}_1} = 98$ GeV, $m_{a_1} = 23$ GeV (our P0 benchmark) against the lifetime of the long-lived singlino $c\tau_{\tilde{N}_1}$. Events are generated with $\sqrt{s} = 13$ TeV considering strong production. Independent prompt and DV cuts are presented. The singlino decay distance $c\tau$ has been tweaked "by hand" in the SLHA files without changing soft parameters for the purposes of illustration [2].

We notice that standard prompt cuts are not very much affected by the singlino lifetime, except for the cut on the ratio of p_T^{miss} and $m_{\text{eff}}(N_j)$, which increases at higher lifetimes. This is because p_T^{miss} is higher at high lifetimes, as explained in Section 8.1.1.

To summarise, with a combination of relaxed DV cuts and prompt SUSY search cuts, one can discover a DGS scenario with $m_{\tilde{g}} \sim 2$ TeV with 300 fb^{-1} data which is not possible with prompt SUSY searches alone. With a full optimisation of relaxed DV cuts + prompt p_T^{miss}-based cuts, we may easily gain a further factor of ten in the

signal efficiency and given almost zero background, as shown above, one could have higher sensitivity to the DGS model in DV + prompt searches as compared to prompt searches. We therefore strongly urge the experiments to perform a dedicated background simulation with optimised cuts.

Part IV

Collider phenomenology of a Higgs triplet model

Chapter 9

Phenomenology of the "123" Higgs triplet model

Here we investigate the phenomenology of the "123" HTM described in Chapter 2. A characteristic of this model is that once the triplet field acquires a vev, a neutrino mass term is generated. The parameters in the neutrino sector include the vev of the triplet and the Yukawa couplings between the two-component fermion $SU(2)$ doublet, including charged leptons and Majorana neutrinos, and the triplet field. In this thesis, we study the collider phenomenology of the "123" model, which is almost decoupled from its neutrino sector [1]. This is why we don't discuss experimental constrains on neutrino masses and mixing angles, which are beyond the scope of this study.

The collider phenomenology of "123" models was studied before in [51, 213], paying particular attention to the consistency of the presence of the Majoron with experimental data. The Majoron is mainly singlet in this model, so its interaction with gauge bosons such as the Z is negligible, making its existence fully consistent with collider data. This is in contrast to what happens in models with spontaneous violation of lepton number without the singlet field and where the Majoron is mainly triplet [214], which are excluded.

A characteristic signature of models with Higgs triplets is the existence of a doubly charged scalar (Δ^{++}), in addition to the existence of a tree-level $H^{\pm}W^{\mp}Z$ vertex, where $H^{\pm}$ is a singly charged Higgs [87]. The LHC collider phenomenology of a doubly charged scalar in Higgs triplet models (in particular the "23" HTM, without the singlet field) has

---

[1] The connection between the neutrino sector of the model and collider physics arises via the decays of the doubly charged Higgs (arising from the triplet) to charged leptons, as these decays involve the same Yukawa couplings above mentioned.

been discussed in [86, 215–221]. Production of doubly charged scalars at $e^+ e^-$ colliders has also been studied in the literature as probes of Higgs triplet models [222–226], the Georgi-Machacek model [227–230] and left-right symmetric models [231], which have a similar phenomenology.

The phenomenology of the neutral scalar sector in Higgs triplet models has been less studied than the charged sector. Production and decays of the neutral Higgs bosons in the "23" HTM were studied in [232–234]. Associated production of the charged and neutral Higgs at the future International Linear Collider (ILC) was studied in [235, 236]. In particular for the "123" HTM, only discovery prospects at colliders were discussed in [51] and a fermiophobic Higgs was studied in [213].

The collider phenomenology of neutral and singly charged Higgs bosons in the HTM has received much less attention in the literature than the doubly charged Higgs. In addition, the phenomenology of the doubly charged Higgs depends directly on neutrino physics we are not evaluating at this time (as noted earlier), so we focus on the neutral sector and singly charged Higgs of the "123" HTM in this thesis.

We study the production and decay of the next to heaviest neutral $CP-$even Higgs h_2, the $CP-$odd Higgs A and the singly charged Higgs $H^{\pm}$ of the "123" HTM. We extend the work in Refs. [51, 213] by identifying the lightest state in the $CP-$even neutral sector, h_1, as the SM-like Higgs discovered at the LHC. This rules out the fermiophobic SM-like Higgs boson scenario described in [51]. Constraints are imposed on the parameter space of the model in order to retain the SM-like Higgs properties. In particular, we define h_1 to be mainly doublet and fix its mass to be $m_{h_1} \approx 125$ GeV. We also identify the necessary constraints on the parameters of the scalar potential to suppress its decays to Majorons, so that its invisible decay width is negligible.

We identify three characteristic benchmarks of the model, related to the composition of h_2. h_2 can be mainly singlet, mainly triplet or a mixture. Note that h_2 can not be mainly a doublet since this is reserved for the SM like Higgs-boson. We compute production cross-sections and decays in these three benchmarks and identify promising channels for discovery at future lepton colliders.

9.1 Restrictions on the parameter space

In this Section we explain our restrictions on the model parameters. We first comment that the invisible decay width of the Z gauge boson in our model is suppressed since the Majoron J is mostly singlet ($O_\varphi^{21} \approx 1$). We define Γ_{inv}^{123} as the decay width of the Z into undetected particles excluding the decay into neutrinos, $Z \to \overline{\nu}\nu$. Experimentally, $\Gamma_{inv}^{123} < 2$ MeV at 95% CL. [93, 237] and in our model there could be a contribution from the mode $Z \to JZ^* \to J\overline{\nu}\nu$. This contribution is automatically suppressed because the Majoron is mainly singlet (see Appendix A.1).

Also, this model includes three $CP-$even Higgs bosons. We assume that the lightest of them is SM-like, and therefore fits with the experimental results. That is, we assume its mass is near 125 GeV, that it is mainly doublet ($O_\chi^{12} \approx 1$), and that its invisible decay width is negligible [238]. This last condition is obtained if we suppress the h_1 coupling to Majorons taking $|\beta_2| \leq 0.05$.

The constraints we implement are:

- $|O_\varphi^{21}| \geq 0.95$ (J mainly singlet)

- The ρ parameter is also very well measured: $\rho = 1.00037 \pm 0.00023$ [237]. In this model it is

$$\rho = 1 - \frac{2v_\Delta^2}{v_\phi^2 + 4v_\Delta^2}. \tag{9.1}$$

  This restricts the value of v_Δ to be smaller than a few GeV. Nevertheless, we consider $v_\Delta < 0.35$ GeV as in Ref. [51] in order to satisfy astrophysics bounds [239].

- $m_{h_1} = 125.09 \pm 0.24$ GeV [92].

- $|O_\chi^{12}| \geq 0.95$ (h_1 mainly doublet)

- $|\beta_2| \leq 0.05$ (small h_1 invisible decay)

- $m_{H^\pm} > 80$ GeV [237].

We make a general scan where we vary all the independent parameters. We generate their values randomly from uniform distributions. We do our scan with positive values of λ_1, β_1 and κ, as negative values of these parameters typically result in negative eigenvalues of the mass matrix in eq. (2.3). The window for v_2 is reduced because of its dependency with the masses of the W and Z bosons [213]. Considering the range of v_2 and v_3, the
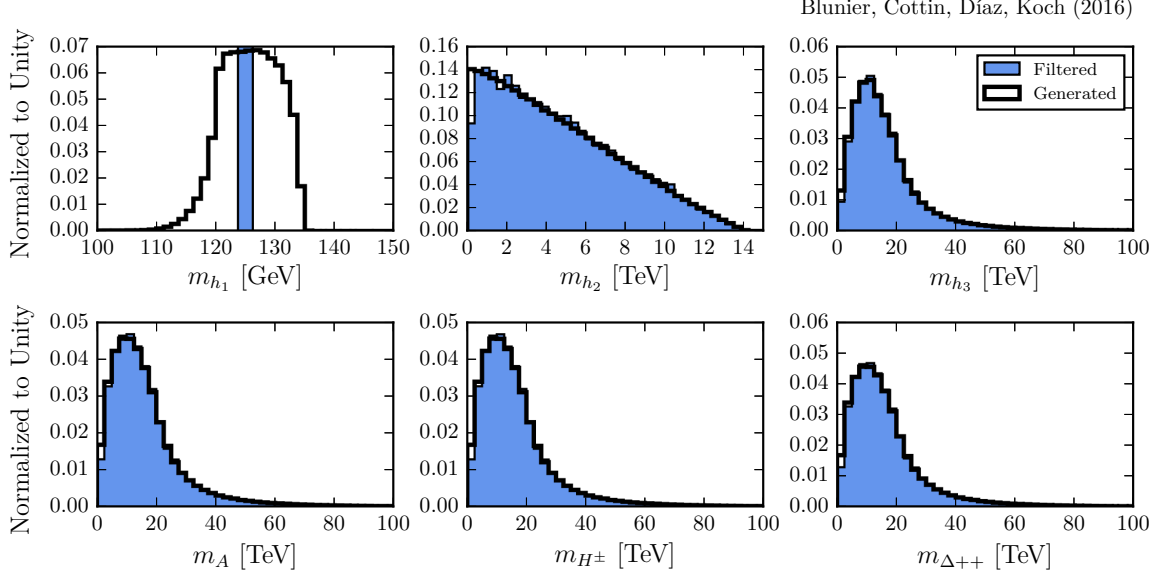
Figure 9.1: Distribution of the physical masses in the general scan before and after all con-
straints are applied. Note that all plots are normalized to unity, so the shape of
the generated and filtered distributions can differ significantly (i.e the filtered blue
bar in the top left plot for m_{h_1} extends to much higher values in the normalized
plot). Parameters are varied as in Table 9.2 [3].

scanned range for λ_1 is mostly fixed due to its strong dependency with $m_{h_1} \approx 125$ GeV,
and also because of the small effects of the mixings with other $CP-$even scalars (see
eq. (2.3)). Terms outside of the mass matrix diagonal are generally much smaller than
those on the diagonal, making the terms in the diagonal leading almost directly to the
masses of h_1, h_2 and h_3. The scanned range for β_2 is forced to be small to avoid a large
h_1 invisible decay (see Section 9.4.1).

After imposing our constraints we note a clear hierarchy where $v_\sigma \gg v_\phi \gg v_\Delta$ that
we have partially imposed: v_Δ is small in order to account for the measured ρ parameter,
and $v_\phi \approx 246$ GeV to account for the Higgs mass. With that, a large value for v_σ comes
naturally.

We find a small effect from our filters in λ_2, λ_3, λ_4, λ_5 and β_3. We note that the value
of κ cannot be zero because in that case the $CP-$odd Higgs A would be massless, and
since it is mostly triplet that would contradict the measurements for the invisible decay
of the Z boson. Its value cannot be to large neither because mixing in the $CP-$even
sector would move h_1 away from the mostly doublet-like scenario (a SM-like Higgs boson).
After the scan and imposing the filters we can see the distribution of the physical masses
in our model. This is shown in Fig. 9.1, where the thick black line shows the distribution

before cuts to appreciate their effect. The most distinctive feature is that we impose the lightest scalar mass to be $m_{h_1} \approx 125$ GeV. All the other masses are free. The model allows for heavier scalars considering that we still have room for large parameters.

We highlight that the Majoron is massless in this model and is naturally mainly singlet, as can be inferred from eq. (A.5), which is related to the exact diagonalization of the $CP-$odd mass matrix shown in Appendix A.1. Also notice that the new scalar states have the tendency to be heavy, with extreme values for the masses obtained for high values of the parameters. The shape of the distributions in Fig. (9.1) of course depends on using a linear generation of random values, which highlights large masses. We consider this to be an argument against building new colliders with small values for the centre of mass (CM) energy.

There is also an ambiguity related to the composition of the h_2 field: it can be mainly singlet, mainly triplet, or anything in between, as long as it is not mainly doublet, which is reserved for h_1, our SM-like Higgs boson. If h_2 is mainly triplet its mass tends to be similar to the masses of A, H^+, and Δ^{++} (all these fields are mainly triplet). If h_2 is mainly singlet, the mass of h_3 tends to be equal to the masses of A, H^+, and Δ^{++}, and in this case, a mainly-singlet h_2 can be lighter. The masses of h_2 and h_3 are strongly correlated with the values of $(M_\chi)^2_{11}$ and $(M_\chi)^2_{33}$ depending on which is mainly singlet or triplet. Obtaining a scenario where h_2 and h_3 are not purely singlet or triplet requires $(M_\chi)^2_{11}$ numerically very close to $(M_\chi)^2_{33}$, making that scenario highly fine-tuned.

The splitting between the mainly triplet fields is controlled by $|\lambda_5|$. This can be algebraically understood starting from the hierarchy $v_\Delta \ll v_\phi, v_\sigma$ and approximating eq. (2.5) to

$$m_A^2 \approx \frac{1}{2}\kappa \frac{v_\sigma v_\phi^2}{v_\Delta}. \tag{9.2}$$

Using the same approximation in eqs. (2.7) and (2.8), we get for the singly and doubly charged Higgs masses,

$$
\begin{aligned}
m_{H^\pm}^2 &\approx m_A^2 - \frac{1}{4}\lambda_5 v_\phi^2 \\
m_{\Delta^{++}}^2 &\approx m_A^2 - \frac{1}{2}\lambda_5 v_\phi^2 \approx m_{H^\pm}^2 - \frac{1}{4}\lambda_5 v_\phi^2.
\end{aligned}
\tag{9.3}
$$

Thus, $H^\pm$, Δ^{++} and A can differ appreciably in mass as long as $|\lambda_5|$ is large.

Benchmark	Composition of h_2	$|O_\chi^{21}|$	$|O_\chi^{22}|$	$|O_\chi^{23}|$
B1	mostly triplet	1.0×10^{-5}	1.5×10^{-3}	1.0
B2	mostly singlet	1.0	9.7×10^{-3}	8.7×10^{-4}
B3	mixed	8.9×10^{-1}	9.8×10^{-4}	4.6×10^{-1}

Table 9.1: Characterization of the three benchmark under study, giving the composition of h_2 [3].

The previous considerations motivate us to define three benchmarks, characterized by the composition of h_2 in Table 9.1. The parameters for each benchmark are defined in Table 9.2. Note that these are chosen thinking of e^+e^- colliders, given the masses below 1 TeV.

Parameter	Scanned Range	B1	B2	B3	Units
v_σ	$[0, 5000]$	1500	3300	2500	GeV
v_ϕ	$[245, 247]$	246	246	246	GeV
v_Δ	$[0, 0.35]$	0.2	0.2	0.3	GeV
λ_1	$[0.127, 0.15]$	0.13	0.13	0.13	-
λ_2	$[-4, 4]$	0.1	0.1	0.1	-
λ_3	$[-4, 4]$	0.1	0.1	0.1	-
λ_4	$[-4, 4]$	0.1	0.1	0.1	-
λ_5	$[-4, 4]$	1.0	0.5	0.8	-
β_1	$[0, 4]$	0.3	0.02	0.008	-
β_2	$[-0.05, 0.05]$	0.02	0.005	0	-
β_3	$[-4, 4]$	0.1	0.5	0.6	-
κ	$[0, 1]$	0.001	0.0015	0.0004	-

Table 9.2: Scanned range for the independent parameters and their values for the different benchmarks [3].

We stress the fact that there is an ambiguity in the composition of h_2. By definition h_1 is mainly doublet. The H^+ and Δ^{++} fields are always mainly triplet. The A field is also always mainly triplet because J is mainly singlet. The composition of h_3 is complementary to the composition of h_2.

Table 9.3 shows the physical masses obtained for the three benchmarks. In B1 h_2 is mainly triplet, thus it has a mass similar to A, $H^\pm$, and Δ^{++} masses, with h_3 heavier.

In B2 h_2 is mainly singlet, thus it is h_3 that has a mass similar to the masses of A, $H^{\pm}$, and Δ^{++}, with h_2 lighter.

Parameter	B1	B2	B3
m_{h_1}	125	125	125
m_{h_2}	476	660	316
m_{h_3}	1162	865	318
m_A	476	865	317
m_{H^+}	460	861	298
$m_{\Delta^{++}}$	443	857	277

Table 9.3: Physical masses in GeV for the different benchmarks [3].

9.2 Production at the LHC[2]

Here we briefly comment on the production cross-section at the LHC for the scalars h_2, A and $H^{\pm}$ for our model benchmarks (which we choose thinking of e^+e^- colliders). We implement the "123" HTM in FEYNRULES [157] and interface the output to the MADGRAPH5 [148] event generator to compute production cross-sections.

When thinking of a SM-like Higgs boson (such as h_1 in our model), the main production mode at the LHC is gluon-gluon fusion (ggF),
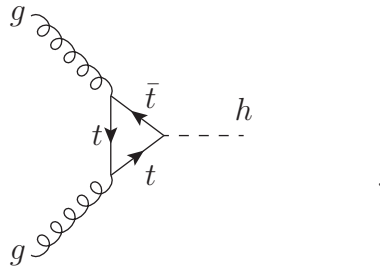
.

This process dominates SM-like Higgs production not only because the $ht\bar{t}$ coupling is large, but also because the parton distribution functions indicate that it is easier to find a gluon inside the proton than a heavy quark or an electroweak gauge boson[3].

Nevertheless, this mechanism is not be efficient for a not-mainly-doublet Higgs boson (which is the case for h_2 and A in our model benchmarks), because that Higgs couples to quarks very weakly. In the model studied here, the ratio of production cross-sections in the gluon-gluon fusion mode for h_1 and h_2 is,

$$\frac{\sigma(ggF, h_2)}{\sigma(ggF, h_1, m_{h_1} = m_{h_2})} = \left(\frac{O_\chi^{22}}{O_\chi^{12}}\right)^2 \approx (O_\chi^{22})^2. \tag{9.4}$$

The last approximation is valid because we have h_1 mainly doublet (SM-like). The production cross-section at $\sqrt{s} = 14$ TeV for h_2 reaches 5.7×10^{-6} pb in B1, 5.7×10^{-5} pb in B2 and 3.9×10^{-6} pb in B3. For A production, the above ratio is proportional to $(O_\varphi^{32})^2$ and we get similar numbers. The cross-section at $\sqrt{s} = 14$ TeV reaches 6.8×10^{-6} pb in B1, 4.0×10^{-7} pb in B2 and is somewhat higher in B3, reaching 2.5×10^{-5} pb. So we conclude that the above ratio is around 10^{-4} at most. This is why, if the model is correct, we may have not seen h_2 (nor A) at the LHC via ggF, as is not a dominant production mode since h_2 does not behave like a SM-like Higgs.

Other production mechanisms that can be relevant at the LHC are electroweak modes, for example vector boson fusion (VBF), but they also produce small cross-sections for our given benchmarks. When considering the sum over all VBF processes such as the diagram below, the highest cross-section at $\sqrt{s} = 14$ TeV obtained is 2.5×10^{-5} pb at B3, for the charged Higgs production,

---
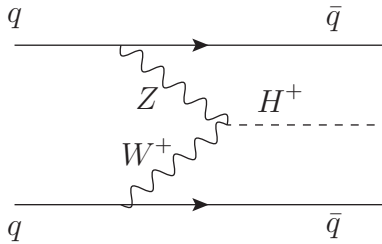
[3] Note that it is easier to find a gluon inside the proton only if the fraction of the proton momentum carried by the gluon, x, is small. This is the case for ggF at the LHC, as $x \sim 10^{-2} - 10^{-3}$ for this process.

Production processes via quark anti-quark annihilation can also be relevant. In the case of h_2 production, the highest contribution comes from the diagram
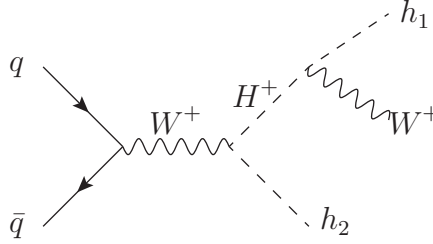
for B1 and B3. The cross-section at $\sqrt{s} = 14$ TeV for B1 is 4.5×10^{-4} pb. Production of A at $\sqrt{s} = 14$ TeV dominates in B1 when in the above diagram we replace h_2 with A, W^+ with a Z, h_1 also with a Z and H^+ with h_2, leading to the AZZ final state. This gives a cross-section of 3.7×10^{-4} pb. It can go higher in B3 in the AJJ final state, with a cross-section reaching 2.3×10^{-3} pb. Charged Higgs production at $\sqrt{s} = 14$ TeV can reach 4.3×10^{-3} pb in B3 in the $H^+W^-W^-$ final state (replacing W^+ and h_1 with W^-, H^+ with Δ^{--} and h_2 with H^+ in the above diagram).

The highest cross-section found in our model benchmarks for each characteristic production mechanism at the LHC is summarized in Table 9.4 for comparison. To finish,

σ	h_2	A	$H^{\pm}$
ggF	5.7×10^{-5} (B2)	2.5×10^{-5} (B3)	$-$
VBF	4.4×10^{-6} (B3)	2.2×10^{-5} (B1)	2.5×10^{-5} (B3)
$q\bar{q}$	4.5×10^{-4} (B1)	2.3×10^{-3} (B3)	4.3×10^{-3} (B3)

Table 9.4: Highest LHC production cross-section (in units of pb) found in our benchmarks for h_2, A and $H^{\pm}$ at $\sqrt{s} = 14$ TeV via the three characteristic production mechanisms: ggF, VBF and $q\bar{q}$ annihilation [3].

not even the HL-LHC [240, 241] will help, because it is expected to have a factor of 10 increase in luminosity[4], and it will not compensate the smallness of the production cross-section.

In summary, it seems hadron colliders are not well equipped to produce the new states h_2, A and $H^{\pm}$. Production for h_2 and A via ggF at the LHC is not efficient

---

[4] The goal of the HL-LHC is to deliver a total of 3000 fb^{-1} running over a decade starting in 2025. For comparison, during 2016, the LHC recorder 40 fb^{-1} of total integrated luminosity [242].

since these Higgs bosons are not-mainly doublet. Productions for h_2, A and $H^\pm$ via VBF can be only as large as $\sim 10^{-5}$ pb for our benchmarks. Electroweak production via quark anti-quark annihilation can be as high as $\sim 10^{-3}$ pb. Given that our benchmarks are not likely to be observed at the LHC (a dedicated analysis is needed to confirm this), the large hadronic background at the LHC and the advantage of a cleaner collider environment at lepton colliders, we focus on the production for these states at future electron-positron colliders.

9.3 Production at e^+e^- colliders[5]

In order to assess the discovery potential of the model, we implement it in FEYN-RULES [157] so we can extract relevant parameters and Feynman rules. We then interface the output to the MADGRAPH5 [148] event generator in order to compute production cross-sections[6], as we did in the previous section.

The FCC-ee machine is a hypothetical circular e^+e^- collider at CERN with a high luminosity but low energy, designed to study with precision the Higgs boson [243]. We consider its highest projected energy 350 GeV with a luminosity of $2.6\,\mathrm{ab}^{-1}$, which was calculated by taking the $0.13\,\mathrm{ab}^{-1}$ quoted in [243] and assuming 4 interaction points and 5 years of running of the experiment.

The canonical program for the ILC [244] includes three CM energies given by 250 GeV, 500 GeV, and 1000 GeV, with integrated luminosities 250 fb^{-1}, 500 fb^{-1} and 1000 fb^{-1}, respectively. CLIC [245] has three operating CM energies: $\sqrt{s} = 350$ GeV, 1.4 TeV and 3 TeV, with estimated luminosities $500\,\mathrm{fb}^{-1}$, $1.5\,\mathrm{ab}^{-1}$ and $2\,\mathrm{ab}^{-1}$, respectively. Based on this, we compute e^+e^- production cross-sections for h_2, A and H^+ for our three benchmarks at different CM energies.

9.3.1 h_2 production

Table 9.5 shows h_2 production cross-sections at e^+e^- colliders, prospected luminosities and CM energies for the FCC-ee, ILC and CLIC colliders. The cross-sections are calculated by summing all $e^+e^- \to h_2XY$ 3-body production modes, plus the 2-body production modes $e^+e^- \to h_2X$, where X is a particle that does not decay. The production cross-

---

[5] Plots and Tables from this Section were generated by Sylvain Blunier.
[6] Note that in this work, no electroweak radiative effects are considered in the production.

$\sqrt{s}$ [TeV]	$\mathcal{L}_{FCCee}$	$\mathcal{L}_{ILC}$	$\mathcal{L}_{CLIC}$	B1: σ	B2: σ	B3: σ
0.250	-	0.25	—	0	0	0
0.350	2.6	—	0.5	0	0	1.7×10^{-5}
0.500	-	0.5	—	3.1×10^{-6}	0	2.5×10^{-2}
1.0	-	1	—	1.4×10^{3}	0.9	3.7×10^{3}
1.4	-	—	1.5	1.1×10^{4}	3.6	4.1×10^{3}
3	-	—	2	6.1×10^{3}	3.5×10^{-2}	2.0×10^{3}

Table 9.5: Production cross-section (in units of ab) for h_2 at an e^+e^- collider for projected energies in the 3 benchmarks. Estimated integrated luminosities are also given in units of ab^{-1} [3].
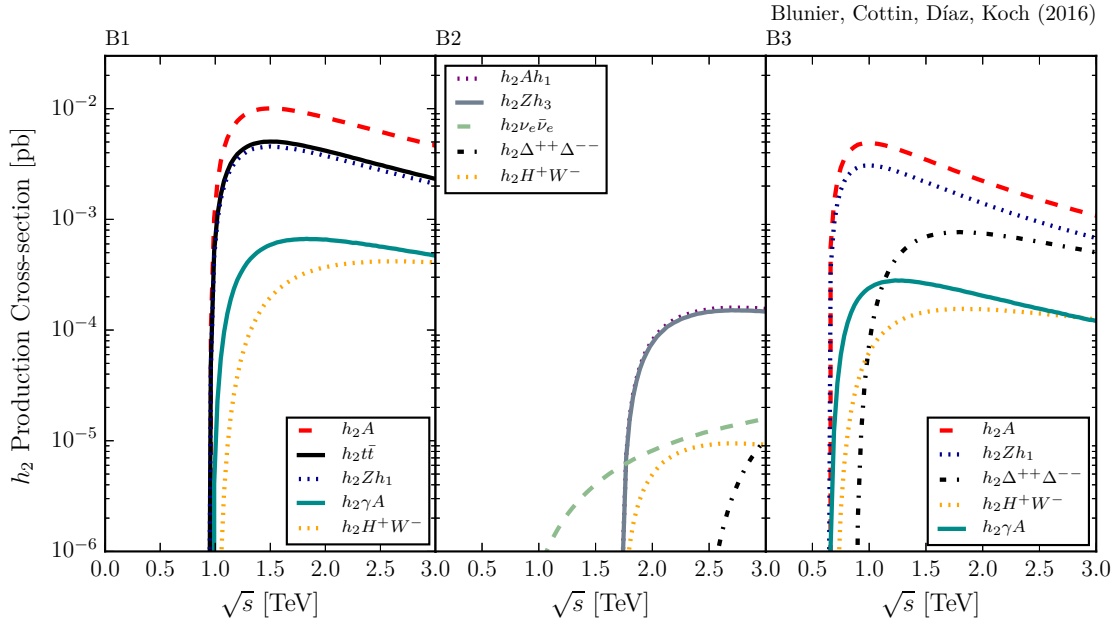
Figure 9.2: Production modes for h_2 at an e^+e^- collider in the 3 benchmarks. The legend shows the final state after the e^+e^- collision [3].

sections shown in Table 9.5 are dominated by the 2-body production process (or mode) $e^+e^- \to h_2 A$ and by 3-body production processes as follows.

In B1 the process $e^+e^- \to h_2 t\bar{t}$ is the most important one. In B2 the dominating process is $e^+e^- \to h_2 A h_1$. In B3 the process $e^+e^- \to h_2 Z h_1$ is dominant. All of them are enhanced when a second heavy particle is also on-shell. We show in Fig. 9.2 the main h_2 production modes for all 3 benchmarks. In B1 (left frame) this particle is

potentially observed at CLIC only when the A scalar is also on-shell. Thus, the main 2-body production mode is the so-called associated production,
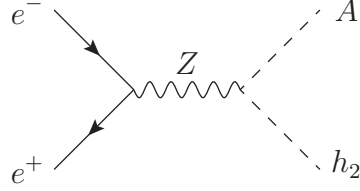
defined when h_2 is produced together with an A. The coupling ZAh_2 is given in Appendix A.2. Since A is mainly triplet, O_φ^{33} is of order 1. In addition, in B1 h_2 is mainly triplet, thus O_χ^{23} is also of order 1. Therefore, the whole coupling ZAh_2 is not suppressed with respect to the gauge coupling g.

The most important 3-body production modes in B1 are also displayed in the left frame of Fig. 9.2. The main production process is $h_2 t\bar{t}$ when A is on-shell. Diagramatically it looks like
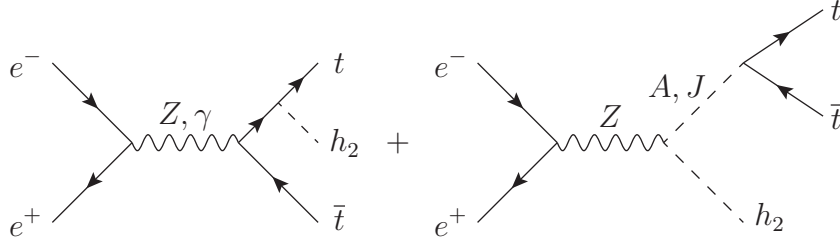
plus a similar graph with h_2 emitted from the anti-quark and another graph with the A boson being replaced by a Z boson. This production process is enhanced when the A scalar boson is on-shell, $e^+ e^- \to h_2 A \to h_2 t\bar{t}$, corroborated by the fact that $B(A \to t\bar{t}) = 0.5$ is large for B1, as shown in Table 9.9.

In the central frame of Fig. 9.2 we see B2. In this case, production cross-sections are systematically smaller because in this benchmark h_2 is mainly singlet and couplings to gauge bosons are smaller. Also the main production modes are different. The process $e^+ e^- \to h_2 t\bar{t}$ is no longer efficient, with a cross-section of the order of 10^{-8} pb and outside of the plot. The reason is that the coupling Zh_2A is small when h_2 is mainly singlet. The main production mode for B2 is $e^+ e^- \to h_2 A h_1$, with Feynman diagrams for the sub-processes given by
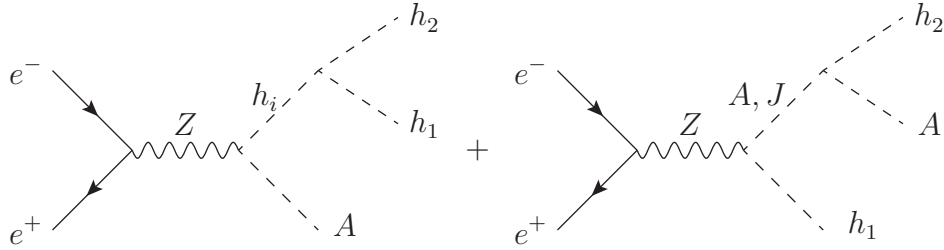
plus Feynman diagrams where in the last sub-process we replace (A, J) by Z and/or interchange h_1 with h_2. This mode is enhanced when h_3 is on-shell, since in B2 h_3 is mainly triplet and the coupling ZAh_3 is large resulting in $e^+e^- \to h_3A \to h_2h_1A$.

B3 is an intermediate situation. Even in this case, h_2 production cross-sections are potentially observable when A is also on-shell. The production cross-section $e^+e^- \to h_2A$ is smaller than in B1, but still large. The main 3-body production mode in this case is $e^+e^- \to h_2Zh_1$, with sub-processes given by
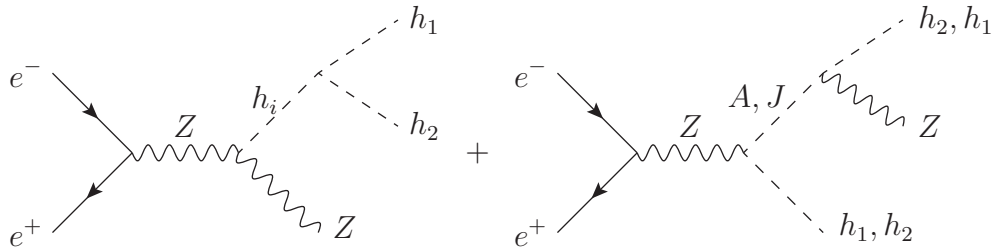
where $i = 1, 2, 3$, and missing are a graph with the $CP-$odd scalar replaced by a Z and one formed with a ZZh_1h_2 quartic coupling. This production mode is enhanced when the A boson is on-shell, $e^+e^- \to h_2A \to h_2h_1Z$, with a branching fraction $B(A \to h_1Z) = 0.9$ as shown in Table 9.9.

Fig. 9.3 shows a scan for the production mode $e^+e^- \to h_2t\bar{t}$ (left frame) and $e^+e^- \to h_2h_1A$ (right frame), two of the important 3-body h_2 production modes. In the case of $e^+e^- \to h_2t\bar{t}$, the production cross-section reaches up to 0.01 pb. The largest cross-sections are seen when h_2 is mainly triplet (black triangular points), with a typical value between 0.001 and 0.01 pb. B1 is shown as a black solid curve. The value of the cross-section drops when h_2 is mainly singlet (orange star points), with values typically smaller than 10^{-4} pb. This is because a singlet does not couple to the Z gauge boson.
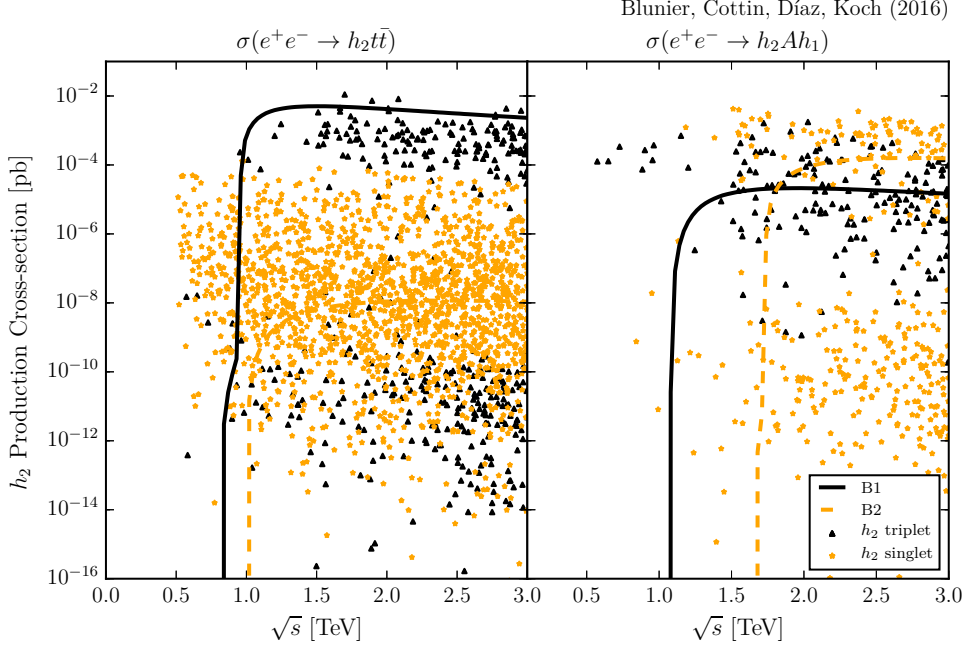
Figure 9.3: Production modes $e^+e^- \to h_2 t\bar{t}$ and $e^+e^- \to h_2 h_1 A$. All parameters are varied according to the scanned range in Table 9.2 for a value of $\sqrt{s}$ which is also scanned randomly between m_{h_1} and 3 TeV [3].

The chosen B2 lies within the cloud of points. The case where h_2 is mixed is much more rare and no point has been generated in this scenario due to its fine-tuned character.

The case of $e^+e^- \to h_2 A h_1$ is shown in the right frame of Fig. 9.3. This is the main process in B2, where h_2 is mainly singlet (orange star points). In this case, cross-sections can reach up to 10^{-3} pb, but can also be as low as 10^{-14} pb, depending on whether h_3 is on-shell or not. In the case where h_2 is mainly triplet (black triangular points) the cross-section is more restricted. It can vary between 10^{-3} and 10^{-8} pb and B1 is a very typical case. Cross-sections are larger when an intermediate heavy scalar is also on-shell.

Notice that the favored modes for the production of a SM-like Higgs boson in a e^+e^- collider, known collectively as vector boson fusion, $e^+e^- \to h_2 e^+e^-$ (fusion of two Z bosons) or $e^+e^- \to h_2 \nu_e \bar{\nu}_e$ (fusion of two W bosons) do not work in our case because the h_2 couplings to vector bosons are suppressed by the triplet vev v_Δ. In addition, most of the charged leptons go through the beam pipe, thus $\sigma(e^+e^- \to h_2 e^+e^-)$ is further penalized when a cut on the charged lepton pseudo-rapidity is imposed. We use MADGRAPH5 default cuts, which impose that the absolute value of the charged lepton pseudo-rapidity is smaller than 2.5.

$\sqrt{s}$ [TeV]	$\mathcal{L}_{FCCee}$	$\mathcal{L}_{ILC}$	$\mathcal{L}_{CLIC}$	B1: σ	B2: σ	B3: σ
0.250	-	0.25	−	0	0	0
0.350	2.6	−	0.5	0	0	1.4×10^{-10}
0.500	-	0.5	−	1.5×10^{-12}	0	1.5×10^{-2}
1.0	-	1	−	1.4×10^{3}	2.2×10^{-5}	2.5×10^{4}
1.4	-	−	1.5	1.1×10^{4}	3.5×10^{-3}	2.1×10^{4}
3	-	−	2	6.2×10^{3}	3.6×10^{3}	7.5×10^{3}

Table 9.6: Production cross-section (in units of ab) for A at an e^+e^- collider for projected energies in the 3 benchmarks. Estimated integrated luminosities are also given in units of ab^{-1} [3].

9.3.2 A production

Table 9.6 shows A production at e^+e^- colliders, expected luminosities and CM energies for the FCC-ee, ILC and CLIC colliders. The cross-sections are calculated in the same manner explained before. In B1 and B2 the dominating process is $e^+e^- \to AZZ$, and in B3 the dominating process is $e^+e^- \to AJJ$, and all of them are enhanced when a second heavy particle is also on-shell.

Fig. 9.4 shows the production cross-sections for an A boson. In B1 (left frame) A is potentially observable at CLIC when produced in association with an h_2. In this case the mode $e^+e^- \to Ah_1$ is suppressed because O_φ^{32} and O_χ^{13} are both small (see Feynman rule in Appendix A.2), thus the coupling $h_1 AZ$ itself is suppressed with respect to g. Three body production modes are also in Fig. 9.4. The dominant 3-body production mode in B1 is $e^+e^- \to AZZ$, represented by the Feynman diagrams
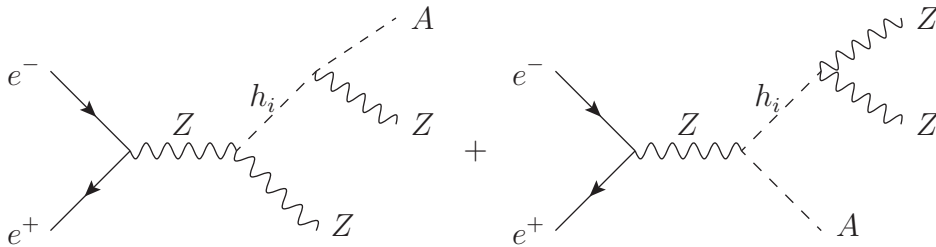
It is enhanced when h_2 is on-shell, with a branching fraction $B(h_2 \to ZZ) = 0.6$, as indicated in Table 9.8. As explained later in the decay Section, the coupling $h_2 ZZ$ is large if h_2 is mainly triplet (B1).
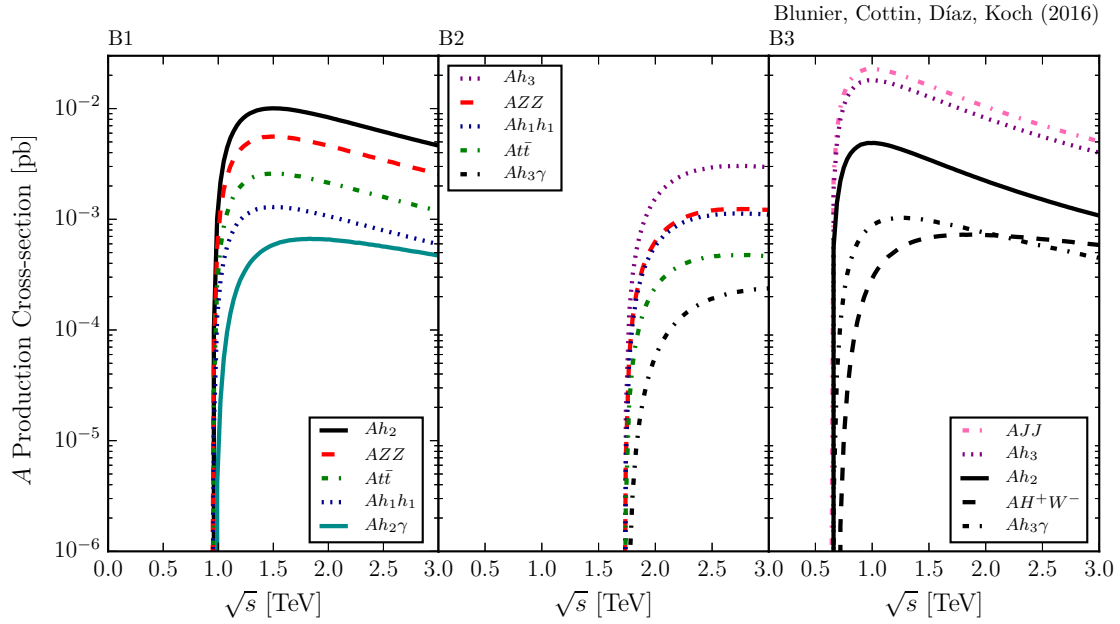
Figure 9.4: Production modes for A at an e^+e^- collider in all 3 benchmarks. The legend shows the final state after the e^+e^- collision [3].

In B2 the $CP-$even Higgs boson created in association with A is no longer h_2 but h_3. If h_2 is mainly singlet, h_3 is mainly triplet, and the coupling ZAh_3 is not suppressed. This is confirmed in the central frame of Fig. 9.4 where we have B2. The most important 2-body production mode is precisely $e^+e^- \to Ah_3$, represented by the Feynman diagram
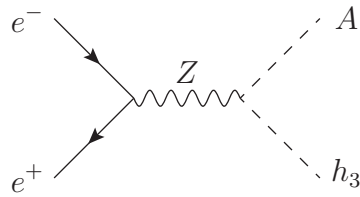
Also in the central frame of Fig. 9.4 we see the main 3-body A production modes. The most important one is again $e^+e^- \to AZZ$, and it is enhanced when h_3 is on-shell.

B3 is an intermediate case, and we can see in the right frame of Fig. 9.4 that the two 2-body production modes $e^+e^- \to Ah_2$ and $e^+e^- \to Ah_3$ are important since both h_2 and h_3 have a large triplet component. Among the 3-body production modes, the largest one is $e^+e^- \to AJJ$,
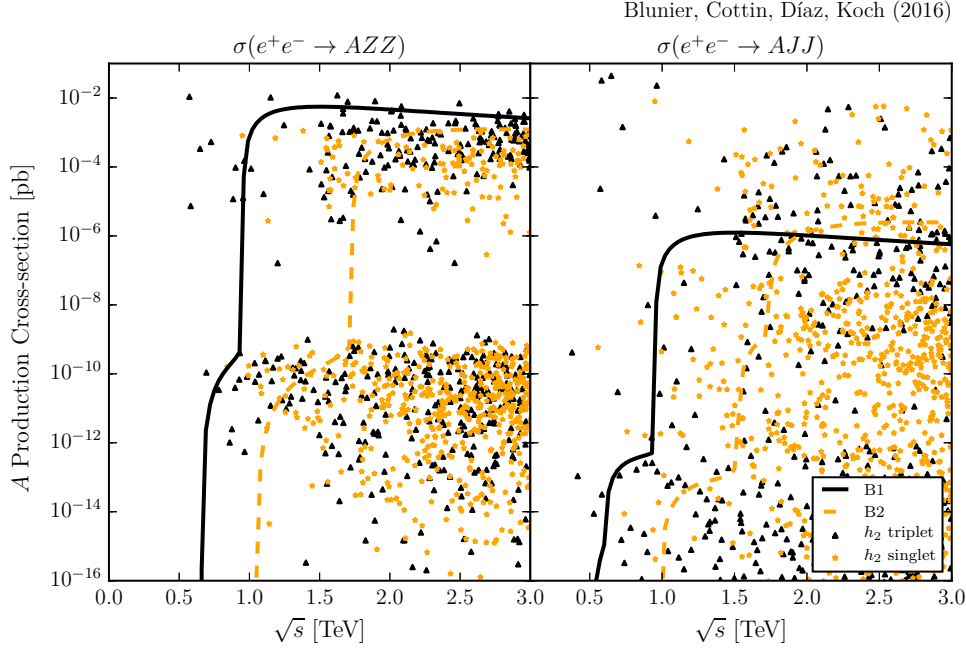
Figure 9.5: Production modes $e^+e^- \to AZZ$ and $e^+e^- \to AJJ$. All parameters are varied according to the scanned range in Table 9.2 for a value of $\sqrt{s}$ which is also scanned randomly between m_{h_1} and 3 TeV [3].
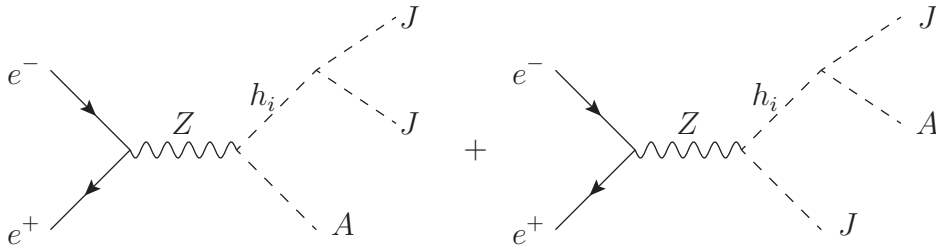
and it is enhanced when h_2 and h_3 are on-shell.

Fig. 9.5 shows scans for the process $e^+e^- \to AZZ$ (left frame), important for B1 and B2, and the process $e^+e^- \to AJJ$ (right frame), important in B3. In the first case, the production cross-section is increased when h_2 is also on-shell, as explained before. The cross-section is not larger than 0.01 pb, and B1 is not far below from that value. In the last process a triple scalar coupling is important, and the exact values of the parameters in the potential are crucial. In this case, B3 is characterized by a large value of β_3 which

$\sqrt{s}$ [TeV]	$\mathcal{L}_{FCCee}$	$\mathcal{L}_{ILC}$	$\mathcal{L}_{CLIC}$	B1: σ	B2: σ	B3: σ
0.250	-	0.25	—	0	0	0
0.350	2.6	—	0.5	0	0	5.8×10^{-3}
0.500	-	0.5	—	1.9×10^{-4}	0	0.5
1.0	-	1	—	1.6×10^{3}	4.1×10^{-3}	1.7×10^{4}
1.4	-	—	1.5	7.0×10^{3}	3.5×10^{-2}	1.5×10^{4}
3	-	—	2	5.0×10^{3}	2.4×10^{3}	6.6×10^{3}

Table 9.7: Production cross-section (in units of ab) for H^+ at an e^+e^- collider for projected energies in the 3 benchmarks. Estimated integrated luminosities are also given in units of ab^{-1} [3].

increases the coupling h_3JJ. As before, in Fig. 9.5 we include the curves corresponding to each benchmark to facilitate comparisons.

9.3.3 $H^{\pm}$ production

Table 9.7 shows H^+ production cross-sections at e^+e^- colliders, expected luminosities and CM energies for the FCC-ee, ILC and CLIC colliders. Besides the 2-body production cross-section for $e^+e^- \to H^+H^-$, in B1 and B2 the 3-body process $e^+e^- \to H^+h_1W^-$ dominates. In B3 the process $e^+e^- \to H^+W^+\Delta^{--}$ dominates. The last case presents a high interest, as the doubly charged Higgs boson gives us an independent window to study neutrinos.

Fig. 9.6 shows the 2-body and 3-body production of an H^+ boson. The charged Higgs boson is potentially observable at CLIC when produced in association with another H^-, represented by the graph
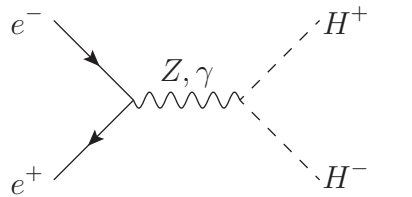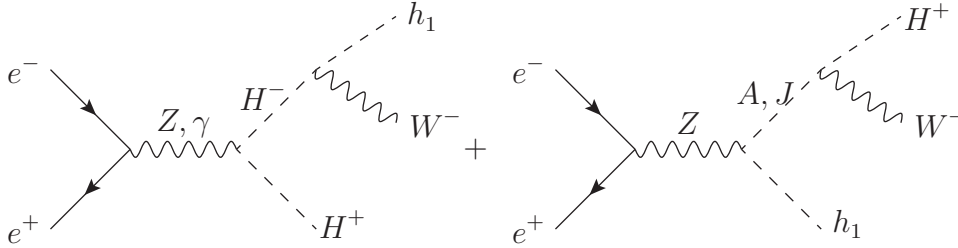

The couplings $H^+H^-\gamma$ and H^+H^-Z are both of the order of electroweak couplings, as can be seen in Appendix A.2. Among the 3-body modes, in B1 and B2 the main
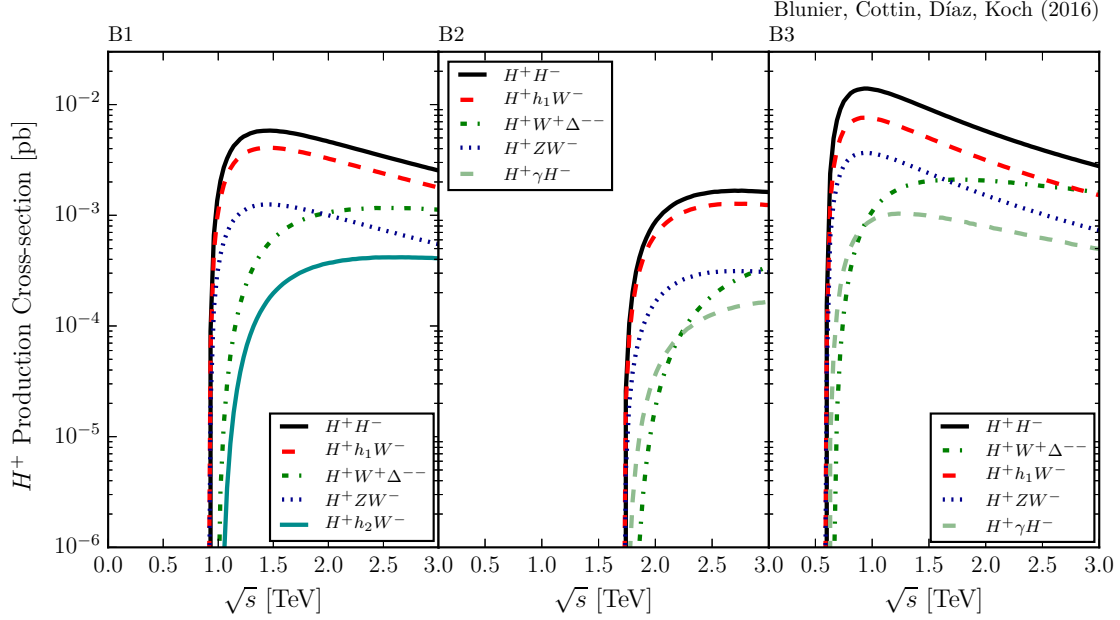
Figure 9.6: Production modes for H^+ at an e^+e^- collider in all 3 benchmarks. The legend shows the final state after the e^+e^- collision [3].

production mode is $e^+e^- \to H^+h_1W^-$, represented by the sub-processes,

plus a graph where the intermediate charged Higgs is replaced by a W and removing the intermediate photon, graphs where the external charged Higgs and the W are interchanged (also removing the photon), a graph where (A, J) is replaced by a Z, graphs that involve quartic couplings, and a graph with a neutrino in the t−channel. This mode is dominated by the graph where the charged Higgs is on-shell. Note that the coupling ZH^+W^- is suppressed by the triplet vev. This mode is enhanced when H^- is also on-shell, corroborated by the fact that $B(H^- \to h_1W^-) = 0.8$ in B2.

Similarly, in Fig. 9.6 we see that the mode $e^+e^- \to H^+W^+\Delta^{--}$ dominates in B3. It is represented by
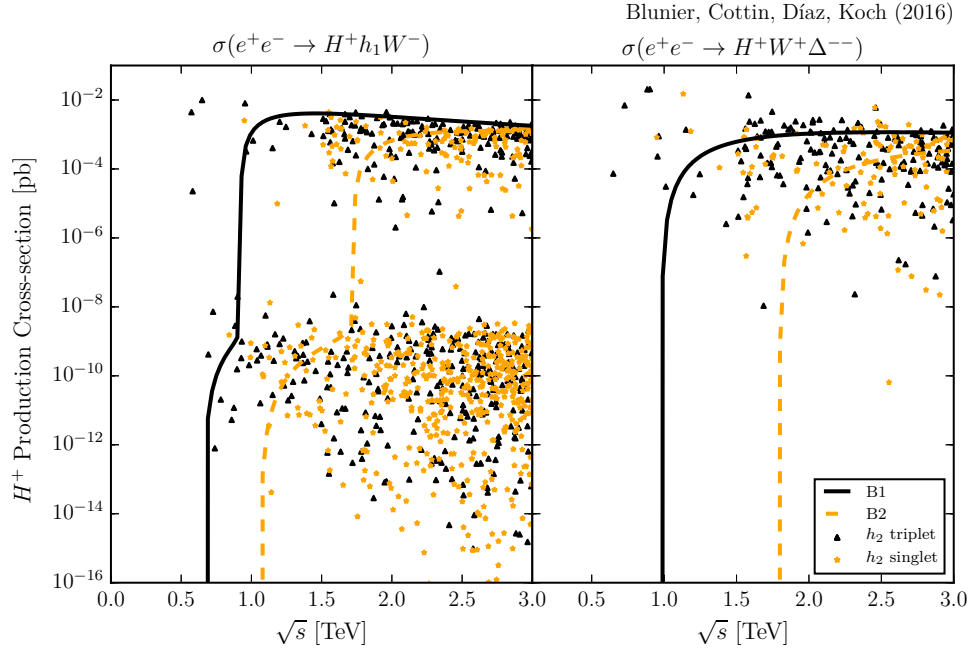
Figure 9.7: Production modes $e^+e^- \rightarrow H^+h_1W^-$ and $e^+e^- \rightarrow H^+W^+\Delta^{--}$. All parameters are varied according to the scanned range in Table 9.2 for a value of $\sqrt{s}$ which is also scanned randomly between m_{h_1} and 3 TeV [3].
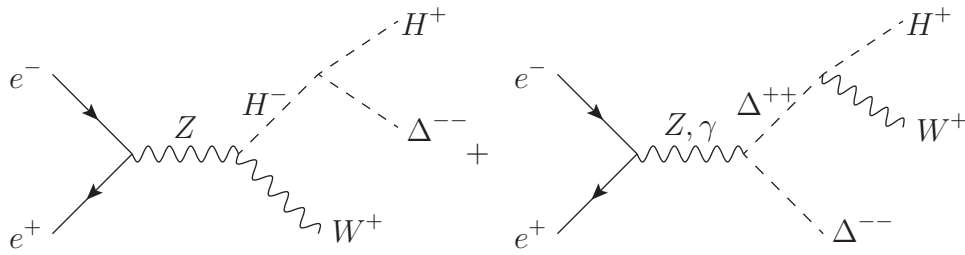
plus a graph where the external particles H^+ and Δ^{--} are interchanged and at the same time the intermediate Δ^{++} is replaced by H^-, plus two graphs where the H^- is replaced by a W^- with Z exchanged for a photon, and two graphs with quartic couplings. As it was mentioned before, the production of a Δ^{++} is important because it could lead to the observation of its decay into two charged leptons, which could probe the mechanism for neutrino masses.

Fig. 9.7 shows a general scan for the 3-body production modes $e^+e^- \rightarrow H^+h_1W^-$ (left frame) and $e^+e^- \rightarrow H^+W^+\Delta^{--}$ (right frame). For the case $e^+e^- \rightarrow H^+h_1W^-$, the majority of the scenarios give a cross-section between 10^{-2} and 10^{-4} pb, as long

as a second heavy particle is also on-shell. In the case of $e^+e^- \to H^+W^+\Delta^{--}$, the cross-section is of the same order between 10^{-3} and 10^{-5} pb, also independent of the composition of h_2. If neutrinos acquire their mass via a coupling to the triplet, the mechanism can be probed through the production of a double charged Higgs boson.

9.4 Decay branching fractions

In this Section, we study the decay modes of the SM-like Higgs boson h_1, the next-to heaviest Higgs h_2, the $CP-$odd Higgs A, and the charged Higgs H^+. For the computation of branching fractions, we consider $B = \Gamma(H \to (XX)_i)/\sum_i \Gamma(H \to (XX)_i)$, with $H = h_1, h_2, A, H^\pm$. For the $CP-$even Higgses we have $XX = \tau\bar{\tau}, b\bar{b}, WW, ZZ, \gamma\gamma, Z\gamma, gg, JJ, JZ$ for h_1 and we include $t\bar{t}$ and $h_1 h_1$ to the previous list for h_2. For A we consider $XX = \tau\bar{\tau}, b\bar{b}, t\bar{t}, h_i Z, h_i J, \gamma\gamma, Z\gamma, gg$, with $i = 1, 2$. For $H^\pm$, we have $XX = t\bar{b}, h_i W^\pm, JW^\pm, ZW^\pm$, with $i = 1, 2$.

We define

$$\lambda(a, b, c) = a^2 + b^2 + c^2 - 2ab - 2ac - 2bc. \tag{9.5}$$

In the special case $b = c$, it is reduced to the function β,

$$\beta(b/a) = \frac{1}{a}\lambda^{1/2}(a, b, b) = \sqrt{1 - 4\frac{b}{a}}. \tag{9.6}$$

9.4.1 h_1 and h_2 Decays

We first mention the decay modes to fermions for h_i ($i = 1, 2$), which include $h_i \to b\bar{b}$ and $h_i \to \tau\bar{\tau}$. The decay $h_2 \to t\bar{t}$ is considered for h_2, but not for h_1. The corresponding Feynman diagram is
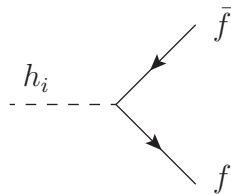
with Feynman rule given in Appendix A.2.

The decay widths are given by

$$\Gamma(h_i \to f\bar{f}) = \frac{N_c m_{h_i}}{8\pi} \beta^3 (m_f^2 / m_{h_i}^2) |\lambda_{h_i ff}|^2, \tag{9.7}$$

where the number of colors is $N_c = 3$ for quarks and $N_c = 1$ for leptons. We define the coupling $\lambda_{h_i ff} = O_\chi^{i2} h_f / \sqrt{2}$, where h_f corresponds to the respective Yukawa coupling in the convention $m_f = h_f v_\phi / \sqrt{2}$.

Since h_1 is always mainly doublet and h_2 is not, decay rates of h_1 to fermions are consistently larger than decay rates of h_2 to fermions. Similarly, since the h_2 component to doublet is larger in B2 compared to B1 and B3, the corresponding decay rate is larger too.

Also important are the vector boson decays $h_i \to W^+ W^-$, $h_i \to ZZ$, with Feynman diagram
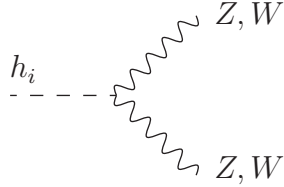
The decay rate where both gauge bosons are on-shell is

$$\Gamma(h_i \to VV) = \frac{m_{h_i}^3 \delta_V'}{128\pi m_V^4} \left[1 - \frac{4m_V^2}{m_{h_i}^2} + \frac{12m_V^4}{m_{h_i}^4} \right] \beta(m_V^2 / m_{h_i}^2) |M_{h_i VV}|^2, \tag{9.8}$$

with $V = Z, W$, $\delta_W' = 2$ and $\delta_Z' = 1$. The decay rate where one vector boson is off-shell is

$$\Gamma(h_i \to VV^*) = \frac{3g_V^2 m_{h_i} \delta_V}{512\pi^3 m_V^2} F(m_V / m_{h_i}) |M_{h_i VV}|^2, \tag{9.9}$$

with $g_W = g$, $g_Z = g/c_W$, $\delta_W = 1$, and $\delta_Z = \frac{7}{12} - \frac{10}{9} s_W^2 + \frac{40}{27} s_W^4$, where s_W and c_W are the sine and cosine of the Weinberg angle. The F function is defined in [246]. The relevant

couplings (with units of mass) can be read from Appendix A.2, from where we define

$$M_{h_i WW} = \frac{1}{2}g^2(O_\chi^{i2}v_\phi + 2O_\chi^{i3}v_\Delta),\tag{9.10}$$

$$M_{h_i ZZ} = \frac{1}{2}(g^2 + g'^2)(O_\chi^{i2}v_\phi + 4O_\chi^{i3}v_\Delta),\tag{9.11}$$

and use them in eq. (9.8) and eq. (9.9). In the case of h_2, since the penalization due to vev is already large ($v_\Delta/v_\phi \sim 10^{-3}$ for our benchmarks), the h_2 component to doublet becomes important. Thus, the couplings $h_2 VV$ are larger for B2, and in turn the decay rate (and branching fractions).

The decay to $\gamma\gamma$ is given by [232, 247],

$$\Gamma(h_i \to \gamma\gamma) = \frac{\alpha^2 g^2}{1024\pi^3}\frac{m_{h_i}^3}{m_W^2}\left| F_0(\tau_{H^+}^i)\frac{m_W}{m_{H_+}^2}M_{h_i H^+ H^-} + 4F_0(\tau_\Delta^i)\frac{m_W}{m_{\Delta^{++}}^2}M_{h_i \Delta^{++}\Delta^{--}} \right.$$
$$\left. + F_1(\tau_W^i)\frac{1}{m_W}M_{h_i WW} + \frac{4\sqrt{2}}{3h_t}F_{1/2}(\tau_t^i)\lambda_{h_i tt} \right|^2,\tag{9.12}$$

where the couplings $M_{h_i H^+ H^-}$ (in our convention $H^+ \equiv h_2^+$), $M_{h_i \Delta^{++}\Delta^{--}}$, and $M_{h_i WW}$ are defined in Appendix A.2 and in eq. (9.10). In eq. (9.12) we have defined $\tau_a^i = 4m_a^2/m_{h_i}^2$ where $a = H^+, \Delta, W$. The F_0, F_1 and $F_{1/2}$ functions are defined in [246].

The decay to $Z\gamma$ is given by [232, 247]

$$\Gamma(h_i \to Z\gamma) = \frac{\alpha g^2}{2048\pi^4 m_W^4}|A|^2 m_{h_i}^3 (1 - \frac{m_Z^2}{m_{h_i}^2})^3,\tag{9.13}$$

where A is defined as

$$A = A_W + A_t + A_0^{H+} + 2A_0^{\Delta^{++}},\tag{9.14}$$

with

$$A_W + A_t = c_W M_{h_i WW} A_1(\tau_W, \lambda_W) + \frac{gm_W}{c_W}N_c Q_t(1 - 4Q_t s_W^2)\lambda_{h_i tt} A_{1/2}(\tau_t, \lambda_t)$$

$$A_0^{H^+} = \frac{m_W^2}{gs_W m_{H^+}^2}\lambda_{ZH^+ H^-} M_{h_i H^+ H^-} A_0(\tau_{H^+}, \lambda_{H^+})$$

$$A_0^{\Delta^{++}} = \frac{m_W^2}{gs_W m_{\Delta^{++}}^2}\lambda_{Z\Delta^{++}\Delta^{--}} M_{h_i \Delta^{++}\Delta^{--}} A_0(\tau_{\Delta^{++}}, \lambda_{\Delta^{++}}),\tag{9.15}$$

where

$$
\begin{aligned}
\lambda_{ZH^+H^-} &= -\frac{g}{2c_W}(s_\beta^2 - 2s_W^2), \\
\lambda_{Z\Delta^{++}\Delta^{--}} &= -\frac{g}{c_W}(c_W^2 - s_W^2),
\end{aligned}
\tag{9.16}
$$

as can be seen from Appendix A.2. The loop functions are,

$$
\begin{aligned}
A_0(\tau, \lambda) &= I_1(\tau, \lambda), \\
A_1(\tau, \lambda) &= 4(3 - \tan^2\theta_W)I_2(\tau, \lambda) + [(1 + 2/\tau)\tan^2\theta_W - (5 + 2/\tau)]I_1(\tau, \lambda), \\
A_{1/2}(\tau, \lambda) &= I_1(\tau, \lambda) - I_2(\tau, \lambda),
\end{aligned}
\tag{9.17}
$$

with $\tau_b = \frac{4m_b^2}{m_{h_i}^2}$, $\lambda_b = \frac{4m_b^2}{m_Z^2}$, $b = t, W, H^+, \Delta^{++}$, and the parametric integrals I_1, I_2 are specified in [246].

We also consider the 1-loop decay to gg for completeness. It is given by [246]

$$
\Gamma(h_i \to gg) = \frac{\alpha_s^2 g^2 m_{h_i}^3}{128\pi^3 m_W^2}\left|\frac{4\sqrt{2}}{3h_t}F_{1/2}(\tau_t^i)\lambda_{h_itt}\right|^2
\tag{9.18}
$$

with the $F_{1/2}$ given in Appendix C of [246].

The decay to Majorons $h_i \to JJ$ and $h_i \to JZ$ proceeds with a negligible Majoron mass. The decay rates are given by

$$
\Gamma(h_i \to JZ) = \frac{m_{h_i}^3}{16\pi m_Z^2}|\lambda_{Zh_iJ}|^2\left(1 - \frac{m_Z^2}{m_{h_i}^2}\right)^3
\tag{9.19}
$$
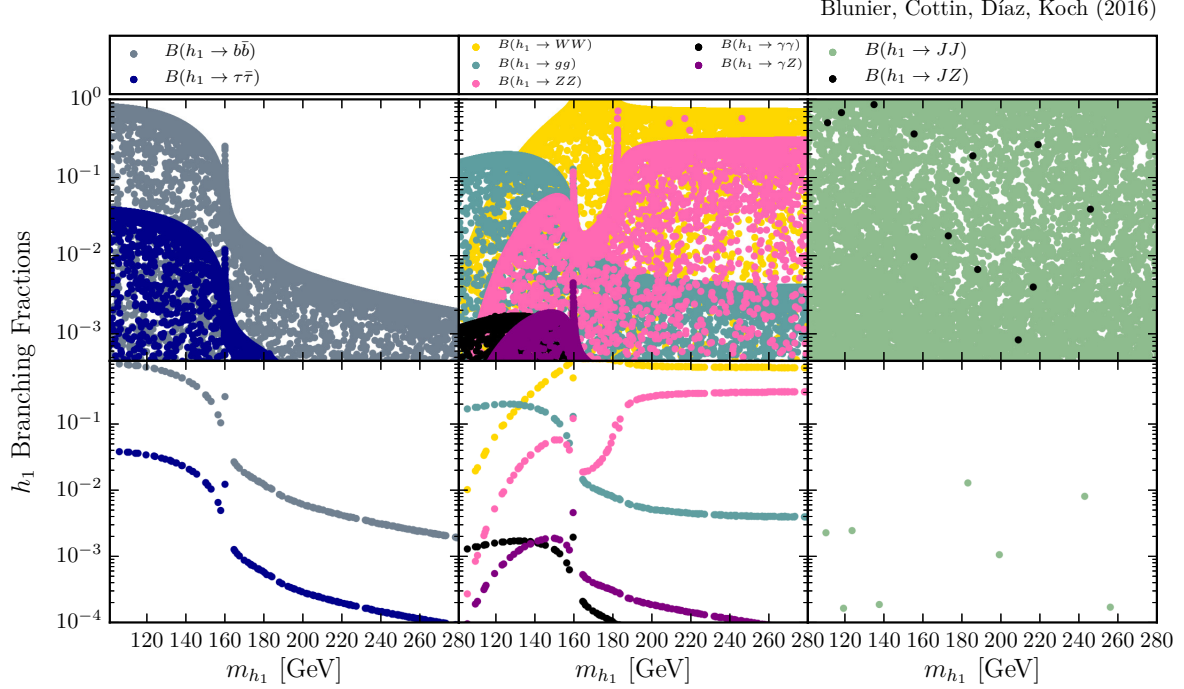
and

$$
\Gamma(h_i \to JJ) = \frac{|M_{h_iJJ}|^2}{32\pi m_{h_i}},
\tag{9.20}
$$

with

$$
\lambda_{Zh_iJ} = \frac{g}{2c_W}(O_\chi^{i2}O_\varphi^{22} - 2O_\chi^{i3}O_\varphi^{23}).
\tag{9.21}
$$

M_{h_iJJ} is defined from the corresponding Feynman rule in Appendix A.2.

Figure 9.8: Branching fractions for the h_1 scalar with (bottom) and without (top) restrictions, as explained in the text [3].

Finally, the decay $h_2 \rightarrow h_1 h_1$ is given by

$$\Gamma(h_2 \rightarrow h_1 h_1) = \frac{\beta(m_{h_1}^2/m_{h_2}^2)}{32\pi m_{h_2}} |M_{h_2 h_1 h_1}|^2, \tag{9.22}$$

where $M_{h_2 h_1 h_1}$ is defined from the corresponding Feynman rule in Appendix A.2.

In the case of h_1 we require that its mass is ≈ 125 GeV and that it is mostly doublet. Besides the usual decay modes for this SM-like Higgs boson, in this model there are two more. These are $h_1 \rightarrow JJ$ and $h_1 \rightarrow JZ$. For the three benchmarks, the branching fractions are $\mathrm{B}(h_1 \rightarrow JJ) \approx 3 \times 10^{-5}$ and $\mathrm{B}(h_1 \rightarrow JZ) \approx 3 \times 10^{-13}$. We are well within experimental constraints on the Higgs invisible width, as branching fractions bigger than 22% are excluded at 95% CL [238]. These modes are suppressed due to two different reasons. The mode $h_1 \rightarrow JZ$ is suppressed because the Majoron J is mostly singlet. The decay mode $h_1 \rightarrow JJ$ is suppressed because in addition we require a small value for β_2.

Fig. 9.8 shows the branching fractions of our light Higgs h_1. In the top frame we scan the parameters without any restriction, varying λ_1 between $[0, 4]$, in order not to constrain the Higgs mass, as we need to make sure the points in the plot are consistent with a

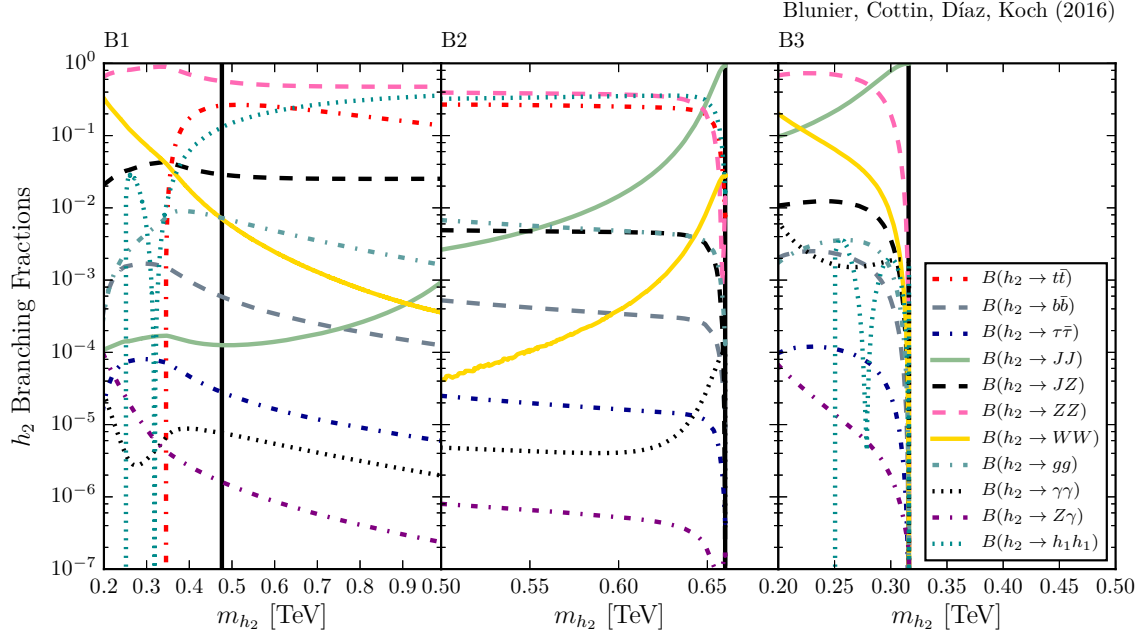| Branching Fraction	B1	B2	B3
$\text{B}(h_2 \to t\bar{t})$	0.3	7.9×10^{-3}	-
$\text{B}(h_2 \to b\bar{b})$	6.0×10^{-4}	9.5×10^{-6}	3.4×10^{-7}
$\text{B}(h_2 \to \tau\tau)$	3.0×10^{-5}	4.5×10^{-7}	1.6×10^{-8}
$\text{B}(h_2 \to WW)$	7.0×10^{-3}	3.0×10^{-2}	3.6×10^{-6}
$\text{B}(h_2 \to ZZ)$	0.6	1.0×10^{-2}	1.3×10^{-4}
$\text{B}(h_2 \to gg)$	7.2×10^{-3}	1.3×10^{-4}	1.0×10^{-6}
$\text{B}(h_2 \to \gamma\gamma)$	7.7×10^{-6}	2.9×10^{-5}	1.8×10^{-3}
$\text{B}(h_2 \to Z\gamma)$	1.6×10^{-6}	1.6×10^{-7}	1.9×10^{-7}
$\text{B}(h_2 \to JJ)$	1.2×10^{-4}	0.9	0.9
$\text{B}(h_2 \to JZ)$	3.0×10^{-2}	3.6×10^{-12}	2.5×10^{-6}
$\text{B}(h_2 \to h_1 h_1)$	0.1	1.7×10^{-2}	1.0×10^{-6}

Table 9.8: Branching fractions for h_2 in the three different benchmarks [3].

SM-like Higgs. Is also useful to keep the mass free to observe the effect of the constraints and to facilitate the comparison with h_2. On the top frame β_2 is not constrained and varies between [-4, 4] so we can clearly see the suppression in the Majoron decays once we constrain its value in the bottom frame. The bottom frame includes all constraints from Section 9.1.

The branching fractions in our three benchmarks for h_2 are given in Table 9.8. We mention first that h_2 has a larger doublet component in B2, and for that reason decay rates to fermions are larger in that benchmark. Nevertheless, this fact is obscured in branching fractions because the total decay rate is also very different. Similarly, decay rates to gauge bosons are larger in B2, but not necessarily the same is true at the level of branching fractions. Clearly, looking at branching fractions, decays of h_2 to two Majorons (invisible decay) dominate in B2 and B3 because h_2 has a large singlet component in those two benchmarks.
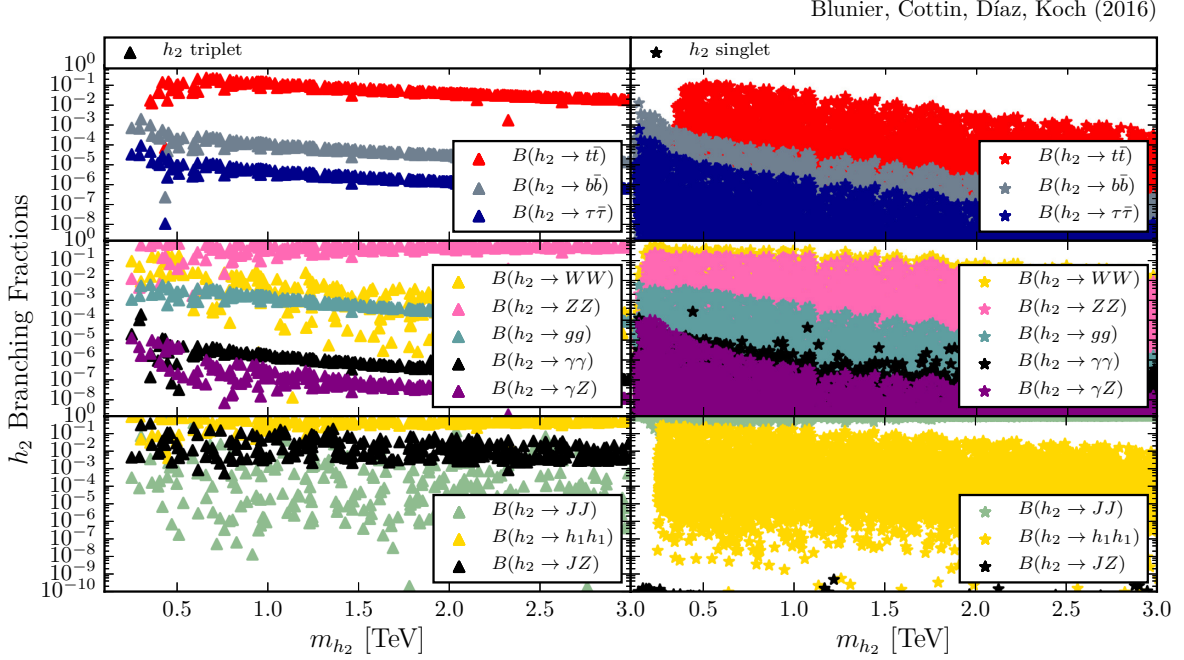
Fig. 9.9 shows the branching fractions as a function of the scalar mass m_{h_2}, evolving from our three benchmarks, while Fig. 9.10 shows a scan of the h_2 decays, with all the constraints from Section 9.1 implemented.

The curves shown in Fig. 9.9 confirms the previous observations. These curves are found by keeping the values of the independent parameters as in the 3 different benchmarks, and varying the value of κ in order to keep m_{h_2} free. Since due to mixing this

Figure 9.9: Branching fractions for the h_2 scalar in the three benchmarks as a function of m_{h_2}. The parameter κ is varied to move m_{h_2}, as explained in the text. The vertical solid line in each frame corresponds to our benchmark point. The plot includes all constraints from Section 9.1 [3].

procedure will also vary the value of $m_{h_1} \approx 125$ GeV, we keep λ_1 also free to compensate, as in Table 9.2. We show also as a vertical solid line the value of m_{h_2} in the corresponding benchmark. In the case of B2, near the vertical line h_2 is mainly singlet, and κ affects very little to m_{h_2}. If κ is sufficiently different from its starting value in B2 h_2 becomes mostly triplet. The value for m_{h_2} cannot be larger than its value in the benchmark because by then h_2 is mostly singlet and κ has little effect. Something similar happens with B3. In all cases $h_2 \to ZZ$ and $h_2 \to WW$ are important. Decays to fermions depend strongly on the (small) h_2 component to doublet. In the scan in Fig. 9.10, we plot h_2 branching fractions while all the parameters are varied according to Table 9.2. We see that the values of the branching fractions separates in two regions, that we plot separately in the two column plot. These two sectors corresponds to a mainly triplet (left column) or mainly singlet (right column) h_2. The scan shows that if h_2 is mainly triplet (as in B1) decay modes $h_2 \to ZZ$ and $h_2 \to h_1 h_1$ can dominate, with $h_2 \to JZ$ sometimes also important. On the contrary, if h_2 is mainly singlet (as in B2) the decay mode $h_2 \to JJ$ dominates by far, with $h_2 \to WW$ and $h_2 \to ZZ$ following in importance. The $h_2 \to t\bar{t}$ branching fractions can be large as long as the other decay rates are also small.

Figure 9.10: Branching fractions for the h_2 scalar as a function of m_{h_2}. The left column shows points where h_2 is triplet-like (i.e $|O_\chi^{23}| > 0.95$). The right column shows points where h_2 is singlet-like (i.e $|O_\chi^{21}| > 0.95$). Parameters are varied according to Table 9.2. The scan includes all constraints from Section 9.1 [3].

9.4.2 *A* Decays

Now we study the decays of the $CP-$odd Higgs boson A. The relevant decays at tree-level are to third generation fermions, $A \to t\bar{t}, A \to b\bar{b}, A \to \tau\tau$, to $CP-$even Higgs bosons and a Majoron, $A \to h_i J$, and to $CP-$even Higgs bosons and a Z gauge boson, $A \to h_i Z$. We also consider the 1-loop decays to $\gamma\gamma$, $Z\gamma$ and gg for completeness.

The decay of A to fermions, represented by the Feynman diagram
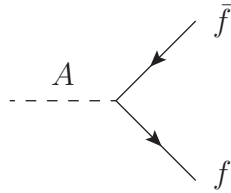
is given by

$$\Gamma(A \to f\bar{f}) = \frac{N_c m_A}{8\pi} \left[1 - 4\frac{m_f^2}{m_A^2} \right]^{\frac{1}{2}} |\lambda_{Aff}|^2, \tag{9.23}$$

with a coupling

$$\lambda_{Aff} = \frac{1}{\sqrt{2}} O_\varphi^{32} h_f, \tag{9.24}$$

as seen in Appendix A.2. h_f is the Yukawa coupling of the fermion. Since A is always mainly triplet, O_φ^{32} is always small. The decay $A \to f\bar{f}$ proceeds just because the A eigenfunction has a small component of doublet, as indicated in eq. (A.5).

The A boson can also decay into a $CP-$even Higgs and a Z boson. The corresponding Feynman diagram is,
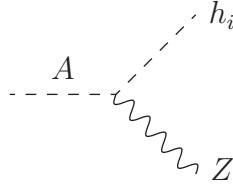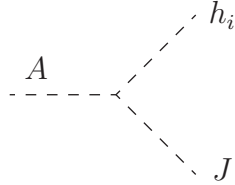

The decay rate is given by the formula,

$$\Gamma(A \to h_i Z) = \frac{\lambda_{Ah_i Z}^2}{16\pi} \frac{m_A^3}{m_Z^2} \lambda^{3/2} \left(1, m_{h_i}^2/m_A^2, m_Z^2/m_A^2 \right), \tag{9.25}$$

with a coupling

$$\lambda_{Ah_i Z} = \frac{g}{2c_W} (O_\chi^{i2} O_\varphi^{32} - 2 O_\chi^{i3} O_\varphi^{33}), \tag{9.26}$$

as seen in Appendix A.2. The λ function is defined in eq. (9.5). In the case $A \to h_2 Z$, since A is always mainly triplet, there is no phase space in B1, where h_2 is also a triplet and has a mass almost equal to the mass of A. In the case $A \to h_1 Z$, since the couplings are more or less similar for B1 and B2, the difference is due to the value of m_A.

The decay to a $CP-$even Higgs boson and a Majoron is represented by the following Feynman diagram

The decay rate is

$$\Gamma(A \to h_i J) = \frac{M_{h_i a_1 a_2}^2}{16\pi m_A} \lambda^{1/2}(1, m_{h_i}^2/m_A^2, m_J^2/m_A^2), \tag{9.27}$$

with the coupling $M_{h_i a_1 a_2}$ (with units of mass) given in Appendix A.2.

The decay to $\gamma\gamma$ is given by [246]

$$\Gamma(A \to \gamma\gamma) = \frac{\alpha^2 g^2 m_A^2}{1024\pi^3 m_W^2} \left| \frac{4\sqrt{2}}{3h_t} F_{1/2}(\tau_t)\lambda_{Att} \right|^2 \tag{9.28}$$

with $\tau_t = 4m_t^2/m_A^2$ and the $F_{1/2}$ function for a pseudoscalar is defined in Appendix C of Ref. [246].

The decay to $Z\gamma$ is given by [246]

$$\Gamma(A \to Z\gamma) = \frac{\alpha g^2}{2048\pi^4 m_W^4} |A_t|^2 m_A^3 (1 - \frac{m_Z^2}{m_A^2})^3, \tag{9.29}$$

where A_t is defined in equation 9.15 (replacing h with A).

Finally, the decay to two gluons is [246]

$$\Gamma(A \to gg) = \frac{\alpha_s^2 g^2 m_A^3}{128\pi^3 m_W^2} \left| \frac{4\sqrt{2}}{3h_t} F_{1/2}(\tau_t)\lambda_{Att} \right|^2. \tag{9.30}$$

Branching fractions for the decay of A for our three benchmarks are given in Table 9.9. The A boson component to doublet is the same for B1 and B2, but m_A is not. This
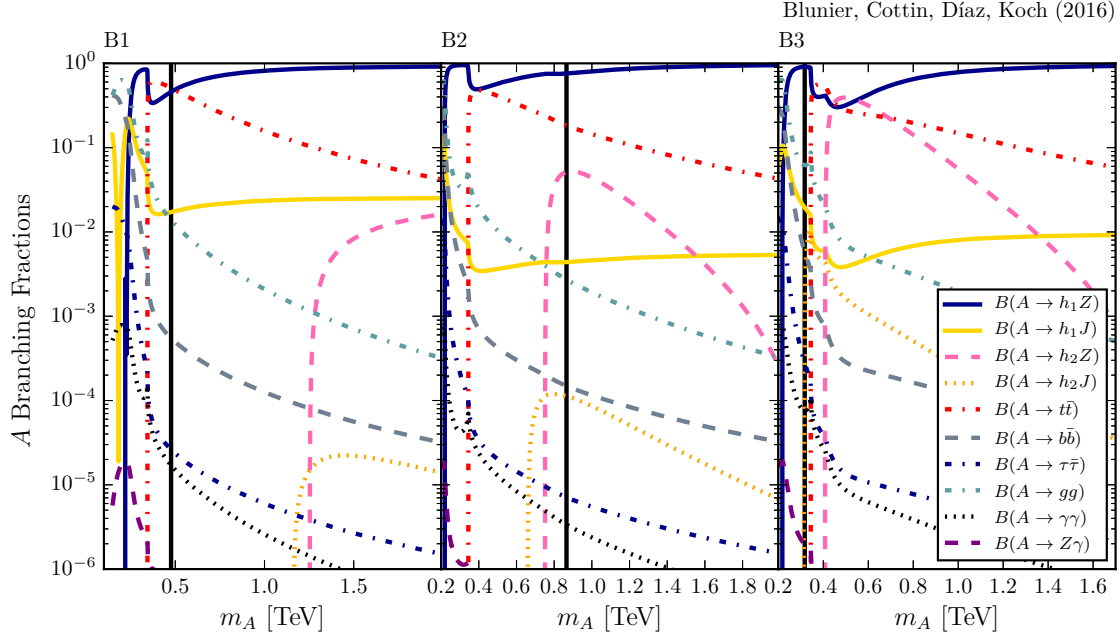
Branching Fraction	B1	B2	B3
$B(A \to t\bar{t})$	0.5	0.2	-
$B(A \to b\bar{b})$	5.5×10^{-4}	1.5×10^{-4}	6.0×10^{-3}
$B(A \to \tau\tau)$	2.6×10^{-5}	7.0×10^{-6}	2.8×10^{-4}
$B(A \to h_1 Z)$	0.5	0.8	0.9
$B(A \to h_1 J)$	1.7×10^{-2}	4.4×10^{-3}	2.0×10^{-2}
$B(A \to h_2 Z)$	-	5.0×10^{-2}	-
$B(A \to h_2 J)$	-	1.1×10^{-4}	-
$B(A \to gg)$	1.4×10^{-2}	2.7×10^{-3}	6.2×10^{-2}
$B(A \to \gamma\gamma)$	1.7×10^{-5}	3.4×10^{-6}	7.7×10^{-5}
$B(A \to Z\gamma)$	8.2×10^{-7}	2.6×10^{-7}	2.0×10^{-6}

Table 9.9: Branching fractions for A in our three different benchmarks [3].

leads to larger decay rates to fermions in B2. Since the total decay rate is also different, this is not observed for branching fractions and in fact, the opposite happens. Note that in B1 and B3 the decays of A to h_2 and a J or a Z are not kinematically allowed. The same happens in B3 for the decay to top quarks. In B2, A can be much heavier than h_2 thus, the decay $A \to h_2 Z$ is open.

Fig. 9.11 shows the branching fractions of A as a function of its mass. The curves are obtained starting from each of the 3 benchmarks and vary κ to change m_A. Since this procedure will also change m_{h_1}, which we want fixed to 125 GeV, we change also the value of λ_1 to recover $m_{h_1} \approx 125$ GeV, as in Table 9.2. In all cases, the modes $A \to h_1 Z$ and $A \to t\bar{t}$ dominate. In B3 the decay mode $A \to h_2 Z$ is open and can be relevant too.

Fig. 9.12 shows a general scan where all the parameters are varied according to Table 9.2. It shows that the decay mode $A \to h_1 Z$ dominates. If the channel is open, when h_2 is mainly singlet, the decay channel $A \to h_2 Z$ is also very important.

Figure 9.11: $CP-$odd Higgs A branching fractions in the three benchmarks as a function of m_A. The parameter κ is varied to move m_A, as explained in the text. The vertical solid line in each frame corresponds to our benchmark point. The plot includes all constraints from Section 9.1 [3].
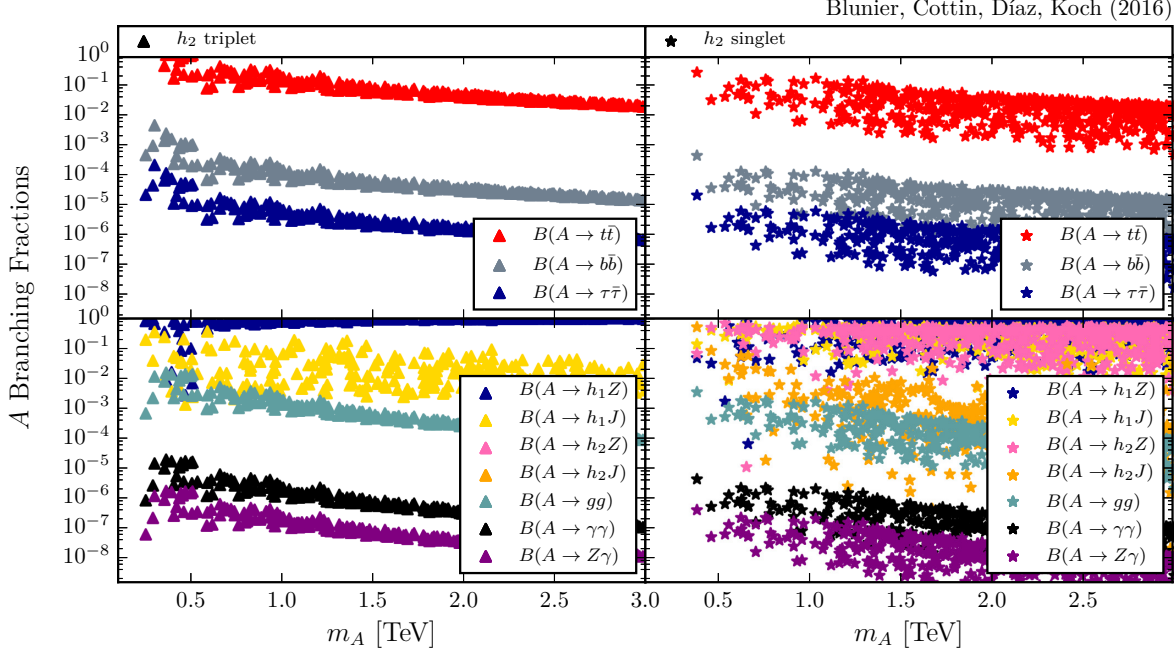
9.4.3 $H^\pm$ decays

In this Section we study tree-level decays of the singly charged Higgs boson. The decay to $t\bar{b}$, represented by the Feynman diagram
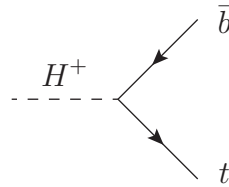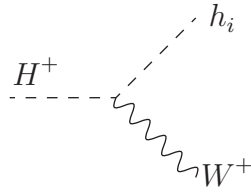

has a rate

$$\Gamma(H^\pm \to t\bar{b}) = \frac{N_c(O_+^{21})^2}{16\pi m_{H^\pm}^3}\Big[(h_t^2 + h_b^2)(m_{H^\pm}^2 - m_t^2 - m_b^2) \\ - 4h_t h_b m_t m_b\Big]\lambda^{1/2}(m_{H^\pm}^2, m_t^2, m_b^2). \tag{9.31}$$

Similarly, the decay $H^\pm \to h_i W^\pm$

Figure 9.12: Branching fractions for the A scalar as a function of m_A. The left column shows points where h_2 is triplet-like (i.e $|O_\chi^{23}| > 0.95$). The right column shows points where h_2 is singlet-like (i.e $|O_\chi^{21}| > 0.95$). Parameters are varied according to Table 9.2. The scan includes all constraints from Section 9.1 [3].
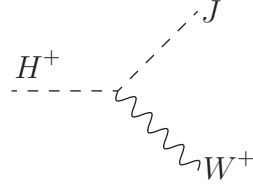

has a rate given by

$$\Gamma(H^\pm \to h_i W^\pm) = \frac{g^2 |\lambda_{H^\pm h_i W^\mp}|^2}{64\pi m_{H^+}^3 m_W^2} \lambda^{3/2}(m_{H^\pm}^2, m_{h_i}^2, m_W^2), \tag{9.32}$$

with,

$$\lambda_{H^\pm h_i W^\mp} = O_+^{21} O_\chi^{i2} - \sqrt{2} O_+^{22} O_\chi^{i3}. \tag{9.33}$$
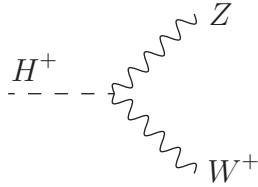
The decay to a Majoron and a $W^\pm$ boson is

with a decay rate,

$$\Gamma(H^\pm \to JW^\pm) = \frac{g^2 |\lambda_{H^\pm JW^\mp}|^2}{64\pi m_{H^+}^3 m_W^2}[m_{H^\pm}^2 - m_W^2]^3, \qquad (9.34)$$

where

$$\lambda_{H^\pm JW^\mp} = O_+^{21}O_\varphi^{22} + \sqrt{2}O_+^{22}O_\varphi^{23}, \qquad (9.35)$$

To finish, the decay to a Z and a $W^\pm$ boson is

and has the following decay rate

$$\Gamma(H^\pm \to ZW^\pm) = \frac{g^4 |M_{H^\pm ZW^\mp}|^2}{256\pi m_W^4 m_{H^\pm}^3}\Big[m_{H^\pm}^4 + m_Z^4 + 10m_Z^2 m_W^2 + m_W^4$$
$$- 2m_{H^\pm}^2(m_W^2 + m_Z^2)\Big]\lambda^{1/2}(m_{H^\pm}^2, m_Z^2, m_W^2), \qquad (9.36)$$

with

$$M_{H^\pm ZW^\mp} = O_+^{21}s_W v_\phi - \sqrt{2}O_+^{22}(1 + s_W^2)v_\Delta. \qquad (9.37)$$

In Table 9.10 we show the singly charged Higgs branching fractions in our three benchmarks.

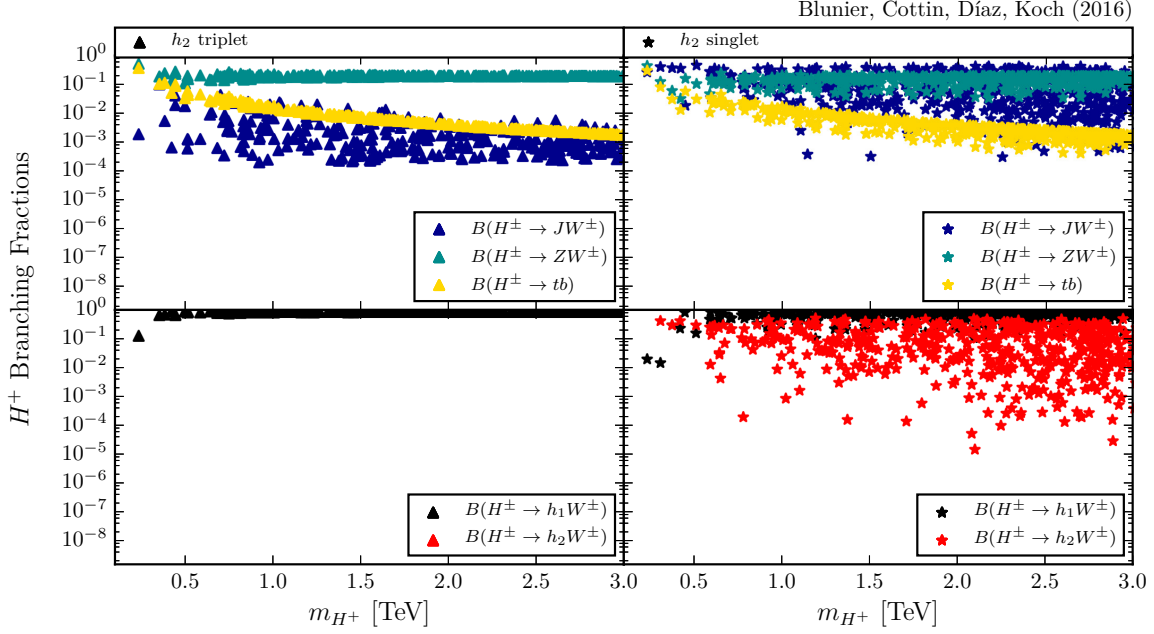| Branching Fraction	B1	B2	B3
$B(H^\pm \to t\bar{b})$	7.0×10^{-2}	2.0×10^{-2}	0.2
$B(H^\pm \to h_1 W^\pm)$	0.7	0.8	0.6
$B(H^\pm \to h_2 W^\pm)$	-	5.7×10^{-3}	-
$B(H^\pm \to J W^\pm)$	3.0×10^{-3}	5.1×10^{-4}	1.6×10^{-3}
$B(H^\pm \to Z W^\pm)$	0.2	0.2	0.3

Table 9.10: Branching fractions for $H^\pm$ in our three benchmarks [3].

Note that the decay $H^\pm \to h_2 W^\pm$ is not kinematically allowed in B1 and B3. Branching fractions of $H^\pm \to h_1 W^\pm$ are dominant in the three benchmarks.
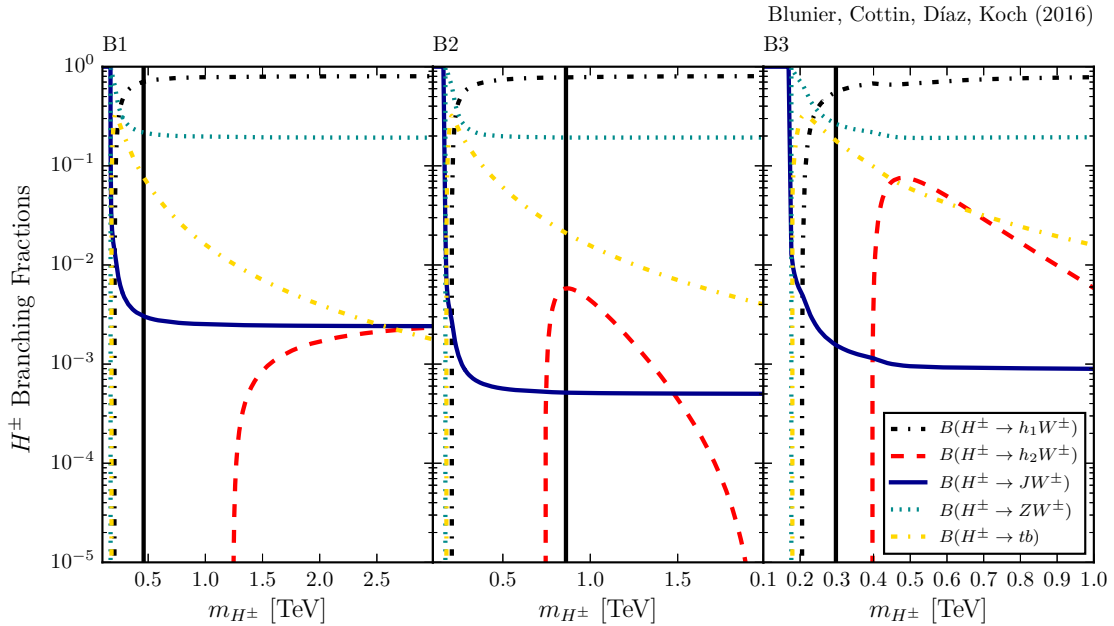
Figure 9.13: Branching fraction for the H^+ scalar in the three benchmarks as a function of m_{H^+}. The parameter κ is varied to move m_{H^+}, as explained in the text. The vertical solid line in each frame corresponds to our benchmark point. The plot includes all constraints from Section 9.1 [3].

Fig. 9.13 shows the branching fractions of $H^\pm$ as a function of its mass. The curves are obtained starting from each of the 3 benchmarks and vary κ according to Table 9.2 to change the value of $m_H^\pm$. λ_1 also varies as in Table 9.2 to recover $m_{h_1} \approx 125$ GeV.

Figure 9.14: Branching fractions for the H^+ scalar as a function of m_{H^+}. The left column shows points where h_2 is triplet-like (i.e $O_\chi^{21} > 0.95$). The right column shows points where h_2 is singlet-like (i.e $O_\chi^{23} > 0.95$). Parameters are varied according to Table 9.2. The scan includes all constraints from Section 9.1 [3].

Fig. 9.14 shows the $H^\pm$ branching fractions as a function of its mass in a general scan. Decays to $h_1 W^\pm$ dominate, independent of the composition of h_2. Decays to $ZW^\pm$ follow in importance. Also important are decays to $h_2 W^\pm$, when h_2 is singlet-like, as when h_2 is triplet-like, its mass is very close to the mass of $m_{H^\pm}$ (as in B1), so there is no phase space for the decay in this case.

9.5 Promising channels for discovery of h_2, A and $H^\pm$

We now briefly comment on the most promising channels for discovery of h_2, A and $H^\pm$ at future e^+e^- colliders.

A promising channel for the discovery of h_2, given its large cross-section as discussed in Section 9.3.1, is $e^+e^- \to h_2 t\bar{t}$. Thinking of B1, the largest decays fractions for h_2 are to ZZ as shown in Table 9.8. Considering leptonic decays of the W and Z, the signal is

$$e^+e^- \to ZZt\bar{t} \to l^+l^-l^+l^-l^+\nu_l l^-\nu_l b\bar{b} \qquad (9.38)$$

with $l = e, \mu$. The signal contains 2 $b-$jets $+$ 6 leptons $+$ p_T^{miss} (missing transverse momenta). For B1 at $\sqrt{s} = 1$ TeV, the cross-section is estimated as

$$
\begin{aligned}
\sigma_{2b6lp_T^{\text{miss}}} &\approx \sigma(e^+e^- \to h_2 t\bar{t}) \times B(h_2 \to ZZ) \\
&\times B(Z \to l^+l^-)^2 \times B(W^\pm \to l^\pm \nu)^2 \\
&\approx 3 \times 10^{-5} \text{ fb}
\end{aligned}
\tag{9.39}
$$

resulting in less than one event to be discoverable with $\mathcal{L} = 1000$ fb^{-1}, so too little to be observed unfortunately. Possible SM backgrounds to this signature include $e^+e^- \to ZZZ$ and $e^+e^- \to ZZt\bar{t}$. Multi-lepton signatures in the "23" HTM were studied in the context of the LHC in Refs. [233, 248], where it was shown that after requiring kinematic cuts in the transverse momenta of the leptons, signatures with 6 leptons have no background, even though the signal is also scarce. Therefore, multi-lepton signatures are relevant for higher integrated luminosities. We could require similar leptonic kinematic cuts in the case of e^+e^-, in addition of requiring 2 $b-$tagged jets and small p_T^{miss} due to the two neutrinos.

For B2 the decay $h_2 \to JJ$ dominates. If one W boson decays hadronically and the other leptonically, then we will have a 4 $b-$jets $+$ p_T^{miss} signature, assuming the lepton escapes undetected. This channel was studied in detail in Ref. [51] for our "123" model, where it was shown that with appropriate cuts in p_T^{miss}, number of jets and invariant mass distributions the background is removed while keeping high signal efficiency.

In the case of the $CP-$odd Higgs A, there are two relevant processes. $e^+e^- \to AZZ$ has the highest cross-section for B1 and B2. In the case where $A \to t\bar{t}$ we have the same signature as before for h_2. The decay $A \to h_1 Z$ also dominates in our benchmarks. The dominant decay $h_1 \to b\bar{b}$ follows, leading to topologies with leptons and $b-$jets (with no missing transverse momenta), depending on the decay of the Z. The cross-section for,

$$
e^+e^- \to AZZ \to h_1 ZZZ \to b\bar{b}l^+l^-l^+l^-l^+l^-
\tag{9.40}
$$

leads to a 2$b-$jet$+$6 leptons signature. The cross-section for B1 at $\sqrt{s} = 1$ TeV is estimated as

$$\begin{aligned}
\sigma_{2b6l} &\approx \sigma(e^+e^- \to AZZ) \times B(A \to h_1 Z) \times B(h_1 \to b\bar{b}) \\
&\quad \times B(Z \to l^+l^-)^3 \\
&\approx 1.0 \times 10^{-4} \text{ fb}
\end{aligned} \tag{9.41}$$

resulting in less than one event with $\mathcal{L} = 1000$ fb^{-1}. Possible backgrounds are very similar and include the ones in equation 9.39, so similar cuts can be applied to suppress them.

The associated production $e^+e^- \to AJJ$ dominates in B3 with $A \to b\bar{b}$, leading to the topology of 2 $b-$jets $+$ p_T^{miss}. This signal was studied for the "23" HTM in [249], with largest background coming from $e^+e^- \to W^+W^-$ and $e^+e^- \to ZZ$. The authors concluded that the most efficient way to improve the signal-to-background ratio is to require $b-$tagged jets and large p_T^{miss}, in addition to charged multiplicity and an invariant mass cut close to the mass of the visibly decaying particle.

Production for the singly charged Higgs dominates in $e^+e^- \to H^+H^- \to H^+h_1W^-$ for most of our benchmarks (see Figure 9.6). This is followed by the decay of $H^+ \to h_1W^+$, which has the highest branching fraction (see Table 9.10). An optimal discovery channel would be when $h_1 \to b\bar{b}$ and when one W boson decays hadronically and the other leptonically,

$$e^+e^- \to H^+h_1W^- \to h_1W^+h_1W^- \to b\bar{b}l^{\pm}\nu_l b\bar{b}q\bar{q} \tag{9.42}$$

resulting in an event topology of $4b-$jets $+$ 2 jets $+$ 1 lepton $+$ p_T^{miss}, where the lepton $l = e, \mu$. This distinctive signature was studied for a charged Higgs in the context of Two-Higgs doublet models [250, 251]. The mass of the singly charged Higgs can be reconstructed and the events can be selected with $b-$tagging techniques, in addition to requiring one isolated lepton. Also, two jets must have the W mass.

We can estimate the visible cross-section for this final state. For $\sqrt{s} = 1$ TeV in B1 we have

$$
\begin{aligned}
\sigma_{4bp_T^{\mathrm{miss}}ljj} &\approx \sigma(e^+e^- \to H^+h_1W^-) \\
&\times B(H^+ \to h_1W^+) \times B(h_1 \to b\bar{b})^2 \\
&\times B(W^\pm \to l^\pm\nu_l) \times B(W^\pm \to q\bar{q}) \\
&\approx 0.04 \text{ fb}
\end{aligned}
\tag{9.43}
$$

and since the ILC has a yearly integrated luminosity of 1000 fb^{-1}, this results in about 40 potentially discoverable events per annum. A relevant SM background for this signature is the process $e^+e^- \to t\bar{t}b\bar{b}$. Our estimation yields a visible cross-section of $\sigma_{\mathrm{SM}\text{-}4bp_T^{\mathrm{miss}}ljj} \approx 0.4$ fb, which is quite significant. The signal-to-background ratio can be enhanced by applying the selection cuts above mentioned. It was also shown in Ref. [250] that one can suppress this big irreducible background to a negligible level by using a technique that allows the reconstruct of the neutrino four-momentum.

Of course a more detailed simulation study should be done in order to suppress backgrounds further and improve signal efficiency for the channels mentioned. A fully fledged study in this direction, considering also detector efficiencies, goes beyond the scope of this work.

Part V

Close

Chapter 10

Concluding remarks

In this thesis we discussed the phenomenology of new physics beyond the Standard Model of particle physics by focusing on three studies.

First, we reported on a search for long-lived massive particles decaying into five or more charged particles where events were selected using jets, or missing transverse momentum. The main experimental signature of the search is a displaced vertex with an invariant mass greater than 10 GeV. This signature corresponds to a wide variety of new physics models, many of which have not been searched for previously. The search uses the full data sample of proton-proton collisions collected by the ATLAS detector at the LHC with a collider center of mass energy of 8 TeV and an integrated luminosity of 20.3 fb^{-1}. Less than one background event is expected in each of the channels, and no events are observed. Upper limits are provided on the cross section for production of particles that give rise to the search signatures in a variety of Supersymmetric models. These upper limits exclude significant regions of the parameter space with particle masses within reach of the LHC.

We have also examined the prospects for discovery or exclusion of the DGS model. The model has some nice properties: the SUSY flavour problem is addressed by gauge mediated SUSY breaking, while the Higgs mass is made heavy enough through the mixing with the NMSSM $CP-$even singlet. This singlet has a mass around 90 GeV, and therefore can be made consistent with some small excesses in the LEP Higgs searches. An interesting feature of the model is the presence of a gravitino LSP and a singlino-like neutralino NLSP that can be long-lived.

As well as having the usual hard jets plus missing transverse momentum signatures, the model predicts possible displaced vertices (DVs) from long-lived singlinos. These

decay into $b\bar{b}$ and missing transverse momentum in the form of gravitinos. However, displaced b's are somewhat problematic since B mesons themselves travel a small distance before visibly decaying and the "displaced displaced" vertices have a very poor signal efficiency for getting past the standard DV cuts. We have illustrated how loosening the DV searches whilst imposing some prompt cuts to control background results in significantly higher signal efficiency, motivating a proper study with a full detector simulation (DV analyses are difficult to perform accurately from outside the experimental collaborations). We have provided a rough approximation to the tracking efficiency that works for two gauge mediation models and one $R-$parity violating model over a range of possible DV lifetimes, but clearly more work can be done to provide a more comprehensive parameterisation.

We have re-cast current 8 TeV prompt searches to bound the gluino mass from below at 1080 GeV, whereas current 13 TeV prompt searches are less restrictive. This is somewhat low compared to naive expectations based on LHC exclusion results quoted for simplified models, but as Figure 8.1 shows, there are many different cascade decays in the model. This means that the Supersymmetric signal ends up being shared out between many different channels, and may not be yet detected in any single one [252, 253]. With 100 fb^{-1} of integrated luminosity at 13 TeV though, the 0-lepton + jets + p_T^{miss} searches should be sensitive to up to 1900 GeV.

We further combine the search strategies in the prompt and displaced channels to demonstrate that a much better sensitivity could be obtained by optimising cuts. In particular, we find that combining the relaxed DV cuts with the hard cuts from the 0-lepton + jets + p_T^{miss} analysis, a $> 3\sigma$ discovery can be made with 300 - 1000 fb^{-1} data for a 2 TeV gluino mass depending on the systematic background. We indicate how this situation could be improved significantly by also relaxing some of the prompt cuts. It is clear that an optimised analysis in a DV + jets + p_T^{miss} channel will yield better sensitivity than for either search method alone and we strongly urge the experimental collaborations to pursue this further.

Finally, we have studied the Higgs phenomenology of a model with a scalar triplet, a scalar singlet and a scalar doublet under $SU(2)$. In this "123" variant of the Higgs triplet model the singlet acquires a vacuum expectation value, which spontaneously breaks lepton number. The vacuum expectation value generated for the triplet provides a mass term for neutrinos. This features makes it a well motivated model to look for at particle colliders.

The lightest $CP-$even Higgs, h_1, has been identified with the SM-like Higgs boson discovered at the LHC, which constrains the parameters in the scalar potential of the model. We studied the production cross-sections and decay ratios of the second heaviest $CP-$even Higgs h_2, the $CP-$odd Higgs A and the singly charged Higgs $H^\pm$. We found that production cross-sections at hadron colliders can be very low for these states, so we perform a numerical analysis assessing the discovery potential at future lepton colliders.

We find characteristic features in cases where h_2 is singlet-like, triplet-like or a mixture. The main 2-body production mode for h_2 is associated production with a $CP-$odd state A. We note that cross-sections for A and $H^\pm$ are enhanced when a second heavy particle is also produced on-shell. Invisible decays of h_2 to Majorons can be very important. Decays of the singly charged Higgs $H^\pm \rightarrow h_1 W^\pm$ dominate. These features lead to promising channels for discovery of h_2 and A, in particular in the $4b-$jets$+p_T^{\text{miss}}$ and $2b-$jets$+p_T^{\text{miss}}$ final states, as shown in Ref. [51] and Ref. [249], respectively, as we estimate the most promising signal with leptons in the final state are too small to be observed (although the sensitivity can improve by considering hadronic decays of the $W^\pm$ and the Z in equations 9.38 and 9.40). The $4b-$jets $+$ 2 jets $+$ 1 lepton $+$ p_T^{miss} final state is optimal for the discovery of the singly charged Higgs. These signals provides a test of the "123" HTM at future e^+e^- colliders.

In summary, three studies of how new physics can manifest at current and future colliders have been given in this thesis. The lack of any experimental sign of new physics in prompt channels and the advantage of a background free search for displaced vertices offers a unique opportunity for this type of signatures at colliders, and will become very relevant for the next runs of the LHC as the luminosity increases. Also relevant in the future is the precise study of the Higgs boson. The understanding of the - possibly extended - Higgs sector also offers a window for new physics beyond the Standard Model.

Appendix A

Conventions and Feynman rules for a Higgs triplet model

In this Appendix we detail some conventions and Feynman rules for the "123" Higgs triplet model under study in this thesis.

A.1 Convention for diagonalization

The diagonalization in the charged scalar sector is,

$$
\begin{bmatrix} h_1^+ \\ h_2^+ \end{bmatrix} \equiv \begin{bmatrix} G^+ \\ H^+ \end{bmatrix} = O_+ \begin{bmatrix} \phi^{-*} \\ \Delta^+ \end{bmatrix} \equiv \begin{pmatrix} -c_\beta & s_\beta \\ s_\beta & c_\beta \end{pmatrix} \begin{bmatrix} \phi^{-*} \\ \Delta^+ \end{bmatrix} \tag{A.1}
$$

and the diagonalization in the neutral scalar sector proceeds as,

$$
\begin{bmatrix} h_1 \\ h_2 \\ h_3 \end{bmatrix} = O_\chi \begin{bmatrix} \chi_\sigma \\ \chi_\phi \\ \chi_\Delta \end{bmatrix}, \qquad \begin{bmatrix} a_1 \\ a_2 \\ a_3 \end{bmatrix} \equiv \begin{bmatrix} G^0 \\ J \\ A \end{bmatrix} = O_\varphi \begin{bmatrix} \varphi_\sigma \\ \varphi_\phi \\ \varphi_\Delta \end{bmatrix}, \tag{A.2}
$$

where O_χ and O_φ are 3×3 matrices.

The mass matrix in eq. (2.4) is diagonalized by the matrix,

$$
O_\varphi = \begin{bmatrix}
0 & \dfrac{1}{N_G} & -\dfrac{2}{N_G}\dfrac{v_\Delta}{v_\phi} \\[2ex]
\dfrac{N_G^2}{N_J} & -\dfrac{2}{N_J}\dfrac{v_\Delta^2}{v_\phi v_\sigma} & -\dfrac{1}{N_J}\dfrac{v_\Delta}{v_\sigma} \\[2ex]
\dfrac{1}{N_A}\dfrac{v_\Delta}{v_\sigma} & \dfrac{2}{N_A}\dfrac{v_\Delta}{v_\phi} & \dfrac{1}{N_A}
\end{bmatrix},
\tag{A.3}
$$

where

$$
\begin{aligned}
N_G &= \sqrt{1 + 4\frac{v_\Delta^2}{v_\phi^2}}, \\
N_J &= \sqrt{N_G^4 + 4\frac{v_\Delta^4}{v_\phi^2 v_\sigma^2} + \frac{v_\Delta^2}{v_\sigma^2}}, \\
N_A &= \sqrt{1 + 4\frac{v_\Delta^2}{v_\phi^2} + \frac{v_\Delta^2}{v_\sigma^2}}.
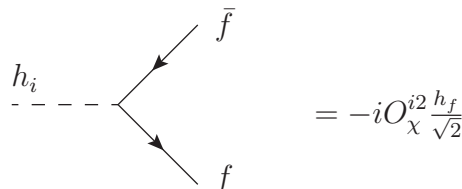\end{aligned}
\tag{A.4}
$$

The mass eigenstate fields are,

$$
\begin{aligned}
G^0 &= \frac{1}{N_G}\varphi_\phi - \frac{2}{N_G}\frac{v_\Delta}{v_\phi}\varphi_\Delta, \\
J &= \frac{N_G^2}{N_J}\varphi_\sigma - \frac{2}{N_J}\frac{v_\Delta^2}{v_\phi v_\sigma}\varphi_\phi - \frac{1}{N_J}\frac{v_\Delta}{v_\sigma}\varphi_\Delta, \\
A &= \frac{1}{N_A}\frac{v_\Delta}{v_\sigma}\varphi_\sigma + \frac{2}{N_A}\frac{v_\Delta}{v_\phi}\varphi_\phi + \frac{1}{N_A}\varphi_\Delta.
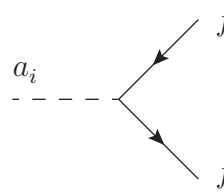\end{aligned}
\tag{A.5}
$$

From here we conclude that the Majoron has the tendency to be mainly singlet and that the neutral Goldstone boson has no singlet component (the singlet does not couple to the Z boson).

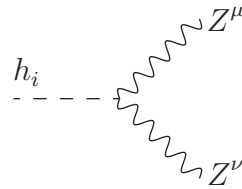## A.2 Feynman rules

A.2.1 One scalar and two fermions

$$
= -iO_\chi^{i2}\frac{h_f}{\sqrt{2}}
$$
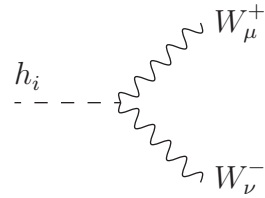
$$a_i \ \text{-----} \ \overset{\bar{f}}{\diagdown} \ \underset{f}{\diagup} \qquad = O_\varphi^{i2} \frac{h_f}{\sqrt{2}} \gamma_5$$

A.2.2 One scalar and two gauge bosons
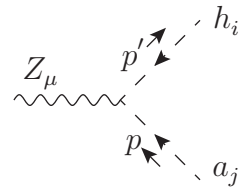
$$h_i \ \text{-----} \ \overset{Z^\mu}{\diagup} \ \underset{Z^\nu}{\diagdown} \qquad = i\frac{1}{2}(g^2 + g'^2)(O_\chi^{i2} v_\phi + 4 O_\chi^{i3} v_\Delta) g^{\mu\nu}$$
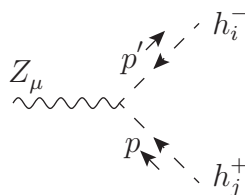
$$h_i \ \text{-----} \ \overset{W_\mu^+}{\diagup} \ \underset{W_\nu^-}{\diagdown} \qquad = i\frac{g^2}{2}(O_\chi^{i2} v_\phi + 2 O_\chi^{i3} v_\Delta) g_{\mu\nu}$$

A.2.3 Two scalars and one gauge boson

$$Z_\mu \ \overset{p'}{\diagup}{}^{h_i} \ \underset{p}{\diagdown}{}_{a_j} \qquad = \frac{g}{2c_W}(O_\chi^{i2} O_\varphi^{j2} - 2 O_\chi^{i3} O_\varphi^{j3})(p + p')_\mu$$

$$Z_\mu \ \overset{p'}{\diagup}{}^{h_i^-} \ \underset{p}{\diagdown}{}_{h_j^+} \qquad = -\frac{ig}{2c_W}\left[O_+^{i1} O_+^{j1}(c_W^2 - s_W^2) - 2 O_+^{i2} O_+^{j2} s_W^2 \right](p + p')_\mu$$

$$= -\frac{ig}{c_W}(c_W^2 - s_W^2)(p + p')_\mu$$

$$= -ie(p + p')_\mu \delta_{ij}$$

$$= -2ie(p + p')_\mu$$

$$= i\frac{g}{2}\big(O_+^{i1}O_\chi^{j2} - \sqrt{2}O_+^{i2}O_\chi^{j3}\big)(p + p')_\mu$$

$$= i\frac{g}{2}\big(O_+^{i1}O_\chi^{j2} + \sqrt{2}O_+^{i2}O_\chi^{j3}\big)(p + p')_\mu$$

A.2.4 Three scalars

For the case with one $CP-$even and two $CP-$odd Higgs bosons, the relevant term in the Lagrangian is

$$\mathcal{L}_{h_i a_j a_k} = M_{h_i a_j a_k} h_i a_j a_k, \tag{A.6}$$

where we sum over i, j, k. The coupling $M_{h_i a_j a_k}$ (with units of mass), after symmetrization in j and k is given by the expression

$$
\begin{aligned}
M_{h_i a_j a_k} = &- \lambda_1 v_\phi O_\chi^{i2} O_\varphi^{j2} O_\varphi^{k2} - (\lambda_2 + \lambda_4) v_\Delta O_\chi^{i3} O_\varphi^{j3} O_\varphi^{k3} - \frac{1}{2}(\lambda_3 + \lambda_5) v_\phi O_\chi^{i2} O_\varphi^{j3} O_\varphi^{k3} \\
&- \frac{1}{2}\left[(\lambda_3 + \lambda_5) v_\Delta + \kappa v_\sigma\right] O_\chi^{i3} O_\varphi^{j2} O_\varphi^{k2} - \beta_1 v_\sigma O_\chi^{i1} O_\varphi^{j1} O_\varphi^{k1} - \frac{1}{2}\beta_2 v_\phi O_\chi^{i2} O_\varphi^{j1} O_\varphi^{k1} \\
&- \frac{1}{2}(\beta_2 v_\sigma + \kappa v_\Delta) O_\chi^{i1} O_\varphi^{j2} O_\varphi^{k2} - \frac{1}{2}\beta_3 v_\Delta O_\chi^{i3} O_\varphi^{j1} O_\varphi^{k1} - \frac{1}{2}\beta_3 v_\sigma O_\chi^{i1} O_\varphi^{j3} O_\varphi^{k3} \\
&- \frac{1}{2}\kappa v_\phi O_\chi^{i2}(O_\varphi^{j1} O_\varphi^{k3} + O_\varphi^{k1} O_\varphi^{j3}) - \frac{1}{2}\kappa v_\phi O_\chi^{i3}(O_\varphi^{j1} O_\varphi^{k2} + O_\varphi^{k1} O_\varphi^{j2}) \\
&- \frac{1}{2}\kappa v_\phi O_\chi^{i1}(O_\varphi^{j2} O_\varphi^{k3} + O_\varphi^{k2} O_\varphi^{j3}) - \frac{1}{2}\kappa v_\Delta O_\chi^{i2}(O_\varphi^{j1} O_\varphi^{k2} + O_\varphi^{k1} O_\varphi^{j2}) \\
&- \frac{1}{2}\kappa v_\sigma O_\chi^{i2}(O_\varphi^{j2} O_\varphi^{k3} + O_\varphi^{k2} O_\varphi^{j3}). \tag{A.7}
\end{aligned}
$$

This leads to the following Feynman rule,

 $= i M_{h_i a_j a_k}$ (twice larger if $j = k$).

For one $CP-$even and two charged Higgs bosons, the relevant term in the Lagrangian is,

$$\mathcal{L}_{h_i h_j^+ h_k^-} = M_{h_i h_j^+ h_k^-} h_i h_j^+ h_k^- \tag{A.8}$$

where we sum over i, j, k. The coupling $M_{h_i h_j^+ h_k^-}$ (with units of mass) is given by the expression

$$
\begin{aligned}
M_{h_i h_j^+ h_k^-} =& \; -2\lambda_1 v_\phi O_\chi^{i2} O_+^{j1} O_+^{k1} - 2(\lambda_2 + \lambda_4) v_\Delta O_\chi^{i3} O_+^{j2} O_+^{k2} - (\lambda_3 + \frac{1}{2}\lambda_5) v_\phi O_\chi^{i2} O_+^{j2} O_+^{k2} \\
& -\lambda_3 v_\Delta O_\chi^{i3} O_+^{j1} O_+^{k1} - \frac{1}{2\sqrt{2}} \lambda_5 v_\phi O_\chi^{i3} O_+^{j2} O_+^{k1} - \frac{1}{2\sqrt{2}} \lambda_5 v_\phi O_\chi^{i3} O_+^{j1} O_+^{k2} \\
& -\frac{1}{\sqrt{2}} (\tfrac{1}{2}\lambda_5 v_\Delta - \kappa v_\sigma) O_\chi^{i2} O_+^{j2} O_+^{k1} - \frac{1}{\sqrt{2}} (\tfrac{1}{2}\lambda_5 v_\Delta - \kappa v_\sigma) O_\chi^{i2} O_+^{j1} O_+^{k2} \\
& -\beta_2 v_\sigma O_\chi^{i1} O_+^{j1} O_+^{k1} - \beta_3 v_\sigma O_\chi^{i1} O_+^{j2} O_+^{k2} + \frac{1}{\sqrt{2}} \kappa v_\phi O_\chi^{i1} O_+^{j2} O_+^{k1} \\
& +\frac{1}{\sqrt{2}} \kappa v_\phi O_\chi^{i1} O_+^{j1} O_+^{k2}
\end{aligned}
\tag{A.9}
$$

and the Feynman rule is,

$$ = i M_{h_i h_j^+ h_k^-}. $$

For one $CP-$even and two doubly charged Higgs bosons, the relevant term in the Lagrangian is

$$
\mathcal{L}_{h_i \Delta^{++} \Delta^{--}} = M_{h_i \Delta^{++} \Delta^{--}} h_i \Delta^{++*} \Delta^{++},
\tag{A.10}
$$

with

$$
M_{h_i \Delta^{++} \Delta^{--}} = -2\lambda_2 v_\Delta O_\chi^{i3} - \lambda_3 v_\phi O_\chi^{i2} - \beta_3 v_\sigma O_\chi^{i1},
\tag{A.11}
$$

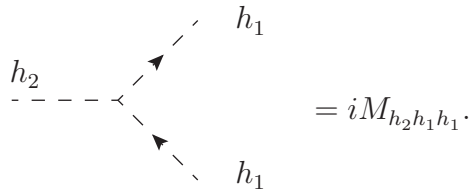leading to the following Feynman rule

$$ = i M_{h_i \Delta^{++} \Delta^{--}}. $$

For three $CP-$even Higgs bosons, the relevant term in the Lagrangian is

$$\mathcal{L}_{h_i h_j h_k} = M_{h_i h_j h_k} h_i h_j h_k, \tag{A.12}$$

where we sum over i, j, k. The coupling $M_{h_i h_j h_k}$ (with units of mass), after symmetrization in j and k, is given by

$$
\begin{aligned}
M_{h_i h_j h_k} =\ & -6\lambda_1 v_\phi O_\chi^{i2} O_\chi^{j2} O_\chi^{k2} - 6(\lambda_2 + \lambda_4) v_\Delta O_\chi^{i3} O_\chi^{j3} O_\chi^{k3} \\
& - (\lambda_3 + \lambda_5) v_\phi \Big[O_\chi^{i2} O_\chi^{j3} O_\chi^{k3} + O_\chi^{k2} O_\chi^{i3} O_\chi^{j3} + O_\chi^{j2} O_\chi^{k3} O_\chi^{i3} \Big] \\
& - \Big[(\lambda_3 + \lambda_5) v_\Delta - \kappa v_\sigma \Big] \Big[O_\chi^{i2} O_\chi^{j2} O_\chi^{k3} + O_\chi^{k2} O_\chi^{i2} O_\chi^{j3} + O_\chi^{j2} O_\chi^{k2} O_\chi^{i3} \Big] \\
& - 6\beta_1 v_\sigma O_\chi^{i1} O_\chi^{j1} O_\chi^{k1} - \beta_2 v_\phi \Big[O_\chi^{i1} O_\chi^{j1} O_\chi^{k2} + O_\chi^{k1} O_\chi^{i1} O_\chi^{j2} + O_\chi^{j1} O_\chi^{k1} O_\chi^{i2} \Big] \\
& - (\beta_2 v_\sigma - \kappa v_\Delta) \Big[O_\chi^{i1} O_\chi^{j2} O_\chi^{k2} + O_\chi^{k1} O_\chi^{i2} O_\chi^{j2} + O_\chi^{j1} O_\chi^{k2} O_\chi^{i2} \Big] \\
& - \beta_3 v_\Delta \Big[O_\chi^{i1} O_\chi^{j1} O_\chi^{k3} + O_\chi^{k1} O_\chi^{i1} O_\chi^{j3} + O_\chi^{j1} O_\chi^{k1} O_\chi^{i3} \Big] \\
& - \beta_3 v_\sigma \Big[O_\chi^{i1} O_\chi^{j3} O_\chi^{k3} + O_\chi^{k1} O_\chi^{i3} O_\chi^{j3} + O_\chi^{j1} O_\chi^{k3} O_\chi^{i3} \Big] \\
& + \kappa v_\phi \Big[O_\chi^{i1} O_\chi^{j2} O_\chi^{k3} + O_\chi^{i1} O_\chi^{k2} O_\chi^{j3} + O_\chi^{j1} O_\chi^{i2} O_\chi^{k3} \\
& + O_\chi^{k1} O_\chi^{i2} O_\chi^{j3} + O_\chi^{j1} O_\chi^{k2} O_\chi^{i3} + O_\chi^{k1} O_\chi^{j2} O_\chi^{i3} \Big] \tag{A.13}
\end{aligned}
$$

The corresponding Feynman rule is given by

$$= i M_{h_2 h_1 h_1}.$$

Colophon

This thesis was made in LaTeX 2_ε using the "hepthesis" class [254].

Bibliography

[1] ATLAS collaboration, G. Aad et al., *Search for massive, long-lived particles using multitrack displaced vertices or displaced lepton pairs in pp collisions at $\sqrt{s} = 8$ TeV with the ATLAS detector*, *Phys. Rev.* **D92** (2015) 072004, [1504.05162].

[2] B. C. Allanach, M. Badziak, G. Cottin, N. Desai, C. Hugonie and R. Ziegler, *Prompt Signals and Displaced Vertices in Sparticle Searches for Next-to-Minimal Gauge Mediated Supersymmetric Models*, *Eur. Phys. J.* **C76** (2016) 482, [1606.03099].

[3] S. Blunier, G. Cottin, M. A. Díaz and B. Koch, *Phenomenology of a Higgs triplet model at future e^+e^- colliders*, *Phys. Rev.* **D95** (2017) 075038, [1611.07896].

[4] S. L. Glashow, *Partial Symmetries of Weak Interactions*, *Nucl. Phys.* **22** (1961) 579–588.

[5] S. Weinberg, *A Model of Leptons*, *Phys. Rev. Lett.* **19** (1967) 1264–1266.

[6] A. Salam and J. C. Ward, *Weak and electromagnetic interactions*, *Nuovo Cim.* **11** (1959) 568–577.

[7] D. J. Gross and F. Wilczek, *Ultraviolet Behavior of Nonabelian Gauge Theories*, *Phys. Rev. Lett.* **30** (1973) 1343–1346.

[8] H. D. Politzer, *Reliable Perturbative Results for Strong Interactions?*, *Phys. Rev. Lett.* **30** (1973) 1346–1349.

[9] G. 't Hooft and M. J. G. Veltman, *Regularization and Renormalization of Gauge Fields*, *Nucl. Phys.* **B44** (1972) 189–213.

[10] M. D. Schwartz, *Quantum Field Theory and the Standard Model*. Cambridge University Press, 2014.

[11] I. by Sandbox Studio Chicago, "The Standard Model of Particle Physics.

`http://www.symmetrymagazine.org/standard-model/`." Mar, 2015.

[12] PARTICLE DATA GROUP collaboration, C. Patrignani et al., *Review of Particle Physics*, *Chin. Phys.* **C40** (2016) 100001.

[13] TEVATRON ELECTROWEAK WORKING GROUP, CDF, DELPHI, SLD ELECTROWEAK AND HEAVY FLAVOUR GROUPS, ALEPH, LEP ELECTROWEAK WORKING GROUP, SLD, OPAL, D0, L3 collaboration, L. E. W. Group, *Precision Electroweak Measurements and Constraints on the Standard Model*, 1012.2367.

[14] ATLAS collaboration, G. Aad et al., *Observation of a new particle in the search for the Standard Model Higgs boson with the ATLAS detector at the LHC*, *Phys. Lett.* **B716** (2012) 1–29, [1207.7214].

[15] CMS collaboration, S. Chatrchyan et al., *Observation of a new boson at a mass of 125 GeV with the CMS experiment at the LHC*, *Phys. Lett.* **B716** (2012) 30–61, [1207.7235].

[16] R. N. Mohapatra, *UNIFICATION AND SUPERSYMMETRY. THE FRONTIERS OF QUARK - LEPTON PHYSICS*. Springer, Berlin, 1986, 10.1007/978-1-4757-1928-4.

[17] B. Gripaios, *Lectures on Physics Beyond the Standard Model*, 1503.02636.

[18] K. G. Wilson, *Confinement of Quarks*, *Phys. Rev.* **D10** (1974) 2445–2459.

[19] G. Altarelli and G. Parisi, *Asymptotic Freedom in Parton Language*, *Nucl. Phys.* **B126** (1977) 298–318.

[20] F. Englert and R. Brout, *Broken Symmetry and the Mass of Gauge Vector Mesons*, *Phys. Rev. Lett.* **13** (1964) 321–323.

[21] P. W. Higgs, *Broken symmetries, massless particles and gauge fields*, *Phys. Lett.* **12** (1964) 132–133.

[22] P. W. Higgs, *Broken Symmetries and the Masses of Gauge Bosons*, *Phys. Rev. Lett.* **13** (1964) 508–509.

[23] G. S. Guralnik, C. R. Hagen and T. W. B. Kibble, *Global Conservation Laws and Massless Particles*, *Phys. Rev. Lett.* **13** (1964) 585–587.

[24] P. W. Higgs, *Spontaneous Symmetry Breakdown without Massless Bosons*, *Phys.*

Rev. **145** (1966) 1156–1163.

[25] T. W. B. Kibble, *Symmetry breaking in nonAbelian gauge theories*, *Phys. Rev.* **155** (1967) 1554–1561.

[26] M. J. G. Veltman, *Radiative Corrections to Vector Boson Masses*, *Phys. Lett.* **B91** (1980) 95–98.

[27] S. Weinberg, *A New Light Boson?*, *Phys. Rev. Lett.* **40** (1978) 223–226.

[28] F. Wilczek, *Problem of Strong p and t Invariance in the Presence of Instantons*, *Phys. Rev. Lett.* **40** (1978) 279–282.

[29] B. C. Allanach, *Beyond the Standard Model Lectures for the 2016 European School of High-Energy Physics*, 1609.02015.

[30] R. Davis, *A review of the Homestake solar neutrino experiment*, *Prog.Part.Nucl.Phys.* **32** (1994) 13–32.

[31] SUPER-KAMIOKANDE COLLABORATION collaboration, Y. Fukuda et al., *Measurements of the solar neutrino flux from Super-Kamiokande's first 300 days*, *Phys.Rev.Lett.* **81** (1998) 1158–1162, [hep-ex/9805021].

[32] SNO COLLABORATION collaboration, Q. Ahmad et al., *Direct evidence for neutrino flavor transformation from neutral current interactions in the Sudbury Neutrino Observatory*, *Phys.Rev.Lett.* **89** (2002) 011301, [nucl-ex/0204008].

[33] KAMLAND COLLABORATION collaboration, K. Eguchi et al., *First results from KamLAND: Evidence for reactor anti-neutrino disappearance*, *Phys.Rev.Lett.* **90** (2003) 021802, [hep-ex/0212021].

[34] K2K COLLABORATION collaboration, M. Ahn et al., *Measurement of Neutrino Oscillation by the K2K Experiment*, *Phys.Rev.* **D74** (2006) 072003, [hep-ex/0606032].

[35] MINIBOONE COLLABORATION collaboration, A. Aguilar-Arevalo et al., *A Search for electron neutrino appearance at the $\Delta m^2 \sim 1 eV^2$ scale*, *Phys.Rev.Lett.* **98** (2007) 231801, [0704.1500].

[36] L. Volders., *Neutral hydrogen in M 33 and M 101*, *Bulletin of the Astronomical Institutes of the Netherlands* **14** (1959) 323–334.

[37] D. Clowe, M. Bradac, A. H. Gonzalez, M. Markevitch, S. W. Randall et al., *A*

direct empirical proof of the existence of dark matter, *Astrophys.J.* **648** (2006)
L109–L113, [astro-ph/0608407].

[38] WMAP Collaboration collaboration, D. Spergel et al., *Wilkinson Microwave
Anisotropy Probe (WMAP) three year results: implications for cosmology*,
Astrophys.J.Suppl. **170** (2007) 377, [astro-ph/0603449].

[39] Supernova Search Team collaboration, A. G. Riess et al., *Observational
evidence from supernovae for an accelerating universe and a cosmological constant*,
Astron.J. **116** (1998) 1009–1038, [astro-ph/9805201].

[40] Planck collaboration, P. A. R. Ade et al., *Planck 2013 results. XVI.
Cosmological parameters*, *Astron. Astrophys.* **571** (2014) A16, [1303.5076].

[41] K. Garrett and G. Duda, *Dark Matter: A Primer*, *Adv. Astron.* **2011** (2011)
968283, [1006.2483].

[42] WMAP collaboration, E. Komatsu et al., *Seven-Year Wilkinson Microwave
Anisotropy Probe (WMAP) Observations: Cosmological Interpretation*, *Astrophys.
J. Suppl.* **192** (2011) 18, [1001.4538].

[43] A. D. Sakharov, *Violation of CP Invariance, c Asymmetry, and Baryon
Asymmetry of the Universe*, *Pisma Zh. Eksp. Teor. Fiz.* **5** (1967) 32–35.

[44] R. N. Mohapatra, *ICTP lectures on theoretical aspects of neutrino masses and
mixings*, in *School on Neutrino Physics and Astrophysics (NEUPAST) Trieste,
Italy, September 23-October 4, 2002*, 2002. hep-ph/0211252.

[45] R. N. Mohapatra and G. Senjanovic, *Neutrino Mass and Spontaneous Parity
Violation*, *Phys. Rev. Lett.* **44** (1980) 912.

[46] S. Weinberg, *Varieties of Baryon and Lepton Nonconservation*, *Phys. Rev.* **D22**
(1980) 1694.

[47] J. W. F. Valle, *Neutrino physics overview*, *J. Phys. Conf. Ser.* **53** (2006) 473–505,
[hep-ph/0608101].

[48] J. W. F. Valle, *Gauge theories and the physics of neutrino mass*, *Prog. Part. Nucl.
Phys.* **26** (1991) 91–171.

[49] Y. Chikashige, R. N. Mohapatra and R. D. Peccei, *Are There Real Goldstone
Bosons Associated with Broken Lepton Number?*, *Phys. Lett.* **B98** (1981) 265–268.

[50] J. Schechter and J. W. F. Valle, *Neutrino Decay and Spontaneous Violation of Lepton Number*, *Phys. Rev.* **D25** (1982) 774.

[51] M. A. Diaz, M. A. Garcia-Jareno, D. A. Restrepo and J. W. F. Valle, *Seesaw Majoron model of neutrino mass and novel signals in Higgs boson production at LEP*, *Nucl. Phys.* **B527** (1998) 44–60, [hep-ph/9803362].

[52] "NuFit, http://www.nu-fit.org/." 2016.

[53] S. P. Martin, *A Supersymmetry primer*, hep-ph/9709356.

[54] R. Barbieri and G. F. Giudice, *Upper Bounds on Supersymmetric Particle Masses*, *Nucl. Phys.* **B306** (1988) 63–76.

[55] P. Athron and D. J. Miller, *A New Measure of Fine Tuning*, *Phys. Rev.* **D76** (2007) 075010, [0705.2241].

[56] "Is SUSY alive and well?, https://workshops.ift.uam-csic.es/susyaaw." Sep, 2016.

[57] A. Strumia, *The Fine-tuning price of the early LHC*, *JHEP* **04** (2011) 073, [1101.2195].

[58] R. Barbieri and A. Strumia, *The 'LEP paradox'*, in *4th Rencontres du Vietnam: Physics at Extreme Energies (Particle Physics and Astrophysics) Hanoi, Vietnam, July 19-25, 2000*, 2000. hep-ph/0007265.

[59] A. Delgado, G. F. Giudice and P. Slavich, *Dynamical mu term in gauge mediation*, *Phys. Lett.* **B653** (2007) 424–433, [0706.3873].

[60] E. Bagnaschi, G. F. Giudice, P. Slavich and A. Strumia, *Higgs Mass and Unnatural Supersymmetry*, *JHEP* **09** (2014) 092, [1407.4081].

[61] N. Arkani-Hamed and S. Dimopoulos, *Supersymmetric unification without low energy supersymmetry and signatures for fine-tuning at the LHC*, *JHEP* **0506** (2005) 073, [hep-th/0405159].

[62] G. Giudice and A. Romanino, *Split supersymmetry*, *Nucl.Phys.* **B699** (2004) 65–89, [hep-ph/0406088].

[63] A. Arvanitaki, N. Craig, S. Dimopoulos and G. Villadoro, *Mini-Split*, *JHEP* **02** (2013) 126, [1210.0555].

[64] H. Arason, D. J. Castano, B. Keszthelyi, S. Mikaelian, E. J. Piard, P. Ramond et al., *Renormalization group study of the standard model and its extensions. 1. The Standard model*, Phys. Rev. **D46** (1992) 3945–3965.

[65] R. Catena and L. Covi, *SUSY dark matter(s)*, Eur. Phys. J. **C74** (2014) 2703, [`1310.4776`].

[66] A. H. Chamseddine, R. L. Arnowitt and P. Nath, *Locally Supersymmetric Grand Unification*, Phys.Rev.Lett. **49** (1982) 970.

[67] R. Barbieri, S. Ferrara and C. A. Savoy, *Gauge Models with Spontaneously Broken Local Supersymmetry*, Phys.Lett. **B119** (1982) 343.

[68] L. E. Ibanez, *Locally Supersymmetric SU(5) Grand Unification*, Phys.Lett. **B118** (1982) 73.

[69] L. J. Hall, J. D. Lykken and S. Weinberg, *Supergravity as the Messenger of Supersymmetry Breaking*, Phys.Rev. **D27** (1983) 2359–2378.

[70] N. Ohta, *GRAND UNIFIED THEORIES BASED ON LOCAL SUPERSYMMETRY*, Prog.Theor.Phys. **70** (1983) 542.

[71] R. Barbier, C. Berat, M. Besancon, M. Chemtob, A. Deandrea et al., *R-parity violating supersymmetry*, Phys.Rept. **420** (2005) 1–202, [`hep-ph/0406039`].

[72] C. Csaki, E. Kuflik and T. Volansky, *Dynamical R-Parity Violation*, Phys.Rev.Lett. **112** (2014) 131801, [`1309.5957`].

[73] S. Dimopoulos, M. Dine, S. Raby and S. D. Thomas, *Experimental signatures of low-energy gauge mediated supersymmetry breaking*, Phys. Rev. Lett. **76** (1996) 3494–3497, [`hep-ph/9601367`].

[74] M. J. Strassler and K. M. Zurek, *Echoes of a hidden valley at hadron colliders*, Phys.Lett. **B651** (2007) 374–379, [`hep-ph/0604261`].

[75] P. Schuster, N. Toro and I. Yavin, *Terrestrial and Solar Limits on Long-Lived Particles in a Dark Sector*, Phys.Rev. **D81** (2010) 016002, [`0910.1602`].

[76] J. Fan, M. Reece and J. T. Ruderman, *Stealth Supersymmetry*, JHEP **1111** (2011) 012, [`1105.5135`].

[77] B. Allanach, M. Badziak, C. Hugonie and R. Ziegler, *Light Sparticles from a Light Singlet in Gauge Mediation*, Phys. Rev. **D92** (2015) 015006, [`1502.05836`].

[78] L. Randall and R. Sundrum, *Out of this world supersymmetry breaking*, *Nucl. Phys.* **B557** (1999) 79–118, [`hep-th/9810155`].

[79] G. F. Giudice, M. A. Luty, H. Murayama and R. Rattazzi, *Gaugino mass without singlets*, *JHEP* **12** (1998) 027, [`hep-ph/9810442`].

[80] G. 't Hooft, *Magnetic Monopoles in Unified Gauge Theories*, *Nucl. Phys.* **B79** (1974) 276–284.

[81] L. J. Hall, K. Jedamzik, J. March-Russell and S. M. West, *Freeze-In Production of FIMP Dark Matter*, *JHEP* **03** (2010) 080, [`0911.1120`].

[82] R. T. Co, F. D'Eramo, L. J. Hall and D. Pappadopulo, *Freeze-In Dark Matter with Displaced Signatures at Colliders*, `1506.07532`.

[83] M. Fairbairn, A. C. Kraan, D. A. Milstead, T. Sjostrand, P. Z. Skands and T. Sloan, *Stable massive particles at colliders*, *Phys. Rept.* **438** (2007) 1–63, [`hep-ph/0611040`].

[84] J. Schechter and J. W. F. Valle, *Neutrino Masses in SU(2) x U(1) Theories*, *Phys. Rev.* **D22** (1980) 2227.

[85] T. P. Cheng and L.-F. Li, *Neutrino Masses, Mixings and Oscillations in SU(2) x U(1) Models of Electroweak Interactions*, *Phys. Rev.* **D22** (1980) 2860.

[86] E. J. Chun, K. Y. Lee and S. C. Park, *Testing Higgs triplet model and neutrino mass patterns*, *Phys. Lett.* **B566** (2003) 142–151, [`hep-ph/0304069`].

[87] E. Accomando et al., *Workshop on CP Studies and Non-Standard Higgs Physics*, `hep-ph/0608079`.

[88] A. G. Akeroyd, M. Aoki and H. Sugiyama, *Probing Majorana Phases and Neutrino Mass Spectrum in the Higgs Triplet Model at the CERN LHC*, *Phys. Rev.* **D77** (2008) 075010, [`0712.4019`].

[89] J. Garayoa and T. Schwetz, *Neutrino mass hierarchy and Majorana CP phases within the Higgs triplet model at the LHC*, *JHEP* **03** (2008) 009, [`0712.1453`].

[90] H. Nishiura and T. Fukuyama, *Determination of the unknown absolute neutrino mass and MNS parameters at the LHC in the Higgs triplet model*, `0909.0595`.

[91] P. S. Bhupal Dev, D. K. Ghosh, N. Okada and I. Saha, *125 GeV Higgs Boson and the Type-II Seesaw Model*, *JHEP* **03** (2013) 150, [`1301.3453`].

[92] ATLAS, CMS collaboration, G. Aad et al., *Combined Measurement of the Higgs Boson Mass in pp Collisions at $\sqrt{s} = 7$ and 8 TeV with the ATLAS and CMS Experiments*, *Phys. Rev. Lett.* **114** (2015) 191803, [1503.07589].

[93] M. Carena, A. de Gouvea, A. Freitas and M. Schmitt, *Invisible Z boson decays at e+ e- colliders*, *Phys. Rev.* **D68** (2003) 113007, [hep-ph/0308053].

[94] E. K. Akhmedov, Z. G. Berezhiani, R. N. Mohapatra and G. Senjanovic, *Planck scale effects on the majoron*, *Phys. Lett.* **B299** (1993) 90–93, [hep-ph/9209285].

[95] V. Berezinsky and J. W. F. Valle, *The KeV majoron as a dark matter particle*, *Phys. Lett.* **B318** (1993) 360–366, [hep-ph/9309214].

[96] M. Lattanzi, *Decaying Majoron Dark Matter and Neutrino Masses*, *AIP Conf. Proc.* **966** (2007) 163–169, [0802.3155].

[97] Yu. A. Golfand and E. P. Likhtman, *Extension of the Algebra of Poincare Group Generators and Violation of p Invariance*, *JETP Lett.* **13** (1971) 323–326.

[98] J. Wess and B. Zumino, *Supergauge Transformations in Four-Dimensions*, *Nucl. Phys.* **B70** (1974) 39–50.

[99] H. E. Haber and G. L. Kane, *The Search for Supersymmetry: Probing Physics Beyond the Standard Model*, *Phys. Rept.* **117** (1985) 75–263.

[100] J. R. Ellis, D. V. Nanopoulos and K. Tamvakis, *Grand Unification in Simple Supergravity*, *Phys. Lett.* **B121** (1983) 123–129.

[101] L. Alvarez-Gaume, J. Polchinski and M. B. Wise, *Minimal Low-Energy Supergravity*, *Nucl. Phys.* **B221** (1983) 495.

[102] G. F. Giudice and R. Rattazzi, *Theories with gauge mediated supersymmetry breaking*, *Phys. Rept.* **322** (1999) 419–499, [hep-ph/9801271].

[103] G. R. Dvali, G. F. Giudice and A. Pomarol, *The Mu problem in theories with gauge mediated supersymmetry breaking*, *Nucl. Phys.* **B478** (1996) 31–45, [hep-ph/9603238].

[104] S. L. Glashow, J. Iliopoulos and L. Maiani, *Weak Interactions with Lepton-Hadron Symmetry*, *Phys. Rev.* **D2** (1970) 1285–1292.

[105] S. Dimopoulos and D. W. Sutter, *The Supersymmetric flavor problem*, *Nucl. Phys.* **B452** (1995) 496–512, [hep-ph/9504415].

[106] J. E. Kim and H. P. Nilles, *The mu Problem and the Strong CP Problem*, *Phys. Lett.* **B138** (1984) 150–154.

[107] U. Ellwanger, C. Hugonie and A. M. Teixeira, *The Next-to-Minimal Supersymmetric Standard Model*, *Phys. Rept.* **496** (2010) 1–77, [0910.1785].

[108] L. Covi, *Gravitino Dark Matter confronts LHC*, *J.Phys.Conf.Ser.* **485** (2014) 012002.

[109] A. Y. Smirnov and F. Vissani, *Upper bound on all products of R-parity violating couplings lambda-prime and lambda-prime-prime from proton decay*, *Phys.Lett.* **B380** (1996) 317–323, [hep-ph/9601387].

[110] M. Hirsch, M. Diaz, W. Porod, J. Romao and J. Valle, *Neutrino masses and mixings from supersymmetry with bilinear R parity violation: A Theory for solar and atmospheric neutrino oscillations*, *Phys.Rev.* **D62** (2000) 113008, [hep-ph/0004115].

[111] H. K. Dreiner and G. G. Ross, *R-parity violation at hadron colliders*, *Nucl. Phys.* **B365** (1991) 597–613.

[112] N. Arkani-Hamed, S. Dimopoulos, G. Giudice and A. Romanino, *Aspects of split supersymmetry*, *Nucl.Phys.* **B709** (2005) 3–46, [hep-ph/0409232].

[113] G. F. Giudice and A. Strumia, *Probing High-Scale and Split Supersymmetry with Higgs Mass Measurements*, *Nucl.Phys.* **B858** (2012) 63–83, [1108.6077].

[114] N. Arkani-Hamed, A. Gupta, D. E. Kaplan, N. Weiner and T. Zorawski, *Simply Unnatural Supersymmetry*, 1212.6971.

[115] P. Gambino, G. Giudice and P. Slavich, *Gluino decays in split supersymmetry*, *Nucl.Phys.* **B726** (2005) 35–52, [hep-ph/0506214].

[116] G. R. Farrar and P. Fayet, *Phenomenology of the Production, Decay, and Detection of New Hadronic States Associated with Supersymmetry*, *Phys.Lett.* **B76** (1978) 575–579.

[117] S. P. Martin, *Generalized messengers of supersymmetry breaking and the sparticle mass spectrum*, *Phys. Rev.* **D55** (1997) 3177–3187, [hep-ph/9608224].

[118] G. F. Giudice and R. Rattazzi, *Extracting supersymmetry breaking effects from wave function renormalization*, *Nucl. Phys.* **B511** (1998) 25–44,

[hep-ph/9706540].

[119] M. Badziak, M. Olechowski and S. Pokorski, *New Regions in the NMSSM with a 125 GeV Higgs*, *JHEP* **06** (2013) 043, [1304.5437].

[120] DELPHI, OPAL, ALEPH, LEP Working Group for Higgs Boson Searches, L3 collaboration, S. Schael et al., *Search for neutral MSSM Higgs bosons at LEP*, *Eur. Phys. J.* **C47** (2006) 547–587, [hep-ex/0602042].

[121] A. Team, "The four main LHC experiments, https://cds.cern.ch/record/40525." Jun, 1999.

[122] ATLAS Collaboration collaboration, A. Collaboration, *The ATLAS Experiment at the CERN Large Hadron Collider*, *JINST* **3** (2008) S08003.

[123] J. Pequenao, "Computer generated image of the whole ATLAS detector, https://cds.cern.ch/record/1095924." Mar, 2008.

[124] ATLAS Collaboration collaboration, A. Collaboration, *Expected Performance of the ATLAS Experiment - Detector, Trigger and Physics*, 0901.0512.

[125] A. Collaboration, "ATLAS Events at 13 TeV - First 2016 Stable Beams. https://cds.cern.ch/record/2148236." Apr, 2016.

[126] J. Pequenao, "Computer generated image of the ATLAS inner detector. https://cds.cern.ch/record/1095926." Mar, 2008.

[127] M. Capeans, G. Darbo, K. Einsweiller, M. Elsing, T. Flick, M. Garcia-Sciveres et al., *ATLAS Insertable B-Layer Technical Design Report*, Tech. Rep. CERN-LHCC-2010-013. ATLAS-TDR-19, CERN, Geneva, Sep, 2010.

[128] R. Mankel, *Pattern recognition and event reconstruction in particle physics experiments*, *Rept. Prog. Phys.* **67** (2004) 553, [physics/0402039].

[129] A. Salzburger, *The ATLAS Track Extrapolation Package*, Tech. Rep. ATL-SOFT-PUB-2007-005, ATL-COM-SOFT-2007-010, 2007.

[130] F. M. Brochu, *Reconstruction of tracks with large impact parameter in the Inner Detector.*, Tech. Rep. ATL-COM-PHYS-2012-039, CERN, Geneva, Jan, 2012.

[131] ATLAS collaboration, *Performance of primary vertex reconstruction in proton-proton collisions at $\sqrt{s} = 7$ TeV in the ATLAS experiment*, .

[132] P. Billoir and S. Qian, *Fast vertex fitting with a local parametrization of tracks*, *Nucl. Instrum. Meth.* **A311** (1992) 139–150.

[133] S. R. Das, *On a new approach for finding all the modified cut-sets in an incompatibility graph)*, *IEEE Transactions on Computers* **v22(2) 187** (1973) .

[134] M. Cacciari, G. P. Salam and G. Soyez, *The Anti-k(t) jet clustering algorithm*, *J. High Energy Phys.* **04** (2008) 063, [0802.1189].

[135] M. Cacciari and G. P. Salam, *Dispelling the N^3 myth for the k_t jet-finder*, *Phys. Lett. B* **641** (2006) 57–61, [hep-ph/0512210].

[136] ATLAS Collaboration, *Jet energy measurement with the ATLAS detector in proton-proton collisions at $\sqrt{s} = 7$ TeV*, *Eur. Phys. J. C* **73** (2013) 2304, [1112.6426].

[137] W. Lampl et al., *Calorimeter clustering algorithms: Description and performance*, *ATL-LARG-PUB-2008-002*, http://cds.cern.ch/record/1099735/ (2008) .

[138] ATLAS Collaboration, *Performance of Missing Transverse Momentum Reconstruction in Proton-Proton Collisions at 7 TeV with ATLAS*, *Eur. Phys. J. C* **72** (2012) 1844, [1108.5602].

[139] ATLAS Collaboration, *Performance of Missing Transverse Momentum Reconstruction in ATLAS studied in Proton-Proton Collisions recorded in 2012 at 8 TeV*, *ATLAS-CONF-2013-082*, http://cds.cern.ch/record/1570993/ (2013) .

[140] E. Gardi, N. Glover and A. Robson, eds., *Proceedings, 69th Scottish Universities Summer School in Physics : LHC Phenomenology (SUSSP69)*, Scottish graduate series, (Cham), Springer, Springer, 2015. 10.1007/978-3-319-05362-2.

[141] R. K. Ellis, W. J. Stirling and B. R. Webber, *QCD and collider physics*, *Camb. Monogr. Part. Phys. Nucl. Phys. Cosmol.* **8** (1996) 1–435.

[142] A. L. Read, *Presentation of search results: The CL(s) technique*, *J. Phys. G* **28** (2002) 2693–2704.

[143] D. Casadei, *Statistical methods used in ATLAS for exclusion and discovery*, in *Proceedings, PHYSTAT 2011 Workshop on Statistical Issues Related to Discovery Claims in Search Experiments and Unfolding, CERN,Geneva, Switzerland 17-20 January 2011*, (Geneva), pp. 94–99, CERN, CERN, 2011. 1108.2288. DOI.

[144] L. Lyons, *STATISTICS FOR NUCLEAR AND PARTICLE PHYSICISTS*. 1986.

[145] T. Sjöstrand, S. Mrenna and P. Z. Skands, *PYTHIA 6.4 Physics and Manual*, *J. High Energy Phys.* **05** (2006) 026, [hep-ph/0603175].

[146] T. Sjostrand, S. Mrenna and P. Z. Skands, *A Brief Introduction to PYTHIA 8.1*, *Comput.Phys.Commun.* **178** (2008) 852–867, [0710.3820].

[147] M. Bahr et al., *Herwig++ Physics and Manual*, *Eur. Phys. J.* **C58** (2008) 639–707, [0803.0883].

[148] J. Alwall, R. Frederix, S. Frixione, V. Hirschi, F. Maltoni, O. Mattelaer et al., *The automated computation of tree-level and next-to-leading order differential cross sections, and their matching to parton shower simulations*, *JHEP* **07** (2014) 079, [1405.0301].

[149] F. S. C. Krauss, "Sketch of a tth event.". available at http://www.opensciencegrid.org/wp-content/uploads/2014/05/event.jpg.."

[150] DELPHES 3 collaboration, J. de Favereau, C. Delaere, P. Demin, A. Giammanco, V. Lemaître, A. Mertens et al., *DELPHES 3, A modular framework for fast simulation of a generic collider experiment*, *JHEP* **02** (2014) 057, [1307.6346].

[151] GEANT4 collaboration, S. Agostinelli et al., *GEANT4: A Simulation toolkit*, *Nucl.Instrum.Meth.* **A506** (2003) 250–303.

[152] B. C. Allanach, *SOFTSUSY: a program for calculating supersymmetric spectra*, *Comput. Phys. Commun.* **143** (2002) 305–331, [hep-ph/0104145].

[153] B. C. Allanach, P. Athron, L. C. Tunstall, A. Voigt and A. G. Williams, *Next-to-Minimal SOFTSUSY*, *Comput. Phys. Commun.* **185** (2014) 2322–2339, [1311.7659].

[154] M. Muhlleitner, A. Djouadi and Y. Mambrini, *SDECAY: A Fortran code for the decays of the supersymmetric particles in the MSSM*, *Comput. Phys. Commun.* **168** (2005) 46–70, [hep-ph/0311167].

[155] P. Z. Skands et al., *SUSY Les Houches accord: Interfacing SUSY spectrum calculators, decay packages, and event generators*, *JHEP* **07** (2004) 036, [hep-ph/0311123].

[156] B. C. Allanach et al., *SUSY Les Houches Accord 2*, *Comput. Phys. Commun.* **180**

(2009) 8–25, [0801.0045].

[157] A. Alloul, N. D. Christensen, C. Degrande, C. Duhr and B. Fuks, *FeynRules 2.0 - A complete toolbox for tree-level phenomenology*, *Comput. Phys. Commun.* **185** (2014) 2250–2300, [1310.1921].

[158] G. Cowan, K. Cranmer, E. Gross and O. Vitells, *Asymptotic formulae for likelihood-based tests of new physics*, *Eur. Phys. J.* **C71** (2011) 1554, [1007.1727].

[159] W. A. Rolke, A. M. Lopez and J. Conrad, *Limits and confidence intervals in the presence of nuisance parameters*, *Nucl. Instrum. Meth.* **A551** (2005) 493–503, [physics/0403059].

[160] ATLAS Collaboration, *Searches for heavy long-lived charged particles with the atlas detector in proton-proton collisions at $\sqrt{s} = 8$ tev*, *J. High Energy Phys.* **01** (2015) 068, [1411.6795].

[161] ATLAS Collaboration, *Search for pair-produced long-lived neutral particles decaying in the ATLAS hadronic calorimeter in pp collisions at $\sqrt{s} = 8$ TeV*, *Phys. Lett. B* **743** (2015) 15–34, [1501.04020].

[162] ATLAS collaboration, M. Aaboud et al., *Search for metastable heavy charged particles with large ionization energy loss in pp collisions at $\sqrt{s} = 13$ TeV using the ATLAS experiment*, *Phys. Rev.* **D93** (2016) 112015, [1604.04520].

[163] ATLAS Collaboration, *Search for long-lived stopped R-hadrons decaying out-of-time with pp collisions using the ATLAS detector*, *Phys. Rev. D* **88** (2013) 112003, [1310.6584].

[164] ATLAS collaboration, G. Aad et al., *Search for charginos nearly mass degenerate with the lightest neutralino based on a disappearing-track signature in pp collisions at $\sqrt{(s)}=8$ TeV with the ATLAS detector*, *Phys. Rev.* **D88** (2013) 112006, [1310.3675].

[165] ATLAS collaboration, G. Aad et al., *Search for nonpointing and delayed photons in the diphoton and missing transverse momentum final state in 8 TeV pp collisions at the LHC using the ATLAS detector*, *Phys. Rev.* **D90** (2014) 112005, [1409.5542].

[166] Z. Liu and B. Tweedie, *The Fate of Long-Lived Superparticles with Hadronic Decays after LHC Run 1*, *JHEP* **06** (2015) 042, [1503.05923].

[167] C. Csaki, E. Kuflik, S. Lombardo, O. Slone and T. Volansky, *Phenomenology of a Long-Lived LSP with R-Parity Violation*, *JHEP* **08** (2015) 016, [1505.00784].

[168] Y. Cui and B. Shuve, *Probing Baryogenesis with Displaced Vertices at the LHC*, *JHEP* **02** (2015) 049, [1409.6729].

[169] C. Csaki, E. Kuflik, S. Lombardo and O. Slone, *Searching for displaced Higgs boson decays*, *Phys. Rev.* **D92** (2015) 073008, [1508.01522].

[170] J. A. Evans and J. Shelton, *Long-Lived Staus and Displaced Leptons at the LHC*, *JHEP* **04** (2016) 056, [1601.01326].

[171] A. Coccaro, D. Curtin, H. J. Lubatti, H. Russell and J. Shelton, *Data-driven Model-independent Searches for Long-lived Particles at the LHC*, 1605.02742.

[172] A. de la Puente and A. Szynkman, *Long-lived Colored Scalars at the LHC*, *Eur. Phys. J.* **C76** (2016) 124, [1504.07293].

[173] N. Barlow, K. Bentdz, J. Bouffard, G. Cottin, J. Ernst, A. Fischer et al., *Search for long-lived, heavy particles using a multi-track displaced vertex, in pp collisions at 8 TeV centre-of-mass energy, with the ATLAS detector at the LHC.*, Tech. Rep. ATL-COM-PHYS-2014-370, CERN, Geneva, Apr, 2014.

[174] ATLAS collaboration, G. Aad et al., *Search for long-lived, weakly interacting particles that decay to displaced hadronic jets in proton-proton collisions at $\sqrt{s} = 8$ TeV with the ATLAS detector*, 1504.03634.

[175] CMS Collaboration, *Search in leptonic channels for heavy resonances decaying to long-lived neutral particles*, *J. High Energy Phys.* **02** (2013) 085, [1211.2472].

[176] CMS collaboration, V. Khachatryan et al., *Search for long-lived particles that decay into final states containing two electrons or two muons in proton-proton collisions at $\sqrt{s} = 8$ TeV*, *Phys.Rev.* **D91** (2015) 052012, [1411.6977].

[177] CMS Collaboration, *Search for "Displaced Supersymmetry" in events with an electron and a muon with large impact parameters*, *Phys. Rev. Lett.* **114** (2015) 061801, [1409.4789].

[178] CMS Collaboration, *Search for long-lived neutral particles decaying to quark-antiquark pairs in proton-proton collisions at sqrt(s) = 8 TeV*, *Phys. Rev. D* **91** (2015) 012007, [1411.6530].

[179] LHCB collaboration, R. Aaij et al., *Search for long-lived particles decaying to jet pairs*, 1412.3021.

[180] BELLE collaboration, D. Liventsev et al., *Search for heavy neutrinos at Belle*, *Phys. Rev. D* **87** (2013) 071102, [1301.1105].

[181] BABAR collaboration, J. P. Lees et al., *Search for Long-Lived Particles in e^+e^- Collisions*, 1502.02580.

[182] D0 collaboration, V. M. Abazov et al., *Search for neutral, long-lived particles decaying into two muons in $p\bar{p}$ collisions at $\sqrt{s}$ = 1.96-TeV*, *Phys. Rev. Lett.* **97** (2006) 161802, [hep-ex/0607028].

[183] D0 collaboration, V. M. Abazov et al., *Search for Resonant Pair Production of long-lived particles decaying to b anti-b in p anti-p collisions at s**(1/2) = 1.96-TeV*, *Phys. Rev. Lett.* **103** (2009) 071801, [0906.1787].

[184] CDF collaboration, F. Abe et al., *Search for long-lived parents of Z^0 bosons in $p\bar{p}$ collisions at $\sqrt{s}$ = 1.8 TeV*, *Phys. Rev. D* **58** (1998) 051102, [hep-ex/9805017].

[185] ALEPH collaboration, A. Heister et al., *Search for gauge mediated SUSY breaking topologies in e^+e^- collisions at center-of-mass energies up to 209-GeV*, *Eur. Phys. J. C* **25** (2002) 339–351, [hep-ex/0203024].

[186] ATLAS collaboration, T. A. collaboration, *Search for long-lived, heavy particles in final states with a muon and a multi-track displaced vertex in proton-proton collisions at sqrt(s) = 8TeV with the ATLAS detector.*, .

[187] ATLAS collaboration, G. Aad et al., *Search for displaced vertices arising from decays of new heavy particles in 7 TeV pp collisions at ATLAS*, *Phys. Lett.* **B707** (2012) 478–496, [1109.2242].

[188] ATLAS collaboration, G. Aad et al., *Search for long-lived, heavy particles in final states with a muon and multi-track displaced vertex in proton-proton collisions at $\sqrt{s}$ = 7 TeV with the ATLAS detector*, *Phys. Lett.* **B719** (2013) 280–298, [1210.7451].

[189] ATLAS collaboration, *ATLAS tunes of PYTHIA 6 and Pythia 8 for MC11*, .

[190] P. M. Nadolsky, H.-L. Lai, Q.-H. Cao, J. Huston, J. Pumplin, D. Stump et al., *Implications of CTEQ global analysis for collider observables*, *Phys. Rev.* **D78** (2008) 013004, [0802.0007].

[191] ATLAS collaboration, G. Aad et al., *The ATLAS Simulation Infrastructure*, *Eur. Phys. J.* **C70** (2010) 823–874, [1005.4568].

[192] R. Mackeprang and D. Milstead, *An Updated Description of Heavy-Hadron Interactions in GEANT-4*, *Eur. Phys. J.* **C66** (2010) 493–501, [0908.1868].

[193] https://twiki.cern.ch/twiki/bin/viewauth/AtlasProtected/ SUSYSignalUncertainties#Signal_cross_sections.

[194] *https://twiki.cern.ch/twiki/bin/viewauth/Atlas/ DataPreparationCheckListForPhysicsAnalysis.*

[195] *https://twiki.cern.ch/twiki/bin/view/AtlasProtected/ SusyObjectDefinitionsr178TeV.*

[196] *https://twiki.cern.ch/twiki/bin/viewauth/AtlasProtected/ HowToCleanJets2012.*

[197] *https://twiki.cern.ch/twiki/bin/viewauth/AtlasProtected/ BCHCleaningTool.*

[198] N. E. Pettersson, *Search for long-lived supersymmetry particles by signature of a high track-multiplicity displaced vertex using the LHC-ATLAS Experiment.* PhD thesis, Tokyo Inst. Tech., 2015-11-17.

[199] ATLAS Collaboration, *Jet energy measurement and its systematic uncertainty in proton-proton collisions at $\sqrt{s} = 7$ TeV with the ATLAS detector*, *Eur. Phys. J. C* **75** (2015) 17, [1406.0076].

[200] ATLAS Collaboration, *Jet energy resolution in proton-proton collisions at $\sqrt{s} = 7$ TeV recorded in 2010 with the ATLAS detector*, *Eur. Phys. J. C* **73** (2013) 2306, [1210.6210].

[201] J. Alwall, M. Herquet, F. Maltoni, O. Mattelaer and T. Stelzer, *MadGraph 5 : Going Beyond*, *J. High Energy Phys.* **06** (2011) 128, [1106.0522].

[202] https://atlas.web.cern.ch/Atlas/GROUPS/PHYSICS/PAPERS/SUSY-2014-02.

[203] T. Sjöstrand, S. Ask, J. R. Christiansen, R. Corke, N. Desai, P. Ilten et al., *An Introduction to PYTHIA 8.2*, *Comput. Phys. Commun.* **191** (2015) 159–177, [1410.3012].

[204] ATLAS collaboration, G. Aad et al., *Improved luminosity determination in pp*

collisions at sqrt(s) = 7 TeV using the ATLAS detector at the LHC, *Eur. Phys. J.* **C73** (2013) 2518, [1302.4393].

[205] M. Baak, G. J. Besjes, D. Cote, A. Koutsman, J. Lorenz and D. Short, *HistFitter software framework for statistical data analysis*, 1410.1280.

[206] U. Ellwanger and C. Hugonie, *NMHDECAY 2.0: An Updated program for sparticle masses, Higgs masses, couplings and decay widths in the NMSSM*, *Comput. Phys. Commun.* **175** (2006) 290–303, [hep-ph/0508022].

[207] U. Ellwanger and C. Hugonie, *NMSPEC: A Fortran code for the sparticle and Higgs masses in the NMSSM with GUT scale boundary conditions*, *Comput. Phys. Commun.* **177** (2007) 399–407, [hep-ph/0612134].

[208] A. Buckley, *PySLHA: a Pythonic interface to SUSY Les Houches Accord data*, *Eur. Phys. J.* **C75** (2015) 467, [1305.4194].

[209] M. Cacciari, G. P. Salam and G. Soyez, *FastJet User Manual*, *Eur. Phys. J.* **C72** (2012) 1896, [1111.6097].

[210] ATLAS collaboration, G. Aad et al., *Search for squarks and gluinos with the ATLAS detector in final states with jets and missing transverse momentum using $\sqrt{s} = 8$ TeV proton–proton collision data*, *JHEP* **09** (2014) 176, [1405.7875].

[211] ATLAS collaboration, M. Aaboud et al., *Search for squarks and gluinos in final states with jets and missing transverse momentum at $\sqrt{s} = 13$ TeV with the ATLAS detector*, 1605.03814.

[212] ATLAS collaboration, G. Aad et al., *Triggers for displaced decays of long-lived neutral particles in the ATLAS detector*, *JINST* **8** (2013) P07015, [1305.2284].

[213] A. G. Akeroyd, M. A. Diaz, M. A. Rivera and D. Romero, *Fermiophobia in a Higgs Triplet Model*, *Phys. Rev.* **D83** (2011) 095003, [1010.1160].

[214] G. B. Gelmini and M. Roncadelli, *Left-Handed Neutrino Mass Scale and Spontaneously Broken Lepton Number*, *Phys. Lett.* **B99** (1981) 411–415.

[215] C.-W. Chiang, T. Nomura and K. Tsumura, *Search for doubly charged Higgs bosons using the same-sign diboson mode at the LHC*, *Phys. Rev.* **D85** (2012) 095023, [1202.2014].

[216] A. G. Akeroyd and S. Moretti, *Production of doubly charged scalars from the decay*

of a heavy SM-like Higgs boson in the Higgs Triplet Model, *Phys. Rev.* **D84** (2011) 035028, [1106.3427].

[217] A. G. Akeroyd and H. Sugiyama, *Production of doubly charged scalars from the decay of singly charged scalars in the Higgs Triplet Model*, *Phys. Rev.* **D84** (2011) 035010, [1105.2209].

[218] A. G. Akeroyd, C.-W. Chiang and N. Gaur, *Leptonic signatures of doubly charged Higgs boson production at the LHC*, *JHEP* **11** (2010) 005, [1009.2780].

[219] A. G. Akeroyd and C.-W. Chiang, *Doubly charged Higgs bosons and three-lepton signatures in the Higgs Triplet Model*, *Phys. Rev.* **D80** (2009) 113010, [0909.4419].

[220] P. Fileviez Perez, T. Han, G.-y. Huang, T. Li and K. Wang, *Neutrino Masses and the CERN LHC: Testing Type II Seesaw*, *Phys. Rev.* **D78** (2008) 015018, [0805.3536].

[221] A. G. Akeroyd and M. Aoki, *Single and pair production of doubly charged Higgs bosons at hadron colliders*, *Phys. Rev.* **D72** (2005) 035011, [hep-ph/0506176].

[222] J.-F. Shen, Y.-P. Bi, Y. Yu and Y.-J. Zhang, *Production of singly and doubly charged Higgs bosons from Higgs triplet model at future linear colliders*, *Int. J. Mod. Phys.* **A30** (2015) 1550096.

[223] J. Cao, Y.-H. Gao and J.-F. Shen, *Associated production of pairs of doubly charged Higgs bosons in the Higgs triplet model at the ILC*, *Europhys. Lett.* **108** (2014) 31003.

[224] J. F. Shen and J. Cao, *Pair production of charged and doubly charged Higgs bosons at ILC in the Higgs triplet model*, *J. Phys.* **G41** (2014) 105003.

[225] J. Cao and J.-F. Shen, *Triple Higgs boson production at ILC in the Higgs triplet model*, *Mod. Phys. Lett.* **A29** (2014) 1450092.

[226] K. Yagyu, *Doubly-charged Higgs bosons in the diboson decay scenario at the ILC*, in *International Workshop on Future Linear Colliders (LCWS13) Tokyo, Japan, November 11-15, 2013*, 2014. 1405.5149.

[227] Y. Yu, Y.-P. Bi and J.-F. Shen, *Associated production of the doubly-charged scalar pair with the Higgs boson in the Georgi–Machacek model at the ILC*, *Phys. Lett.* **B759** (2016) 513–519.

[228] C.-W. Chiang, S. Kanemura and K. Yagyu, *Phenomenology of the Georgi-Machacek model at future electron-positron colliders*, *Phys. Rev.* **D93** (2016) 055002, [1510.06297].

[229] K.-m. Cheung, R. J. N. Phillips and A. Pilaftsis, *Signatures of Higgs triplet representations at TeV e+ e- colliders*, *Phys. Rev.* **D51** (1995) 4731–4737, [hep-ph/9411333].

[230] R. Godbole, B. Mukhopadhyaya and M. Nowakowski, *Triplet Higgs bosons at e+ e- colliders*, *Phys. Lett.* **B352** (1995) 388–393, [hep-ph/9411324].

[231] G. Barenboim, K. Huitu, J. Maalampi and M. Raidal, *Constraints on doubly charged Higgs interactions at linear collider*, *Phys. Lett.* **B394** (1997) 132–138, [hep-ph/9611362].

[232] F. Arbabifar, S. Bahrami and M. Frank, *Neutral Higgs Bosons in the Higgs Triplet Model with nontrivial mixing*, *Phys. Rev.* **D87** (2013) 015020, [1211.6797].

[233] A. G. Akeroyd, S. Moretti and H. Sugiyama, *Five-lepton and six-lepton signatures from production of neutral triplet scalars in the Higgs Triplet Model*, *Phys. Rev.* **D85** (2012) 055026, [1201.5047].

[234] A. G. Akeroyd and C.-W. Chiang, *Phenomenology of Large Mixing for the CP-even Neutral Scalars of the Higgs Triplet Model*, *Phys. Rev.* **D81** (2010) 115007, [1003.3724].

[235] Y.-J. Zhang, J. Cao and W.-Q. Zhang, *Associated Production of the Charged and Neutral Higgs Bosons at the ILC within the Higgs Triplet Model*, *Int. J. Theor. Phys.* **55** (2016) 3981–3992.

[236] J.-F. Shen, Y.-P. Bi and Z.-X. Li, *Pair production of scalars at the ILC in the Higgs triplet model under the non-degenerate case*, *Europhys. Lett.* **112** (2015) 31002.

[237] PARTICLE DATA GROUP collaboration, K. A. Olive et al., *Review of Particle Physics*, *Chin. Phys.* **C38** (2014) 090001.

[238] A. Falkowski, F. Riva and A. Urbano, *Higgs at last*, *JHEP* **11** (2013) 111, [1303.1812].

[239] J. E. Kim, *Light Pseudoscalars, Particle Physics and Cosmology*, *Phys. Rept.* **150** (1987) 1–177.

[240] P. Vankov, *ATLAS Upgrade for the HL-LHC: Meeting the challenges of a five-fold increase in collision rate*, *EPJ Web Conf.* **28** (2012) 12069, [1201.5469].

[241] CMS collaboration, *Projected Performance of an Upgraded CMS Detector at the LHC and HL-LHC: Contribution to the Snowmass Process*, in *Proceedings, Community Summer Study 2013: Snowmass on the Mississippi (CSS2013): Minneapolis, MN, USA, July 29-August 6, 2013*, 2013. 1307.7135.

[242] https://twiki.cern.ch/twiki/bin/view/AtlasPublic/LuminosityPublicResultsRun2.

[243] TLEP Design Study Working Group collaboration, M. Bicer et al., *First Look at the Physics Case of TLEP*, *JHEP* **01** (2014) 164, [1308.6176].

[244] H. Baer, T. Barklow, K. Fujii, Y. Gao, A. Hoang, S. Kanemura et al., *The International Linear Collider Technical Design Report - Volume 2: Physics*, 1306.6352.

[245] CLIC Detector and Physics Study collaboration, H. Abramowicz et al., *Physics at the CLIC e+e- Linear Collider – Input to the Snowmass process 2013*, in *Proceedings, Community Summer Study 2013: Snowmass on the Mississippi (CSS2013): Minneapolis, MN, USA, July 29-August 6, 2013*, 2013. 1307.5288.

[246] J. F. Gunion, H. E. Haber, G. L. Kane and S. Dawson, *The Higgs Hunter's Guide*, *Front. Phys.* **80** (2000) 1–404.

[247] M. Carena, I. Low and C. E. M. Wagner, *Implications of a Modified Higgs to Diphoton Decay Width*, *JHEP* **08** (2012) 060, [1206.1082].

[248] F. del Aguila and J. A. Aguilar-Saavedra, *Distinguishing seesaw models at LHC with multi-lepton signals*, *Nucl. Phys.* **B813** (2009) 22–90, [0808.2468].

[249] F. de Campos, O. J. P. Eboli, J. Rosiek and J. W. F. Valle, *Searching for invisibly decaying Higgs bosons at LEP-2*, *Phys. Rev.* **D55** (1997) 1316–1325, [hep-ph/9601269].

[250] S. Moretti, *Detection of heavy charged higgs bosons in e+ e- —> t anti-b H- production at future linear colliders*, *Eur. Phys. J.* **C34** (2004) 157–163, [hep-ph/0306297].

[251] S. Komamiya, *Searching for Charged Higgs Bosons at O (1/2-tev to 1-tev) e^+e^- Colliders*, *Phys. Rev.* **D38** (1988) 2158.

[252] ATLAS collaboration, G. Aad et al., *Summary of the ATLAS experiment's sensitivity to supersymmetry after LHC Run 1 — interpreted in the phenomenological MSSM*, *JHEP* **10** (2015) 134, [1508.06608].

[253] A. Barr and J. Liu, *First interpretation of 13 TeV supersymmetry searches in the pMSSM*, 1605.09502.

[254] A. Buckley, "The hepthesis LATEX class."